PARAMETERIZATION AND MODELING OF COUPLED HEAT AND MASS TRANSPORT IN THE VADOSE ZONE

A Dissertation

by

ZHENLEI YANG

Submitted to the Office of Graduate and Professional Studies of
Texas A&M University
in partial fulfillment of the requirements for the degree of

DOCTOR OF PHILOSOPHY

Chair of Committee,	Binayak P. Mohanty
Committee Members,	Yalchin Efendiev
	Anthony T. Cahill
	Patricia K. Smith
Head of Department,	Stephen W. Searcy

December 2017

Major Subject: Biological and Agricultural Engineering

ABSTRACT

The coupled heat and mass transport in the vadose zone is essentially a multiphysics issue. Addressing this issue appropriately has remarkable impacts on soil physical, chemical and biological processes. That is, knowledge of heat, water and vapor transport in the shallow subsurface affects the soil evaporation pattern and rate, the contaminant volatilization and transport, and the greenhouse gas CO_2 transfer and emission, as well as seed germination, plant growth and soil microbial activity. In addition, the 2007 Phoenix Mars Mission also included specifically designed instrument to measure soil thermal properties, soil temperature and moisture content due to the central significance of soil heat and water dynamics to understanding land-atmosphere exchange and the possible life environment on Mars.

Most coupled heat and water transport modeling to date has focused on the interactions between liquid water, water vapor and heat transport in homogeneous soils. Comparatively little work has been done on evaporation from layered dry soils that involves simultaneous heat and water transport under diurnal field condition. Moreover, the classic coupled heat and water model usually neglected physical processes such as adsorptive water retention, nonwetting phase air flow, etc., which were found to be significant under specific conditions. However, it is largely elusive so far on the transport parameterizations (e.g., relative air permeability) and their associated effects (e.g., extended full range water retention) on coupled heat and water transport modeling under highly transient field conditions.

In order to address the above mentioned limitations, this dissertation aims to develop and validate a predictive multiphysics modeling framework with associated improved transport parameterizations for coupled soil heat and water transport in the homogeneous and heterogeneous shallow subsurface. To this end, the following research work is specifically conducted: (a) propose improved parameterizations to better predict the nonwetting phase relative permeability; (b) explore the effects of full range water retention curve on coupled heat and water transport in homogeneous soils; and (c) investigate the nonisothermal evaporation characteristics from layered dry soils considering the additional adsorptive water retention.

The results of this study showed that: (a) the proposed modified nonwetting phase relative permeability models are much more accurate, which can be readily adopted for improved parameterization in the nonisothermal two phase flow models for structured soils evaporation; (b) considering the full range water retention is important for better soil moisture and evaporation prediction in homogeneous soils under dry conditions where water is very limited (e.g., arid and semiarid environments); and (c) the upper layer properties (layering thicknesses and sequences) and hydraulic characteristics (capillary and adsorptive water retention) have important impacts on overall evaporation water losses in layered soil profiles.

DEDICATION

This dissertation is dedicated to my dear parents.

ACKNOWLEDGEMENTS

It is my great honor to thank so many people who helped me finish this dissertation successfully. I am sincerely grateful to my family, advisors, colleagues and friends for their constant encouragement and unselfish support during my PhD study at Biological and Agricultural Engineering Department, Texas A&M University.

I would like to thank my committee chair, Dr. Binayak P. Mohanty, for bringing me to his vadose zone research group. I gratefully acknowledge his tremendous support (both financially and mentally), constant encouragement, inspirational guidance and consistent patience during my whole PhD study. I also learned from him that to be a good researcher, one needs to have and keep the faith of passion, courageous conviction and strong sense of self. I am very grateful to my committee members Dr. Yalchin Efendiev, Dr. Anthony T. Cahill and Dr. Patricia K. Smith for their guidance, advice and support throughout the course of the research.

I would also like to thank Dr. Masaru Sakai for the help of modified Hydrus-1D code. I gratefully acknowledge Dr. Jan W. Hopmans, Dr. Xingxing Kuang and Dr. Jiu Jimmy Jiao for providing part of the relative air permeability data sets used in the study. I acknowledge the financial support of NSF (CMG/DMS 0934837) grants and OGAPS Dissertation Fellowships. In addition, I would also like to thank Dr. Zhuping Sheng and Dr. Ignacio Rodriguez-Iturbe very much for providing me the financial support at the final stage of my degree program.

I am very thankful to many friends, particularly Chao Li, Huijuan Cui, Hao Xu, Xingxing Kuang, Xin Liu, Xin Tong and VZRG group members (Nandita, Jonggun, Neelam, Samagra, Champa, Yongchul, Dipankar, Bhavna, and Raghu) for their unselfish assistance and helpful suggestions. I would personally acknowledge Nandita Gaur very much for her continuous encouragement and kind support so that I have the courage to not give up during those extremely difficult time. I am so blessed to have her as my group mate during my PhD study and I would cherish this friendship forever.

Thanks also go to the Biological and Agricultural Engineering Department faculty and staff for making my time at Texas A&M University a great experience.

Last, but definitely not the least, my heartfelt gratitude goes to my parents (Liansong Yang and Yuexian Zhang), my relatives (particularly, uncle Junlong Zhang, aunt Lianying Yang, and aunt Lixian Zhang), and my high school teacher (Zengwei Hua) for their unwavering encouragement and support. May God bless them all.

CONTRIBUTORS AND FUNDING SOURCES

This work was supervised by a dissertation committee consisting of Professor Binayak P. Mohanty [advisor] and Professor Patricia K. Smith of the Department of Biological and Agricultural Engineering, Professor Yalchin Efendiev of the Department of Mathematics, and Professor Anthony T. Cahill of the Department of Civil Engineering.

The data analyzed for Section 3 and 4 was partly provided by Professor Jan W. Hopmans, Professor Xingxing Kuang, and Professor Jiu Jimmy Jiao. The modified Hydrus-1D code for Section 5 and 6 was provided by Professor Masaru Sakai.

All other work conducted for the dissertation was completed by the student independently.

This work was made possible in part by National Science Foundation under Grant Number CMG/DMS 0934837.

Its contents are solely the responsibility of the authors and do not necessarily represent the official views of the National Science Foundation.

Graduate study was partly supported by a dissertation fellowship from Texas A&M University.

TABLE OF CONTENTS

Page

LIST OF FIGURES

Page

LIST OF TABLES

Page

1 GENERAL INTRODUCTION

1.1 Problem statement

Coupled heat and water movement in the vadose zone has been recognized and studied extensively. It is well known that there are two established approaches to analyze the coupled heat and water movement in the unsaturated porous media [*Ten Berge and Bolt*, 1988; *Feddes et al.*, 1988; *Raats*, 2001], i.e., the mechanistic approach [*Philip and de Vries*, 1957; *de Vries*, 1958] and the irreversible thermodynamic approach [*Taylor and Cary*, 1964; *Cary*, 1965; *Weeks et al.*, 1968]. However, it is noticed that the mechanistic approach is still widely used nowadays [e.g., *Bittelli et al.*, 2008; *Heitman et al.*, 2008a, 2008b; *Zeng et al.*, 2009, 2011a, 2011b; *Sakai et al.*, 2009, 2011; *Novak*, 2010; *Deb et al.*, 2011a, 2011b; *Garcia Gonzalez et al.*, 2012; *Banimahd and Zand-Parsa*, 2013] compared to the irreversible thermodynamic approach. As *Milly* [1982] pointed out, the limited use of irreversible thermodynamic approach is likely induced by two reasons, one is the lack of rigorous consideration of integration from microscopic pore scale to the macroscopic Darcy scale continuum equations; the other is the difficult obtainment of transport coefficients in this approach.

The theoretical framework of the mechanistic approach for coupled heat and water transport, was first established by *Philip and de Vries* [1957] (hereinafter referred to as PdV), who proposed a mathematical model to describe interactions between liquid water, water vapor and heat transport in porous media. The PdV model, was physically incomplete and consequently extended by several researchers via accounting for more

processes such as soil heterogeneity and hysteresis of moisture retention [*Milly*, 1982], vapor convection [*Cahill and Parlange*, 1998; *Parlange et al.*, 1998], gas flow and phase change [*Grifoll et al.*, 2005; *Smits et al.*, 2011], and adsorptive forces of soil moisture retention [*Mohanty and Yang*, 2013], etc. Despite the conceptual advances achieved compared to the original PdV theory [*Cahill and Parlange*, 1998; *Parlange et al.*, 1998; *Grifoll et al.*, 2005; *Smits et al.*, 2011; *Mohanty and Yang*, 2013], it is not necessarily conclusive that these additional physical processes are significantly important for the coupled heat and water transport descriptions in soils and across the soil-atmosphere interface, particularly for highly transient natural field conditions. For example, a recent detailed numerical analysis of coupled water-vapor-air-heat transport in field soils [*Novak*, 2016] casted doubts on the conclusions of *Cahill and Parlange* [1998] and *Parlange et al.* [1998]. Using the same Davis, California bare field soil (Yolo silt loam) data sets as in *Cahill and Parlange* [1998] and *Parlange et al.* [1998], *Novak* [2016] found that the diurnal soil heating (natural convection), the low-frequency barometric pressure fluctuations (forced convection), and the enhancement of soil vapor diffusion all have the negligible effects on evaporation under natural field conditions. *Novak* [2016] concluded that the original version of the PdV theory is consistent with the *Cahill and Parlange* [1998]'s field measurements. The consideration of thermal vapor/air convection is probably more important and relevant for highly permeable porous media (e.g., structured macropore soils and fractured rocks) but not the homogeneous or layered low permeability soils [*Levintal et al.*, 2017]. In fact, to date, the PdV theory and its extensions [e.g., *de Vries*, 1958; *Milly*, 1982] have long been accepted and used

successfully to determine the coupled heat and water transport in soils (mainly low permeability) [e.g., *Novak*, 2010, 2016; *Garcia et al.*, 2011; *Garcia Gonzalez et al.*, 2012; *Hou et al.*, 2016; *Dijkema et al.*, 2017].

For high permeability (permeability ranging from 10^{-7} to 10^{-6} m^2) soil evaporation [*Weisbrod and Dragila*, 2006; *Weisbrod et al.*, 2009; *Levintal et al.*, 2017], it is important to adopt the nonisothermal two phase mass flow model, in which nonwetting phase relative permeability is an indispensable parameter. However, it is found that the study on nonwetting phase relative permeability is relatively limited compared to the research upon the wetting phase relative permeability (i.e., relative hydraulic conductivity). This is reflected by the limited experimental nonwetting phase relative permeability data available in literature. Consequently, the accuracy of the existing nonwetting phase relative permeability models (e.g., *Brooks and Corey* [1964]-*Burdine* [1953] and *van Genuchten* [1980]-*Mualem* [1976]) for predicting relative air permeability is not very clear because of the rather limited model-data comparison effort with respect to the nonwetting phase relative permeability parameter [*Webb*, 2006].

For low permeability (permeability$<10^{-7}$ m^2) soil evaporation, the application of the PdV theory and its extensions [e.g., *de Vries*, 1958; *Milly*, 1982] is still widely acceptable. However, for dry soils under arid and semiarid environments [e.g., *Scanlon et al.*, 1997; *Hou et al.*, 2016; *Dijkema et al.*, 2017], liquid film flow induced by the adsorptive forces may play a significant role in the soil evaporations [*Scanlon et al.*, 1997; *Mohanty and Yang*, 2013]. Unfortunately, using extended full range water retention curve to model soil state variables and land surface evaporation fluxes for

natural dry field conditions with experimental data in the context of coupled heat and water transport is not common yet for homogeneous soils and even less known for layered heterogeneous soils.

1.2 Motivation

The coupled heat and water transport in the vadose zone is essentially a multiphysics issue. Addressing this issue appropriately can better facilitate the research upon the land and atmosphere interactions. Motivated by the limitations discussed in section 1.1, this dissertation aims to address these limitations by (1) proposing better parameterizations on nonwetting phase relative permeability, which can be used in nonisothermal two phase flow models in high permeability soils; and (2) investigating extended full range water retention curve effect on water content and evaporation prediction in low permeability homogeneous and layered soils at Darcy scale in the context of coupled heat and water modeling.

1.3 Research objectives

The overarching objective of the dissertation is to develop and validate a predictive multiphysics modeling framework with associated improved transport parameterizations for coupled soil heat and water transport in the homogeneous and heterogeneous shallow subsurface. To this end, the following objectives will be specifically pursued:

1. Propose improved parameterizations to better predict the nonwetting phase relative permeability for nonisothermal two phase mass flow modeling in high permeability porous media such as structured macropore soils and fractured rocks.

2. Determine the effects of full range water retention curve on coupled heat and water transport in homogeneous low permeability soils at Darcy scale.

3. Investigate the nonisothermal evaporation dynamics from layered dry low permeability soils with the further consideration of additional adsorptive water retention at Darcy scale.

In Section 2, the research work on coupled soil heat and water transport is briefly reviewed and summarized.

In Section 3, effective and improved parameterizations of Burdine, Mualem and Alexander and Skaggs models for relative air permeability predictions are proposed by adopting the Kosugi water retention function.

Section 4 explores the predictive ability of ten relative air permeability models via adopting the Assouline et al. water retention function.

In Section 5, coupled heat and water transport characteristics in the homogeneous shallow subsurface are investigated. Specifically, the extended full range water retention curve effect on dry low permeability soils evaporation is explored.

Section 6 investigates the impact of full range (saturation to oven dryness) water retention curve on evaporation and water redistribution from layered low permeability soils.

2 LITERATURE REVIEW

2.1 Synopsis

Coupled heat and water movement in the vadose zone is briefly summarized, with a focus on the increasing theoretical, numerical and experimental progresses achieved during the past several decades. It is increasingly important to incorporate the air flow into the traditional vapor diffusion based heat and water transport model in high permeability soils. The full range hydraulic properties should be adopted for the better evaporation prediction in dry soils. Several controversial constitutive relationships including the soil hydraulic, thermal, and air parameters are analyzed in greater detail. With the continuous improved numerical solution, it is more imperative to acquire more accurate laboratory and field experimental data to validate the theoretical and numerical models. Finally, the possible future research challenges are discussed.

2.2 Introduction

Coupled heat and water movement in vadose zone has been recognized and studied for a long time [*Bouyoucos*, 1915]. It has always been of vital interest to the fields of vadose zone hydrology, environmental engineering, and agronomy. The simultaneous moisture and heat transfer in unsaturated porous media has remarkable impacts on soil physical processes such as soil evaporation that consequently affects exchange of mass and energy fluxes between land surface and atmosphere [*Brubaker and Entekhabi*, 1996; *Judge et al.*, 2003; *Brutsaert*, 2005; *Garcia Gonzalez et al.*, 2012], chemical processes such as contaminant volatilization and transport [*Cohen and Ryan*,

1989; *Nassar et al.*, 1999], and biological processes such as seed germination, plant growth and soil microbial activity [*Sung et al.*, 2002; *Ji et al.*, 2009]. In particular, the central significance of soil heat and water dynamics to understanding land and atmosphere interaction which is closely related to weather and climate situations even resulted in the Phoenix Mars Mission included specifically designed instrument, i.e., the thermal and electrical conductivity probe [*Zent et al.*, 2009], to measure soil thermal properties, temperature and moisture content [*Zent et al.*, 2010].

Considering such far-reaching importance of coupled heat and water transfer in vadose zone, review work on this topic is relatively limited. In the early 1980s, *Childs and Malstaff* [1982] comprehensively summarized the simultaneous heat and water flow in unsaturated soils in their final reports. *De Vries* [1987] briefly revisited and reviewed the *Philip and de Vries*' [1957] theory (hereinafter referred to as PdV) of coupled heat and moisture transport in porous media. Both *Feddes et al.* [1988] and *Milly* [1988] included concise nonisothermal unsaturated water flow sections in their overviews upon modeling of soil water transport in the unsaturated zone. A more recent review on soil heat and water movement was published by *Parlange et al.* [1998], who mainly proposed the new convectively enhanced water vapor transport theory that is due to natural advection of air. To date, no relatively detailed review concerning coupled heat and water transfer in vadose zone can be found in soil hydrology, despite continuous theoretical, numerical and experimental progresses have been achieved.

The most significant theoretical advances in this topic is probably the recognition of the importance of the gas phase effect in traditional water vapor diffusion based

theory of *Philip and de Vries* [1957] and consequently the formulation of a general nonisothermal water and gas two phase mass model [*Grifoll et al.*, 2005; *Grifoll*, 2013; *Smits et al.*, 2011, 2012; *Zeng et al.*, 2011a, 2011b; *Mosthaf et al.*, 2011, 2014; *Davarzani et al.*, 2014; *Trautz et al.*, 2015]. This is particularly important for high permeability (permeability ranging from 10^{-7} to 10^{-6} m^2) soils instead of low permeability (permeability<10^{-7} m^2) soils [*Novak*, 2016; *Levintal et al.*, 2017]. It is well recognized that the PdV theory could not capture the appropriate transfer mechanisms [e.g., *Westcot and Wierenga*, 1974; *Cahill and Parlange*, 1998] in shallow subsurface soils most of the time [e.g., neglect of adsorptive water retention, natural and forced vapor/air convection, etc.].

The mathematical formulation of the coupled heat and water transfer model is a set of highly nonlinear partial differential equations (PDEs) that typically make the analytical solution extremely difficult, if not impossible. Therefore, the numerical solution method is required to solve the set of PDEs. In addition to the consistent development in numerical approaches such as finite difference, finite element and finite volume methods as well as the mixed form, a variety of well documented public or commercial codes are also available like Hydrus, Tough2, and COMSOL Multiphysics, which greatly facilitate the numerical modeling and analysis of this complicated and coupled two phase mass and energy transfer processes.

With regard to the experimental advances, some new measurement apparatus such as heat pulse probe (HPP) are designed to capture fine scale, transient soil heat and water transport in vadose zone. They provide the necessary accurate experimental data in

laboratory as well as in field conditions that could be used to test and further develop the coupled heat and water transfer theory.

Inspired by these advances and due to the limited review work, we try to present a relatively comprehensive overview on coupled heat and water transfer in vadose zone with a focus on soils porous media in this dissertation. Furthermore, we mainly restrict our work at continuum Representative Elementary Volume (REV) scale and in unfrozen unsaturated porous media (review on porous media such as fracture rock [e.g., *Tsang et al.*, 2009] or frozen soils [e.g., *Liu et al.*, 2012] could be found elsewhere).

This literature review is divided into eight sections. Section 2.3 describes the conceptual model development on coupled soil heat and water movement. In section 2.4, several new insights on hydraulic, thermal and air parameters are presented. Section 2.5 discusses the approaches used to solve this coupled model. Conducting laboratory and field experiments to validate the conceptual model is provided in section 2.6. Section 2.7 introduces some new measurement techniques. Section 2.8 addresses the influences of coupled heat and water transport on soil evaporation. The outlook and further research challenges are given in section 2.9.

2.3 Conceptual models formulation and development

Typically in soil hydrology literature, there are two well-established approaches to analyze the coupled heat and water movement in unsaturated porous media [*Ten Berge and Bolt*, 1988; *Feddes et al.*, 1988; *Raats*, 2001], that is, the mechanistic approach [*Philip and de Vries*, 1957; *de Vries*, 1958] and the irreversible thermodynamic approach [*Taylor and Cary*, 1964; *Cary*, 1965; *Weeks et al.*, 1968]. It is worth noting

that the mechanistic approach is still widely accepted and used today [e.g., *Saito et al.*, 2006; *Bittelli et al.*, 2008; *Heitman et al.*, 2008b; *Zeng et al.*, 2009, 2011a, 2011b; *Sakai et al.*, 2009, 2011; *Novak*, 2010; *Garcia Gonzalez et al.*, 2012] compared to the irreversible thermodynamic approach.

2.3.1 The mechanistic formulation

The transfer mechanisms on coupled heat and water movement (Figure 2.1) in shallow soils have been described in greater detail by *Heitman and Horton* [2011]. In this section, we mainly discuss six important conceptual models that reflected the advances in mechanistic formulation approach.

Philip and de Vries [1957], firstly proposed a mathematical model to describe interactions between liquid water, water vapor and heat transport in porous media under nonisothermal conditions by extending the well-known isothermal Richards equation. This PdV model consists of a water mass balance equation that takes into account the liquid as well as the vapor phases in response to gravity, soil moisture content and temperature gradients and an energy balance equation that considers both heat conduction and latent heat of vaporization. The PdV approach was subsequently extended by *de Vries* [1958], who further took heat of wetting, transfer of sensible heat and explicit distinction between changes of moisture content in the liquid and the vapor phases into consideration. *De Vries* [1987] revisited the PdV theory and discussed the assumptions and limitations of the PdV theory. Based on *de Vries* [1987], the PdV model has the following main shortcomings:

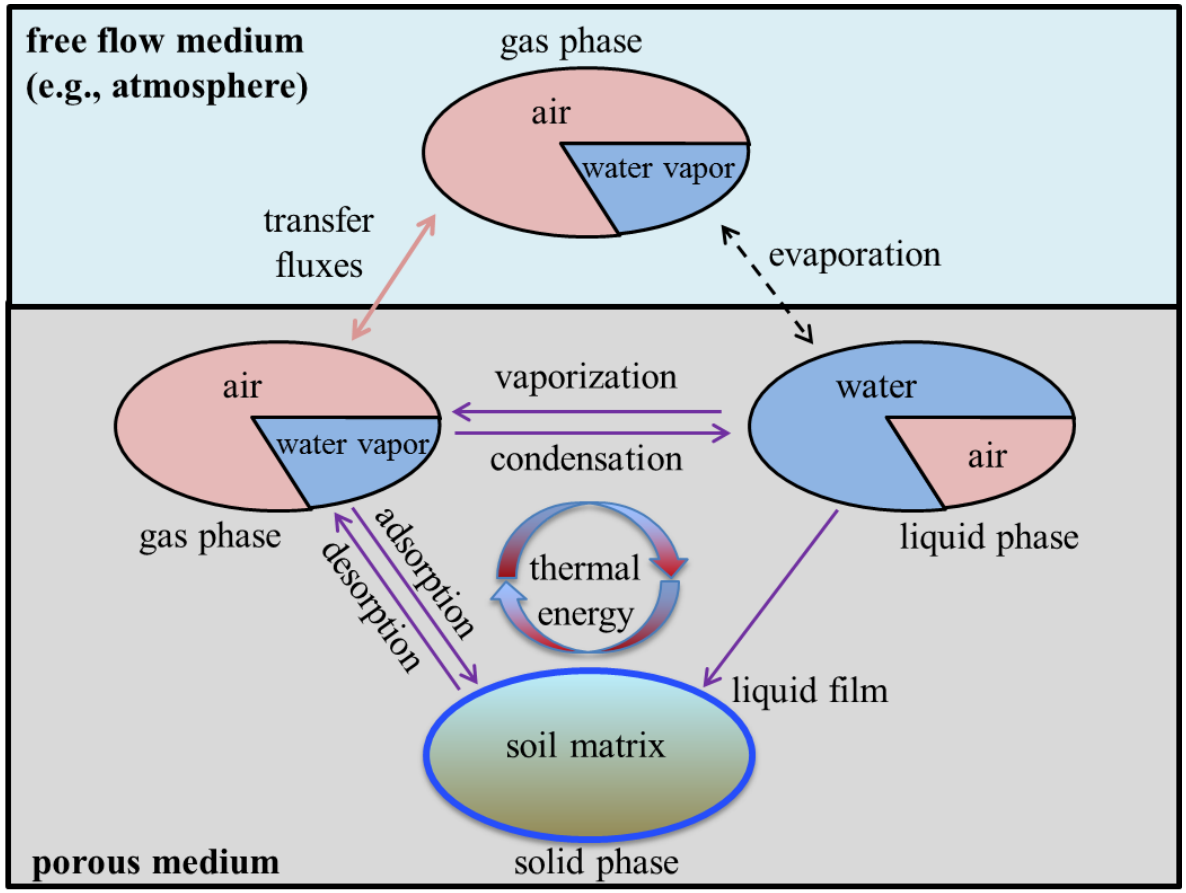

Figure 2.1 Model concept of coupled heat and water transfer with a single phase in the free flow that interacts with two fluid phases in the porous medium (modified from Mosthaf et al. [2011]).

(a) Hysteresis and adsorption of soil water retention curves and unsaturated hydraulic conductivity coefficients is not taken into account.

(b) The model does not apply when the porous media is not inert and rigid (such as deformable rocks or shrinking and swelling clay soils) and is not homogeneous (horizontal or vertical heterogeneous) and isotropic.

(c) The theory is not applicable in frozen soils (i.e., freezing and thawing processes are excluded) as well as in saline soils (osmotic potential is not considered).

(d) The local thermodynamic nonequilibrium (mainly, chemical nonequilibrium) within the porous media is not accounted for (e.g., kinetic interface mass and energy transfer could not be modeled).

(e) The convection and Knudsen diffusion in the gas phase are not considered.

(f) The water vapor enhancement theory has no direct experimental evidence.

The above limitations are emphasized here because they indicated that the PdV approach is not physically complete and the further test and improvement of this theory is warranted. Furthermore, the most controversial aspect of this pioneering model is the enhanced water vapor transport theory which was originally proposed to improve the agreement between the model and measured data. However, this theory was questioned recently by several investigators [*Webb and Ho*, 1998; *Shokri et al.*, 2009; *Shahraeeni and Or*, 2012].

Recognizing the PdV theory is only applicable to homogeneous porous media due to that water content is discontinuous across the interface between different sediment textures in layered soil profiles, *Sophocleous* [1979] firstly tried to modify the

PdV model so as to make it valid in non-homogeneous unsaturated and saturated porous media. However, two main theoretical errors existed in the formulation of Sophocleous approach [*Herkelrath*, 1981; *Milly*, 1982] and this consequently restricted the popularity of Sophocleous's model. On the basis of the work of *Sophocleous* [1979], *Milly* [1982] modified the PdV theory and suggested using soil matric pressure head instead of moisture content as a dependent variable in order to take soil vertical heterogeneity and soil water retention hysteresis into consideration. The heat of wetting was also accounted for in Milly's model, which is physically more rigorous. As such, Milly model is still widely used when researchers deal with coupled heat and water movement in unsaturated porous media if the soil profile is not vertically homogeneous [e.g., *Scanlon and Milly*, 1994; *Braud et al.*, 1995; *Garcia Gonzalez et al.*, 2012].

When it comes to the salty soils, which is not uncommon in natural settings, *Nassar and Horton* [1989b, 1992] developed a mathematical model by extending the PdV theory to additionally include osmotic potential effects in unsaturated soils. As such, their approach is particularly applicable for analysis of simultaneous movement of water, solute and heat in salty, partially saturated soils under nonisothermal conditions. Later, *Nassar and Horton* [1997, 1999] modified their theory in terms of using matric potential instead of moisture content as the dependent variable in their theory in order to make the theory suitable in non-homogeneous saline soil profiles inspired by Milly's approach. It should be noted that their theory only accounts for one solute and does not take into account the effect of the osmotic potential on the soil hydraulic coefficient, *Yakirevich* [1997] addressed these problems.

Cahill and Parlange [1998] found remarkable discrepancies between the measured vapor fluxes in field soils and those calculated from the PdV model. They thus asserted that the PdV theory on water vapor transport is incomplete and the vapor transport theory needs to be revisited. Subsequently, *Parlange et al.* [1998] proposed that volume expansion and contraction of near surface soil air resulted from diurnal warming and cooling could transfer water vapor in the gas phase by convection and this thermal convective vapor flux was larger and more significant than diffusive vapor flux which was predicted by the classic PdV theory. They demonstrated that the inclusion of such mechanism in addition to the PdV theory is able to increase the predictive capability of the new model in field environment.

It should be mentioned that there are two kinds of gas convection in porous media, i.e., forced convection caused by the gas pressure gradient and natural convection induced by gas density differences in a gravitational field, typically produced by the temperature gradient [*Webb and Ho*, 1998]. Apparently the convectively enhanced water vapor transport mechanism considered in *Parlange et al.* [1998] model belongs to the natural convection but not forced convection. It is interesting to note that the work of *Cahill and Parlange* [1998] and *Parlange et al.* [1998] indicated that the enhanced vapor flow due to natural gas convection should be significant in homogeneous field soils. Recently, *Weisbrod et al.* [2009] suggested that this natural convection mechanism is probably more significant in macropores and fractures in structured porous media at nighttime during a diurnal time scale based on their filed experimental measurement because of the larger permeability of macropores and fractures. Moreover, forced

convection produced by the gas pressure gradient is also existing in the field environment and enhanced convective vapor flow caused by such forced gas convection may also need to be accounted for [e.g., *Zeng et al.*, 2011a, 2011b]. However, some investigators claimed that such forced gas convection is not very significant [e.g., *Rose*, 1968a, 1968b; *Novak*, 2016] in the field. It is believed that simultaneously considering these two kinds of gas convection is probably more important because it is difficult to explicitly separate these two convections in natural field environments. However, a detailed numerical analysis of coupled water-vapor-air-heat transport in field soils [*Novak*, 2016] questioned the conclusions of *Cahill and Parlange* [1998] and *Parlange et al.* [1998]. Using the same Davis, California bare field soil (Yolo silt loam) data sets as in *Cahill and Parlange* [1998] and *Parlange et al.* [1998], *Novak* [2016] found that the diurnal soil heating (natural convection), the low-frequency barometric pressure fluctuations (forced convection), and the enhancement of soil vapor diffusion all have the negligible effects on evaporation under natural field conditions. *Novak* [2016] concluded that the original version of the PdV theory is consistent with the *Cahill and Parlange* [1998]'s field measurements. In addition, a recent experimental analysis [*Levintal et al.*, 2017] demonstrated that the thermal vapor/air convection typically occurs for highly permeable porous media (e.g., structured macropore soils and fractured rocks) with permeability ranging from 10^{-7} to 10^{-6} m^2. The findings of *Levintal et al.* [2017] are consistent with the results of *Novak* [2016] in that the natural and forced convection is found to be insignificant and negligible in low permeability ($<10^{-7}$ m^2) soils under natural field conditions.

Grifoll et al. [2005] proposed a general coupled water mass and heat energy transfer theory in variably saturated porous media by explicitly accounting for the gas phase effect. Their model considered gas phase convection, water vapor convection and dispersion and sensible heat dispersion in liquid phase in addition to the mechanisms taken into account by the PdV theory. This model did not use empirical water vapor enhancement factor postulated by PdV and the phase change water flux (i.e., kinetic interphase water mass transfer) was taken into account in the model formulation. However, the phase change flux had no explicit mathematical formulation but was solved during the numerical modeling process as a complete fitting term. The gas convection considered in this formulation is attributed to both gas density temperature effects and changes in gas phase volume caused by variation in liquid water content. The forced gas convection due to atmospheric pressure fluctuation was also ignored just as the previous *Parlange et al.* [1998] model. One interesting finding of this work was that the water vapor dispersion mechanism, which was usually ignored in coupled heat and water transfer theory [e.g., *Philip and de Vries*, 1957; *Mosthaf et al.*, 2011], is important in the near surface soil layer although water vapor convection is very small based on the analysis of two field studies. Apparently whether or not the water vapor dispersion mechanism is important is not conclusive so far and needs further research.

More recently, *Smits et al.* [2011] also developed a nonequilibrium mechanistic approach to simulate simultaneous, transient water, gas and heat movement in partially saturated porous media by explicitly taking into account the not instantaneous phase change rate between liquid water and water vapor. This model is different from *Grifoll et*

al. [2005] in that it has an explicit empirical first-order kinetic interphase water mass change term that has a fitting parameter. The vaporization rate followed the similar assumption as was done in *Bixler* [1985] and *Zhang and Datta* [2004]. Comparing the traditional equilibrium as well as this nonequilibrium based approaches with their laboratory sand column experimental data, *Smits et al.* [2011] arrived at the conclusion that the nonequilibrium liquid/gas phase change should be taken into account for modeling coupled heat and water movement under highly transient field conditions. However, the comment by *Novak* [2012] and the reply by *Smits et al.* [2012] indicated that the nonequilibrium based approach is still controversial and inconclusive so far. The empirical vaporization rate term with a fitting parameter is unable to describe the kinetic interphase water mass transfer from a clear physically based perspective [*Niessner and Hassanizadeh*, 2009; *Ahrenholz et al.*, 2011].

The respective mechanisms considered in these six classic and important conceptual models are shown in Table 2.1 for comparison. These six models are all in 1 Dimension and could be extended to 2 Dimension [e.g., *Chung and Horton*, 1987] or 3 Dimension when necessary. On the basis of the above analysis and the conceptual model (Figure 2.1), one can easily formulate the two phase mass and heat transfer model based on the conservation of mass, energy, and momentum (expressed in the extended general Darcy's law).

To this point, testing the above different models received attentions recently [e.g., *Heitman et al.*, 2008b; *Novak*, 2010], however, comprehensive and systematic comparison of the different models using laboratory or field experiments data is still

Table 2.1 Mechanisms considered by six mechanistic conceptual models

Process	Mechanisms	PdV [1957]	Milly [1982]	Nassar et al. [1989]	Parlange et al. [1998]	Grifoll et al. [2005]	Smits et al. [2011]
Water flow	gravity	Y	Y	Y	Y	Y	Y
	matric potential gradient	Y	Y	Y	Y	Y	Y
	temperature gradient	Y	Y	Y	Y	Y	
	osmotic pressure gradient			Y			
	hysteresis		Y				
Vapor flow	vapor diffusion	Y	Y	Y	Y	Y	Y
	vapor convection				Y	Y	Y
	vapor dispersion					Y	
Gas flow	mixing of vapor and air				Y	Y	Y
Heat flow	conduction	Y	Y	Y	Y	Y	Y
	flow of latent and sensible heat	Y	Y	Y	Y	Y	Y
	dispersion					Y	

lacking, which is extremely important and should be able to shed new insights for the future research.

In addition, due to the ubiquitous horizontal inhomogeneity in the field settings such as macropores, fractures, root channels and other preferential flow phenomena, development of the conceptual coupled heat and water models describing the preferential evaporation flows in unsaturated soils is pressing and meaningful. Since the preferential infiltration flow was well studied in area of coupled water and solute transport [e.g., reviews by *Šimůnek et al.*, 2003; *Gerke*, 2006; *Köhne et al.*, 2009] or nonisothermal unsaturated water flow in heterogeneous fracture rocks [see a review by *Tsang et al.*, 2009], techniques such as dual porosity and dual permeability inspired from these areas seem promising. As *Milly* [1988] pointed out, the macropores would provide the escape paths for air trapped below wetting fronts, therefore, including air flow in the coupled heat and water model is particularly important but few in the context of developing appropriate nonisothermal two phase mass models in structured soils. This is extremely important because natural or forced vapor/air convection is typically significant and nonnegligible in high permeability soils such as structured macropore soils and fractured rocks, whereas for the low permeability soils (permeability$<10^{-7}$ m^2), such natural and forced convection is insignificant and thus negligible [*Rose*, 1968a, 1968b; *Novak*, 2016; *Levintal et al.*, 2017].

2.3.2 The thermodynamic formulation

The thermodynamic formulation is based on irreversible thermodynamics approach and generally considered to be a physically rigorous method due to the

foundations of this theory are rested on sound thermodynamic principles. This approach was fully studied by *Taylor and Cary* [1964], *Cary* [1965], *Weeks et al.* [1968], *Groenevelt and Kay* [1974], *Kay and Groenevelt* [1974] and others in 1960s-1970s. Comparing this thermodynamic approach with mechanistic approach could be found in *Cassel et al.* [1969], *Raats* [1975] and *Ten Berge and Bolt* [1988].

This thermodynamic approach has lacked rigorous consideration of the problem of integration from the microscopic pore scale to the macroscopic continuum equations [*Milly*, 1982], furthermore, measurement of the parameters of this approach is difficult to achieve. Moreover, soil water was treated as a single-component fluid in this approach [*Heitman and Horton*, 2011], which is also probably incorrect. These reasons probably lead to the unpopularity of this method nowadays, although we could still find little research on this approach [e.g., *Prunty*, 2002].

However, based on a series of works by *Hassanizadeh and Gray* [1979a, 1979b, 1980], *Niessner and Hassanizadeh* [2008, 2009] pointed out the drawbacks of classical mechanical approach discussed in section 2.3.1 in three ways: 1. The assumption that Darcy's law is applicable simultaneously for liquid and gas convective flow in porous media is empirical and questionable because Darcy's law was originally derived for a homogeneous saturated sand column; 2. There are no definite meaning of capillary pressure at REV scale; 3. The mechanic approach ignores the interphase energy transfer (Figure 2.2) although nonequilibrium based approach [*Smits et al.*, 2011] empirically accounts for kinetic mass transfer between liquid water and vapor water in porous media. Due to the inherit limitation of the classical mechanical approach, one should

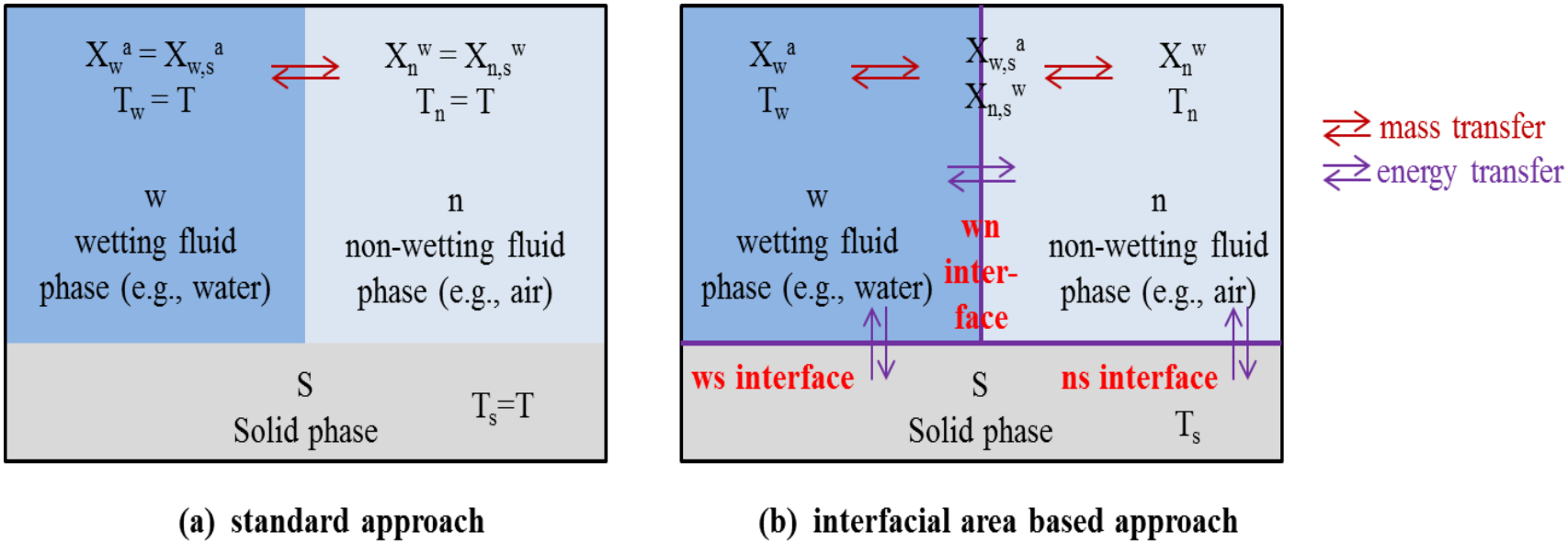

Figure 2.2 Conceptual models of energy and mass transfer on the macro REV scale using a standard approach and an interfacial area based approach (modified from Niessner and Hassanizadeh [2009]).

regard the six conceptual models introduced in section 2.3.1 as working assumption models but not totally physically based models.

There are five alternative approaches as suggested by *Niessner* [2009] to overcome the weakness of the classical mechanical approach:

(1) Mixture theory approach by *Bowen* [1982].

(2) Rational thermodynamics approach by *Hassanizadeh and Gray* [1980, 1990, 1993a, 1993b].

(3) Thermodynamically constrained averaging theory (TCAT) by *Gray and Miller* [2005] and *Miller and Gray* [2005] as well as *Jackson et al.* [2009]. For the details of the TCAT approach, there was a review on this topic [*Gray et al.*, 2013].

(4) Averaging and nonequilibrium thermodynamics by *Marle* [1981] and *Kalaydjian* [1987].

(5) Approach based on formulation of balance equations for percolating and non-percolating fraction of each phase by *Hilfer* [2006].

Among these five approaches, approaches (2) and (3) are most widely recognized and used. This is perhaps because only these two approaches include interfacial area as a state variable and thus make it possible to physically accounting for interphase mass and energy transfer using these two approaches [*Ahrenholz et al.*, 2011]. However, these two approaches also have weaknesses in that the parameters typically based on the pore scale upscaling values that are not easily measured. Moreover, these approaches are mathematically more complicated than that of the mechanical approach [*Ahrenholz et al.*, 2011]. Therefore, although these alternative approaches are highly physically based,

the usefulness is still limited compared to the classical mechanical approach in soil hydrology area. However, these models are evolving models as suggested by *Miller et al.* [2013] and certainly deserve deeper research.

2.4 Hydraulic, air and thermal parameters

As stated previously, the mechanical formulation (still the most widely used modeling approach today) needs the constitutive relationship to make the model solvable. Therefore, the determination of hydraulic, air and thermal parameters is central to the accuracy of model parameterization and the corresponding solution. However, to date, a number of parameters are still very controversial and uncertain that will be discussed in this section.

2.4.1 Isothermal unsaturated hydraulic conductivity

Usually, isothermal unsaturated hydraulic conductivity could be estimated from water retention and saturated hydraulic conductivity data by assuming that the unsaturated porous medium behaves like a bundle of capillary tubes [e.g., *Burdine*, 1953; *Brooks and Corey*, 1964; *Mualem*, 1976; *van Genuchten*, 1980], a recent review on this topic was given by *Assouline and Or* [2013]. This method is commonly used in soil water modeling and proved to be effective when the soil is wet or moist. However, as *Scanlon et al.* [1997] and *Goss and Madliger* [2007] pointed out, in many arid and semiarid areas such as desert environment, water may be adsorbed as films and the traditional hydraulic functions are not suitable to describe the water retention curve at low water content (WC) condition [*Ross et al.*, 1991; *Campbell and Shiozawa*, 1992; *Rossi and Nimmo*, 1994; *Fayer and Simmons*, 1995; *Morel-Seytoux and Nimmo*, 1999;

Webb, 2000; *Khlosi et al.*, 2006; *Lebeau and Konrad*, 2010; *Zhang*, 2011]. In addition, the unsaturated hydraulic conductivity [*Tuller and Or*, 2001; *Peters and Durner*, 2008; *Lebeau and Konrad*, 2010; *Zhang*, 2011; *Peters*, 2013; *Rudiyanto et al.*, 2015] at low moisture content is considerably higher than that would be predicted with the classical capillary flow based *van Genuchten* [1980] and *Mualem* [1976] model or many other similar approaches.

It is well known that coupled heat and water movement is particularly significant in water limited areas such as desert since water vapor would become important in such environment [*Scanlon and Milly*, 1994; *Zeng et al.*, 2009, 2011a, 2011b; *Garcia Gonzalez et al.*, 2012], therefore, extending water retention curve and hydraulic conductivity for full range saturation (e.g., Table 2.2) should be taken into account when dealing with heat and water movement in dry soils. This would provide us new insights on estimates of soil evaporation. For example, the evaporation rate would be underestimated if one does not consider adsorption forces and isothermal film flow in low water content soils [e.g., *Goss and Madliger*, 2007; *Peters and Durner*, 2008; *Mohanty and Yang*, 2013; *Ciocca et al.*, 2014; *Yang et al.*, 2017a].

Andraski and Jacobson [2000] were probably among the first to conduct research on this topic. They compared the simulated results derived by using the Rossi-Nimmo (RN) full range function and the common Brooks-Corey function. They found that RN function can improve prediction of water potential in top soils especially under dry conditions and soil temperature throughout the profile. They claimed that such

Table 2.2 Unextended and extended water retention curve and unsaturated hydraulic conductivity

Models	Unextended water retention curve	Extended water retention curve
Fayer and Simmons [1995]	$\theta = \theta_r + (\theta_s - \theta_r)\left[\frac{h_b}{h}\right]^{\lambda}$	$\theta = \theta_a\left(1-\frac{\ln(h)}{\ln(h_0)}\right)+\left(\theta_s-\theta_a\left(1-\frac{\ln(h)}{\ln(h_0)}\right)\right)\left[\frac{h_b}{h}\right]^{\lambda}$
	$\theta = \theta_r + (\theta_s - \theta_r)\left[\frac{1}{1+(\alpha h)^n}\right]^{\left(1-\frac{1}{n}\right)}$	$\theta = \theta_a\left(1-\frac{\ln(h)}{\ln(h_0)}\right)+\left(\theta_s-\theta_a\left(1-\frac{\ln(h)}{\ln(h_0)}\right)\right)\left[\frac{1}{1+(\alpha h)^n}\right]^{\left(1-\frac{1}{n}\right)}$
Webb [2000]	$\theta = \theta_r + (\theta_s - \theta_r)\left[\frac{1}{1+(\alpha h)^n}\right]^{\left(1-\frac{1}{n}\right)}$	$h = 10^{[\gamma(\theta-\theta_{wm})+\log 10 h_m]}(\eta_w < \eta_{wm}) + \alpha^{-1}\left(S_w^{-(1/m)}-1\right)^{(1/n)}(\eta_w \geq \eta_{wm})$
Khlosi et al. [2006]	$\theta = \theta_r + (\theta_s - \theta_r)erfc\left[\frac{\ln\left(\frac{h}{h_m}\right)}{\sqrt{2}\sigma}\right]$	$\theta = \theta_a\left(1-\frac{\ln(h)}{\ln(h_0)}\right)+\frac{1}{2}\left(\theta_s-\theta_a\left(1-\frac{\ln(h)}{\ln(h_0)}\right)\right)erfc\left[\frac{\ln\left(\frac{h}{h_m}\right)}{\sqrt{2}\sigma}\right]$

Table 2.2 Continued

Models	Unextended hydraulic conductivity	Extended hydraulic conductivity
Peters and Durner [2008]	$K_r = S_e^{\tau}\left[\frac{\int_0^{S_e} h^{-k} dS_e(h)}{\int_0^1 h^{-k} dS_e(h)}\right]^{\beta}$	$K_r = (1-w)S_e^{\tau}\left[\frac{\int_0^{S_e} h^{-k} dS_e(h)}{\int_0^1 h^{-k} dS_e(h)}\right]^{\beta} + wS_e^{\tau_2}$
Lebeau and Konrad [2010]	$K_r^{cap} = S_e^{\tau}\left[\frac{\int_0^{S_e} h^{-k} dS_e(h)}{\int_0^1 h^{-k} dS_e(h)}\right]^{\beta}$	$K_r = S_e^{\tau}\left[\frac{\int_0^{S_e} h^{-k} dS_e(h)}{\int_0^1 h^{-k} dS_e(h)}\right]^{\beta} + \left(1-\frac{\theta_c}{\theta_s}\right)K_r^{film}$ $K_r^{film} = \frac{1}{k_s}\left[\frac{4\rho_0 g}{\pi\mu_0 D}(1-n)\delta^3\right] \quad \delta \geq 10nm$ $K_r^{film} = \frac{1}{k_s}\left[\frac{4\rho_0 g}{\pi\mu_0 D}(1-n)\delta^3\right] \quad \delta < 10nm$
Zhang [2011]	$K_r^{cap} = S_e^{\tau}\left[\frac{\int_0^{S_e} h^{-k} dS_e(h)}{\int_0^1 h^{-k} dS_e(h)}\right]^{\beta}$	$K_r = S_e^{\tau}\left[\frac{\int_0^{S_e} h^{-k} dS_e(h)}{\int_0^1 h^{-k} dS_e(h)}\right]^{\beta} + K_r^{film}$ $K_r^{film} = fb(1-\phi)\sqrt{d_g}\left[1+\frac{\rho g d_g \lvert h\rvert^{-1.5}}{2\sigma}\right]$

improvement could be important for calculations of liquid and vapor flow in near-surface soils and in deep unsaturated zones of arid and semiarid regions.

Katata et al. [2007] used the *Webb* [2000] full range water retention function in their model. *Sakai et al.* [2009, 2011] adopted the *Fayer and Simmons* [1995] full range water retention function in their model. *Gran et al.* [2011] also used the full range water retention function similar to the *Fayer and Simmons* [1995] in their simulation upon coupled water, solute and heat transfer in porous media. More recently, *Mohanty and Yang* [2013] also employed the *Fayer and Simmons* [1995] full range water retention function in their synthetic coupled heat and water numerical simulation.

Researchers increasingly recognized this important aspect and more research could be expected on this topic in the future. However, most investigators to date are just using the full range water retention curve in their simulation, which was combined with the *Mualem* [1976] unsaturated hydraulic conductivity model. It seems that using the full range unsaturated hydraulic conductivity is also needed however very few for now [*Smits et al.*, 2012]. It should be emphasized that as long as water retention curve is extended to oven dry, the difference between unextended and extended full range unsaturated hydraulic conductivity is not significant at all [*Lebeau and Konrad*, 2010].

2.4.2 Relative air permeability

The relative air permeability is an indispensable parameter to modeling nonisothermal water and gas two phase flow in unsaturated porous media. There existed some reviews on this relative air permeability parameter [e.g., *Miller et al.*, 1998; *Chen et al.*, 1999; *Scanlon et al.*, 2002]. Notice that the available relative air permeability

models typically overestimate the measured values due to that the pore tortuosity-connectivity factor for liquid water and gas phase is usually assumed to be the same, which is probably not appropriate [*Tuli and Hopmans*, 2004; *Tuli et al.*, 2005; *Yang and Mohanty*, 2015; *Yang et al.*, 2017b]. The summary of the available relative air permeability model is given in Table 2.3. This parameter is critical in describing air convection process in the coupled heat and mass model when considering gas phase effect, therefore, the choice of accurate relative air permeability model summarized in Table 2.3 is thus important.

2.4.3 Thermal vapor coefficient

It is well known that when *Philip and de Vries* [1957] proposed their coupled heat and water model, they also simultaneously suggested using an enhancement factor in thermal vapor molecular diffusivity coefficient in order to match the calculated vapor flux with the observed values. They supposed two pore scale effects that could result in enhancement of water vapor diffusion through unsaturated porous media. First, water vapor has the ability to pass through capillary-held liquid islands by condensation on one side and evaporation on the other. Secondly, temperature gradient in individual air-filled pores would be enhanced relative to the bulk temperature gradient across whole soil profile due to differences in thermal conductivities of soil particle, air and water. Combing the two pore scale processes could yield a mechanistic enhancement factor η [*Cass et al.*, 1984; *Shokri et al.*, 2009]. Note that phenomenological enhancement factor that is based on experimental approach was firstly proposed by *Cary* [1964, 1965, 1966] and developed subsequently by *Jury and Letey* [1979] and *Cass et al.* [1984].

Table 2.3 Available relative air permeability models (modified from Chen et al. [1999])

Models	Water retention functions	Relative air permeability functions
VGM/VGB/VGKJ (van Genuchten-Mualem/Burdine/Kuang and Jiao)	$S_{ew} = \left[1 + (\alpha h)^n\right]^{-m}$	(1) VGM: (m=1-1/n) $k_{ra} = (1 - S_{ew})^{0.5}\left[1 - S_{ew}^{1/m}\right]^{2m}$ (2) VGB: (m=1-2/n) $k_{ra} = (1 - S_{ew})^{2}\left[1 - S_{ew}^{1/m}\right]^{m}$ (3) VGKJ: (m=1-1/n) $k_{ra} = (1 - S_{ew})^{0.5}\left[1 - S_{ew}^{1/m}\right]^{4m}$
BCM/BCB (Brooks and Corey-Mualem/Burdine)	$S_{ew} = \left(\frac{h_e}{h}\right)^{\lambda}$	(4) BCM $k_{ra} = (1 - S_{ew})^{0.5}\left[1 - S_{ew}^{1+1/\lambda}\right]^{2}$ (5) BCB $k_{ra} = (1 - S_{ew})^{2}\left[1 - S_{ew}^{1+2/\lambda}\right]$
BRB (Brutsaert-Burdine)	$S_{ew} = \frac{\beta}{\beta + h^r}$	$k_{ra} = (1 - S_{ew})^{3-2/\gamma}$
GDM (Gardner-Mualem)	$S_{ew} = \left[1 + \frac{1}{2}\alpha_g h\right] e^{-\frac{1}{2}\alpha_g h}$	$k_{ra} = \left(1 - e^{-\frac{1}{2}\alpha_g h}\right)^{2}$
KOM (Kosugi-Mualem)	$S_{ew} = F_n\left[\ln(h/h_m)/\sigma\right]$	$k_{ra} = (1 - S_{ew})^{0.5}\left\{1 - F_n\left[F_n^{-1}(S_{ew}) + \sigma\right]\right\}^{2}$ $F_n(x) = \frac{1}{\sqrt{2\pi}}\int_{-\infty}^{x}\exp\left(-\frac{x^2}{2}\right)dx = \frac{1}{2}erfc\left(\frac{x}{\sqrt{2}}\right)$

Cass et al. [1984] and *Campbell* [1985] proposed the following widely used mechanistic empirical equation for the vapor enhancement factor η:

$$\eta = 9.5 + 3\frac{\theta}{\theta_s} - 8.5\exp\left\{-\left[\left(1+\frac{2.6}{\sqrt{f_c}}\right)\frac{\theta}{\theta_s}\right]^4\right\} \tag{2.1}$$

where f_c is mass fraction of clay in the soil (unitless), θ_s is the saturated water content and θ is soil volumetric water content.

This enhancement factor is commonly used in a number of codes such as Tough2 [*Pruess et al.*, 1999], UNSAT-H [*Fayer*, 2000] and Hydrus-1D [*Saito et al.*, 2006; *Šimůnek et al.*, 2008] and others. This is probably because it could help match the predicted and observed vapor fluxes. Even with such great popularity of this enhancement factor, to date, a physically based theory regarding this enhancement factor is still missing [*Smits et al.*, 2011]. Only recently, *Shahraeeni and Or* [2012] started to conduct this research based on pore scale modeling and experiment.

Webb and Ho [1998] firstly challenged the validity of the primary mechanisms postulated in PdV to explain enhanced vapor transport by asserting that, until today, there was no direct evidence for enhanced vapor transport mechanisms. More recently, *Shokri et al.* [2009] argued that enhancement factors are not needed to be used if coupling between capillary flow and vapor diffusion is considered. However, *Smits et al.* [2011] applied the enhancement factor to both thermal and isothermal vapor terms based on the experiments results of *Webb and Ho* [1998], although PdV approach only suggested using this enhancement factor when there existed a temperature gradient in the porous media. It should be mentioned that the laboratory experiment of *Shokri et al.*

[2009] was performed under the isothermal condition, namely, no obvious temperature gradient occurred in the sand column, therefore, the conclusion of *Shokri et al.* [2009] is thus at best uncertain.

Lu et al. [2011] concluded that the *Cass et al.* [1984] empirical model at least is not very applicable to the silty clay soil. As such, to test the uncertainties of applying the results from *Cass et al.* [1984]'s two soils to other soils with different textures is still meaningful yet very little.

Apparently the pore scale experiments, although challenging, are still necessarily needed to demonstrate the existence or nonexistence of these enhanced vapor transport mechanisms, including the enhanced water vapor convection mechanism induced by temperature gradient (i.e., natural convection) proposed by *Parlange et al.* [1998]. The enhanced vapor transport effect caused by pressure gradient (forced convection) was recently investigated by *Zeng et al.* [2011a] and *Novak* [2016]. *Shahraeeni and Or* [2012] conducted the pore scale modeling and experiment to address this problem.

Another important aspect is investigating the uncertainties of the widely used *Cass et al.* [1984] empirical method (equation 2.1) when it is applied to clay soils as suggested by *Lu et al*. [2011].

2.4.4 Thermal liquid and isothermal vapor coefficient

Usually, these two coefficients are not very questionable because thermal liquid flux and isothermal vapor flux are typically small [e.g., *Saito et al.*, 2006] and could be reasonably ignored [e.g., *Smits et al.*, 2011].

Prunty [2009] published a short review to examine the inappropriate use of the thermal liquid diffusivity coefficient in PdV theory. It indicated that there is a need to revisit this seemingly unquestionable coefficient.

2.4.5 Thermal conductivity coefficients

The thermal conductivity coefficients are usually not controversial. This is probably due to that a good agreement between measured and calculated soil temperatures could be achieved using existing empirical formula [e.g., *de Vries*, 1963; *Chung and Horton*, 1987] and coupled heat and water models. Recently, *Smits et al.* [2010, 2013] attempted to get more accurate description of thermal conductivity coefficients based on the laboratory experimental sand data. However, experimental data on other soil textures but not only sand are also needed in future.

2.5 The numerical solutions

The mathematical formulations of coupled soil heat and water movement (partial differential equations (PDEs)) are highly nonlinear mainly due to the dependence of most coefficients on the dependent variables themselves. Hence, one typically resorts to numerical methods such as finite difference method (FDM), finite element method (FEM), finite volume method (FVM) or mixed form to solve these PDEs. Analytical or semi-analytical solutions could only be achieved under very simplified domain and boundary conditions [e.g., *Milly*, 1984; *Bear et al.*, 1991; *Shepherd and Wiltshire*, 1995]. More recently, *Miller et al.* [2013] reviewed the numerical solutions and computer modeling techniques used to solve the water sources problems such as isothermal two

phase flow model, which should be also very useful and instructive in the nonisothermal two phase flow model numerical solution.

Using FDM to get the numerical solutions in one dimension problem was published by *Sophocleous* [1979], *Nassar et al.* [1997], *Bittelli et al.* [2008] and others. *Milly* [1982], *Passerat de Silans* [1989], *Scanlon and Milly* [1994], and *Zeng et al.* [2011a, 2011b] among others used the FEM to solve this coupled model. *Sidiropoulos and Tzimopoulos* [1983] employed both FDM and FEM to solve coupled heat and water transfer in partially saturated soil and they claimed that these two methods would yield very similar solutions. However, *Gaudu and Bacon* [1979] concluded that of the FDM and FEM investigated, finite element approach produced the best results. More recently, *Grifoll et al.* [2005] adopted the finite volume method to solve their one-dimensional coupled water, gas and heat transport equations.

Nowadays, a number of well documented codes are available and commonly used, such as Hydrus-1D [*Šimůnek et al.*, 2008], Tough2 [*Pruess et al.*, 1999] and so on, see Table 2.4 for a brief summary.

Hydrus-1D is very popular in soil hydrology area and Tough2 is commonly used in engineering area, however, these codes are not very flexible compared to the COMSOL Multiphysics codes, which could allow users to define their own PDEs and solve these coupled equations based on the finite element method [e.g., *Novak*, 2010, 2016; *Smits et al.*, 2011, 2012; *Davarzani et al.*, 2014; *Trautz et al.*, 2015]. Note that most codes adopted finite element method to solve these PDEs, this is probably because FEM is more powerful to deal with irregular boundary problems compared to FDM.

Table 2.4 Numerical codes available to solve couple heat and water equations

Codes	Comments	Numerical method	Vapor	Reference
Hydrus-1D	water, vapor and energy transport in vadose zone	Finite element method	Enhanced vapor diffusion	Šimůnek et al. [2008]
TOUHG 2	Multiphase, multicomponent flows	Integral finite difference method	Optional, enhancement factor	Pruess et al. [1999]
UNSAT-H	water, vapor and energy transport in vadose zone	Finite difference method	Enhanced vapor diffusion	Fayer [2000]
FEHM	Multiphase, multicomponent flows	Finite element method	No vapor diffusion	Zyvoloski et al. [1997]
COMSOL	Multiphysics	Finite element method	User defined	

A new trend to simulate the coupled heat and water processes in soil profile using these advanced codes is that researchers tended to discretize the near surface soil layer remarkably finely [e.g., *Novak*, 2010; *Sakai et al.*, 2011; *Smits et al.*, 2011].

One work could be done is the intercode comparisons for simulating heat and water balance of these codes with available experimental data, which is similar to the work of *Scanlon et al.* [2002], who compared HELP, Hydrus-1D, SHAW, SoilCover, SWIM, UNSAT-H, and VS2DTI for simulating only water balance of surficial sediments in semiarid regions. Such intercode comparisons could help for further developing the codes as *Šimůnek et al.* [2003] suggested.

2.6 Validating the numerical solutions

Before using a numerical model to conduct prediction, the numerical model should be validated against a real-world (laboratory or field) system [*Pruess and Wang*, 2001]. Since typically few analytical solutions could be achieved to verify the coupled soil heat and water movement models, validation through laboratory and field experiments data is particularly important in this sense.

2.6.1 Laboratory experiment to validate the model

Most early laboratory experiments were carried out in closed and nonisothermal soil columns in which there was no water movement into or out of the soil boundaries [e.g. *Gurr et al*., 1952; *Taylor and Cavazza*, 1954; *Cassel et al*., 1969; *Nassar and Horton*, 1989a; *Nassar et al.*, 1992; *Prunty and Horton*, 1994; *Bachmann et al.*, 2001]. Another point noteworthy is that destructive sampling (i.e., gravimetry) was used to measure soil moisture content distributions [e.g., *Rose*, 1968a; *Nassar and Horton*,

1989a; *Nassar et al.*, 1992; *Prunty*, 1992; *Prunty and Horton*, 1994; *Bachmann et al.*, 2001; *Prunty*, 2003] and this traditional moisture measurement method could not provide transient and continuous wetness information of the soil profile. Therefore, using these laboratory experiments data to test the theory could not arrive at very definitive conclusions. It is still pressing to evaluate coupled heat and water movement theory under controlled laboratory conditions.

Recently, *Heitman et al.* [2008b] and *Smits et al.* [2011] started to address this issue. For example, in *Smits et al.* [2011]'s sand column experiment, the sand column was not closed and soil atmosphere boundary condition or evaporation could be considered. In order to create a strict one dimensional experiment condition, they used insulation materials around the sand column in case heat would dissipate laterally. However, in laboratory, it is still difficult to produce diurnal varying heating and cooling boundary condition as in the realistic field environment.

2.6.2 Field experiment to validate the model

Although one can perform well-controlled experiment in laboratory, we are also well aware that natural field is the most ideal place to validate the coupled transfer theory. Thus conducting field experiments to test the theory is always necessary and indispensable. *Parlange et al*. [1998] published a concise review concerning heat and water transport in field soils. They claimed that field experiments to test existing theory is still not common and a satisfactory comparison between PdV theory's calculated and these few field observations' vapor fluxes is never achieved. Table 2.5 shows some classic field experiments carried out at the different places around the world.

Table 2.5 Field experiments on coupled heat and water movement in vadose zone conducted at different places

Reference	Location	Soil Texture	WC measurement	Temperature measurement	Observation depth
Rose [1968a, 1968b]	Alice Springs, Australia	loamy sand/bare soil	gravimetry	thermistors	top 15 cm
Jackson [1973, 1974]	Phoenix, Arizona	Adelanto loam	gravimetry	thermocouples	near surface
Scanlon [1992]	Chihuahuan desert, Texas	deep profile	neutron probe	thermocouple psychrometers	0-40 m
Cahill et al. [1998]	University of California, Davis	Yolo silt loam	time domain reflectometry	platinum resistance temperature detectors	top 15 cm
Schelde et al. [1998]	Research centre foulum, Denmark	sandy loam/bare soil	time domain reflectometry	thermistor-based probes	top 25 cm
Saito et al. [2006]	Riverside, California	Arlington fine sandy loam	time domain reflectometry	thermocouples	2, 7, and 12 cm
Bittelli et al. [2008]	Holtville, California	silty clay loam	ECH_2O probes	thermocouples	top 7 cm

We noticed that typically separate instruments were used in these field experiments to measure soil moisture and temperature. As such, it is difficult to get the observation moisture and temperature data exactly at the same point, this probably results in some inconsistency in experimental data that also caused the deviation and disagreement between the theory and observation data. Furthermore, unlike in the laboratory, conducting rigorously one dimensional experiment is extremely challenging under field conditions. More importantly, equipments such as time domain reflectometry (TDR) have notorious temperature effects and this would also cause uncertainty and error in the observation data [*Or and Wraith*, 2000; *Cahill and Parlange*, 2000].

The field experiments summarized in Table 2.5 were mainly conducted at bare soils, therefore, in the future, considering vegetation [e.g., *Garcia et al.*, 2011] effects or other land surface covers such as mulch [e.g., *Chung and Horton*, 1987] are also important. This would be helpful for the application and extension of coupled heat and water transport model into those landscapes in addition to the bare soils.

2.7 New measurement techniques

Up to date, very few detailed experiment observations of coupled transient heat and water transport in soils are available in the literature, additionally, available data is scarce and incomplete, making it very difficult to test the proposed theories on coupled heat and water flow [*Smits et al.*, 2011]. More importantly, due to the temperature effect of common measurement instruments (e.g., TDR), the conclusion drawn from analysis of these observation data is sometimes plausible. It is thus pressing and critical to carry out detailed experiment observations using some new measurement techniques.

Among the new measurement techniques, heat pulse probe (HPP) is very promising. *Campbell et al.* [1991] firstly introduced the use of heat transport to estimate soil thermal properties and presented the dual-probe heat pulse (DPHP) method. Further developments in this technique have resulted in the simultaneous measurement of soil thermal properties, soil moisture content, and electrical conductivity using combined HPP and TDR [*Noborio et al.*, 1996; *Ren et al.*, 1999]. Over the past few years, these multi-functional measurements of vadose zone processes have attracted more attention, for example, *Mortensen et al.* [2006] combined heat pulse probe with a Wenner array and successfully developed a multi-functional heat pulse probe (MFHPP) technique to study simultaneous water, heat and solute transport in unsaturated porous media. Recently, *Robinson et al.* [2008] reviewed this heat pulse sensors briefly.

According to *Mortensen et al.* [2006], MFHPP technique has three major advantages. First, examination of the nature of coupled heat and water interdependency is possible by monitoring several parameters at the exact same place and time. Second, parameter uncertainty and error are greatly decreased via using combined soil measurements of moisture content and temperature. Thirdly, it is not necessary now to interpolate different measurement types in space and time because the use of the same instrument for various measurements within approximately the same measurement volume at around the same time. Therefore, it is extremely advisable to apply this technique in the simultaneous soil heat and water movement measurement experiments as is done in *Heitman et al.* [2008a].

It should also be noted that when the vadose zone is very dry, measuring relative humidity and temperature instead of monitoring liquid moisture content and temperature could yield some new insights on soil water movement and evaporation [*Goss and Madliger*, 2007]. This is because under extremely dry condition, liquid moisture measurement equipment has large uncertainty in monitoring soil water content [e.g., *Zeng et al.*, 2011a].

2.8 Evaporation prediction

The water mass and heat energy balances are coupled at the land-atmosphere interface largely through the evaporation term [e.g., *Milly*, 1982, 1984; *Sakai et al.*, 2011; *Smits et al.*, 2011]. Therefore, the major application of the study on coupled heat and water movement in the shallow vadose zone is the better evaporation prediction [e.g., *Garcia Gonzalez et al.*, 2012].

As a matter of fact, the above-mentioned sections all have great impacts on the evaporation estimation. Soil water evaporation estimated by Fick's law of diffusion applied within the soil perhaps does not adequately describe the water vapor transport. Therefore, *Parlange et al.* [1998], *Grifoll et al.* [2005], *Smits et al.* [2011], and *Zeng et al.* [2011a] presented their own respective theory on the vapor or gas transport mechanisms in addition to the vapor molecular diffusion that is based on the PdV formulation. However, recent studies by *Novak et al.* [2016] and *Levintal et al.* [2017] convincingly showed that the natural or forced vapor/air convection should be significant and nonnegligible in high permeability soils, but not the low permeability soils investigated in *Parlange et al.* [1998], *Grifoll et al.* [2005], *Smits et al.* [2011], and

Zeng et al. [2011a]. Because of this controversy, it is very important to continue further research on this topic in order to better understand the evaporation processes adjacent to the soil surface.

In addition, as *Goss and Madliger* [2007] and *Peters and Durner* [2008] pointed out, evaporation rate would be underestimated if one does not take into account the isothermal film flow in dry soils. Therefore, for the purpose of predicting evaporation rate more accurately in relatively dry vadose zone, using extended water retention curve and hydraulic conductivity model is justified and necessary [*Mohanty and Yang,* 2013; *Peters*, 2013; *Ciocca et al.*, 2014; *Vanderborght et al.*, 2017; *Yang et al.*, 2017a].

Furthermore, *Sakai et al.* [2011] asserted that a near-surface "undetectable zone" [e.g., *Novak*, 2010] existed in the soil profile through adopting their advanced modeling (i.e., dividing the near-surface extremely finely) as well as the state-of-the-art measurement technique heat pulse probes (HPP).

In fact, the soil evaporation process involves the extremely complex land-atmosphere mass, momentum and energy interaction. Recently, *Mosthaf et al.* [2011, 2014] presented a coupling concept (Figure 2.1) for the two-phase compositional porous-medium (in soils porous media) and single-phase compositional free flow (in atmosphere). Understanding this complicated coupling between soils and atmosphere is the main motivation of the coupled heat and water research in unsaturated soils. Investigating the physical process at the exact land surface requires the improved understanding of the transport processes occurring in soils as well as in the near surface atmosphere simultaneously [*Mosthaf et al.*, 2011, 2014; *Davarzani et al.*, 2014; *Fetzer et*

al., 2017; *Vanderborght et al.*, 2017]. It should be noticed that this new coupling concept is still at its theoretical development stage and mainly applicable to the laboratory experiment condition but not the more realistic and complex field condition yet [*Smits et al.*, 2012; *Davarzani et al.*, 2014; *Fetzer et al.*, 2017; *Vanderborght et al.*, 2017].

2.9 Summary and conclusions

For the past several decades, very few efforts have been spent on reviewing systematically upon the coupled heat and water movement in the vadose zone. In order to address this issue, at the beginning of this dissertation, we attempt to fix this gap in order to facilitate for future research. Several possible future directions are identified for the further research.

(1) Considering gas convection, vapor dispersion, phase change (nonequilibrium approach) into current coupled heat and water movement model is necessary and reasonable in some situations such as improved prediction of evaporation in high permeability soils. It should be noted that current conceptual model [e.g., *Parlange et al.*, 1998; *Grifoll et al.*, 2005; *Smits et al.*, 2011] needs to be modified in order to be applicable in non-homogeneous vadose zone in the context of presence of macropores, root channerls or cracks. *Weisbrod et al.* [2009] showed that natural convective gas exchange is obvious through fractured cracks at nighttime. In fact, the natural convection [*Parlange et al.*, 1998] and forced convection [*Zeng et al.*, 2011a] is typically important and nonnegligible in high permeability porous media (e.g., structured macropore soils and fractured rocks) but not the low permeability soils [*Novak*, 2016; *Levintal et al.*, 2017]. In soil hydrology, the coupled heat and water model considering air flow dealing

with heterogeneous soils such as existence of macropores or cracks seems missing, one promising technique is to follow the similar approach developed in nonisothermal water flow in fracture rocks.

(2) Although the mechanistic approach is the most widely used formulation to simulate the coupled heat and water model in vadose zone, it is still not physically rigorous. Therefore, the evolving models such as TCAT or Rational thermodynamics approach deserve the future research because these two approaches include interfacial area as dependent variable in the model formulations. As such, kinetic interphase mass and energy transfer (Figure 2.2) can be physically described.

(3) Using extended full range water retention curve together with unsaturated hydraulic conductivity model as isothermal unsaturated hydraulic parameters (i.e., accounting for both adsorption forces and isothermal film flow) to simulate simultaneous heat and water flow in dry unsaturated zone is necessary however not common. It is believed that with the improvement of the empirical formulation of full range water retention curve and unsaturated hydraulic conductivity, more research efforts would be directed toward this direction.

(4) Despite the widely acceptance and usage of enhancement vapor factor conception, pore scale experiments to prove or disprove this factor are still needed as indicated by *Shahraeeni and Or* [2012]. Furthermore, more experiment to determine the uncertainty on *Cass et al.* [1984] empirical formulation is also needed.

(5) Using the state-of-the-art instrument such as HPP to get high quality data to test, validate and modify the coupled conceptual heat and water model is still pressing.

Testing and comparing the different well-documented computer codes is meaningful but still missing yet.

(6) The previous work has mainly focused on bare soil environment, even in desert environment under certain conditions, vegetation could be to some extent significant. Therefore, incorporating the vegetation effect into the current coupled heat and water model can be very important to the ecohydrology of water-limited ecosystems.

(7) Continuing the research on the coupling concept between unsaturated soils and atmosphere that was started from *Mosthaf et al.* [2011] is significantly important for the better evaporation prediction and deep understanding of the complicated land surface processes [*Mosthaf et al.*, 2011, 2014; *Davarzani et al.*, 2014; *Fetzer et al.*, 2017; *Vanderborght et al.*, 2017]. This coupling concept is at its theoretical development stage and largely applied to the controlled laboratory conditions [*Smits et al.*, 2012], however, making this coupling concept to be readily applicable to transient field conditions should be explored in future.

3 EFFECTIVE PARAMETERIZATIONS OF THREE NONWETTING PHASE RELATIVE PERMEABILITY MODELS*

3.1 Synopsis

Describing convective nonwetting phase flow in unsaturated porous media requires knowledge of the nonwetting phase relative permeability. This study was conducted to formulate and derive a generalized expression for the nonwetting phase relative permeability via combining with the Kosugi water retention function. This generalized formulation is then used to flexibly investigate the Burdine, Mualem and Alexander and Skaggs models' prediction accuracy for relative nonwetting phase permeability. The model and data comparison results show that these three permeability models, if used in their original form, but applied to the nonwetting phase, could not predict the experimental data well. The optimum pore tortuosity and connectivity value is thus obtained for the improved prediction of relative nonwetting phase permeability. As a result, the effective parameterization of (α, β, η) parameters in the modified Burdine, modified Mualem and modified Alexander and Skaggs permeability models were found to be (2.5, 2, 1), (2, 1, 2) and (2.5, 1, 1), respectively. These three suggested models display the highest accuracy among the nine relative permeability models investigated in this study. However, the corresponding discontinuous nonwetting phase and the liquid film flow should be accounted for in future for the improved prediction of

*This section is reprinted with permission from "Effective parameterizations of three nonwetting phase relative permeability models" by Yang, Z., and B. P. Mohanty (2015), Water Resour. Res., 51, 6520-6531, doi:10.1002/2014WR016190, Copyright 2015 American Geophysical Union.

nonwetting phase relative permeability at very high and very low water saturation range, respectively.

3.2 Introduction

Knowledge and understanding of the Nonwetting Phase Relative Permeability (NPRP) are important for accurate characterization of nonwetting phase convective transport processes in the subsurface environment, which subsequently has significant implications for investigating the fate, emission and transport behavior of volatile organic compounds in the underground [*Falta et al.*, 1989], for describing oil-water flow in fractured rock reservoir [*Honarpour et al.*, 1986] and for studying the gas exchange and transfer at land-atmosphere interface [*Smits et al.*, 2012]. In fact, the relative permeability of the nonwetting phase is an indispensable parameter for the numerical simulation of multiphase flow in the unsaturated zone under both isothermal [*Kueper and Frind*, 1991; *Szymkiewicz et al.*, 2011] and nonisothermal conditions [*Mosthaf et al.*, 2011; *Mohanty and Yang*, 2013].

In a multiphase system of a porous medium, the relative permeability for a given phase is generally described as a function of the corresponding phase saturation [*Fischer et al.*, 1997]. Usually in the unsaturated porous media, liquid water and gas designate the wetting phase and nonwetting phase, respectively [*Dury et al.*, 1999; *Kuang and Jiao*, 2011]. Therefore, in this study, relative nonwetting phase permeability and relative gas permeability are used interchangeably.

Without accounting for nonwetting phase entrapment or discontinuities, the existing relative gas permeability-saturation constitutive models can be classified into

two categories, namely, the empirical and the statistical models [*Demond and Roberts*, 1993; *Dury et al.*, 1999; *Kuang and Jiao*, 2011]. The empirical models generally express NPRP as polynomial functions of wetting phase or nonwetting phase saturation [e.g., *Corey*, 1954; *Falta et al.*, 1989]. Apart from the phase saturation, this group of models does not require further parameters to predict the NPRP. As such, the empirical models have the limitation of obtaining the same relative gas permeability for a given effective saturation irrespective of the texture or structure of the porous media [*Dury et al.*, 1999]. The statistical models, however, employ idealizations of the pore configuration as a bundle of capillary tubes and utilize the Water Retention Function (WRF) to predict the relative gas permeability-saturation relationships. A large variety of expressions have been proposed to describe the WRFs [e.g., *Brooks and Corey*, 1964; *Brutsaert*, 1966; *van Genuchten*, 1980; *Kosugi*, 1996; *Assouline et al.*, 1998]. Combining these WRFs with pore bundle models [e.g., *Burdine*, 1953; *Mualem*, 1976; *Alexander and Skaggs*, 1986] will lead to specific NPRP functions [*Chen et al.*, 1999; *Dury et al.*, 1999]. For instance, *Chen et al.* [1999] presented seven different closed forms of relative gas permeability functions, which are the Brooks and Corey-Burdine (BCB), Brooks and Corey-Mualem (BCM), van Genuchten-Burdine (VGB), van Genuchten-Mualem (VGM), Russo-Mualem (RUM), Brutsaert-Burdine (BRB) and Kosugi-Mualem (KOM) models. Among them, the BCB and VGM models are so far the most commonly used NPRP representations [*Gerhard and Kueper*, 2003].

It is noticed that the existing statistical models are mostly obtained through the combination of earlier WRFs [e.g., *Brooks and Corey*, 1964; *van Genuchten*, 1980] with

pore bundle models. The more recent WRFs [e.g., *Kosugi*, 1996; *Assouline et al.*, 1998] are less frequently combined with pore bundle models to derive NPRP models, with the exception of KOM model derived by *Chen et al.* [1999]. The *Assouline et al.* [1998] WRF has not been used so far for evaluating relative gas permeability. Although mathematically more complicated, the advantage of adopting WRF of *Kosugi* [1996] is that the parameters of Kosugi model can be directly related to the statistical properties of the pore size distribution [*Kosugi*, 1999]. Therefore, in this study, we choose the Kosugi WRF given the fact that the lognormal pore size distribution has been well documented in various studies for both textured [e.g., *Kosugi*, 1994] and structured [e.g., *Seki*, 2007] porous media.

The existing relative gas permeability models are derived mainly based on the similar principles as used for deriving the relative hydraulic conductivity, with the common practice of using identical pore tortuosity-connectivity exponent values for both relative gas and water permeability for prediction purposes [e.g., *Parker et al.*, 1987]. *Tuli and Hopmans* [2004] and *Tuli et al.* [2005] conducted a comparative study between the experimental measured data and the relative gas/water permeability model. They concluded that the tortuosity-connectivity parameter for gas and water relative permeability should be different, largely due to the connections of the corresponding fluid phases and separate flow paths in the porous media. However, they did not suggest the optimum tortuosity-connectivity parameter for predictive relative gas permeability models. Although the tortuosity-connectivity parameter for relative hydraulic

conductivity was obtained to be 0.5 by *Mualem* [1976], a comparable study could not be found with respect to the NPRP to date [*Dury et al.*, 1999].

Motivated by this and other limitations, such as the less use of the recent WRF and lack of model comparison with a wide variety of soil textures' measured data, this study first formulated and derived a generalized expression for the NPRP model by adopting the Kosugi WRF. Then based on the generalized NPRP formulation and its application to the observed data sets having a large diversity in soil texture, we specifically investigated the effective parameterizations of three pore bundle permeability models [i.e., *Burdine*, 1953; *Mualem*, 1976; *Alexander and Skaggs*, 1986] for their improved descriptions of the relative gas permeability. Meanwhile, the optimum tortuosity-connectivity parameter for the NPRP is obtained for the three investigated relative permeability models.

3.3 Theory

3.3.1 Water retention function

When conceptualizing the porous medium as a bundle of intersecting capillary tubes with a pore radii distribution function, $f(r)$ (L^{-1}), the contribution of water-filled pores of radii $r \rightarrow r+dr$ to the volumetric water content θ ($L^3\ L^{-3}$) can be formulated as $d\theta(r) = f(r)dr$ ($L^{-1}\ L$) [*Mualem*, 1976; *Assouline*, 2001; *Nasta et al.*, 2013a]. According to *Kosugi* [1996], the $f(r)$ function based on a lognormal probability distribution is expressed as

$$f(r) = \frac{\theta_s - \theta_r}{r\sigma\sqrt{2\pi}} \exp\left\{-\left[\frac{\ln(r/r_m)}{\sigma\sqrt{2}}\right]^2\right\} \tag{3.1}$$

where θ_s (L^3 L^{-3}) and θ_r (L^3 L^{-3}) denote the saturated and residual volumetric water content, respectively. $\ln r_m$ and σ are the mean and standard deviation of the natural logarithm of the porous media pore radius r (L), respectively. The soil matric potential head h (L), is associated with the pore radius r (L), through the Young-Laplace capillary pressure function

$$h = \frac{2\gamma \cos \varpi}{r \rho_w g} \tag{3.2}$$

in which γ is the surface tension between the liquid water and gas (F L^{-1}), ϖ is the contact angle between the solid and liquid water, ρ_w is the density of liquid water (M L^{-3}), and g is the gravitational acceleration (L T^{-2}). Typically, the value of $2\gamma \cos \varpi / \rho_w g$ for gas-water-porous media system is approximately equal to a constant $1.49 \times 10^{-5}\,\mathrm{m}^2$ when h and r are expressed in units of meters [*Brutsaert*, 1966].

On the basis of equations (3.1) and (3.2), *Kosugi* [1996] derived the following WRF

$$S_e(h) = \frac{\theta - \theta_r}{\theta_s - \theta_r} = \frac{1}{2} erfc\left[\frac{\ln(h / h_m)}{\sigma \sqrt{2}} \right] \tag{3.3}$$

where S_e represents effective wetting phase saturation that varies from 0 (when $\theta = \theta_r$) to 1 (when $\theta = \theta_s$), *erfc* denotes the complementary error function. Notice that h_m ($h_m = 1.49 \times 10^{-5} / r_m$) represents the median matric potential head (m) for which $S_e(h_m) = 0.5$ [*Kosugi*, 1996; *Tuli and Hopmans*, 2004].

3.3.2 General expression for NPRP

Combining the Hagen-Poiseuille equation which is valid at the pore scale with the Darcy equation which is valid at the Representative Elementary Volume (continuum) scale, the statistical approach can be employed to derive the wetting phase [e.g., *Mualem and Dagan*, 1978] and nonwetting phase [e.g., *Helmig*, 1997] relative permeabilities. After *Helmig* [1997] and *Kuang and Jiao* [2011], the generalized expression for the NPRP $k_{rn}(S_e)$, can be written as

$$k_{rn}(S_e) = \frac{k_n(S_e)}{k_{sn}} = T(S_e)G(S_e)\left\{\frac{\int_{S_e}^{1} h^{-\beta} dS_e(h)}{\int_{0}^{1} h^{-\beta} dS_e(h)}\right\}^{\eta} = (1-S_e)^{\alpha}\left\{\frac{\int_{S_e}^{1} h^{-\beta} dS_e(h)}{\int_{0}^{1} h^{-\beta} dS_e(h)}\right\}^{\eta} \quad (3.4)$$

where k_n (L T^{-1}) and k_{sn} (L T^{-1}) are the unsaturated and saturated nonwetting phase permeability [*Tuli and Hopmans*, 2004], respectively. $T(S_e)$ is a tortuosity factor that accounts for flow path eccentricity (departure from ideal straight capillaries), and $G(S_e)$ accounts for connectivity among the gas-conducting pores [*Kuang and Jiao*, 2011; *Nasta et al.*, 2013a]. It is worth mentioning that equation (3.4) neglects the possible presence of a discontinuous nonwetting phase (trapped and locally accessible) in the porous media [*Fischer et al.*, 1997; *Dury et al.*, 1999], therefore, the NPRP is described as a function of the total nonwetting phase saturation in equation (3.4) [*Fischer et al.*, 1997; *Dury et al.*, 1999].

The parameter α in equation (3.4), originally proposed by *Burdine* [1953] and later adopted by *Mualem* [1976] as well as other researchers [e.g., *Alexander and Skaggs*, 1986; *Luckner et al.*, 1989], is related to the pore tortuosity-connectivity of the

porous media. The parameter β in equation (3.4) is associated with the microscopic pore tortuosity [*Fatt and Dykstra*, 1951; *Kosugi*, 1999]. Whereas the parameter η in equation (3.4) defines the pore configuration and reflects the way to evaluate the effective pore radius [*Raats*, 1992; *Kosugi*, 1999]. The parameters (α, β, η) in equation (3.4) can be varied to obtain more specific functional expressions. For the *Purcell* [1949] and *Burdine* [1953] models, parameters (α, β, η) are equal to (0, 2, 1) and (2, 2, 1) respectively, for the *Mualem* [1976] and *Alexander and Skaggs* [1986] models, parameters (α, β, η) are specified as (0.5, 1, 2) and (1, 1, 1) respectively, whereas for the *Luckner et al.* [1989] and *Kuang and Jiao* [2011] models, parameters (α, β, η) are equal to (1/3, 1, 2) and (0.5, 1, 4) respectively. In the *Assouline* [2001] model, $\alpha = 0$, $\beta = 1$ and η is proposed to be linked to the coefficient of variation of the WRF. It should be pointed that the *Purcell* [1949] model and *Mualem* [1976] model were originally developed for the relative water permeability prediction. They were extended for the NPRP evaluation later by *Burdine* [1953], *Parker et al.* [1987] and other researchers, who usually adopted the same α values as those in the corresponding relative water permeability models, which is probably inappropriate [*Dury et al.*, 1999; *Tuli and Hopmans*, 2004; *Tuli et al.*, 2005].

3.3.3 Generalized formulation for NPRP with Kosugi WRF

Inserting equation (3.3) into equation (3.4), one can obtain the generalized relative gas permeability model based on the lognormal pore size distribution (see Appendix B for the derivation)

$$k_{rn} = (1 - S_e)^{\alpha} \left\{ 1 - \frac{1}{2} erfc\left[erfc^{-1}(2S_e) + \frac{\beta\sigma}{\sqrt{2}} \right] \right\}^{\eta} \tag{3.5}$$

where $erfc^{-1}$ is the inverse complementary error function. It should be noted that equation (3.5) is an extension of equation (12) in *Kosugi* [1999] which described the generalized relative hydraulic conductivity model. However, to our knowledge, the generalized equation (3.5) was obtained for the first time in the literature in terms of relative gas permeability, although one specific case of equation (3.5), i.e., the KOM model, was already derived by *Chen et al.* [1999].

3.4 Materials and methods

3.4.1 Testing data sets

Seventeen experimental data sets [*Kuang and Jiao*, 2011; *Ghanbarian-Alavijeh and Hunt*, 2012] are taken from the literature to evaluate the performance of the generalized k_{rn} model expressed by equation (3.5). These data sets consisted of laboratory measured curves for both soil water retention and relative nonwetting phase permeability. All these 17 porous media samples (15 unconsolidated soils and 2 consolidated sandstones) shown in the Table 3.1 are under disturbed conditions and thus have unimodal pore system.

The Kosugi WRF was fitted to the observed water retention data pairs $S(h)$. Here S denotes wetting phase (water) saturation and can be transferred to volumetric water content θ (L^3 L^{-3}) through the expression $\theta = \phi S$, in which ϕ (L^3 L^{-3}) is the porosity of the media. For each porous medium, the optimized parameters θ_s, θ_r, h_m

Table 3.1 Data sets investigated in this study and fitted parameters for the Kosugi Water Retention Function

Reference	Medium type	Condition	Porosity	θ_s	θ_r	h_m, (m)	σ	RMSE	R^2
Collis-George [1953]	Cambridge sand	Disturbed	0.380	0.380	0.034	0.148	0.136	0.012	0.995
Brooks and Corey [1964]	Volcanic sand	Unconsolidated	0.351	0.351	0.055	0.229	0.272	0.010	0.993
Brooks and Corey [1964]	Glass beads	Unconsolidated	0.370	0.370	0.036	0.323	0.091	0.011	0.994
Brooks and Corey [1964]	Fine sand	Unconsolidated	0.377	0.377	0.066	0.503	0.269	0.007	0.997
Brooks and Corey [1964]	Touchet silt loam	Unconsolidated	0.485	0.485	0.186	1.044	0.272	0.008	0.994
Brooks and Corey [1964]	Fragmented mixture	Unconsolidated	0.443	0.443	0.134	0.226	0.253	0.009	0.995
Brooks and Corey [1964]	Fragmented Fox Hill	Unconsolidated	0.470	0.470	0.156	0.151	0.445	0.007	0.997
Brooks and Corey [1964]	Berea sandstone	Consolidated	0.206	0.206	0.066	0.515	0.269	0.002	0.994
Brooks and Corey [1964]	Hygiene sandstone	Consolidated	0.250	0.250	0.151	0.640	0.193	0.002	0.992
Brooks and Corey [1966]	Poudre river sand	Unconsolidated	0.364	0.364	0.060	0.171	0.263	0.008	0.995
Brooks and Corey [1966]	Amarillo silty clay loam	Unconsolidated	0.455	0.455	0.138	0.512	0.346	0.010	0.993
Touma and Vauclin [1986]	Grenoble sand	Disturbed	0.370	0.310	0.054	0.318	0.782	0.003	0.998
Stonestrom [1987]	Oakley sand	Disturbed	0.365	0.322	0.105	0.459	0.315	0.009	0.989
Dury [1997]	Mixed sand	Disturbed	0.360	0.285	0.021	0.339	0.316	0.006	0.995
Springer et al. [1998]	Silty sand	Disturbed	0.431	0.431	0.026	0.963	1.939	0.014	0.986
Tuli and Hopmans [2004]	Columbia sandy loam	Disturbed	0.466	0.432	0.098	2.068	1.491	0.007	0.996
Tuli and Hopmans [2004]	Oso Flaco fine sand	Disturbed	0.419	0.406	0.072	0.559	0.287	0.014	0.981

and σ in equation (3.3) were determined using the 'lsqcurvefit' function in the MATLAB optimization toolbox (The MathWorks, Inc.). The fitted values are shown in Table 3.1. From Table 3.1, one can notice that all 17 porous media samples can be described by the Kosugi WRF reasonably well because the root mean square error (RMSE) is usually small and the coefficient of determination (R^2) of the curve fitting was always greater than 0.98. The σ values of Glass beads and Silty sand are the smallest and the largest, respectively. Figure 3.1(a) displays the observed soil water retention data and the respective optimized curves of Glass beads and Silty sand computed from equation (3.3). Whereas Figure 3.1(b) plots the pore size distribution of these two soil samples calculated based on equation (3.1).

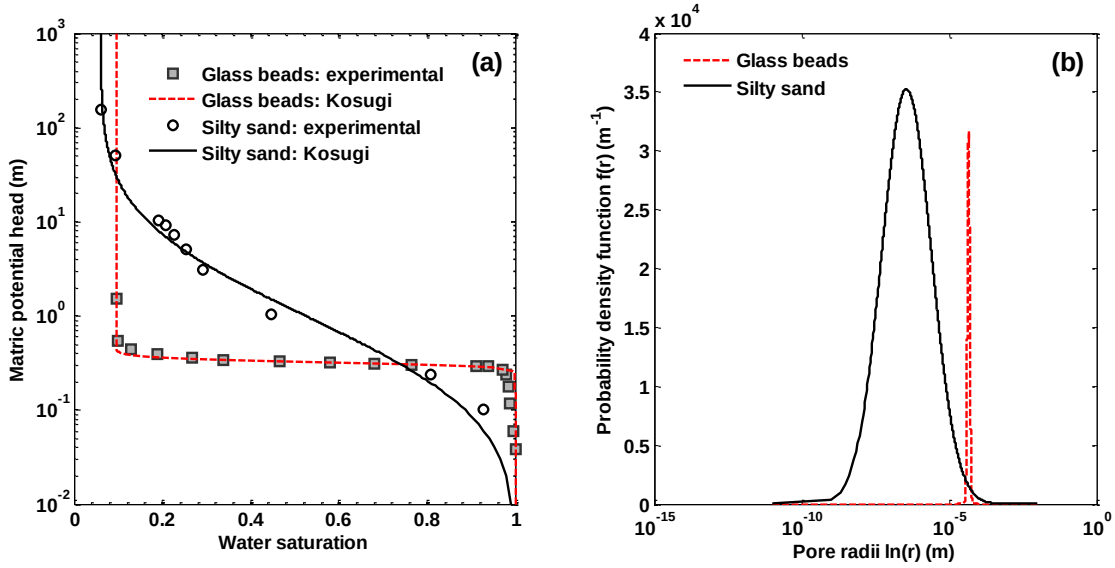

Figure 3.1 (a) Water retention curves and (b) Pore size distribution of Glass beads and Silty sand.

3.4.2 Model test

Similar to *Kosugi* [1999] and *Kuang and Jiao* [2011], the root mean square error (RMSE) between experimental data and model prediction, was chosen as the objective function and calculated for each porous medium sample to evaluate the performance of equation (3.5).

$$RMSE = \sqrt{\frac{1}{N-m}\sum_{i=1}^{N}\left[k_{rn,i} - \hat{k}_{rn,i}\left(S_{ei}\right)\right]^2} \tag{3.6}$$

where $k_{rn,i}$ and $\hat{k}_{rn,i}\left(S_{ei}\right)$ are the observed and calculated relative gas permeability, respectively. N is the number of measurements for each experimental sample. m is the number of fitted parameters. The accuracy of equation (3.5) for the entire data sets was evaluated by employing the average value of the RMSE (aveRMSE) for all the 17 porous media samples [*Kosugi*, 1999; *Kuang and Jiao*, 2011]. For the consistency with previous researchers [*Tuli and Hopmans*, 2004; *Kuang and Jiao*, 2011; *Ghanbarian-Alavijeh and Hunt*, 2012] who used the same data sets to perform the computation and analysis on linear scale, the results obtained on the linear scale are presented below, which are similar to that acquired on the logarithmic scale (Appendix C Figures C1, C2 and C3).

Equation (3.5) was tested in its ability to describe the observed nonwetting phase relative permeability data. As Table 3.2 shows, first, the k_{rn} prediction was tested by using the original coefficients given by the models of Burdine (B), Mualem (M) and Alexander and Skaggs (AS), respectively. Then, 21 other model combinations were created by allowing first one, then two, and eventually all three semiempirical

Table 3.2 Average (aveRMSE), standard deviation (stdRMSE), and maximum (maxRMSE) values of root mean square error (RMSE) for the 17 data sets by the cases B1 through AS8

Cases	α	β	η	aveRMSE	stdRMSE	maxRMSE
B1[a]	2	2	1	0.092	0.066	0.270
B2	fitted	2	1	0.048	0.039	0.154
B3	2	fitted	1	0.056	0.065	0.287
B4	2	2	fitted	0.063	0.067	0.287
B5[b]	fitted	fitted	1	0.044	0.037	0.147
B6	fitted	2	fitted	0.047	0.043	0.164
B7	2	fitted	fitted	0.050	0.071	0.307
B8[c]	fitted	fitted	fitted	0.035	0.029	0.126
M1[a]	0.5	1	2	0.153	0.078	0.330
M2	fitted	1	2	0.048	0.037	0.141
M3	0.5	fitted	2	0.047	0.032	0.123
M4	0.5	1	fitted	0.058	0.049	0.199
M5	fitted	fitted	2	0.042	0.034	0.129
M6[d]	fitted	1	fitted	0.043	0.033	0.135
M7	0.5	fitted	fitted	0.038	0.031	0.118
M8[c]	fitted	fitted	fitted	0.035	0.029	0.126
AS1[a]	1	1	1	0.160	0.060	0.307
AS2	fitted	1	1	0.048	0.038	0.148
AS3	1	fitted	1	0.051	0.036	0.148
AS4	1	1	fitted	0.055	0.042	0.146
AS5[b]	fitted	fitted	1	0.044	0.037	0.147
AS6[d]	fitted	1	fitted	0.043	0.033	0.135
AS7	1	fitted	fitted	0.041	0.039	0.151
AS8[c]	fitted	fitted	fitted	0.035	0.029	0.126

[a]Predictive models
[b]B5 and AS5 are the identical case from the fitting perspective
[c]B8, M8 and AS8 are the identical case from the fitting perspective
[d]M6 and AS6 are the identical case from the fitting perspective

parameters (α, β and η) to vary [*Kosugi*, 1999; *Hoffmann-Riem et al.*, 1999]. These 21 model sets with one, two, or finally three degrees of freedom were fitted to the measured data and compared with respect to the accuracy of the fits. The fitting was conducted via using the 'globalsearch' function in the MATLAB global optimization toolbox. With

respect to the boundary of the optimized parameter space, both α and β were set to range from -20 to 20 based on the prior knowledge from *Kosugi* [1999], whereas η was set to range from 0.1 to 10 according to the previous experience from *Assouline* [2001] and *Nasta et al.* [2013a, 2013b].

3.5 Results and discussions

3.5.1 Model and data comparison

3.5.1.1 No fitted parameter case

Figures 3.2, 3.3 and 3.4 display the scatter charts of observed versus calculated relative gas permeability based on the model sets B1 to AS8 listed in the Table 3.2. Figures 3.2(a) and 3.4(a) show that both B1 and AS1 cases mainly overestimated the measured relative gas permeability values, although they could underestimate the measured data significantly for some relatively fine textured soils. It can be seen in Figure 3.3(a) that the M1 case overestimated for all the 17 samples. Notice that the B1, M1 and AS1 cases are identical to the original Burdine, Mualem and Alexander and Skaggs' predictive models, respectively. The significant deviations from the 1:1 lines for the cases B1, M1 and AS1 indicated some inadequate predictions of k_{rn} values by the Burdine, Mualem and Alexander and Skaggs models. In addition, the average value of RMSE for the whole data sets is the largest for the case AS1, followed by the case M1 and case B1 among the twenty four scenarios (Table 3.2). As such, further improvement is clearly warranted for the improved relative gas permeability description of the original Burdine, Mualem and Alexander and Skaggs pore bundle models.

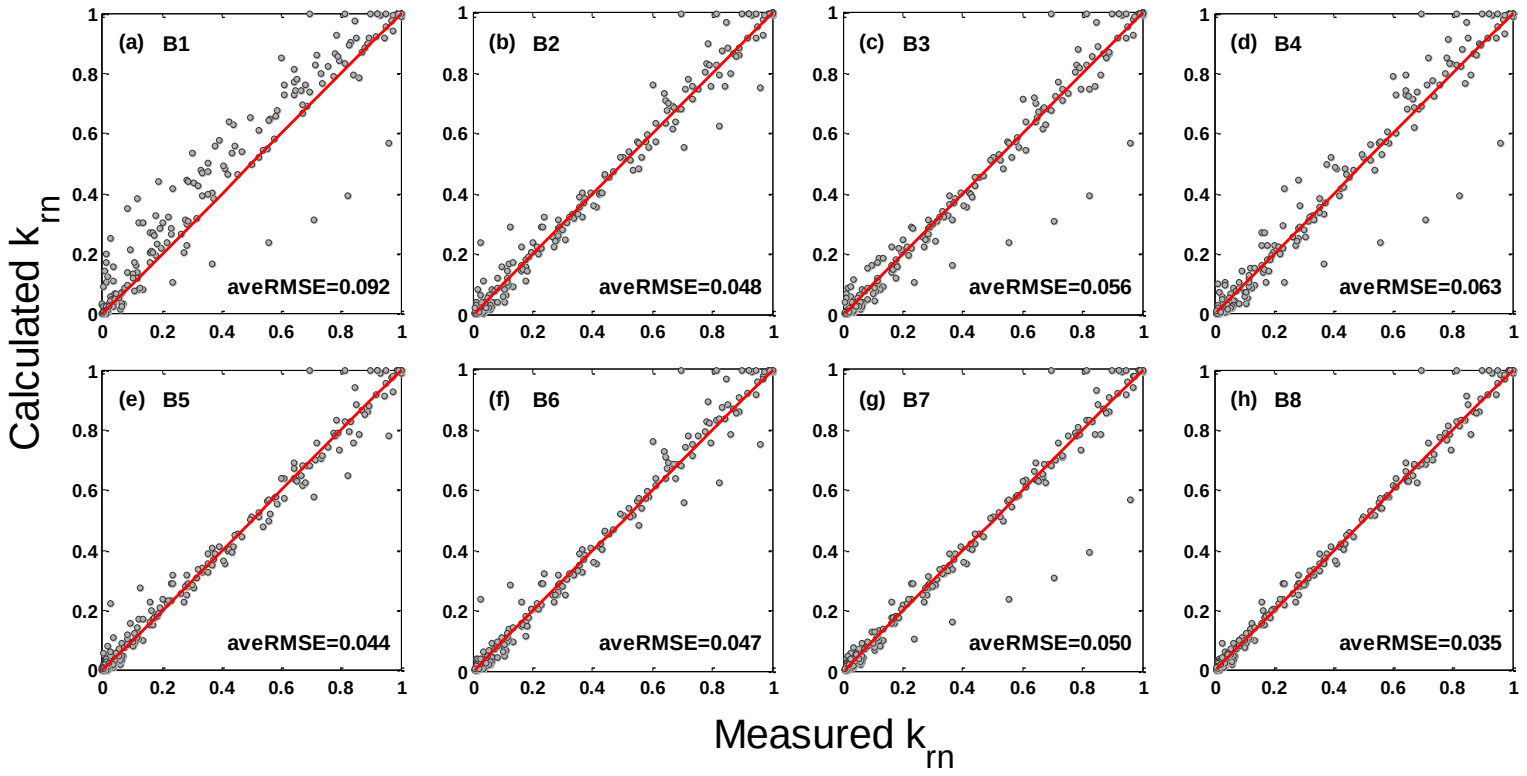

Figure 3.2 Scatter charts of measured versus calculated relative gas permeability for the cases (a) B1, (b) B2, (c) B3, (d) B4, (e) B5, (f) B6, (g) B7, and (h) B8 for the 17 data sets.

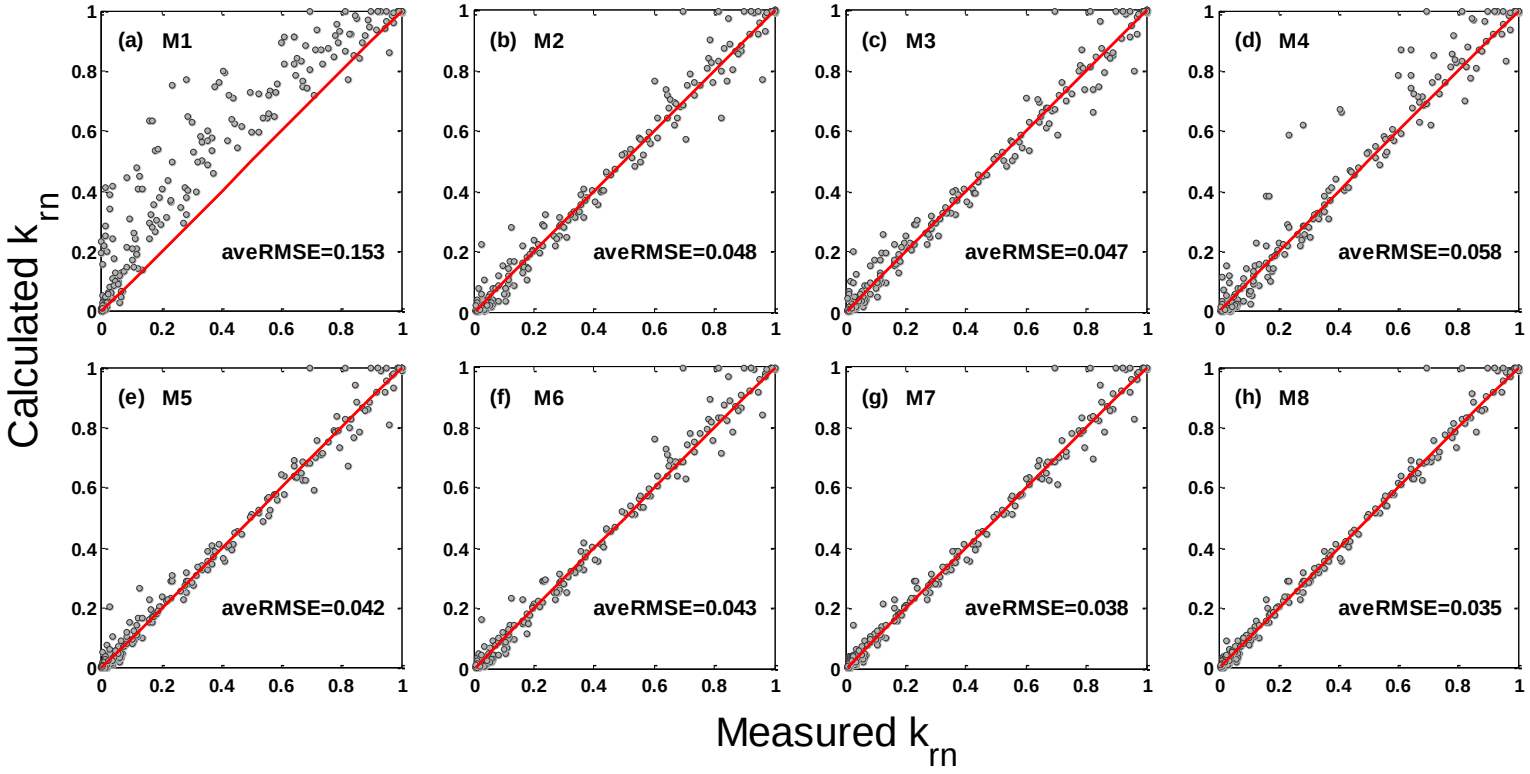

Figure 3.3 Scatter charts of measured versus calculated relative gas permeability for the cases (a) M1, (b) M2, (c) M3, (d) M4, (e) M5, (f) M6, (g) M7, and (h) M8 for the 17 data sets.

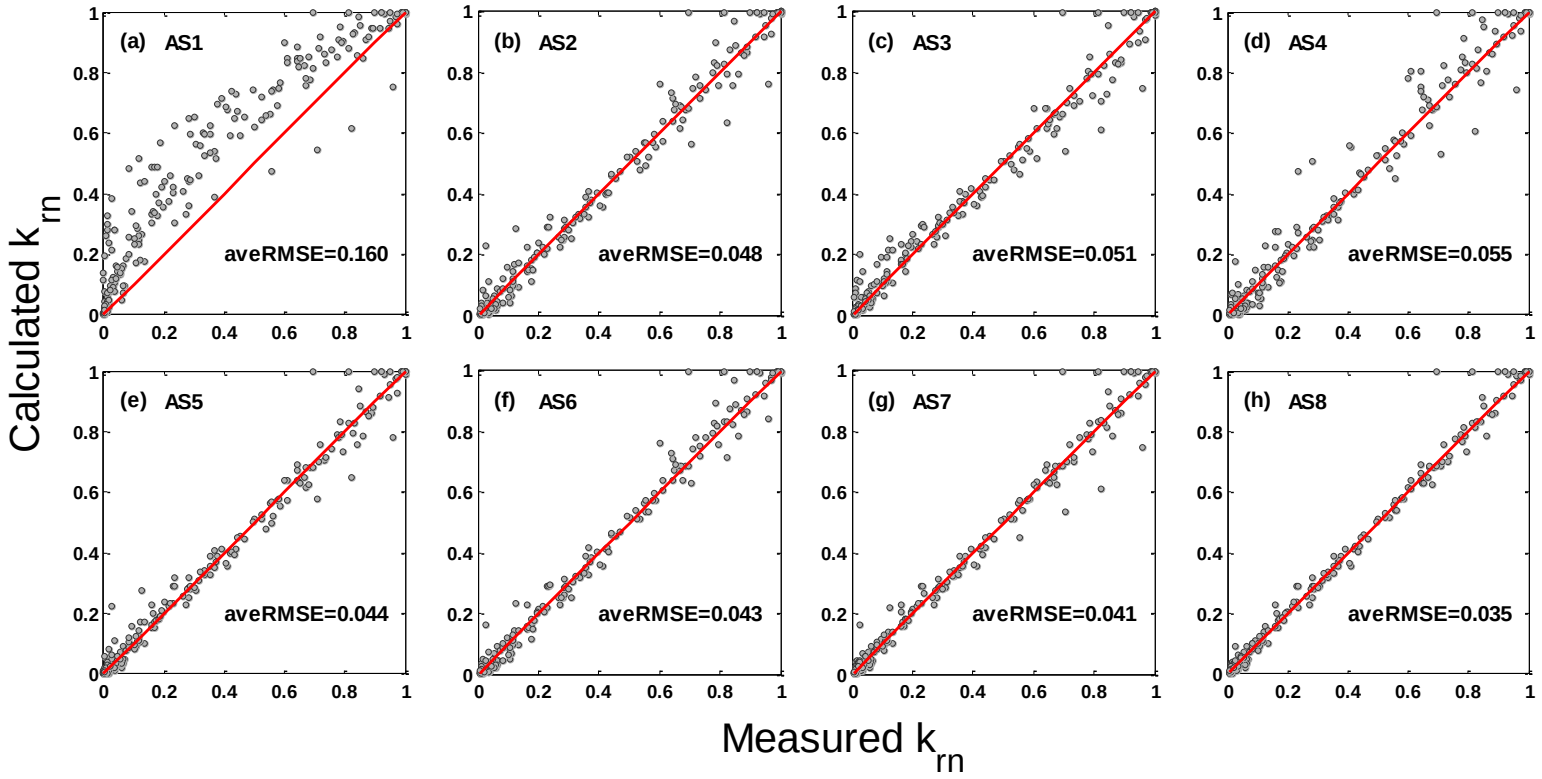

Figure 3.4 Scatter charts of measured versus calculated relative gas permeability for the cases (a) AS1, (b) AS2, (c) AS3, (d) AS4, (e) AS5, (f) AS6, (g) AS7, and (h) AS8 for the 17 data sets.

3.5.1.2 Fitted parameter case

Figures 3.2(b), 3.2(c), 3.2(d), 3.3(b), 3.3(c), 3.3(d), 3.4(b), 3.4(c) and 3.4(d) show that the estimation of k_{rn} values are improved via treating one of the parameters (α, β and η) as an optimized parameter. Such improvement occurs mainly because the overestimation errors are largely reduced. As a result, the aveRMSE is reduced nearly one order of magnitude compared to that of the original Burdine, Mualem and Alexander and Skaggs relative permeability models. The reductions in aveRMSE were 48%, 39% and 31% for the cases B2, B3 and B4, respectively, compared to the case B1, 69%, 70% and 62% for the cases M2, M3 and M4, respectively, compared to the case M1, and 70%, 68% and 65% for the cases AS2, AS3 and AS4, respectively, compared to the case AS1 (see Table 3.2). The range of optimized α value is (1.00, 4.49), (0.89, 3.60) and (0.95, 4.25) with the average values 2.73, 1.95 and 2.52 for the cases B2, M2 and AS2, respectively. Whereas the fitted β value is mostly negative. This is reflected by the fact that the averages of optimized β value in B3, M3 and AS3 cases are -0.08, -0.77 and -2.14, respectively. The reductions in aveRMSE were the smallest when treating η as a fitting parameter compared to that of treating either α or β as a fitting parameter.

Figures 3.2(e), 3.2(f), 3.2(g), 3.3(e), 3.3(f), 3.3(g), 3.4(e), 3.4(f) and 3.4(g) show that the prediction of k_{rn} values are further improved by treating two of the three parameters as fitted ones. It is worth pointing out that such further improvement is not quite significant compared to the cases using only one fitted parameter. As a matter of

fact, the aveRMSE value obtained using two fitted parameters is on the same order of magnitude with that of using one fitted parameter (Table 3.2).

The prediction of k_{rn} values in cases B8, M8 and AS8 versus measured values is plotted in Figures 3.2(h), 3.3(h) and 3.4(h), which display an excellent linearity around 1:1 lines. It is expected that the B8, M8 and AS8 cases have the smallest aveRMSE since they have the largest degree of freedom of fitted parameters.

3.5.2 Optimum alpha parameter for NPRP

The model and comparison results shown above indicate that the original B, M and AS pore bundle models lead to the worst predictions of the NPRP, allowing one parameter (either one) to vary can improve the fit significantly, and further increasing the degrees of freedom to two and three yields an even better fit, though with less improvement as compared to the one fitted parameter case. This finding is consistent with *Kuang and Jiao* [2011], who modified the η value in Mualem model from 2 to 4 to arrive at their new NPRP model that increases the predictive ability. However, in this study we attempt to modify the α value in the B, M and AS relative permeability models as the way to solve the problem that the optimum α values in the three permeability models are largely unknown so far [*Dury et al.*, 1999]. To that end, similar to *Kuang and Jiao* [2011], several discrete values of α which ranged from 0 to 4.5 were adopted in this work. For each sample and each value of α, the RMSE between model and data was calculated. Then at each discrete α value the average RMSE was computed for the entire 17 samples. Figures 3.5(a), 3.5(b) and 3.5(c) plot the variations of the average RMSE with α for the Burdine, Mualem and Alexander and Skaggs

models, respectively. As a result, the optimum α values for the respective pore bundle models can be obtained. Notice that in Firgure 3.5(a), $\alpha = 0$ corresponds to the *Purcell* [1949] model, which has the largest mean RMSE. This indicated that the pore tortuosity and conectivity effect for calculating k_{rn} value should not be ignored. Firgure 3.5(a) displays that the optimum α value is 2.5 for the Burdine model. The $\alpha = 1/3$ in Figure 3.5(b) corresponds to the *Luckner et al.* [1989] model which has a large average RMSE value 0.178. The optimum α value for Mualem model is 2 as shown in Firgure 3.5(b). Whereas Figure 3.5(c) illustrates that for the Alexander and Skaggs model, the optimum α value is 2.5.

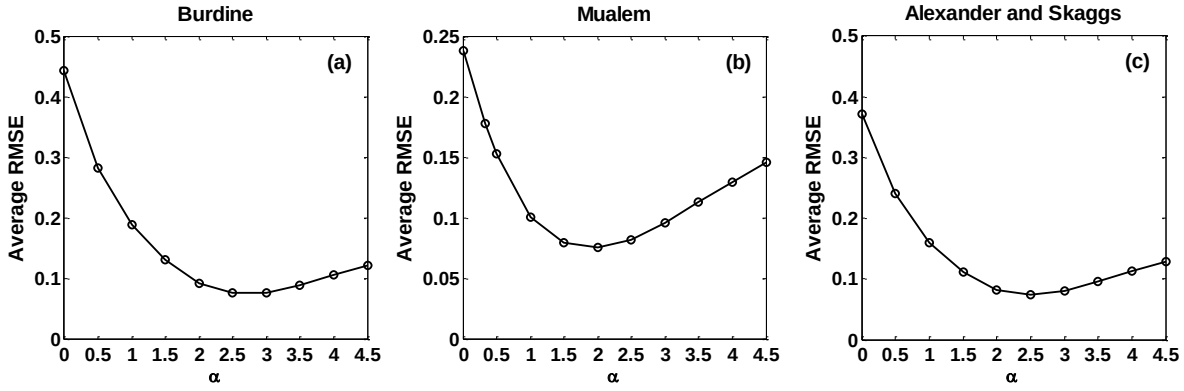

Figure 3.5 Variations of the average RMSE with alpha of the (a) Burdine, (b) Mualem and (c) Alexander and Skaggs model.

As such, for the purpose of estimating k_{rn} values, the parameterizations of α, β, and η values are suggested to be equal to (2.5, 2, 1), (2, 1, 2) and (2.5, 1, 1) for the

Burdine, Mualem and Alexander and Skaggs models, respectively. The average RMSE of these three suggested models and the other six commonly used statistical models are summarized in Table 3.3. It can be seen from Table 3.3 that among the 9 investigated models, the modified Burdine, modified Mualem and modified Alexander and Skaggs permeability models have the lowest average RMSE values, which are 1.2, 2.0 and 2.2 times smaller than that of their corresponding original models, respectively. It is noticed that the improvement of prediction of k_{rn} value is more significant for the Mualem and Alexander and Skaggs models compared to the Burdine model.

Table 3.3 The average RMSE of the existing and suggested relative gas permeability models

Models	α	β	η	Average RMSE
Purcell [1949]	0	2	1	0.443
Burdine [1953]	2	2	1	0.092
Mualem [1976]	0.5	1	2	0.153
Alexander and Skaggs [1986]	1	1	1	0.160
Luckner et al. [1989]	1/3	1	2	0.178
Kuang and Jiao [2011]	0.5	1	4	0.089
This study (modified Burdine)	2.5	2	1	0.076
This study (modified Mualem)	2	1	2	0.075
This study (modified AS)	2.5	1	1	0.074

A somewhat different predictive permeability model was proposed by *Assouline* [2001], who linked the η value to the coefficient of variation of *Assouline et al.* [1998] WRF. *Nasta et al.* [2013b] recently related the η value to the coefficient of variation of Kosugi WRF for the prediction of relative hydraulic conductivity. However, extending

Assouline [2001] model to calculate relative gas permeability is not quite feasible at present. This is mainly because of the scarcity of the available experimental data for simultaneously collected water retention and relative nonwetting phase permeability in the literature, compared to the vast data sets on both water retention and relative hydraulic conductivity. Therefore, a good relationship between η parameter and the coefficient of variation of *Kosugi* [1996] or *Assouline et al.* [1998] WRF on relative gas permeability cannot be determined for now. For the similar reason, any good relationship between β and σ or α and σ also cannot be found at this stage for NPRP, although *Kosugi* [1999] obtained such relationship for relative hydraulic conductivity.

3.5.3 Limitations of the study

Despite the relatively comprehensive data set used and the improved models obtained in this study, there are certain limitations of our work. First, the optimum α value for relative gas permeability obtained in this study is likely to depend on the investigated data sets. One typical example in this case is that the optimum α value for relative hydraulic conductivity obtained by *Mualem* [1976] based on 45 soil samples is 0.5 while a mean value of $\alpha = -0.72$ was acquired by *Leij et al.* [1997] on the basis of another 401 soils. Therefore, it is likely that when using a different data set in future (e.g., undisturbed structured soil samples), the optimum α value for relative gas permeability will be different from the results obtained in this work. The percolation theory [*Ghanbarian-Alavijeh and Hunt*, 2012] or gas-water interfacial area based

variable tortuosity-connectivity approach [*Khaleel*, 2008] could be explored in future to solve this data sets dependent optimum α value problem.

Second, the equation (3.5) is expected to not have good predictive capability at both very high and very low water saturation range. For the high water saturation range, equation (3.5) could overestimate the observed relative gas permeability, in particular, the model would still predict very small relative gas permeability while the observed NPRP is nil. This can be clearly seen from Figure 3.6(b) for Mixed sand that has the largest difference between the saturated water content and porosity, indicating the existence of a significant amount of entrapped nonwetting phase of this soil. In contrast, as Figure 3.6(a) shows, such overestimation is not quite significant for Amarillo silty clay loam which does not have large amounts of discontinuous gas (saturated water content and porosity are equal for this soil). Although the modified Mualem model can to some extent reduce the overestimation, in order to totally solve the overestimation issue at the high water saturation range, the NPRP model should take into account the discontinuous nonwetting phase as *Fischer et al.* [1997] and *Dury et al.* [1999] suggested. As a result, the NPRP model will become a function of continuous nonwetting phase saturation, rather than the total nonwetting phase saturation. However, these "analogy based" models accounting for the discontinuous nonwetting phase have the difficulty of independently and effectively determining the emergence points (i.e., the partitioning point of the total nonwetting phase into continuous and discontinuous domains) [*Dury et al.*, 1999]. On the other hand, equation (3.5) based on the capillary pore bundle theory ignores the liquid film flow which is known to dominate at the low

water saturation range [*Tuller and Or*, 2001]. As a consequence, the NPRP model in this study would predict that the relative gas permeability is always equal to 1 when the soil water content is between 0 and θ_r, despite the possibility that the measured relative gas permeability may gradually increase to 1 in this saturation range. Therefore, as Figures 3.6(a) and 3.6(b) display, the equation (3.5) tends to overestimate the measured relative gas permeability at very low water saturation for both the Amarillo silty clay loam and the Mixed sand. This shortcoming can be addressed in future by incorporating the liquid film flow into equation (3.5) when the water content is below residual.

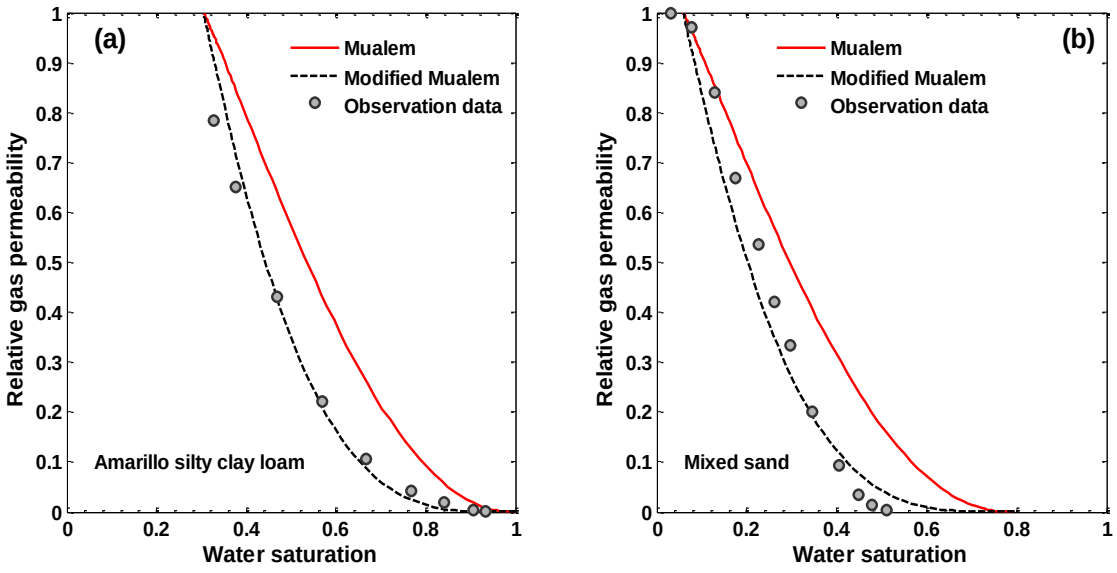

Figure 3.6 Comparison of measured data obtained for (a) Amarillo silty clay loam and (b) Mixed sand with predicted results using the Mualem and the Modified Mualem model.

3.6 Summary and conclusion

The relative nonwetting phase permeability is indispensable for describing the convective nonwetting phase flow in the unsaturated porous media. Combined with the Kosugi water retention function, this study formulated and derived a generalized expression for the nonwetting phase relative permeability, which can be used to flexibly investigate the NPRP prediction accuracy of three pore bundle models [i.e., *Burdine*, 1953; *Mualem*, 1976; *Alexander and Skaggs*, 1986]. The subsequent model and data comparison results indicate that the Burdine, Mualem and Alexander and Skaggs models, if used in their original form, but applied to the nonwetting phase, will lead to the worst predictions of measured relative gas permeability. However, allowing one parameter (either one) among the three semi-empirical parameters (α, β and η) of the generalized NPRP model to vary can improve the fit significantly, and further increasing the degrees of freedom to two and three yields an even better fit, though with less improvement as compared to the one fitted parameter case. To this end, the optimum α value for NPRP is obtained to effectively parameterize the three investigated permeability models. Accordingly, the modified Burdine (2.5, 2, 1), the modified Mualem (2, 1, 2) and the modified Alexander and Skaggs (2.5, 1, 1) permeability model were suggested for the improved prediction of the nonwetting phase relative permeability. These three suggested permeability models have the lowest average RMSE values among all the nine investigated permeability models. In addition, the average RMSE of the modified Burdine, modified Mualem and modified Alexander and Skaggs

permeability models are 1.2, 2.0 and 2.2 times smaller than that of their corresponding original form for NPRP, respectively.

It is admitted that the optimum pore tortuosity-connectivity results for NPRP obtained in this work is likely to depend on specific data sets investigated, hence the percolation theory [*Ghanbarian-Alavijeh and Hunt*, 2012] or gas-water interfacial area based variable tortuosity-connectivity approach [*Khaleel*, 2008] should be employed in future to further investigate this parameter. In addition, the generalized expression for NPRP acquired in this study (i.e., equation 3.5) does not have good predictive capability at both very high and very low water saturation ranges. To solve this issue, the future NPRP model should take into account the discontinuous nonwetting phase and liquid film flow, respectively.

4 PREDICTION OF RELATIVE AIR PERMEABILITY FROM WATER RETENTION FUNCTION BASED ON SOIL FRAGMENTATION PROCESS

4.1 Synopsis

Modeling the convective air movement in unsaturated porous media requires appropriate characterization of the relative air permeability (RAP). Using the *Assouline et al.* [1998] water retention function (WRF) that is based on a soil fragmentation process, this study is conducted to derive seven new predictive RAP models. They are the Assouline et al.–Purcell (AP), Assouline et al.–Burdine (AB), Assouline et al.–Alexander and Skaggs (AAS), Assouline et al.–Luckner et al. (AL), Assouline et al.–modified Burdine (AMB), Assouline et al.–modified Mualem (AMM) and Assouline et al.–modified Alexander and Skaggs (AMAS) models. These seven new models, together with the other three predictive RAP models derived by *Assouline et al.* [2016], namely, the Assouline et al.–Mualem (AM), Assouline et al.–Kuang and Jiao (AKJ) and Assouline et al.–Assouline et al. (AA) models, are then compared with the 30 disturbed samples measured data. The data and model comparison results show that the AP model significantly overestimates the measured RAP for the whole data sets and thus has the poorest performance for the RAP prediction. The AA model, followed by the AL, AM, and AAS models, tends to generally overestimate the measured RAP data, but with a gradually reduced overestimation error. The KAJ model has an average performance and the AB model has a reasonably good performance for the RAP prediction. However, the AMB, AMM, and AMAS models demonstrate the improved RAP prediction and have

the highest accuracy among the ten RAP models investigated in this research. It is confirmed by this study that the pore tortuosity and connectivity parameter for water and air relative permeability in the statistical models should be different.

4.2 Introduction

Appropriate modeling of air movement in unsaturated porous media is becoming increasingly important in various science and engineering fields, such as soil hydrology, agriculture science, petroleum engineering, and environmental engineering [*Honarpour et al.*, 1986; *Falta et al.*, 1989; *Dury et al.*, 1999; *Kuang and Jiao*, 2011; *Smits et al.*, 2012]. It requires the definition of the Relative Air Permeability (RAP) as a function of air content, or equivalently, a function of water content [*Fischer et al.*, 1997; *Kuang and Jiao*, 2011]. The RAP, is in fact an indispensable parameter for the subsurface isothermal and nonisothermal multiphase flow numerical simulation [*Kueper and Frind*, 1991; *Szymkiewicz et al.*, 2011; *Mosthaf et al.*, 2011; *Mohanty and Yang*, 2013].

When ignoring the air entrapment or discontinuities, mainly two categories of RAP–water content constitutive models can be identified in the literature, that is, the empirical and the statistical models [*Dury et al.*, 1999; *Kuang and Jiao*, 2011; *Yang and Mohanty*, 2015]. The empirical models typically express the RAP as polynomial functions of water content [*Corey*, 1954; *Falta et al.*, 1989]. Although mathematically simple, the empirical models usually suffer from the problem that arriving at the same RAP for a given water content irrespective of the texture or structure of the porous media [*Dury et al.*, 1999]. The statistical models, however, overcome the shortcoming inherent in the empirical models and take into account the attributes of the pore space

(e.g., pore tortuosity, connectivity and pore size distribution) for the RAP prediction. They conceptualize the porous media as a bundle of intersecting capillary tubes and use the Water Retention Function (WRF) to predict the RAP. A large number of expressions have been developed to characterize the WRFs [e.g., *Brooks and Corey*, 1964; *Brutsaert*, 1966; *van Genuchten*, 1980; *Kosugi*, 1996; *Assouline et al.*, 1998]. A recent review on the proposed WRFs can be found in *Assouline and Or* [2013]. These WRFs can be utilized in combination with the relative permeability models [e.g., *Purcell*, 1949; *Burdine*, 1953; *Mualem*, 1976; *Alexander and Skaggs*, 1986; *Luckner et al.*, 1989; *Assouline*, 2001; *Kuang and Jiao*, 2011] to derive specific RAP functions [*Chen et al.*, 1999; *Dury et al.*, 1999; *Yang and Mohanty*, 2015]. For example, the Brooks and Corey-Burdine (BCB) model derived by *Brooks and Corey* [1964] and the van Genuchten-Mualem (VGM) model derived by *Parker et al.* [1987] are the two frequently used RAP representations in the subsurface multiphase flow numerical modeling [*Gerhard and Kueper*, 2003; *Smits et al.*, 2012].

It is noticed that compared to the earlier WRFs such as *Brooks and Corey* [1964] and *van Genuchten* [1980], the more recently developed WRFs [*Kosugi*, 1996; *Assouline et al.*, 1998] are less frequently combined with the relative permeability models to derive RAP models. *Chen et al.* [1999] derived the RAP expression by combining the *Kosugi* [1996] WRF with *Mualem* [1976] relative permeability model. This Kosugi–Mualem (KM) RAP model was also adopted in *Tuli and Hopmans* [2004]. *Yang and Mohanty* [2015] recently developed a generalized RAP expression with the Kosugi WRF. By setting specific values to the (α, β, η) parameters in the generalized RAP model, one

can arrive at the specific RAP expressions, such as Kosugi–Purcell (KP), Kosugi–Burdine (KB), KM, Kosugi–Alexander and Skaggs (KAS), Kosugi–Luckner et al. (KL) and Kosugi–Kuang and Jiao (KKJ) RAP models. The RAP models and experimental observed data comparison in *Yang and Mohanty* [2015] shows that the tortuosity-connectivity parameter α for water and air relative permeability should be different. The optimum tortuosity-connectivity parameter α for the Burdine, Mualem and Alexander and Skaggs relative permeability models was correspondingly obtained, and the resulting Kosugi–modified Burdine (KMB), Kosugi–modified Mualem (KMM), and Kosugi–modified Alexander and Skaggs (KMAS) models demonstrate the improved RAP prediction when compared with the KP, KB, KM, KAS, KL and KKJ models [*Yang and Mohanty*, 2015]. The WRF developed by *Assouline et al.* [1998] is used even less for the RAP evaluation. Only recently, *Assouline et al.* [2016] proposed a new model for the accurate RAP prediction by combining the *Assouline et al.* [1998] WRF with the *Assouline et al.* [2016] relative permeability model. This new RAP model is an extension of the approach developed by *Assouline* [2001] for the relative hydraulic conductivity prediction. This Assouline et al.–Assouline et al. (AA) RAP model is found to predict the RAP better than the Assouline et al.–Mualem (AM) and Assouline et al.–Kuang and Jiao (AKJ) models in the sandy loam and silty clay loam soils cases. However, it is still largely unknown the performance of the other relative permeability models such as Burdine and Alexander and Skaggs for the RAP prediction when adopting the *Assouline et al.* [1998] WRF. In addition, according to *Dury et al.* [1999], the choice of the relative permeability model (e.g., Burdine or Mualem) is critical and

decisive for the RAP prediction in the statistical models. Therefore, it should be interesting and meaningful to investigate the other commonly used relative permeability models (e.g., Burdine and Alexander and Skaggs)'s performance for the RAP prediction when combining with the *Assouline et al.* [1998] WRF.

As such, the main objectives of this study are (1) to derive and formulate the RAP models of Assouline et al.–Purcell (AP), Assouline et al.–Burdine (AB), Assouline et al.–Alexander and Skaggs (AAS), Assouline et al.–Luckner et al. (AL), Assouline et al.–modified Burdine (AMB), Assouline et al.–modified Mualem (AMM) and Assouline et al.–modified Alexander and Skaggs (AMAS) and (2) to conduct a comparison between the experimental measured data and ten predictive RAP models (seven are derived in this study and the other three are proposed by *Assouline et al.* [2016]).

4.3 Theory

4.3.1 Water retention function

In this study, the WRF developed by *Assouline et al.* [1998] is adopted. This model [*Assouline and Tartakovsky*, 2001] hypothesized that the soil structure evolves from a uniform and random fragmentation process and that a particle fragmentation's probability is proportional to its volume. The resulting soil particle size distribution tends asymptotically to an exponential distribution (i.e., a particular case of the Weibull distribution). A power function relationship was then used to transform the particle volume into the pore volume. The consequent pore volume probability distribution function turned out to be the general Weibull distribution [*Assouline and Tartakovsky*, 2001]. Substituting the Young-Laplace capillary pressure function into the pore volume

probability distribution function yields the WRF of *Assouline et al.* [1998], which is expressed as

$$S_e(h) = \frac{\theta - \theta_r}{\theta_s - \theta_r} = 1 - \exp\left[-\xi \left(\frac{1}{h} - \frac{1}{h_L} \right)^{\mu} \right] \qquad 0 \le h \le h_L \tag{4.1}$$

where S_e (dimensionless) represents the effective water saturation that varies from 0 (when $\theta = \theta_r$) to 1 (when $\theta = \theta_s$), h (L) is the soil pressure head (absolute value), θ (L^3 L^{-3}) is the volumetric water content, θ_s (L^3 L^{-3}) and θ_r (L^3 L^{-3}) denote the saturated and residual volumetric water content, respectively, ξ (L^{μ}) and μ (dimensionless) are the fitting parameters, and h_L (L) is the pressure head corresponding to the residual water content θ_r, as *Assouline et al.* [2016] suggested, when measured information on h_L is unavailable, h_L can be considered equal to 152.957 m.

The *Assouline et al.* [1998] WRF in equation (4.1) is mainly characterized by the first and second moments [*Assouline*, 2001], i.e., the mean r_G, and the variance σ^2:

$$r_G = \xi^{-1/\mu} \Gamma(1 + 1/\mu) + 1/h_L \tag{4.2}$$

$$\sigma^2 = \xi^{-2/\mu} \left\{ \Gamma(1 + 2/\mu) - \Gamma^2(1 + 1/\mu) \right\} \tag{4.3}$$

where Γ is the Gamma function. The coefficient of variation ε, is the statistical parameter that addresses both the mean and variance of the *Assouline et al.* [1998] WRF and it is defined as:

$$\varepsilon = \frac{\sigma}{r_G} = \frac{\xi^{-1/\mu} \left[\Gamma(1 + 2/\mu) - \Gamma^2(1 + 1/\mu) \right]^{0.5}}{\xi^{-1/\mu} \Gamma(1 + 1/\mu) + 1/h_L} \tag{4.4}$$

4.3.2 General expression for RAP

Linking the Hagen-Poiseuille equation (valid at the pore scale) with the Darcy equation (valid at the Representative Elementary Volume scale), the statistical approach can be used to derive the relative air permeability. The generalized expression for the RAP k_{ra} (dimensionless), can be represented as [*Kuang and Jiao*, 2011; *Yang and Mohanty*, 2015]

$$k_{ra}(S_e) = \frac{k_a(S_e)}{k_{sa}} = (1 - S_e)^{\alpha} \left\{ \frac{\int_{S_e}^{1} h^{-\beta} dS_e(h)}{\int_{0}^{1} h^{-\beta} dS_e(h)} \right\}^{\eta} \tag{4.5}$$

where k_a (L T^{-1}) and k_{sa} (L T^{-1}) are the unsaturated and saturated air permeability, respectively [*Tuli and Hopmans*, 2004; *Yang and Mohanty*, 2015; *Assouline et al.*, 2016]. In equation (4.5), the parameter α is associated with the porous media's pore tortuosity-connectivity [*Dury et al.*, 1999], the parameter β is related to the microscopic pore tortuosity [*Fatt and Dykstra*, 1951; *Kosugi*, 1999], and the parameter η defines the pore configuration and reflects the approach to assess the effective pore radius [*Raats*, 1992; *Kosugi*, 1999]. As Table 4.1 shows, the (α, β, η) parameters in equation (4.5) can be varied to obtain the ten specific functional expressions. It should be mentioned that the power value η in *Assouline et al.* [2016] relative permeability model is found to be a decreasing exponential function of the coefficient of variation ε of *Assouline et al.* [1998] WRF, which can be expressed as [*Assouline et al.*, 2016]

$$\eta = 2.80e^{-1.15\varepsilon} \qquad \left(r^2 = 0.89\right) \tag{4.6}$$

Table 4.1 Identification of the ten relative permeability models with the generalized model given by equation (4.5)

Relative Permeability Models	α	β	η
Purcell [1949]	0	2	1
Burdine [1953]	2	2	1
Mualem [1976]	0.5	1	2
Alexander and Skaggs [1986]	1	1	1
Luckner et al. [1989]	1/3	1	2
Kuang and Jiao [2011]	0.5	1	4
modified Burdine [Yang and Mohanty, 2015]	2.5	2	1
modified Mualem [Yang and Mohanty, 2015]	2	1	2
modified Alexander and Skaggs [Yang and Mohanty, 2015]	2.5	1	1
Assouline et al. [2016]	0	1	$2.80e^{-1.15\varepsilon}$

4.3.3 Ten RAP models with Assouline et al. WRF

Inserting equation (4.1) into equation (4.5) with the specific (α, β, η) values given in the Table 4.1, which represents the respective relative permeability models, one can derive and obtain the ten RAP models based on the Assouline et al. WRF (Table 4.2). The derivation of the Assouline et al.–Burdine (AB) model is given in the Appendix D as an example, and the rest nine RAP models can be derived in the similar manner. Noted that in equations (4.7)–(4.16) in Table 4.2, $\gamma(s,x)$ and $\Gamma(x)$ denote the incomplete and complete gamma functions, respectively, and $x = \left(h^{-1} - h_L^{-1}\right)^{\mu}$.

Table 4.2 Relative air permeability models derived by combining the Assouline et al. water retention function with the ten relative permeability models as given by equation (4.5) with the specific (alpha, beta, eta) values shown in Table 4.1

Model	Reference	Relative Air Permeability	Equation Number
Assouline et al. – Purcell (AP)	This study	$k_{ra}=\left[1-\frac{\xi^{-2/\mu}\frac{2}{\mu}\gamma\left(\frac{2}{\mu},\xi x\right)+\frac{2}{h_L}\xi^{-1/\mu}\frac{1}{\mu}\gamma\left(\frac{1}{\mu},\xi x\right)-\frac{1}{h^2}e^{-\xi x}+\frac{1}{h_L^2}}{\xi^{-2/\mu}\frac{2}{\mu}\Gamma\left(\frac{2}{\mu}\right)+\frac{2}{h_L}\xi^{-1/\mu}\frac{1}{\mu}\Gamma\left(\frac{1}{\mu}\right)+\frac{1}{h_L^2}}\right]$	(4.7)
Assouline et al. – Burdine (AB)[a]	This study	$k_{ra}=\left(1-S_e\right)^2\left[1-\frac{\xi^{-2/\mu}\frac{2}{\mu}\gamma\left(\frac{2}{\mu},\xi x\right)+\frac{2}{h_L}\xi^{-1/\mu}\frac{1}{\mu}\gamma\left(\frac{1}{\mu},\xi x\right)-\frac{1}{h^2}e^{-\xi x}+\frac{1}{h_L^2}}{\xi^{-2/\mu}\frac{2}{\mu}\Gamma\left(\frac{2}{\mu}\right)+\frac{2}{h_L}\xi^{-1/\mu}\frac{1}{\mu}\Gamma\left(\frac{1}{\mu}\right)+\frac{1}{h_L^2}}\right]$	(4.8)
Assouline et al. – Mualem (AM)	Assouline et al. [2016]	$k_{ra}=\left(1-S_e\right)^{0.5}\left[1-\frac{\xi^{-1/\mu}\frac{1}{\mu}\gamma\left(\frac{1}{\mu},\xi x\right)-\frac{1}{h}e^{-\xi x}+\frac{1}{h_L}}{\xi^{-1/\mu}\frac{1}{\mu}\Gamma\left(\frac{1}{\mu}\right)+\frac{1}{h_L}}\right]^2$	(4.9)
Assouline et al. – Alexander and Skaggs (AAS)	This study	$k_{ra}=\left(1-S_e\right)\left[1-\frac{\xi^{-1/\mu}\frac{1}{\mu}\gamma\left(\frac{1}{\mu},\xi x\right)-\frac{1}{h}e^{-\xi x}+\frac{1}{h_L}}{\xi^{-1/\mu}\frac{1}{\mu}\Gamma\left(\frac{1}{\mu}\right)+\frac{1}{h_L}}\right]$	(4.10)
Assouline et al. – Luckner et al. (AL)	This study	$k_{ra}=\left(1-S_e\right)^{1/3}\left[1-\frac{\xi^{-1/\mu}\frac{1}{\mu}\gamma\left(\frac{1}{\mu},\xi x\right)-\frac{1}{h}e^{-\xi x}+\frac{1}{h_L}}{\xi^{-1/\mu}\frac{1}{\mu}\Gamma\left(\frac{1}{\mu}\right)+\frac{1}{h_L}}\right]^2$	(4.11)
Assouline et al. – Kuang and Jiao (AKJ)	Assouline et al. [2016]	$k_{ra}=\left(1-S_e\right)^{0.5}\left[1-\frac{\xi^{-1/\mu}\frac{1}{\mu}\gamma\left(\frac{1}{\mu},\xi x\right)-\frac{1}{h}e^{-\xi x}+\frac{1}{h_L}}{\xi^{-1/\mu}\frac{1}{\mu}\Gamma\left(\frac{1}{\mu}\right)+\frac{1}{h_L}}\right]^4$	(4.12)
Assouline et al. – Modified Burdine (AMB)	This study	$k_{ra}=\left(1-S_e\right)^{2.5}\left[1-\frac{\xi^{-2/\mu}\frac{2}{\mu}\gamma\left(\frac{2}{\mu},\xi x\right)+\frac{2}{h_L}\xi^{-1/\mu}\frac{1}{\mu}\gamma\left(\frac{1}{\mu},\xi x\right)-\frac{1}{h^2}e^{-\xi x}+\frac{1}{h_L^2}}{\xi^{-2/\mu}\frac{2}{\mu}\Gamma\left(\frac{2}{\mu}\right)+\frac{2}{h_L}\xi^{-1/\mu}\frac{1}{\mu}\Gamma\left(\frac{1}{\mu}\right)+\frac{1}{h_L^2}}\right]$	(4.13)

Table 4.2 Continued

Model	Reference	Relative Air Permeability	Equation Number
Assouline et al. – Modified Mualem (AMM)	This study	$k_{ra} = (1-S_e)^2 \left[1 - \frac{\xi^{-1/\mu} \frac{1}{\mu} \gamma\left(\frac{1}{\mu}, \xi x\right) - \frac{1}{h} e^{-\xi x} + \frac{1}{h_L}}{\xi^{-1/\mu} \frac{1}{\mu} \Gamma\left(\frac{1}{\mu}\right) + \frac{1}{h_L}} \right]^2$	(4.14)
Assouline et al. – Modified Alexander and Skaggs (AMAS)	This study	$k_{ra} = (1-S_e)^{2.5} \left[1 - \frac{\xi^{-1/\mu} \frac{1}{\mu} \gamma\left(\frac{1}{\mu}, \xi x\right) - \frac{1}{h} e^{-\xi x} + \frac{1}{h_L}}{\xi^{-1/\mu} \frac{1}{\mu} \Gamma\left(\frac{1}{\mu}\right) + \frac{1}{h_L}} \right]$	(4.15)
Assouline et al. – Assouline (AA)[b]	Assouline et al. [2016]	$k_{ra} = \left[1 - \frac{\xi^{-1/\mu} \frac{1}{\mu} \gamma\left(\frac{1}{\mu}, \xi x\right) - \frac{1}{h} e^{-\xi x} + \frac{1}{h_L}}{\xi^{-1/\mu} \frac{1}{\mu} \Gamma\left(\frac{1}{\mu}\right) + \frac{1}{h_L}} \right]^{\eta}$	(4.16)

[a]The derivation of AB model is shown in the Appendix D, and the rest nine RAP models can be derived in the similar manner.
[b]The η value in AA model is calculated based on equation (4.6), which is shown in the Table 4.3.

4.4 Results and discussions

4.4.1 Testing data sets

Experimental data on soil water retention and relative air permeability for a relatively large range of porous media types [*Kuang and Jiao*, 2011; *Ghanbarian-Alavijeh and Hunt*, 2012; *Yang and Mohanty*, 2015; *Assouline et al.*, 2016] are selected from the literature to evaluate the predictive ability of the ten RAP models given in Table 4.2. These data sets consisted of 30 porous media samples (28 unconsolidated soils and 2 consolidated sandstones). The 30 samples shown in the Table 4.3 are all under disturbed conditions and hence have a unimodal pore system.

The Assouline et al. WRF (equation (4.1)) was fitted to the measured soil water retention data pairs $S(h)$. Notice that S (dimensionless) here represents the water saturation, and it can be transferred to the volumetric water content θ (L^3 L^{-3}) via the expression $\theta = \phi S$, in which ϕ (L^3 L^{-3}) denotes the porosity of the porous media. For each porous media sample, the parameters θ_s, θ_r, ξ and μ in equation (4.1) were determined, using the 'lsqcurvefit' function in the MATLAB optimization toolbox (The MathWorks, Inc.). The fitted values are shown in Table 4.3. In addition, Table 4.3 also shows the coefficient of variation ε and the corresponding power value η for each sample, calculated by equation (4.4) and equation (4.6), respectively. It can be seen from Table 4.3 that all the 30 samples can be characterized by the Assouline et al. WRF reasonably well. This is because the root mean square error (RMSE) is usually small, and the coefficient of determination (R^2) of the curve fitting is always larger than 0.97.

Table 4.3 Data sets investigated in this study, fitted parameters for the Assouline et al. Water Retention Function, and the calculated epsilon and predicted eta value based on equation (4.4) and equation (4.6), respectively

Reference	Medium type	Porosity	θ_s	θ_r	ξ	μ	ε	η -Eq.(4.6)	RMSE	R^2
Collis-George [1953]	Cambridge sand	0.380	0.380	0.034	2.1E-8	9.080	0.132	2.407	0.012	0.994
Brooks and Corey [1964]	Volcanic sand	0.351	0.351	0.055	2.6E-3	3.767	0.296	1.993	0.005	0.998
Brooks and Corey [1964]	Glass beads	0.370	0.370	0.036	6.7E-7	12.214	0.099	2.498	0.007	0.998
Brooks and Corey [1964]	Fine sand	0.377	0.377	0.059	0.042	4.056	0.276	2.038	0.008	0.996
Brooks and Corey [1964]	Touchet silt loam	0.485	0.485	0.180	0.799	3.995	0.279	2.032	0.004	0.998
Brooks and Corey [1964]	Fragmented mixture	0.443	0.443	0.132	9.8E-4	4.347	0.260	2.077	0.007	0.997
Brooks and Corey [1964]	Fragmented Fox Hill	0.470	0.470	0.144	0.007	2.398	0.444	1.681	0.006	0.998
Brooks and Corey [1964]	Berea sandstone	0.206	0.206	0.065	0.025	5.109	0.224	2.165	0.001	0.999
Brooks and Corey [1964]	Hygiene sandstone	0.250	0.250	0.147	0.051	5.914	0.196	2.236	0.001	0.997
Brooks and Corey [1966]	Poudre river sand	0.364	0.364	0.042	6.0E-4	4.007	0.280	2.030	0.005	0.998
Brooks and Corey [1966]	Amarillo silty clay loam	0.455	0.455	0.110	0.105	2.973	0.365	1.840	0.012	0.991
Touma and Vauclin [1986]	Grenoble sand	0.370	0.308	0.003	0.244	1.114	0.897	0.998	0.004	0.998
Stonestrom [1987]	Oakley sand	0.365	0.322	0.099	0.035	3.808	0.292	2.000	0.009	0.992
Dury [1997]	Mixed sand	0.360	0.285	0.017	0.013	3.650	0.304	1.974	0.006	0.997
Tuli and Hopmans [2004]	Columbia sandy loam	0.466	0.429	0.082	1.230	0.722	1.401	0.559	0.005	0.998
Tuli and Hopmans [2004]	Oso Flaco fine sand	0.419	0.406	0.062	0.083	3.663	0.303	1.977	0.017	0.972
Tuli et al. [2005]	D41	0.443	0.437	0.104	2.107	0.715	1.407	0.555	0.006	0.991
Tuli et al. [2005]	D44	0.508	0.447	0.063	1.806	0.724	1.391	0.566	0.006	0.994
Tuli et al. [2005]	D59	0.421	0.421	0.152	3.725	1.579	0.637	1.346	0.013	0.973
Tuli et al. [2005]	D126	0.521	0.481	0.064	2.024	0.744	1.345	0.596	0.012	0.977
Tuli et al. [2005]	D127	0.470	0.465	0.169	2.795	1.338	0.744	1.191	0.009	0.988
Tuli et al. [2005]	D128	0.515	0.467	0.136	1.978	0.730	1.375	0.576	0.003	0.998
Tuli et al. [2005]	D129	0.444	0.442	0.178	2.880	1.068	0.920	0.972	0.005	0.993
Tuli et al. [2005]	D131	0.476	0.469	0.168	1.641	1.187	0.837	1.069	0.014	0.976

Table 4.3 Continued

Reference	Medium type	Porosity	θ_s	θ_r	ξ	μ	ε	η -Eq.(4.6)	RMSE	R^2
Tuli et al. [2005]	D132	0.466	0.462	0.161	3.238	1.725	0.589	1.422	0.009	0.991
Tuli et al. [2005]	D134	0.449	0.449	0.187	3.164	1.321	0.752	1.180	0.006	0.992
Tuli et al. [2005]	D139	0.464	0.442	0.172	3.474	1.586	0.635	1.349	0.012	0.978
Tuli et al. [2005]	D140	0.465	0.438	0.122	1.442	0.734	1.374	0.577	0.007	0.990
Tuli et al. [2005]	D142	0.556	0.556	0.100	0.979	0.370	3.586	0.045	0.009	0.991
Tuli et al. [2005]	D143	0.457	0.425	0.164	2.527	1.137	0.868	1.032	0.010	0.974

It is worth mentioning that the $k_{ra}(\theta)$ experimental data in *Tuli et al.* [2005] is not directly available. Therefore, based on the $k_a(\theta)$ data given in *Tuli et al.* [2005], we estimate the saturated air permeability k_{sa} using the power function $k_a(S_e) = k_{sa}(1-S_e)^{\gamma}$ as suggested by *Tuli and Hopmans* [2004] and *Assouline et al.* [2016]. The k_{sa} and γ are treated as two fitting parameters. After obtaining the saturated air permeability k_{sa}, the relative air permeability k_{ra} can be calculated for the data sets of *Tuli et al.* [2005] according to $k_{ra} = k_a / k_{sa}$.

4.4.2 Illustrative examples

Four soils (Glass beads, Poudre river sand, Oakley sand and Columbia sandy loam) are chosen to graphically illustrate the comparisons between the predicted and measured soil water retention and relative air permeability curves in this section. As can be seen from Figure 4.1, the fitted Assouline et al. WRF is able to reproduce accurately the experimental water retention data for the Glass beads and Poudre river sand (Figure 4.1a) and the Oakley sand and Columbia sandy loam (Figure 4.1b).

Figures 4.2 and 4.3 depict the comparison between the measured and predicted relative air permeability values for the four soils. The AP model is found to significantly overpredict the measured RAP over the whole range of water saturation for all the four soils (Figures 4.2a, 4.2d, 4.3a and 4.3d). The AB model provides a slight RAP overestimation for Glass beads and Poudre river sand when the water saturation is smaller than 0.6 (Figures 4.2a and 4.2d). The slight overestimation of RAP predicted by the AB model is noticed for Oakley sand and Columbia sandy loam when the water

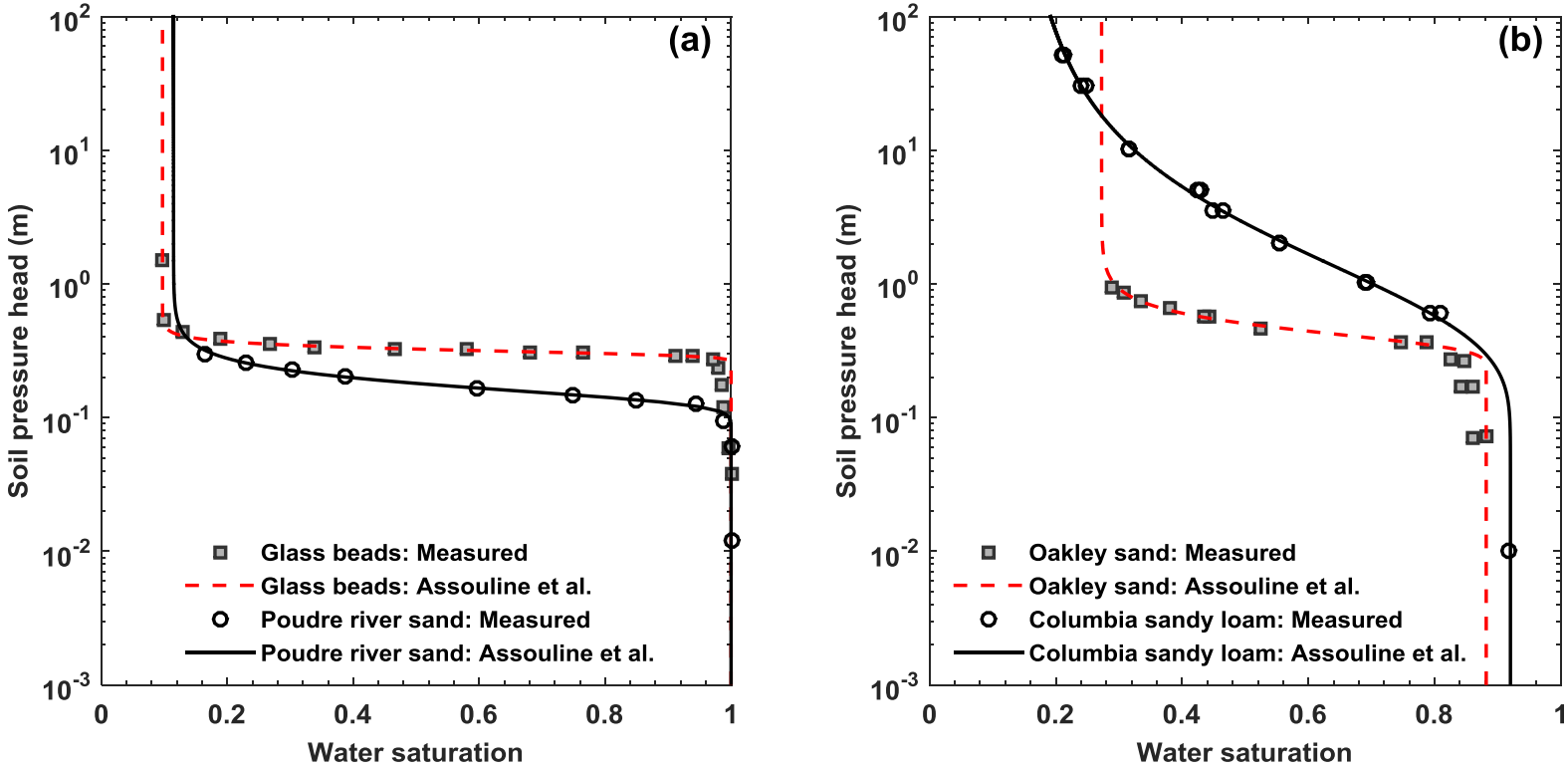

Figure 4.1 The measured data points and the fitted Assouline et al. water retention function for (a) Glass beads and Poudre river sand and (b) Oakley sand and Columbia sandy loam.

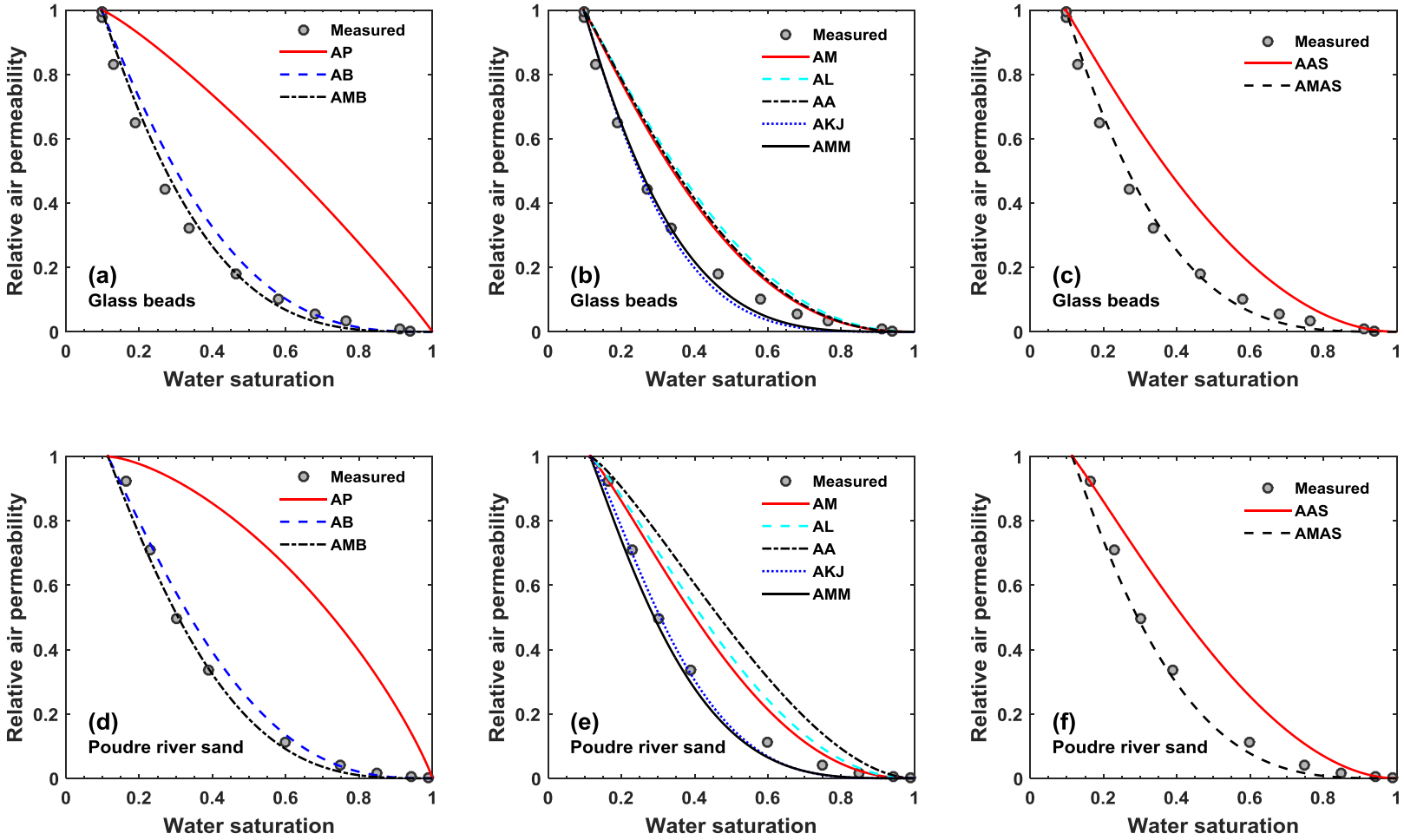

Figure 4.2 Comparison of measured data obtained for Glass beads ((a), (b) and (c)) and Poudre river sand ((d), (e) and (f)) with predicted results using the AP, AB, and AMB ((a) and (d)), AM, AL, AA, AKJ and AMM ((b) and (e)), and AAS and AMAS ((c) and (f)) relative air permeability models.

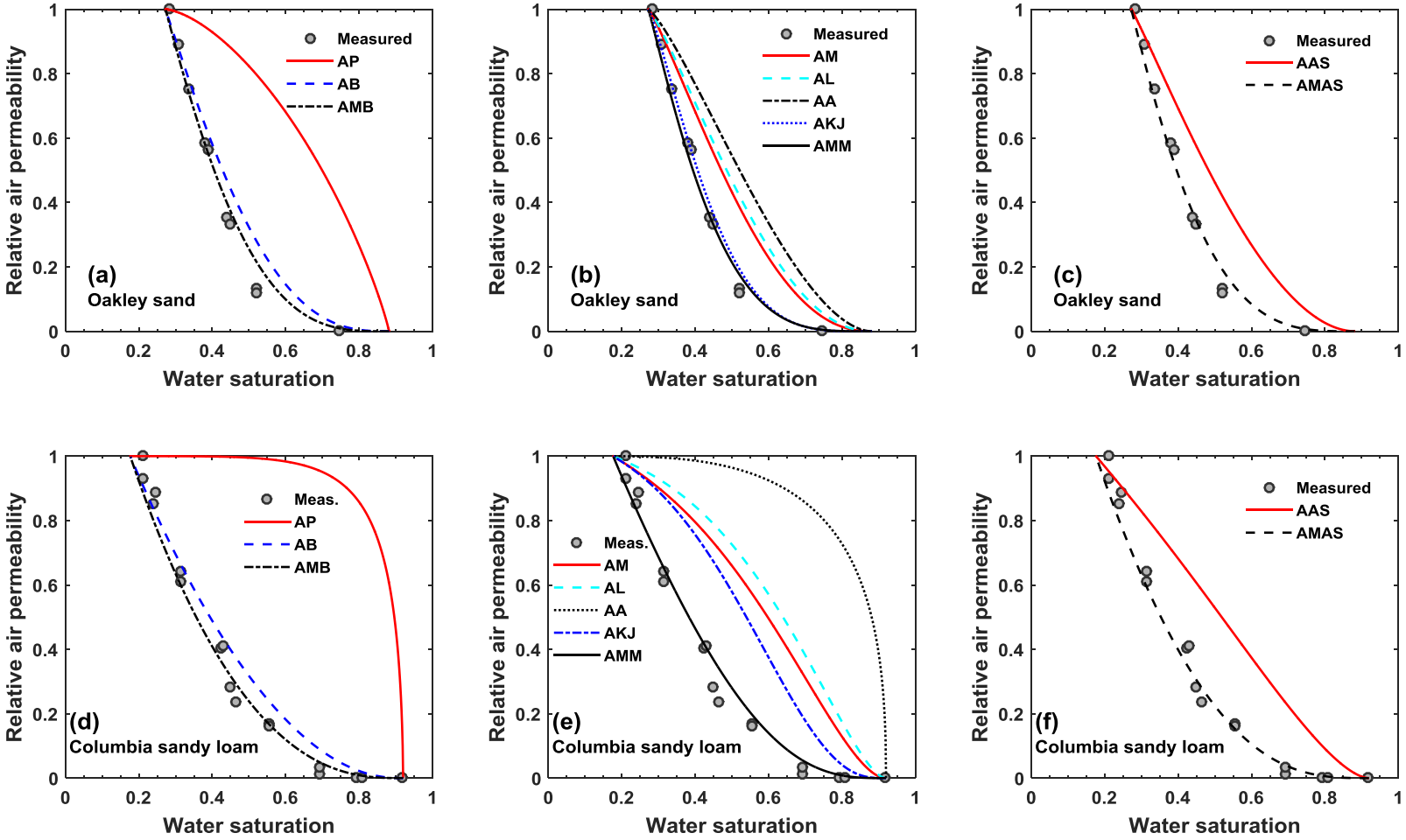

Figure 4.3 Comparison of measured data obtained for Oakley sand ((a), (b) and (c)) and Columbia sandy loam ((d), (e) and (f)) with predicted results using the AP, AB, and AMB ((a) and (d)), AM, AL, AA, AKJ and AMM ((b) and (e)), and AAS and AMAS ((c) and (f)) relative air permeability models.

saturation is greater than 0.45 (Figures 4.3a and 4.3d). The AMB model produces a slight improved RAP prediction for the four soils compared to the AB model (Figures 4.2a, 4.2d, 4.3a and 4.3d).

The AM, AA and AL models all present an overestimated RAP prediction for Glass beads when the water saturation is smaller than 0.7 (Figure 4.2b). In addition, for this Glass beads, the different predicted curves by the AM, AA and AL models are virtually undistinguishable. The overprediction of the measured RAP for Glass beads is reduced largely by both the AKJ and AMM models, although these two models provide a slight underestimation of the RAP when the water saturation is larger than 0.45 (Figure 4.2b). Furthermore, it is noticed that the difference between the AKJ and AMM predicted curves is very small as shown in Figure 4.2b. Figure 4.2e display that for the Poudre river sand, the AA model yields a significant overestimation of the measured RAP when the water saturation is smaller than 0.9. The AL and AM models also produce a clear RAP overestimation when the water saturation is smaller than 0.8. However, such overestimation error can be remarkably reduced by both the AKJ and AMM models. In addition, the different predicted curves by the AKJ and AMM models are hardly distinguishable, particularly for the water saturation greater than 0.45.

It can be seen from Figure 4.3b that for the Oakley sand, the AA, AL and AM models largely overestimate the measured RAP values. The improved and accurate RAP prediction is successfully obtained by both the AKJ and AMM models. Furthermore, the predicted RAP curve of the AKJ model is still very close to that of the AMM model. Figure 4.3e illustrates that for the Columbia sandy loam, the AA model significantly

overestimates the measured RAP values. The AL, AM and AKJ models yield the gradually decreasing overestimation of the measured RAP values when the water saturation is less than 0.9. On the contrary, the AMM model presents a quite accurate RAP prediction for this Columbia sandy loam.

Figures 4.2c, 4.2f, 4.3c and 4.3f clearly show that for all the four illustrated soils, the AAS model significantly overpredicts the measured RAP values. However, the AMAS model presents an improved and accurate RAP prediction of the measured data.

4.4.3 Statistical analysis

Further comparison of the ten predicted RAP models with the whole measured data sets is implemented by calculating the root mean square error (RMSE). The RMSE, computed as equation (4.17), quantifies the level of agreement between the experimental measured data and model prediction.

$$RMSE = \sqrt{\frac{1}{N}\sum_{i=1}^{N}\left[k_{ra,i} - \hat{k}_{ra,i}\left(S_{ei}\right)\right]^2} \tag{4.17}$$

where $k_{ra,i}$ and $\hat{k}_{ra,i}\left(S_{ei}\right)$ are the measured and predicted relative air permeability, respectively, and N is the number of measurement points for each porous media sample. Table 4.4 lists the RMSE of the ten predicted RAP models for the whole 30 data sets, including the four soil samples described in section 4.4.2. The average value of the RMSE (aveRMSE) for all the 30 porous media samples [*Kosugi*, 1999; *Kuang and Jiao*, 2011; *Yang and Mohanty*, 2015] was calculated to generally evaluate the prediction accuracy of each RAP model for the entire data sets.

Table 4.4 RMSE values obtained with the ten (AP, AB, AM, AAS, AL, AKJ, AMB, AMM, AMAS, and AA) RAP models, which are mathematically given by Equations (4.7)-(4.16) in Table 4.2

		RMSE									
Reference	Medium type	AP	AB	AM	AAS	AL	AKJ	AMB	AMM	AMAS	AA
Collis-George [1953]	Cambridge sand	0.362	0.012	0.068	0.114	0.090	0.074	0.034	0.067	0.045	0.089
Brooks and Corey [1964]	Volcanic sand	0.319	0.018	0.070	0.085	0.088	0.031	0.024	0.042	0.037	0.129
Brooks and Corey [1964]	Glass beads	0.313	0.063	0.102	0.136	0.117	0.033	0.037	0.028	0.031	0.109
Brooks and Corey [1964]	Fine sand	0.356	0.041	0.096	0.112	0.114	0.024	0.029	0.041	0.038	0.154
Brooks and Corey [1964]	Touchet silt loam	0.448	0.139	0.192	0.205	0.209	0.123	0.114	0.108	0.107	0.249
Brooks and Corey [1964]	Fragmented mixture	0.313	0.048	0.100	0.112	0.116	0.042	0.030	0.040	0.034	0.148
Brooks and Corey [1964]	Fragmented Fox Hill	0.387	0.031	0.115	0.109	0.137	0.051	0.037	0.050	0.053	0.219
Brooks and Corey [1964]	Berea sandstone	0.576	0.188	0.266	0.299	0.292	0.110	0.135	0.100	0.116	0.329
Brooks and Corey [1964]	Hygiene sandstone	0.408	0.045	0.097	0.130	0.118	0.064	0.041	0.062	0.049	0.140
Brooks and Corey [1966]	Poudre river sand	0.354	0.041	0.099	0.114	0.118	0.025	0.027	0.040	0.037	0.159
Brooks and Corey [1966]	Amarillo silty clay loam	0.428	0.019	0.096	0.108	0.121	0.021	0.035	0.054	0.053	0.197
Touma and Vauclin [1986]	Grenoble sand	0.542	0.087	0.170	0.120	0.209	0.086	0.132	0.114	0.146	0.415
Stonestrom [1987]	Oakley sand	0.445	0.092	0.172	0.189	0.197	0.037	0.050	0.038	0.043	0.252
Dury [1997]	Mixed sand	0.456	0.071	0.134	0.158	0.159	0.050	0.065	0.075	0.075	0.222
Tuli and Hopmans [2004]	Columbia sandy loam	0.628	0.066	0.285	0.199	0.332	0.229	0.050	0.048	0.051	0.580
Tuli and Hopmans [2004]	Oso Flaco fine sand	0.367	0.049	0.052	0.069	0.069	0.080	0.078	0.097	0.092	0.120
Tuli et al. [2005]	D41	0.596	0.150	0.108	0.047	0.164	0.064	0.196	0.181	0.206	0.524
Tuli et al. [2005]	D44	0.780	0.109	0.348	0.257	0.403	0.270	0.058	0.081	0.048	0.714
Tuli et al. [2005]	D59	0.438	0.056	0.098	0.076	0.126	0.059	0.097	0.103	0.114	0.272
Tuli et al. [2005]	D126	0.681	0.051	0.177	0.096	0.231	0.095	0.095	0.080	0.105	0.593
Tuli et al. [2005]	D127	0.719	0.214	0.366	0.329	0.401	0.271	0.162	0.165	0.145	0.575
Tuli et al. [2005]	D128	0.775	0.094	0.326	0.238	0.380	0.244	0.045	0.065	0.035	0.703
Tuli et al. [2005]	D129	0.669	0.055	0.224	0.176	0.266	0.125	0.017	0.020	0.020	0.522

Table 4.4 Continued

Reference	Medium type	RMSE									
		AP	AB	AM	AAS	AL	AKJ	AMB	AMM	AMAS	AA
Tuli et al. [2005]	D131	0.763	0.279	0.444	0.396	0.478	0.368	0.226	0.238	0.211	0.648
Tuli et al. [2005]	D132	0.424	0.046	0.082	0.063	0.111	0.050	0.095	0.103	0.114	0.247
Tuli et al. [2005]	D134	0.511	0.065	0.111	0.082	0.146	0.056	0.109	0.112	0.126	0.342
Tuli et al. [2005]	D139	0.375	0.129	0.074	0.065	0.082	0.123	0.169	0.174	0.184	0.199
Tuli et al. [2005]	D140	0.775	0.104	0.365	0.266	0.421	0.285	0.046	0.073	0.036	0.715
Tuli et al. [2005]	D142	0.812	0.142	0.524	0.352	0.600	0.509	0.080	0.138	0.078	0.821
Tuli et al. [2005]	D143	0.748	0.185	0.355	0.308	0.395	0.260	0.133	0.141	0.118	0.614
	Average RMSE	0.526	0.090	0.191	0.167	0.223	0.129	0.082	0.089	0.085	0.367

As can be seen from Figure 4.4, the AP model tends to significantly overestimate the measured relative air permeability for the whole data sets (Figure 4.4a). The aveRMSE of AP model is equal to 0.526, which is the largest among the ten RAP models. The AA model, followed by the AL, AM, and AAS models, also tends to generally overestimate the measured RAP values for the entire 30 samples as shown in Figures 4.4j, 4.4e, 4.4c and 4.4d. The aveRMSE of AA, AL, AM and AAS models is gradually decreasing, which indicates that the overestimation error of these four models is gradually reduced. The AKJ model to some extent shows the improved RAP prediction (Figure 4.4f) and the aveRMSE is 0.129. The aveRMSE of AB model is equal to 0.090, indicating that the original Burdine relative permeability model is not very poor for the RAP prediction. In addition, the comparison of AP and AB models (Figures 4.4a and 4.4b) implies that it is important to appropriately account for the pore tortuosity and conectivity for the RAP prediction in the statistical models. This is evidenced by the fact that compared to the AP model (equation (4.7)), the overestimation error was largely reduced by the AB model (equation (4.8)), which takes into account the pore tortuosity and conectivity effect ($(1-S_e)^2$).

A much better linearship between the predicted and measured RAP values can be found in the AMB, AMM, and AMAS models (Figures 4.4g, 4.4h, and 4.4i). Furthermore, it can be seen from Table 4.4 and Figure 4.4 that among the ten investigated RAP predictive models, the AMB, AMM, and AMAS models have the lowest aveRMSE values, which are 1.1, 2.1 and 2.0 times smaller than that of their corresponding original relative permeability models (i.e., AB, AM, and AAS models),

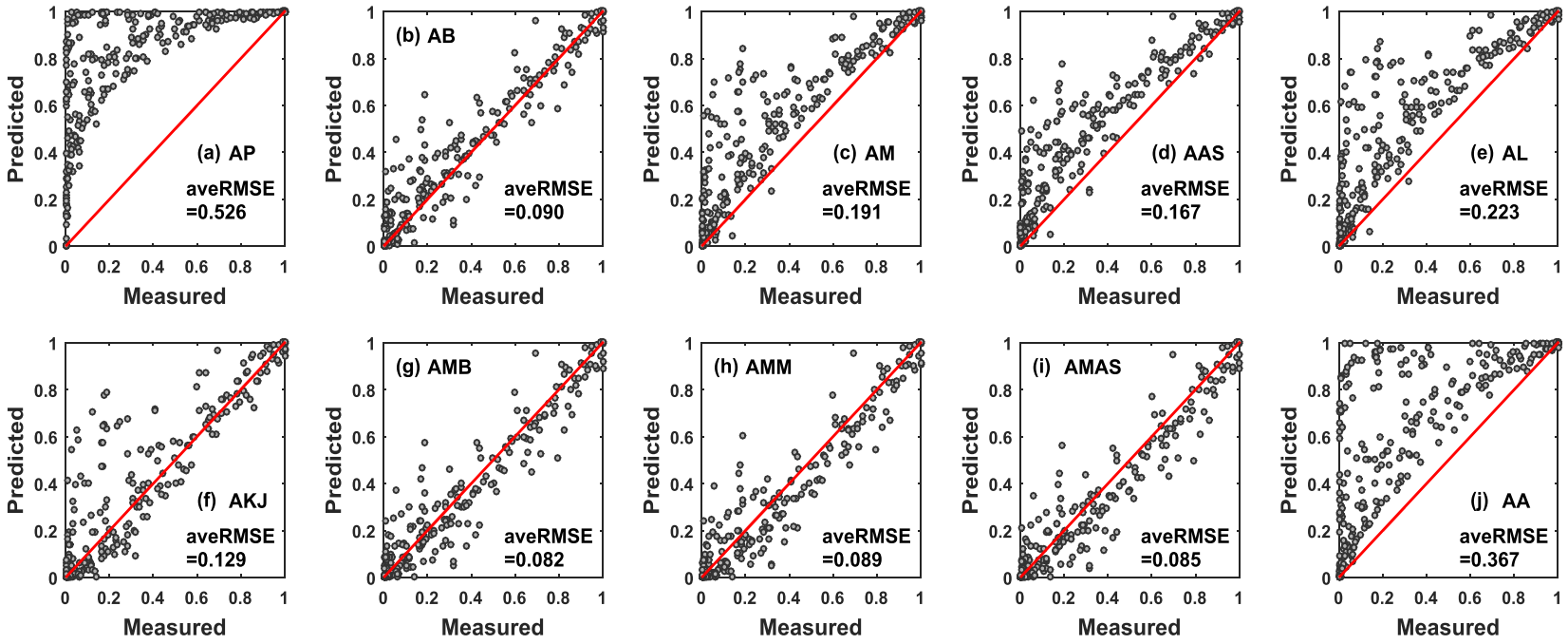

Figure 4.4 Scatter charts of measured versus predicted relative air permeability values by the (a) AP, (b) AB, (c) AM, (d) AAS, (e) AL, (f) AKJ, (g) AMB, (h) AMM, (i) AMAS, and (j) AA models.

respectively. It should be further emphasized that among the three modified relative permeability models suggested by *Yang and Mohanty* [2015], the improvements of RAP prediction are more significant for the modified Mualem and modified Alexander and Skaggs models compared to the modified Burdine model.

The optimum tortuosity-connectivity parameter α for the modified Burdine, modified Mualem and modified Alexander and Skaggs models obtained in *Yang and Mohanty* [2015] probably depends on the investigated data sets. As such, with the incorporation of more data sets adopted in this work, the optimum parameter α for the RAP models may or may not change. In order to investigate this issue, similar to *Kuang and Jiao* [2011] and *Yang and Mohanty* [2015], the variations of the average RMSE (of entire 30 samples) with α for the Burdine, Mualem and Alexander and Skaggs models are obtained and plotted in Figure 4.5. It can be seen from Figure 4.5 that based on the 30 disturbed porous media samples used in this study, the optimum α value for the Burdine, Mualem and Alexander and Skaggs RAP models is still 2.5, 2 and 2.5, respectively. However, it is worth mentioning that as Figure 4.5c displays, for the Alexander and Skaggs model, when $\alpha = 2.5$, the average RMSE is 0.0849, which is very close to the case that the average RMSE arrives at 0.0850 when $\alpha = 2$. This fact indicates that the optimum α value obtained in this study is still data set dependent and not definitely conclusive yet. It is very likely that one might obtain different optimum α value for relative air permeability in future when using a different data set. In spite of this shortcoming, this study further confirms that in the statistical models, the pore tortuosity-connectivity parameter α for water and air relative permeability should be

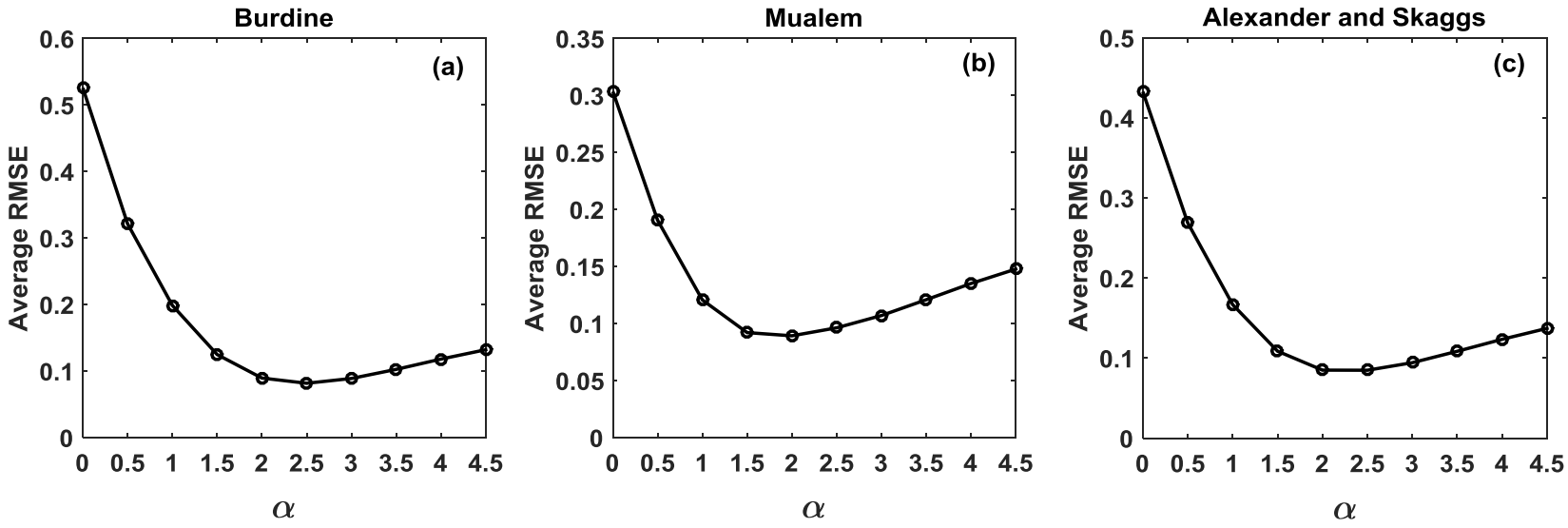

Figure 4.5 Variations of the average RMSE with alpha of the (a) Burdine, (b) Mualem and (c) Alexander and Skaggs model.

different, which is consistent with the findings of *Tuli and Hopmans* [2004], *Tuli et al.* [2005] and *Yang and Mohanty* [2015].

4.5 Summary and conclusion

The relative air permeability (RAP) is an indispensable parameter for modeling the convective air flow in the unsaturated porous media. By adopting the *Assouline et al.* [1998] water retention function (WRF), this study first derived and formulated seven new predictive relative air permeability models. They are the Assouline et al.–Purcell (AP), Assouline et al.–Burdine (AB), Assouline et al.–Alexander and Skaggs (AAS), Assouline et al.–Luckner et al. (AL), Assouline et al.–modified Burdine (AMB), Assouline et al.–modified Mualem (AMM) and Assouline et al.–modified Alexander and Skaggs (AMAS) models. These seven new models, together with the other three RAP models derived by *Assouline et al.* [2016], namely, the Assouline et al.–Mualem (AM), Assouline et al.–Kuang and Jiao (AKJ) and Assouline et al.–Assouline et al. (AA) models, were subsequently compared with 30 disturbed porous media samples to investigate the performance of each model for the RAP prediction.

It is found that the AP model significantly overestimates the measured RAP for the entire data sets and the average RMSE of AP model is the biggest among the ten investigated predictive models. The AA model, followed by the AL, AM, and AAS models, also generally overpredicts the measured RAP values for the entire 30 samples. The overestimation error of AA, AL, AM and AAS models is gradually reduced as reflected by the gradually decreased average RMSE of these four models. The average RMSE of AKJ and AB models is further decreased and equals to 0.129 and 0.090,

respectively. The relatively low average RMSE of AB model implies that the original Burdine relative permeability model is not too bad for the RAP prediction. However, the AMB, AMM, and AMAS models have the lowest average RMSE values among the ten predictive RAP models, which equal to 0.082, 0.089 and 0.085, respectively. In addition, the average RMSE of the AMB, AMM, and AMAS models are 1.1, 2.1 and 2.0 times smaller than that of their corresponding original relative permeability models (i.e., AB, AM, and AAS models), respectively. As such, the AMB, AMM, and AMAS RAP models are the recommended parameterizations to be used in the subsurface multiphase flow numerical modeling.

It is admitted that the optimum pore tortuosity and connectivity α value obtained in this work is likely data sets dependent, and future researchers might arrive at different optimum α value when using a different data set. Despite of this possible shortcoming, it is confirmed that the α value for water and air relative permeability in the statistical models is supposed to be different. This conclusion is consistent with the previous findings of *Tuli and Hopmans* [2004], *Tuli et al.* [2005] and *Yang and Mohanty* [2015].

5 EFFECTS OF THE FULL RANGE WATER RETENTION CURVE ON HEAT AND WATER TRANSPORT IN THE VADOSE ZONE

5.1 Synopsis

Understanding coupled heat and water transfer appropriately in the shallow subsurface is of vital significance for accurate prediction of soil evaporation that would improve the coupling between land surface and atmosphere. The theory of Philip and de Vries (1957) and its extensions (de Vries, 1958; Milly, 1982), although physically incomplete, are still adopted successfully to describe the coupled heat and water movement in low permeability field soils. However, the adsorptive water retention, which was ignored in Philip and de Vries theory and its extensions for characterizing soil hydraulic parameters, was shown to be nonnegligible for soil moisture and evaporation flux in dry field soils based on a recent synthetic analysis (Mohanty and Yang, 2013). In this study, we attempt to comprehensively investigate the effects of full range water retention curve on coupled heat and water transport simulation with a focus on soil moisture, temperature and evaporative flux, based on two synthetic (sand and loam) and two field sites (Riverside, California and Audubon, Arizona) analyses. The results of synthetic sand and loam coupled modeling showed that when neglecting adsorptive water retention, resulting simulated soil water content would be larger, and evaporative flux would be lower, respectively, compared to that obtained by the full range water retention model. Moreover, the evaporation underestimation was mainly caused by isothermal hydraulic conductivity underprediction. These synthetic findings

were further fully corroborated by Audubon, Arizona field experimental data and to certain extent confirmed by Riverside, California field experimental data owing to its extremely dry soil surface.

5.2 Introduction

Coupled heat and water movement in unsaturated soils has been recognized and studied extensively. It has always been of vital interest to the fields of vadose zone hydrology, environmental engineering, and agronomy. The simultaneous heat and moisture transfer in the unsaturated porous media has remarkable impacts on soil physical processes such as soil evaporation that consequently affects exchange of mass and energy fluxes between land surface and atmosphere [*Brubaker and Entekhabi*, 1996; *Brutsaert*, 2005; *Garcia Gonzalez et al.*, 2012], chemical processes such as contaminant volatilization and transport [*Nassar et al.*, 1999; *Reichman et al.*, 2013a, 2013b], and biological processes such as seed germination, plant growth and soil microbial activity [*Sung et al.*, 2002; *Ji et al.*, 2009].

It is acknowledged that there are two established approaches to analyze coupled heat and water movement in variably saturated porous media [*Ten Berge and Bolt*, 1988; *Feddes et al.*, 1988], i.e., the mechanistic approach [*Philip and de Vries*, 1957; *de Vries*, 1958] and the irreversible thermodynamic approach [*Taylor and Cary*, 1964; *Cary*, 1965; *Weeks et al.*, 1968]. It is worth noting that the mechanistic approach is still widely accepted and used nowadays [e.g., *Heitman et al.*, 2008; *Zeng et al.*, 2009, 2011a, 2011b; *Sakai et al.*, 2009, 2011; *Deb et al.*, 2011a, 2011b; *Novak*, 2010, 2016; *Garcia Gonzalez et al.*, 2012; *Grifoll*, 2013; *Mosthaf et al.*, 2011, 2014; *Davarzani et al.*, 2014;

Trautz et al., 2015; *Fetzer et al.*, 2017; *Vanderborght et al.*, 2017] compared to the irreversible thermodynamic approach. As *Milly* [1982, 1988] pointed out, the limited use of irreversible thermodynamic approach is likely induced by two reasons. One is the lack of rigorous proof of integration from pore scale to Darcy scale continuum equations when treating unsaturated porous media by means of irreversible thermodynamic approach [*Milly*, 1982]. The other is the little useful information regarding the nature of transport coefficients in irreversible thermodynamic approach [*Milly*, 1988]. Therefore, the mechanistic approach is adopted in this work.

It is generally accepted that the mechanistic approach was first proposed by *Philip and de Vries* [1957] (hereafter referred to as PdV), who presented a mathematical model to describe the interactions between liquid water, water vapor and heat transport in unsaturated porous media. This PdV model consists of a water balance equation and an energy balance equation. The water balance equation was an extension of the isothermal Richards equation, employing Darcy's law for liquid water flux and Fick's law for water vapor diffusion flux, with the hypothesis of chemical equilibrium between liquid and vapor phases [*Novak*, 2016]. The energy balance equation included both heat conduction (Fourier's law) and latent heat of vaporization transported by water vapor diffusion. Shortly thereafter, *de Vries* [1958] extended the original PdV theory to incorporate processes such as heat of wetting, advection of sensible heat by water (liquid plus vapor), and moisture content and latent heat storage in vapor phase but these were conceived to be of secondary importance [*Novak*, 2016]. The PdV theory was further improved by *Milly* [1982], who converted the *de Vries* [1958] formulation to the one

based on matric potential rather than soil moisture content as dependent variable, so as to account for soil heterogeneity and moisture retention hysteresis. The transport of adsorbed liquid water induced by temperature gradients, known as thermal liquid film flow [*Kay and Groenevelt*, 1974], was also taken into account in *Milly* [1982] model.

Cahill and Parlange [1998] noticed that there exists a significant discrepancy between the estimated diffusive vapor flux predicted by the PdV theory and the measured vapor flux in bare field soil of Yolo silt loam. The measured vapor flux in *Cahill and Parlange* [1998] was inferred based on the residuals of respective energy balance equation and mass balance equation using observed soil temperature and moisture content data. These authors thus concluded that the PdV theory, which considered vapor diffusion only, was physically incomplete with respect to the characterization of vapor transport, even though the vapor enhancement factor was already included in PdV model to rectify vapor diffusive flux. As such, *Parlange et al.* [1998] subsequently proposed that the volume expansion and contraction of near surface soil air resulted from diurnal warming and cooling could transfer water vapor in gas phase by convection. This natural convective vapor flux was larger and more significant than the diffusive vapor flux predicted by the PdV theory. They demonstrated that incorporation of this thermally driven vapor convection mechanism into PdV theory can significantly increase the agreement between their calculated and measured vapor fluxes in field Yolo silt loam soil. *Grifoll et al.* [2005] proposed a coupled water-gas-vapor-heat transfer model in unsaturated porous media by further incorporating the gas phase convection, vapor convection and dispersion, and sensible heat dispersion in liquid phase

compared to the PdV model. Notice that the liquid-vapor phase exchange (i.e., kinetic interphase mass transfer) was unambiguously considered in *Grifoll et al.* [2005] model formulation but without explicit analytical expression. However, this chemical nonequilibrium liquid-vapor mass transfer has an explicit mathematical formulation in the works of *Smits et al.* [2011, 2012], *Davarzani et al.* [2014], and *Trautz et al.* [2015].

Despite the conceptual progresses achieved compared to the original PdV theory [*Cahill and Parlange*, 1998; *Parlange et al.*, 1998; *Grifoll et al.*, 2005; *Smits et al.*, 2011], it is not necessarily conclusive that these additional physical processes are significantly important for the coupled heat and water transport descriptions in soils and across the soil-atmosphere interface, particularly for highly transient natural field conditions. For instance, a detailed numerical analysis of coupled water-vapor-air-heat transport in field soils [*Novak*, 2016] casted doubts on the conclusions of *Cahill and Parlange* [1998] and *Parlange et al.* [1998]. Using the same Davis, California bare field soil (Yolo silt loam) data sets as in *Cahill and Parlange* [1998] and *Parlange et al.* [1998], *Novak* [2016] found that the diurnal soil heating (natural convection), the low-frequency barometric pressure fluctuations (forced convection), and the enhancement of soil vapor diffusion all have the negligible effects on evaporation under natural field conditions. *Novak* [2016] concluded that the original version of the PdV theory is consistent with the *Cahill and Parlange* [1998]'s field measurements. In addition, a recent experimental analysis [*Levintal et al.*, 2017] demonstrated that the thermal vapor/air convection typically occurs for highly permeable porous media (e.g., structured macropore soils and fractured rocks) with permeability ranging from 10^{-7} to 10^{-6} m^2. As

a consequence, the thermal vapor/air convection conjectured by *Parlange et al.* [1998] is unlikely to occur under natural daily changes of temperature because the permeability of Yolo silt loam in *Cahill and Parlange* [1998] and *Parlange et al.* [1998] is approximately equal to 10^{-14} m^2, which obviously belonged to low permeability ($<10^{-7}$ m^2) porous media [*Levintal et al.*, 2017]. The findings of *Levintal et al.* [2017] are consistent with the results of *Novak* [2016] in that the natural and forced convection is found to be insignificant and negligible in low permeability ($<10^{-7}$ m^2) soils under natural field conditions. Correspondingly, to date, the PdV theory and its extensions [e.g., *de Vries*, 1958; *Milly*, 1982] have long been accepted and used successfully to determine the coupled heat and water transport in soils (mainly low permeability) and across the soil-atmosphere interface, especially for natural field conditions [e.g., *Saito et al.*, 2006; *Bittelli et al.*, 2008; *Ji et al.*, 2009; *Zeng et al.*, 2009; *Saito and Šimůnek*, 2009; *Novak*, 2010, 2016; *Garcia et al.*, 2011; *Deb et al.*, 2011a, 2011b; *Garcia Gonzalez et al.*, 2012; *Hou et al.*, 2016; *Dijkema et al.*, 2017].

It is widely observed that the mechanistic coupled heat and water models [e.g., *Philip and de Vries*, 1957; *de Vries*, 1958; *Milly*, 1982] are typically used to investigate the evaporation process in relatively dry soils under arid and semiarid environments [e.g., *Scanlon et al.*, 1997; *Saito et al.*, 2006; *Bittelli et al.*, 2008; *Zeng et al.*, 2009, 2011a, 2011b; *Hou et al.*, 2016; *Dijkema et al.*, 2017]. Under such dry soil conditions, liquid film flow induced by the adsorptive forces may play a significant role in the soil evaporations [*Scanlon et al.*, 1997; *Mohanty and Yang*, 2013]. Both isothermal simulation [*Peters and Durner*, 2008; *Peters*, 2013; *Wang et al.*, 2013] and field

observation results [*Goss and Madliger*, 2007] all indicated that the evaporation rate in dry soils would be underpredicted due to the underestimation of isothermal hydraulic conductivity, which is caused by neglecting the adsorbed water. In fact, there is little doubt that improved modeling of evaporation process in low water content field soils is likely to require better understanding of the thermodynamics of adsorbed water and improving parameterizations of the water retention curves, especially near the dry end [*Scanlon et al.*, 1997; *Webb*, 2000; *Smits et al.*, 2012; *Mohanty and Yang*, 2013; *Ciocca et al.*, 2014].

Various commonly used capillary force based water retention functions [e.g., *Brooks and Corey*, 1964; *van Genuchten*, 1980] have been improved and extended to represent full range (saturated to oven dry) soil water retention curves [e.g., *Campbell and Shiozawa*, 1992; *Rossi and Nimmo*, 1994; *Fayer and Simmons*, 1995; *Webb*, 2000; *Khlosi et al.*, 2006; *Silva and Grifoll*, 2007; *Lebeau and Konrad*, 2010; *Zhang*, 2011; *Wang et al.*, 2013; *Peters*, 2013]. While these extended full range retention functions provide significantly improved parameterizations of the soil water retention characteristics (low water content range in particular), their application and testing in numerical heat and water transport models has been rather limited [*Silva and Grifoll*, 2007; *Peters*, 2013; *Ciocca et al.*, 2014], especially for highly transient field conditions. However, it seems important and more suited to adopt the extended full range water retention curve, which accounted for both capillary and adsorptive forces, in the coupled heat and water modeling for better description of evaporation process under relatively dry soil conditions [*Scanlon et al.*, 1997; *Ciocca et al.*, 2014; *Vanderborght et al.*, 2017].

Andraski and Jacobson [2000] were perhaps among the earliest to explicitly test the performance of a full range water retention curve in modeling water potential and temperature in field soils. They included the *Rossi and Nimmo* [1994] full range water retention function into the modified UNSAT-H numerical model [*Fayer and Jones*, 1990] to simulate the coupled water, vapor and heat transport in a layered Nevada desert soil. Then they compared the field measured and simulated water potential and temperature values. Their results showed that the Rossi and Nimmo (RN) full range retention function can improve the prediction of both water potentials in near-surface soils (especially under dry conditions) and temperatures throughout the soil profile. But unfortunately the influence of using RN function on land surface fluxes such as evaporation has not been investigated in *Andraski and Jacobson* [2000]'s work. Following *Sakai et al.* [2009, 2011], *Mohanty and Yang* [2013] recently used the *Fayer and Simmons* [1995] parameterization in the synthetic coupled water-vapor-heat simulation under field conditions, to explore the necessity of employing full range water retention function in a dry sandy soil. The results of *Mohanty and Yang* [2013]'s numerical modeling demonstrated that without accounting for the adsorptive water retention (i.e., *van Genuchten* [1980] function), the resulting simulated soil water content would be greater, and the evaporative flux would be smaller, respectively, compared to that obtained by the full range water retention curve model (i.e., *Fayer and Simmons* [1995] function). In addition, *Ciocca et al.* [2014] also obtained the similar results as *Mohanty and Yang* [2013] in their synthetic isothermal coupled water-vapor simulations in arid loam and sandy-loam soils by using *van Genuchten* [1980], modified *van*

Genuchten [1980], and *Webb* [2000] water retention models. It should be emphasized that there are no observed field experimental data to corroborate the synthetic analysis results of *Mohanty and Yang* [2013] under nonisothermal conditions and of *Ciocca et al.* [2014] under isothermal conditions.

So far it would largely seem missing to examine the impacts of using extended full range water retention curve on modeling both the soil state variables and land surface fluxes for natural field conditions, with observed experimental data in the context of coupled heat and water transport simulation. Motivated by this limitation, in this work, we investigate the effects of full range water retention curve on coupled heat and water transport simulation with a focus on soil moisture content, temperature and soil evaporative flux, with synthetic (sand and loam) experiments, and field observed (Riverside, California and Audubon, Arizona) data analysis by using a modified HYDRUS-1D numerical code [*Sakai et al.*, 2009, 2011]. In addition to the hydrological and land-atmosphere interaction importance, this research is applicable to various engineering and industrial applications such as reservoir CO_2 injection [*Zhang et al.*, 2016].

5.3 Materials and methods

5.3.1 Numerical model formulations

As outlined above, the PdV theory and its extensions [e.g., *de Vries*, 1958; *Milly*, 1982], although physically incomplete [*Cahill and Parlange*, 1998; *Parlange et al.*, 1998; *Grifoll et al.*, 2005; *Smits et al.*, 2011], are still widely accepted and adopted successfully to describe the coupled heat and water movement in low permeability ($<10^{-}$

^{7} m^2) soils and across the soil-atmosphere interface under highly transient field conditions [*Bittelli et al.*, 2008; *Zeng et al.*, 2009; *Saito and Šimůnek*, 2009; *Novak*, 2010, 2016; *Garcia et al.*, 2011; *Deb et al.*, 2011a, 2011b; *Garcia Gonzalez et al.*, 2012; *Hou et al.*, 2016; *Dijkema et al.*, 2017]. The modified computer program HYDRUS-1D [*Saito et al.*, 2006; *Šimůnek et al.*, 2008; *Sakai et al.*, 2009, 2011], used in this study to simulate coupled water-vapor-heat transport, was mainly based on the PdV theory and its extensions [*de Vries*, 1958; *Milly*, 1982]. The governing balance equations of water and vapor flow and heat transport in the vadose zone, as well as the associated soil hydraulic and thermal properties employed in modified HYDRUS-1D are briefly presented in sections 5.3.1.1, 5.3.1.2 and 5.3.1.3, respectively. The initial and boundary conditions are briefly described in section 5.3.1.4. More details can be easily found in *Saito et al.* [2006], *Šimůnek et al.* [2008] and *Sakai et al.* [2009, 2011].

5.3.1.1 Mass and energy balance equations

The water mass conservation equation for one-dimensional vertical flow of liquid water and water vapor in a variably saturated rigid bare soil is given as follows [*Saito et al.*, 2006]:

$$\frac{\partial \theta}{\partial t} = -\frac{\partial (q_{Lh} + q_{LT})}{\partial z} - \frac{\partial (q_{vh} + q_{vT})}{\partial z}$$

$$= \frac{\partial}{\partial z}\left[K_{Lh}\left(\frac{\partial h}{\partial z} + 1\right) + K_{LT}\frac{\partial T}{\partial z} + K_{vh}\frac{\partial h}{\partial z} + K_{vT}\frac{\partial T}{\partial z}\right] \quad (5.1)$$

where θ is the total volumetric water content (L^3 L^{-3}), defined as the sum of volumetric liquid water content θ_l (L^3 L^{-3}) and volumetric water vapor content θ_v

(expressed as an equivalent water content, $L^3\ L^{-3}$); t is time (T); q_{Lh} and q_{LT} are the isothermal and thermal liquid water flux densities ($L\ T^{-1}$), respectively; q_{vh} and q_{vT} are the isothermal and thermal water vapor flux densities ($L\ T^{-1}$), respectively; z is the spatial coordinate positive upward (L); h is the pressure head (negative suction head) (L); T is the temperature (K); K_{Lh} ($L\ T^{-1}$) and K_{LT} ($L^2\ K^{-1}\ T^{-1}$) are the isothermal and thermal hydraulic conductivities for liquid water fluxes due to gradients in h and T, respectively; and K_{vh} ($L\ T^{-1}$) and K_{vT} ($L^2\ K^{-1}\ T^{-1}$) are the isothermal and thermal vapor hydraulic conductivities for water vapor fluxes, respectively.

Considering conductive (first term on right-hand side of (5.2)), convective sensible heat (second and third term), and latent heat transfer (fourth term), the heat energy conservation equation for one-dimensional vertical movement in a variably saturated rigid bare soil is described as follows [*Saito et al.*, 2006]:

$$\frac{\partial C_p T}{\partial t} + L\frac{\partial \theta_v}{\partial t} = \frac{\partial}{\partial z}\left[\lambda(\theta)\frac{\partial T}{\partial z}\right] - C_l\frac{\partial q_L T}{\partial z} - C_v\frac{\partial q_v T}{\partial z} - L\frac{\partial q_v}{\partial z} \tag{5.2}$$

where $C_p = C_s\theta_s + C_l\theta_l + C_v\theta_v$ when assuming local thermal equilibrium (i.e., presuming temperatures in solid, liquid, and gas phases are the same); θ_s is the volumetric fraction of solid phase ($L^3\ L^{-3}$); C_p, C_s, C_l, and C_v are the volumetric heat capacities ($M\ L^{-1}\ T^{-2}\ K^{-1}$) of the moist soil, solid phase, liquid water, and water vapor, respectively; L is the volumetric latent heat of vaporization of liquid water ($M\ L^{-1}\ T^{-2}$) and is given by $L = L_w\rho_w$, in which L_w is the latent heat of vaporization of liquid water ($L^2\ T^{-2}$) and ρ_w is the density of liquid water ($M\ L^{-3}$); $\lambda(\theta)$ is the apparent thermal

conductivity of soil (M L T^{-3} K^{-1}); and $q_L\,(=q_{Lh}+q_{LT})$ and $q_v\,(=q_{vh}+q_{vT})$ are the flux densities of liquid water and water vapor (L T^{-1}), respectively.

5.3.1.2 Soil hydraulic properties

A number of statistical models [*Yang and Mohanty*, 2015; *Yang et al.*, 2017b] have been proposed to predict the isothermal unsaturated hydraulic conductivity K_{Lh} from water retention function. Among the most popular and widely used, the statistical pore size distribution model put forward by *Mualem* [1976] was employed in this work and may be written as follows:

$$K_{Lh}=K_s S_e^{0.5}\left[\frac{\int_0^{S_e} dS_e/|h|}{\int_0^1 dS_e/|h|}\right]^2 \tag{5.3}$$

where K_s is the saturated hydraulic conductivity (L T^{-1}); and S_e is the effective saturation (dimensionless).

The water retention curve model developed by *van Genuchten* [1980] is widely used to characterize water retention at wet and intermediate soil moisture content. The *van Genuchten* [1980] model, which considers capillary force only, is expressed as:

$$\theta_l(h)=\theta_r+(\theta_s-\theta_r)\left[1+|\alpha h|^n\right]^{-m} \tag{5.4}$$

where θ_s and θ_r are the saturated and residual water contents (L^3 L^{-3}), respectively; and α (L^{-1}), n (unitless), and $m\,(=1-1/n)$ are empirical shape parameters.

Substituting equation (5.4) into equation (5.3), one can obtain the K_{Lh} for the van Genuchten model as:

$$K_{Lh} = K_s S_e^{0.5}\left[1-\left(1-S_e^{1/m}\right)^m\right]^2 \tag{5.5}$$

The van Genuchten (VG) model commonly failed to accurately describe soil water retention in the dry range. The full range water retention model proposed by *Fayer and Simmons* [1995], however, can represent the soil water retention function well in both the dry and wet regions simultaneously. The Fayer and Simmons (FS) model takes into account the adsorption of water on soil under relatively dry conditions via modifying the residual water content in the VG model:

$$\theta_l(h) = \chi\theta_a + \left(\theta_s - \chi\theta_a\right)\left[1+\left|\alpha h\right|^n\right]^{-m} \tag{5.6}$$

where θ_a ($L^3\ L^{-3}$) is a curve fitting parameter representing the volumetric water content when $|h|=1$; $\chi\theta_a$ represents the adsorption of water on soil and χ is described as $\chi(h)=1-\ln(|h|)/\ln(|h_m|)$, where h_m is the pressure head in which the water content equals to zero (L). According to *Fayer and Simmons* [1995], $|h_m|$ is generally taken to be 10^7 cm and may be higher for fine textured soils such as clay.

The closed form analytical expression of isothermal hydraulic conductivity K_{Lh} for the FS model is obtained by inserting equation (5.6) into equation (5.3):

$$K_{Lh} = K_s S_e^{0.5}\left[\frac{\int_0^{S_e} dS_e/|h|}{\int_0^1 dS_e/|h|}\right]^2 = K_s S_e^{0.5}\left[\frac{\Gamma_s(h)}{\Gamma_{\max}}\right]^2 \tag{5.7}$$

The expressions of both $\Gamma_s(h)$ and $\Gamma_{\max}$ are detailed and given in the appendix of *Fayer and Simmons* [1995]. It should be noticed that the implementation of FS model is not available in current HYDRUS-1D code [*Saito et al.*, 2006; *Šimůnek et al.*, 2008] and thus is incorporated in its modified version [*Sakai et al.*, 2009, 2011] that is used in this study.

Considering the temperature dependence of the pressure head (i.e., influence of temperature on surface tension), the thermal hydraulic conductivity K_{LT}, for the thermal liquid water flux is defined as follows [*Noborio et al.*, 1996; *Saito et al.*, 2006]:

$$K_{LT} = K_{Lh}\left(hG_{wT}\frac{1}{\gamma_0}\frac{d\gamma}{dT} \right) \tag{5.8}$$

where G_{wT} is the gain factor (unitless), which corrects the temperature dependence of the surface tension [*Nimmo and Miller*, 1986]; γ is the surface tension of soil water (M T^{-2}); and γ_0 is the surface tension at 25°C, which equals to 71.89 g s^{-2}.

The vapor hydraulic conductivities under isothermal condition K_{vh}, and under thermal condition K_{vT}, are, respectively, defined as [*Noborio et al.*, 1996; *Fayer*, 2000]:

$$K_{vh} = \frac{D}{\rho_w}\rho_{sv}\frac{Mg}{RT}H_r \tag{5.9}$$

$$K_{vT} = \frac{D}{\rho_w}\eta H_r\frac{d\rho_{sv}}{dT} \tag{5.10}$$

where D is the vapor diffusivity in soil (L^2 T^{-1}); ρ_{sv} is the saturated vapor density (M L^{-3}); M is the molecular weight of water (M mol^{-1}) and equals to 0.018015 kg mol^{-1}; g is the gravitational acceleration (L T^{-2}, =9.81 m s^{-2}); R is the universal gas

constant (M L^2 T^{-2} mol^{-1} K^{-1}, =8.314 J mol^{-1} K^{-1}); η is the enhancement factor (unitless) [*Cass et al.*, 1984]; and H_r is the relative humidity (unitless), which can be calculated from the pressure head, h, using a thermodynamic relationship (Kelvin equation) between liquid water and water vapor in soil pores [*Philip and de Vries*, 1957] as $H_r = \exp(hMg / RT)$.

5.3.1.3 Soil thermal properties

The apparent thermal conductivity of soil, $\lambda(\theta)$, in equation (5.2) is defined as the sum of the thermal conductivity of soil in absence of water flow and the macrodispersivity that is assumed to be a linear function of water velocity [*Hopmans et al.*, 2002]. The apparent thermal conductivity (M L T^{-3} K^{-1}), $\lambda(\theta)$, may thus be expressed as follows [*Saito et al.*, 2006]:

$$\lambda(\theta) = \lambda_0(\theta) + \beta C_l |q_L| \tag{5.11}$$

in which β is the thermal dispersivity (L). The thermal conductivity, $\lambda_0(\theta)$, considers the tortuosity of the soil and is calculated by *Chung and Horton* [1987]:

$$\lambda_0(\theta) = b_1 + b_2\theta + b_3\theta^{0.5} \tag{5.12}$$

where b_1, b_2, and b_3 are the empirical regression parameters (M L T^{-3} K^{-1}) that are related to soil textures (e.g., sand, loam, and clay).

5.3.1.4 Initial and boundary conditions

Initial conditions for the water (mass) and heat (energy) balance equations are respectively given by:

$$h(z,0) = h_i(z) \tag{5.13}$$

$$T(z,0) = T_i(z) \tag{5.14}$$

where $h_i(z)$ and $T_i(z)$ represent the initial soil pressure head and soil temperature, respectively.

In field soils when the surface observed soil temperature is not available, the top surface boundary conditions for the soil water and heat conservation equations based on the surface mass and energy balance can then be, respectively, defined by:

$$q_w(0,t) = P - E \tag{5.15}$$

$$G(0,t) = R_n - H - LE \tag{5.16}$$

where $q_w = q_L + q_v$ is the total water flux density (L T^{-1}); P represents the natural precipitation or human irrigation (L T^{-1}); E is the evaporation rate (L T^{-1}); G is the conductive soil heat flux density (M T^{-3}); R_n is net radiation (M T^{-3}); H is sensible heat flux density (M T^{-3}); LE is the latent heat flux density (M T^{-3}); and L is the volumetric latent heat (M L^{-1} T^{-2}).

The net radiation, R_n, in the field is determined by:

$$R_n = R_{ns} + R_{nl} = (1-a)R_s + \varepsilon_s\sigma\left(\varepsilon_a T_a^4 - T_s^4\right) \tag{5.17}$$

in which R_{ns} and R_{nl} are the net shortwave radiation and net longwave radiation, respectively (M T^{-3}); a is the surface albedo (unitless); R_s is the incoming shortwave solar radiation (M T^{-3}); ε_s is the soil surface emissivity (unitless) describing the reflection of the longwave radiation at the soil surface; σ is the Stefan-Boltzmann

constant (5.67×10^{-8} W m^{-2} K^{-4}); ε_a is atmospheric emissivity of clear sky (unitless); and T_a and T_s are the air temperature and soil surface temperature, respectively (K).

The sensible heat flux in equation (5.16) is defined as [*Saito et al.*, 2006]:

$$H = C_a \frac{T_s - T_a}{r_H} \tag{5.18}$$

where C_a is the volumetric heat capacities (M L^{-1} T^{-2} K^{-1}) of air; and r_H is the aerodynamic resistance to heat transfer (T L^{-1}).

Soil surface evaporation, in general, is controlled mainly by atmospheric conditions (i.e., stage 1 evaporation), surface moisture content, and water transport in the soil (i.e., stage 2 and 3 evaporation). A model accounting for all these factors can be expressed as [*Saito et al.*, 2006]:

$$E = \frac{\rho_{vs} - \rho_{va}}{\rho_w (r_a + r_s)} \tag{5.19}$$

where ρ_{vs} is the water vapor density at soil surface (M L^{-3}); ρ_{va} is the atmospheric vapor density (M L^{-3}); r_a is the aerodynamic resistance for water vapor transfer (T L^{-1}); and r_s is the soil surface resistance for water vapor transfer (T L^{-1}).

The aerodynamic resistance to heat transfer (r_H) is usually very close to the aerodynamic resistance to water vapor transfer (r_a), therefore, it can be assumed that $r_H = r_a$. They can be computed from the surface roughness properties and wind speed as follows [*Saito et al.*, 2006; *Bittelli et al.*, 2008]:

$$r_H = r_a = \frac{1}{Uk^2}\left[\ln\left(\frac{z_m - d + z_{om}}{z_{om}}\right) + \phi_m\right]\cdot\left[\ln\left(\frac{z_h - d + z_{oh}}{z_{oh}}\right) + \phi_h\right] \tag{5.20}$$

where z_m and z_h are the measurement heights of wind speed and temperature, respectively (L); d (L) is the zero plane displacement (=0 for bare soils); z_{om} and z_{oh} are the surface roughness lengths for momentum flux and heat flux, respectively (L); ϕ_m and ϕ_h are the atmospheric stability correction factors for momentum flux and heat flux, respectively (unitless); U is the measured wind speed (L T^{-1}) at height z_m; and k is the von Karman constant (=0.41). For bare soils, surface roughness values z_{om} and z_{oh} are both assumed to be equal to 0.001 m.

The soil surface resistance r_s for water vapor transfer proposed by *van de Griend and Owe* [1994] used the following exponential function:

$$r_s = \begin{cases} r_{sl}\exp\left(A\left(\theta_{\min} - \theta_0\right)\right) & \theta_0 \le \theta_{\min} \\ r_{sl} & \theta_0 > \theta_{\min} \end{cases} \tag{5.21}$$

where r_{sl} (=10 s m^{-1}) is the resistance to molecular diffusion of water surfaces as a lower reference; A (=35.63) is the curve-fitted parameter (dimensionless); $\theta_{\min}$ (=0.15 L^3 L^{-3}) is the empirical minimum water content above which the soil is capable of delivering vapor at a potential rate; and θ_0 (L^3 L^{-3}) is the soil moisture content in the top 1 cm. *Bittelli et al.* [2008] compared three different soil surface resistance formulations (i.e., *Sun* [1982], *Camillo and Gurney* [1986], and *van de Griend and Owe* [1994]) and found that the *van de Griend and Owe* [1994] model adopted in this study produced the best estimates of soil evaporation. The estimation of soil surface resistance r_s based on

equation (5.21) was employed in a number of laboratory [e.g., *Smits et al.*, 2011, 2012] and field [e.g., *Bittelli et al.*, 2008; *Saito and Šimůnek*, 2009; *Zeng et al.*, 2011a, 2011b] studies due to its comparatively high accuracy. It should be emphasized that the soil surface resistance r_s is introduced and adopted to explicitly account for the possible chemical nonequilibrium between liquid and vapor phase at the vicinity of dry soil surface [*Saito et al.*, 2006].

Zero gradients of the pressure head and temperature are applied as the boundary conditions at the bottom of the soil profile, $z = z_b$, and given by:

$$\frac{\partial h}{\partial z}(z_b, t) = 0 \tag{5.22}$$

$$\frac{\partial T}{\partial z}(z_b, t) = 0 \tag{5.23}$$

5.3.2 Synthetic and field data

For the synthetic numerical simulations, two different soil textures (i.e., sand and loam) are considered. The sand parameters for VG model is from *Zeng et al.* [2009, 2011a, 2011b], who obtained this soil from the Badain Jaran Desert in China. The FS model's parameters for sand is based on *Mohanty and Yang* [2013]. The VG model parameterized with values from *Carsel and Parrish* [1988] was used for the loam. In addition, the FS model parameters for the loam soil is assumed in this study based on the fact that the water retention curve plotted by FS model is different with that of VG model only in the low moisture range [e.g., *Campbell and Shiozawa*, 1992; *Webb*, 2000; *Lebeau and Konrad*, 2010; *Zhang*, 2011; *Peters*, 2013]. The hydraulic parameters employed for the two synthetic soils are shown in Table 5.1, and Figure 5.1 depicts the

modelled soil water retention curves. As seen in Figure 5.1, the water retention curves ranging from saturated to residual water content are practically identical between the VG and FS models for both the sand and loam soils, whereas in the range of residual and zero water content, the retention curves show significant difference between the VG and FS models. The FS retention curve illustrates that the matric suction head (negative pressure head) ranging from residual and zero water content (the dry region) is a linear function of water content on a semilogarithmic plot as observed by *Campbell and Shiozawa* [1992]. However, the VG retention curve displays that the water content asymptotically reaches its residual value with the gradually increasing matric suction (Figure 5.1). The fact that water content is not allowed to be below the residual value as illustrated by VG retention curve is physically unrealistic [*Silva and Grifoll*, 2007], particularly in the case of evaporation. It was previously found that the VG model would easily yield the numerical simulation instabilities (especially for coarse textured soils such as sand) and markedly underpredict the unsatureated hydraulic conductivity for dry regions close to the residual water contents [*Sakai et al.*, 2009, 2011]. But the water retention curve characterized by the FS model can effectively overcome the shortcomings inherit in the VG model described above. In addition, due to the smaller residual water content of sand, one can notice that sand has smaller adsorptive water retention than loam (Figure 5.1). It should be mentioned that clay is not considered in current synthetic numerical simulations because the zero water content suction head $|h_m|$ should be usually larger than 10^7 cm [*Fayer and Simmons*, 1995; *Smits et al.*, 2012]. On the other hand, the parameters b_1, b_2, and b_3 (equation (5.12)) for sand and loam used in

Table 5.1 Hydraulic and thermal parameters used in the synthetic numerical simulations

Sample	Hydraulic Property						Thermal Conductivity		
	θ_s	θ_r	θ_a	α (cm^{-1})	n	K_s ($cm\ d^{-1}$)	b_1 ($W\ m^{-1}\ °C^{-1}$)	b_2 ($W\ m^{-1}\ °C^{-1}$)	b_3 ($W\ m^{-1}\ °C^{-1}$)
Sand (VG)[a]	0.382	0.017	/	0.00236	3.6098	172.8	0.228	-2.406	4.909
Sand (FS)[b]	0.382	/	0.037	0.00236	3.80	172.8	0.228	-2.406	4.909
Loam (VG)[c]	0.430	0.078	/	0.036	1.56	24.96	0.243	0.393	1.534
Loam (FS)[d]	0.430	/	0.160	0.038	1.65	24.96	0.243	0.393	1.534

[a]The van Genuchten (VG) model parameters for sand are from *Zeng et al.* [2009, 2011a, 2011b].
[b]The Fayer and Simmons (FS) model parameters for sand are from *Mohanty and Yang* [2013].
[c]The van Genuchten (VG) model parameters for loam are from *Carsel and Parrish* [1988].
[d]The Fayer and Simmons (FS) model parameters for loam are assumed in this study.

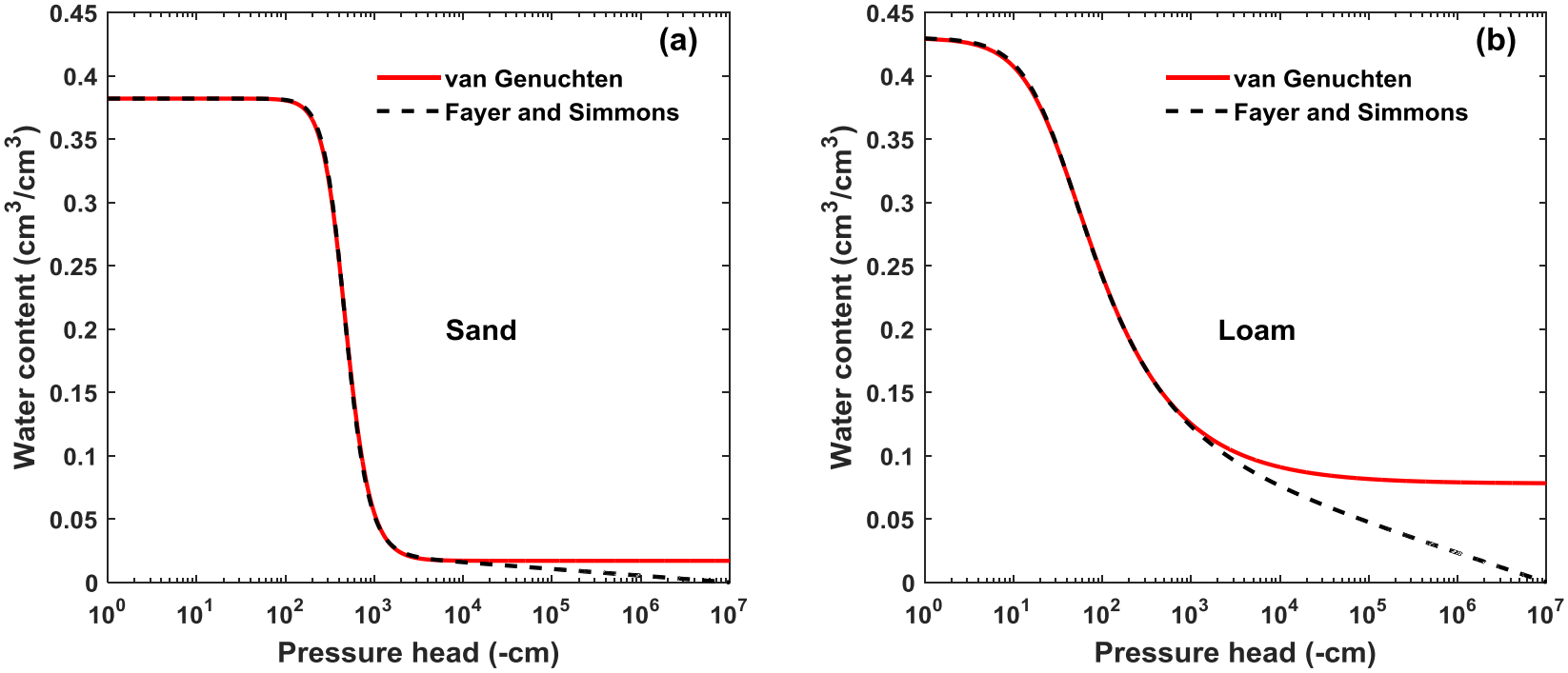

Figure 5.1 Unextended van Genuchten and extended full range Fayer and Simmons water retention curves of (a) sand, and (b) loam used in the synthetic numerical simulations, based on the hydraulic parameters shown in Table 5.1.

Chung and Horton [1987] are also adopted in this study for the synthetic sand and loam, respectively. These thermal conductivity parameters are shown in Table 5.1.

The coupled heat and water numerical model was then tested in two natural field sites. The first is the bare field site near the University of California Agricultural Experimental Station in Riverside, California (Latitude 33.58 N, Longitude 117.19 W, and elevation 306 m). Time series of soil volumetric water content and temperature were measured using the time domain reflectometry (TDR) probes and thermocouples at 40 and 20 minutes intervals, respectively, near the soil-atmosphere interface at the 2, 7, and 12 cm depths during the fall 1995 (24 November (Day of Year, DOY 328)-6 December (DOY 340)) [*Mohanty et al.*, 1998; *Saito et al.*, 2006]. The Riverside field site was irrigated twice during the experimental period on DOY 334.50-334.55 and DOY 335.40-335.43 with 0.55 and 0.20 cm of water, respectively, using a sprinkler system having several laterals and outlet ports. Irrigation rates were measured using catch cans adjacent to the measuring location and correspondingly, equal to 10.98 and 7.96 cm d^{-1}, respectively. The meteorological data (i.e., hourly solar radiation, air temperature, relative humidity, precipitation, and wind speed) for the Riverside field site were downloaded from the California Irrigation Management Information System (CIMIS) public domain website (http://www.cimis.water.ca.gov/WSNReportCriteria.aspx). No natural precipitation was observed at the weather station during DOY 328-340. The soil at the Riverside site was categorized as an Arlington fine sandy loam. The VG model parameters for the Arlington fine sandy loam were obtained by *Saito et al.* [2006], while the FS model parameters for this soil are assumed in this study (Table 5.2) to ensure that

Table 5.2 Hydraulic and thermal parameters used in the two field sites numerical simulations

Sample	Hydraulic Property						Thermal Conductivity		
	θ_s	θ_r	θ_a	α (cm^{-1})	n	K_s ($cm\ d^{-1}$)	b_1 ($W\ m^{-1}\ °C^{-1}$)	b_2 ($W\ m^{-1}\ °C^{-1}$)	b_3 ($W\ m^{-1}\ °C^{-1}$)
Arlington fine sandy loam (VG)[a]	0.445	0.011	/	0.0277	1.38	34.2	0.243	0.393	1.534
Arlington fine sandy loam (FS)[b]	0.445	/	0.063	0.0280	1.43	34.2	0.243	0.393	1.534
Sandy loam (VG)[c]	0.410	0.065	/	0.075	1.89	106.1	0.228	-2.403	4.915
Sandy loam (FS)[b]	0.410	/	0.108	0.080	1.95	106.1	0.228	-2.403	4.915

[a]The van Genuchten (VG) model parameters for Arlington fine sandy loam (Riverside, California) are from *Saito et al.* [2006].
[b]The Fayer and Simmons (FS) model parameters for Arlington fine sandy loam (Riverside, California) and Sandy loam (Audubon, Arizona) are both assumed in this study.
[c]The van Genuchten (VG) model parameters for Sandy loam (Audubon, Arizona) are from *Carsel and Parrish* [1988].

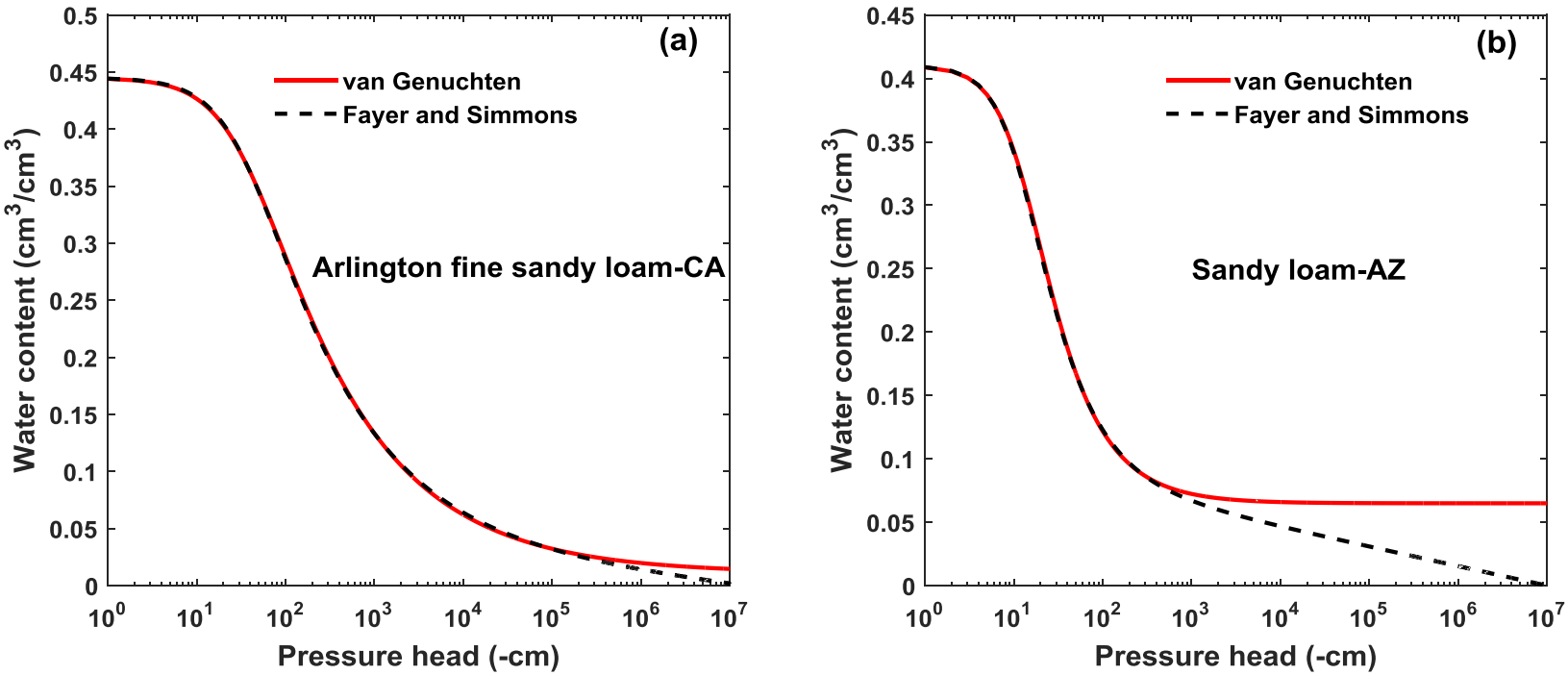

Figure 5.2 Unextended van Genuchten and extended full range Fayer and Simmons water retention curves of (a) Arlington fine sandy loam (Riverside, California), and (b) sandy loam (Audubon, Arizona) used in the field sites numerical simulations, based on the hydraulic parameters shown in Table 5.2.

the moisture retention curve depicted by FS model is distinct with that of VG model only in the dry range [e.g., *Campbell and Shiozawa*, 1992; *Webb*, 2000; *Lebeau and Konrad*, 2010]. The thermal conductivity parameters for loam used in *Chung and Horton* [1987] are employed for this Arlington fine sandy loam (Table 5.2). Figure 5.2a shows that the adsorptive water retention is not significantly important for this Arlington fine sandy loam due to its relatively small residual water content (θ_r =0.011 L^3 L^{-3}).

The second field site investigated in this work is located at Audubon, Arizona (Latitude 31.59 N, Longitude 110.51 W, and elevation 1469 m), which is a temperate arid site with an annual average precipitation of 438.35 mm and mean annual temperature 14.85 ºC [*Thompson et al.*, 2011; *Garcia Gonzalez et al.*, 2012]. This Audubon, Arizona site is part of the AmeriFlux network (http://ameriflux.lbl.gov/sites/siteinfo/US-Aud), from where we downloaded the measured half-hourly interval soil state variables (moisture content and temperature), land surface fluxes (e.g., latent heat flux) and meteorological data used in the nonisothermal numerical modeling. The soil volumetric water contents are measured at 10 and 20 cm depths, while the soil temperatures are observed at 2 and 4 cm depths. This Audubon, Arizona data set has been used previously by *Garcia Gonzalez et al.* [2012], who implemented the *Milly* [1982] model in their coupled water-vapor-heat simulations. The Audubon, Arizona site consists of a sandy loam soil and is assumed to be homogeneous in the soil profile [*Garcia Gonzalez et al.*, 2012]. The VG model parameters for the Audubon sandy loam are obtained based on *Carsel and Parrish* [1988], while the FS model parameters for this soil are assumed in this work (Table 5.2)

to guarantee that the soil water retention curve displayed by FS model is dissimilar with that of VG model only in low water content range [e.g., *Campbell and Shiozawa*, 1992; *Webb*, 2000; *Lebeau and Konrad*, 2010]. The thermal conductivity parameters for sandy loam used in *Deb et al.* [2011b] are adopted for this Audubon sandy loam (Table 5.2). From Figure 5.2b, one can notice that the Audubon sandy loam has a significant adsorptive water retention (as depicted by the FS curve) because of its relatively large residual water content (θ_r =0.065 L^3 L^{-3}).

5.3.3 Numerical simulation procedure

The soil water and heat balance equations (equations (5.1) and (5.2)) subject to the initial and boundary conditions were solved using the modified numerical HYDRUS-1D code [*Saito et al.*, 2006; *Šimůnek et al.*, 2008; *Sakai et al.*, 2009, 2011], which employs the finite element method for spatial discretization and finite difference for temporal discretization. The one-dimensional soil profile extended from $z = 0$ to $z = z_b = 50$ cm deep, with a spatial discretization of 0.2 cm (i.e., 251 nodes) for both the synthetic and field simulations. The discretization in time varied between a minimum and maximum time step, which were controlled by the time step criterions detailed in *Saito et al.* [2006] and *Sakai et al.* [2009, 2011].

The initial and boundary conditions for both the synthetic and field simulations were detailed and presented in Table 5.3. It should be pointed out that for the synthetic sand and loam scenarios, the meteorological data (hourly solar radiation, air temperature, wind speed, and relative humidity) needed to determine the surface conductive soil heat flux and surface evaporation are obtained from the Riverside, California field site

Table 5.3 Initial and boundary conditions for both two synthetic and two field sites numerical simulations

Scenarios	Processes	Initial Conditions	Top Boundary Conditions	Bottom Boundary Conditions
Synthetic sand (VG)	Water balance	$h(z,0) = -1500$	$q_w(0,t) = I_1 - E$	$\frac{\partial h}{\partial z}(50,t) = 0$
	Heat balance	$T(z,0) = 16 + \frac{22-16}{50} z$	$G(0,t) = R_n - H - LE$	$\frac{\partial T}{\partial z}(50,t) = 0$
Synthetic sand (FS)	Water balance	$h(z,0) = -1506$	$q_w(0,t) = I_1 - E$	$\frac{\partial h}{\partial z}(50,t) = 0$
	Heat balance	$T(z,0) = 16 + \frac{22-16}{50} z$	$G(0,t) = R_n - H - LE$	$\frac{\partial T}{\partial z}(50,t) = 0$
Synthetic loam (VG)	Water balance	$h(z,0) = -500$	$q_w(0,t) = I_1 - E$	$\frac{\partial h}{\partial z}(50,t) = 0$
	Heat balance	$T(z,0) = 16 + \frac{22-16}{50} z$	$G(0,t) = R_n - H - LE$	$\frac{\partial T}{\partial z}(50,t) = 0$
Synthetic loam (FS)	Water balance	$h(z,0) = -494.5$	$q_w(0,t) = I_1 - E$	$\frac{\partial h}{\partial z}(50,t) = 0$
	Heat balance	$T(z,0) = 16 + \frac{22-16}{50} z$	$G(0,t) = R_n - H - LE$	$\frac{\partial T}{\partial z}(50,t) = 0$
Arlington fine sandy loam (VG)	Water balance	$h(z,0) = -1000$	$q_w(0,t) = I_2 - E$	$\frac{\partial h}{\partial z}(50,t) = 0$
	Heat balance	$T(z,0) = 16 + \frac{22-16}{50} z$	$G(0,t) = R_n - H - LE$	$\frac{\partial T}{\partial z}(50,t) = 0$
Arlington fine sandy loam (FS)	Water balance	$h(z,0) = -996.67$	$q_w(0,t) = I_2 - E$	$\frac{\partial h}{\partial z}(50,t) = 0$
	Heat balance	$T(z,0) = 16 + \frac{22-16}{50} z$	$G(0,t) = R_n - H - LE$	$\frac{\partial T}{\partial z}(50,t) = 0$

Table 5.3 Continued

Scenarios	Processes	Initial Conditions	Top Boundary Conditions	Bottom Boundary Conditions
Sandy loam (VG)	Water balance	$h(z,0) = -100000$	$q_w(0,t) = P - E$	$\frac{\partial h}{\partial z}(50,t) = 0$
	Heat balance	$T(z,0) = 19 + \frac{38-19}{50} z$	$G(0,t) = R_n - H - LE$	$\frac{\partial T}{\partial z}(50,t) = 0$
Sandy loam (FS)	Water balance	$h(z,0) = -8631.73$	$q_w(0,t) = P - E$	$\frac{\partial h}{\partial z}(50,t) = 0$
	Heat balance	$T(z,0) = 19 + \frac{38-19}{50} z$	$G(0,t) = R_n - H - LE$	$\frac{\partial T}{\partial z}(50,t) = 0$

I_1 denotes the assumed irrigation rate (6.5 cm/day) at DOY 334.95-335.00.
I_2 denotes the applied irrigation rate (10.98 and 7.96 cm/day) at DOY 334.50-334.55 and DOY 335.40-335.43, respectively.
P denotes the three small precipitation rates plotted in Figure 5.4e.

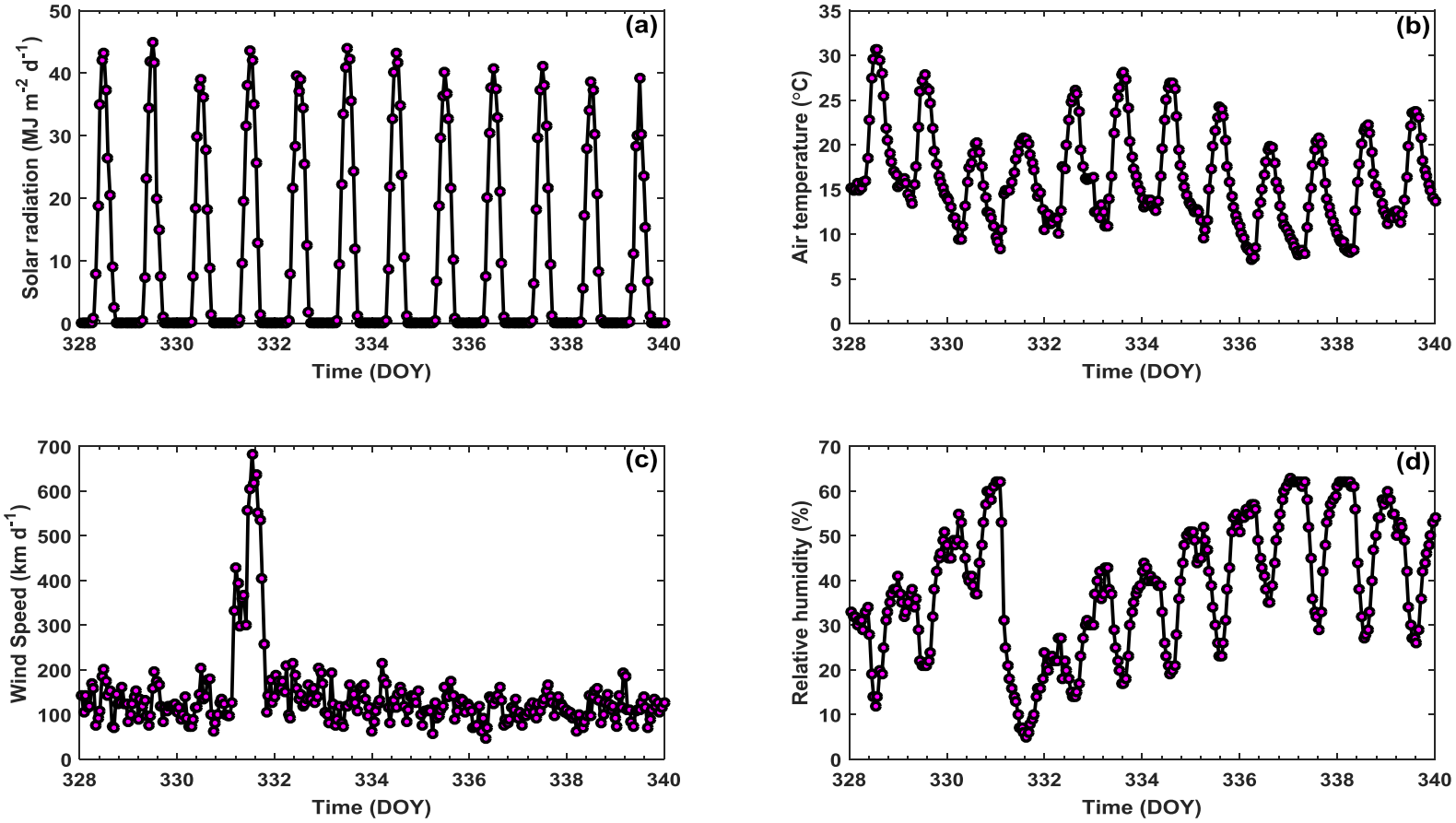

Figure 5.3 Diurnal changes of meteorological variables: (a) solar radiation, (b) air temperature, (c) wind speed, and (d) relative humidity during the simulation period from 24 November (Day of the Year (DOY) 328) to 5 December (DOY 339), 1995 at the nearby CIMIS U.C. Riverside weather station (hourly measured values) close to the University of California Agricultural Experimental Station-Riverside, California field site.

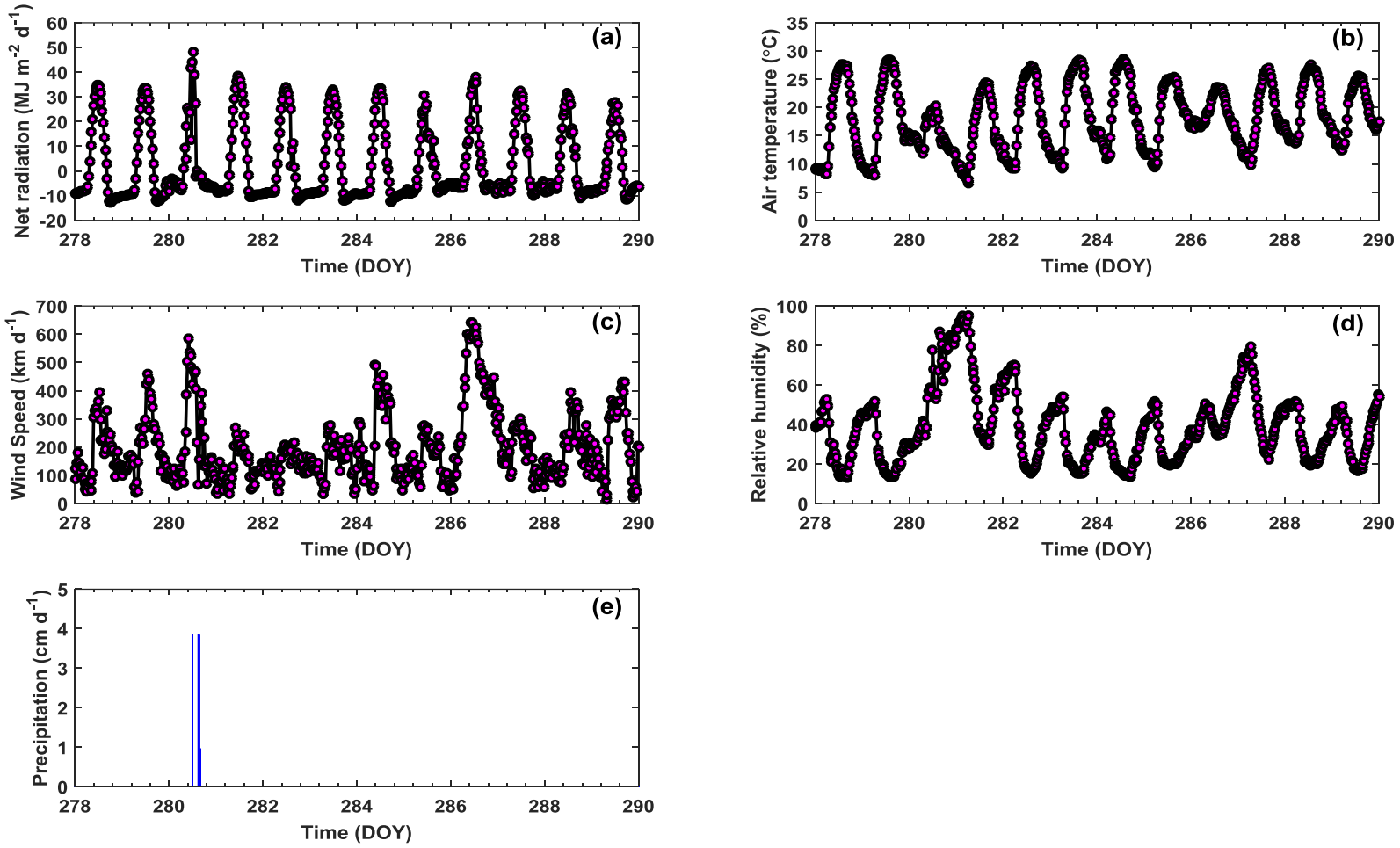

Figure 5.4 Diurnal changes of meteorological variables: (a) net radiation, (b) air temperature, (c) wind speed, (d) relative humidity, and (e) precipitation (half-hourly measured values) during the simulation period from 5 October (Day of the Year (DOY) 278) to 17 October (DOY 290), 2002 at the Audubon, Arizona field site.

(Figure 5.3), where no precipitation event was observed during the simulation period. I_1 in Table 5.3 represents the assumed irrigation rate (6.5 cm/day) at DOY 334.95-335.00 in two synthetic simulations, whereas I_2 in Table 5.3 denotes the applied two irrigation rates (10.98 and 7.96 cm/day) at DOY 334.50-334.55 and DOY 335.40-335.43, respectively in Riverside, California site modeling. On the other hand, the meteorological data (half-hourly net radiation, air temperature, wind speed, relative humidity, and precipitation) for the Audubon, Arizona field site are plotted in Figure 5.4. As seen in Figure 5.4e, there are three small precipitation events (3.84, 3.84 and 0.96 cm/day) occurring at DOY 280.48-280.50, DOY 280.60-280.65, and DOY 280.65-280.67, respectively, at the Audubon, Arizona field site.

5.4 Results and discussions

We first present the simulated soil water content, temperature, and evaporation for the synthetic sand and loam scenarios in sections 5.4.1.1 and 5.4.1.2. Then we discuss the liquid water and water vapor flux of loam in section 5.4.1.3 to analyze the evaporation underestimation when neglecting adsorptive water retention. Finally, the results of Riverside, California and Audubon, Arizona field sites are given in sections 5.4.2 and 5.4.3, respectively.

5.4.1 Synthetic sand and loam results

5.4.1.1 Simulated soil water content and temperature

Figure 5.5 depicts the simulated soil water content and soil temperature of synthetic sand at depths 5 cm (a and b) and 10 cm (c and d) between FS and VG water retention curve models in coupled water, vapor and heat HYDRUS-1D modeling from

DOY 328 to 340. As can be seen from Figures 5.5a and 5.5c, the simulated soil water contents (in sand) at both 5 cm and 10 cm depths with FS model are noticeably smaller than that with VG model, whereas the simulated soil temperatures between FS and VG model display no significant difference for both 5 and 10 cm depths (Figures 5.5b and 5.5d). As seen in Figure 5.6, for loam, the simulated soil water contents and temperatures for FS and VG model show the very similar characteristics to that of sand observed in Figure 5.5. However, compared to Figure 5.5c the sand case, the simulated loam soil water content at depth 10 cm (Figure 5.6c) did not show significant increase in response to the irrigation occurred at DOY 334.95-335.00. This is mainly caused by the much smaller isothermal hydraulic conductivity of loam compared to that of sand, therefore, the infiltration into deeper loam right after the irrigation should be much slower than that of sand.

5.4.1.2 Simulated evaporation

Figure 5.7 shows the evaporation rate and cumulative evaporation of synthetic sand (a and b) and synthetic loam (c and d) between FS and VG water retention curve models in coupled water, vapor and heat HYDRUS-1D modeling from DOY 328 to 340. Based on Figure 5.7a, one can notice that the evaporation rate with FS model is typically greater than that with VG model during the daytime of DOY 328-334 when the synthetic sand is continuously drying. The irrigation (6.5 cm/day) occurred at DOY 334.95-335.00 (beginning of DOY 335) efficiently increased the shallow subsurface soil water content, which consequently increased the evaporation flux at the daytime of DOY 335. However, because of this irrigation event, the evaporation rate with FS model becomes

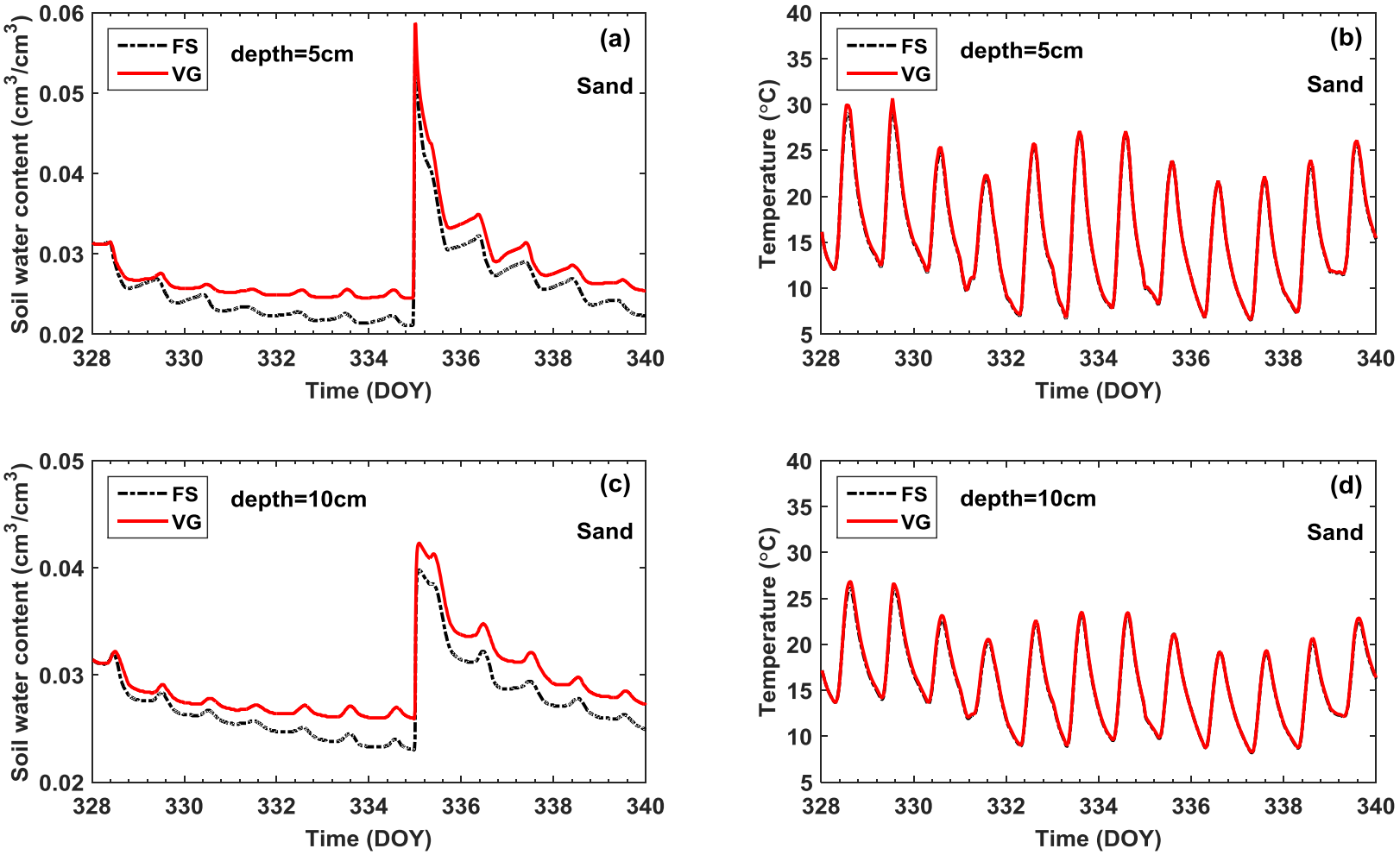

Figure 5.5 Simulated soil water content and soil temperature of synthetic sand at depths 5 cm (a and b) and 10 cm (c and d) between Fayer and Simmons (FS) and van Genuchten (VG) water retention curve models in coupled water, vapor and heat HYDRUS-1D modeling from DOY 328 to DOY 340.

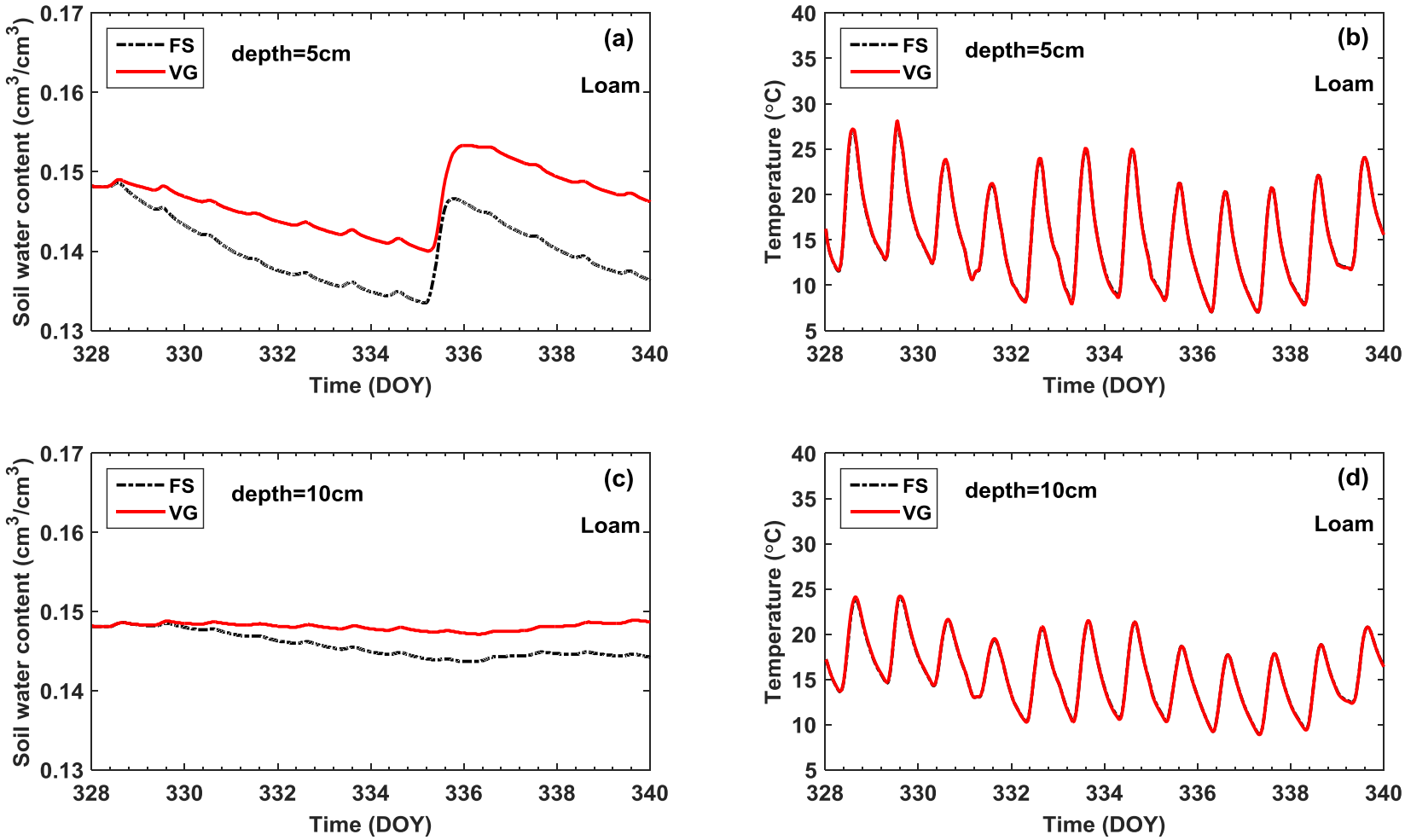

Figure 5.6 Simulated soil water content and soil temperature of synthetic loam at depths 5 cm (a and b) and 10 cm (c and d) between Fayer and Simmons (FS) and van Genuchten (VG) water retention curve models in coupled water, vapor and heat HYDRUS-1D modeling from DOY 328 to DOY 340.

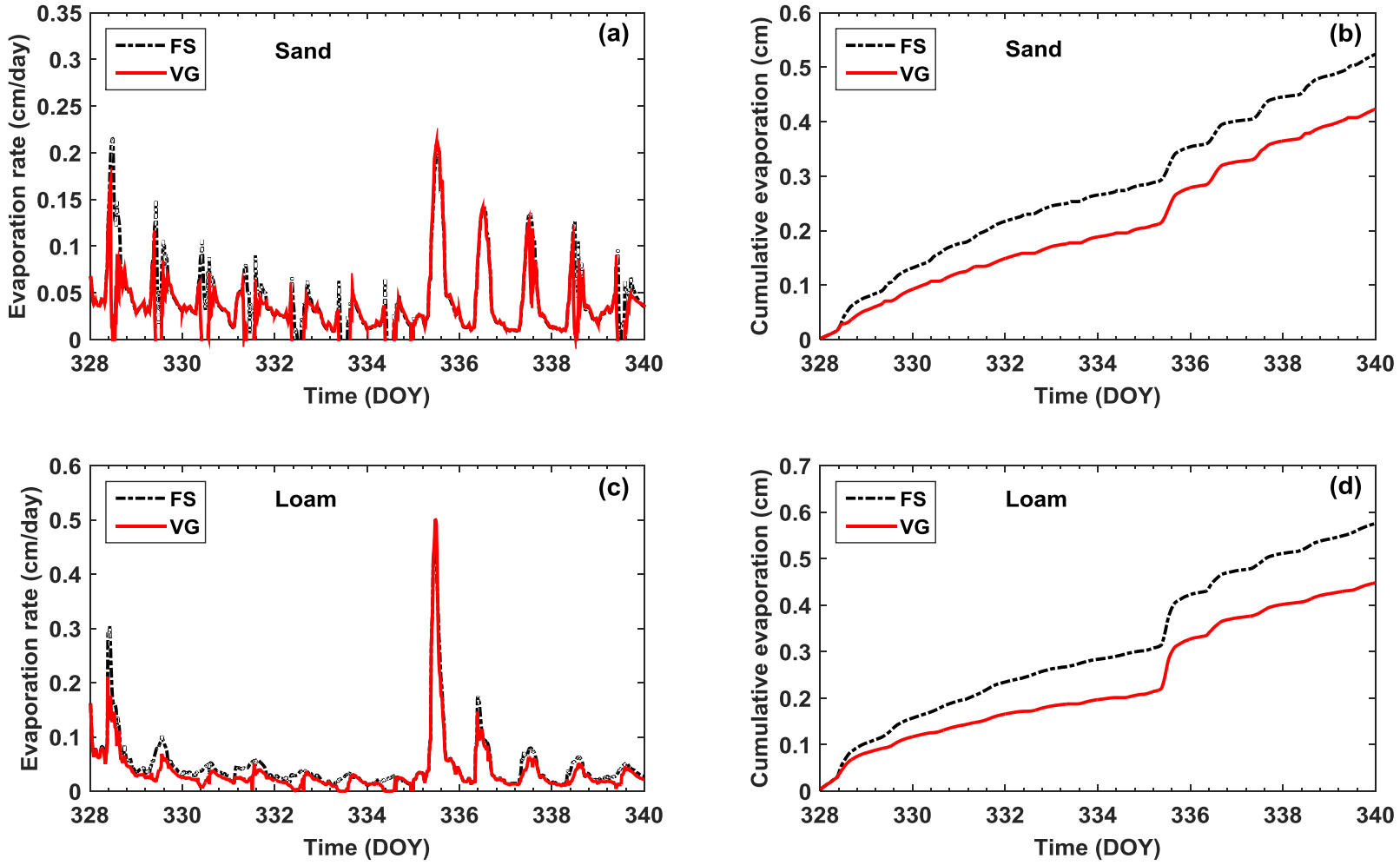

Figure 5.7 Evaporation rate and cumulative evaporation of synthetic sand (a and b) and synthetic loam (c and d) between Fayer and Simmons (FS) and van Genuchten (VG) water retention curve models in coupled water, vapor and heat HYDRUS-1D modeling from DOY 328 to DOY 340.

quite close to that with VG model during DOY 335-337 when the near surface soil is not very dry. With progressively continuous drying of the sand, the evaporation flux with FS model is again larger than that with VG model from DOY 338-340. Similar to the synthetic sand, the above temporal variation pattern of evaporation rate can be generally observed in synthetic loam (Figure 5.7c). However, notice that the evaporation rate with FS model is very similar to that with VG model only from DOY 335-336 for the loam, in comparison to DOY 335-337 in the sand. Figure 5.7b indicates that during the entire simulation period (DOY 328-340), the cumulative evaporation with FS model (0.524 cm) is greater than that with VG model (0.423 cm) for the sand, whereas for the loam (Figure 5.7d) case, the cumulative evaporation with FS model (0.576 cm) is also larger than that with VG model (0.448 cm). The cumulative evaporation difference between FS and VG model for sand (19.3%) is slightly smaller than that of loam (22.2%). Figure 5.7 clearly demonstrated that without considering adsorptive component in soil water retention curve, the resulting evaporation rate and cumulative evaporation would be significantly smaller under relatively dry soil conditions for both the synthetic sand and loam. In following section 5.4.1.3, by taking synthetic loam as an example, we analyzed four component fluxes to investigate why the evaporation is remarkably lower (underestimated) when ignoring the adsorptive water retention.

5.4.1.3 Liquid water and water vapor fluxes

The calculated vertical profiles of isothermal and thermal fluxes of liquid water and water vapor of synthetic loam between FS and VG water retention models at DOY 329.5, DOY 330.0, DOY 335.5, and DOY 337.5 are depicted in Figures 5.8a, 5.8b, 5.8c,

and 5.8d, respectively. While the graphs in Figures 5.8a and 5.8b illustrate four component fluxes on a typical dry day at daytime and nighttime, the effects of irrigation on these fluxes at daytime of DOY 335.5 and 337.5 are shown in Figures 5.8c and 5.8d, respectively. The thermal liquid flux obtained by FS model is very similar to that of VG model before and after irrigation (i.e., for all the four selected time). In addition, compared to the other three fluxes, the thermal liquid flux was almost always negligible on the dry days [*Saito et al.*, 2006], except at DOY 335.5 (noon right after irrigation), a very small downward thermal liquid water flux was observed near the soil surface. As such, the thermal liquid flux was reasonably ignored in the discussion below.

Vertical distributions of soil water content and soil temperature of synthetic loam between FS and VG models before (DOY 329.5 and 330.0) and after (DOY 335.5 and 337.5) irrigation are displayed in Figure 5.9. At DOY 329.5 (i.e., noon of DOY 329), both the isothermal liquid water and water vapor fluxes are upward (Figure 5.8a) due to an upward pressure head gradient (inferred by Figure 5.9a), whereas the thermal water vapor flux is downward at this time driven by a large downward temperature gradient at DOY 329.5 (Figure 5.9b). In addition, all the three component fluxes obtained by FS model are larger than that of VG model (Figure 5.8a). The upward isothermal water vapor flux was larger than the downward thermal vapor flux, which resulted in the upward net water vapor flux in the top soil layer (1 cm depth for the VG model and 0.4 cm depth for the FS model). This upward net water vapor flux is the supply of water for evaporation from the land surface to the atmosphere during the daytime at DOY 329.5 (Figure 5.8a). Furthermore, the origin for this upward net water vapor flux was found to

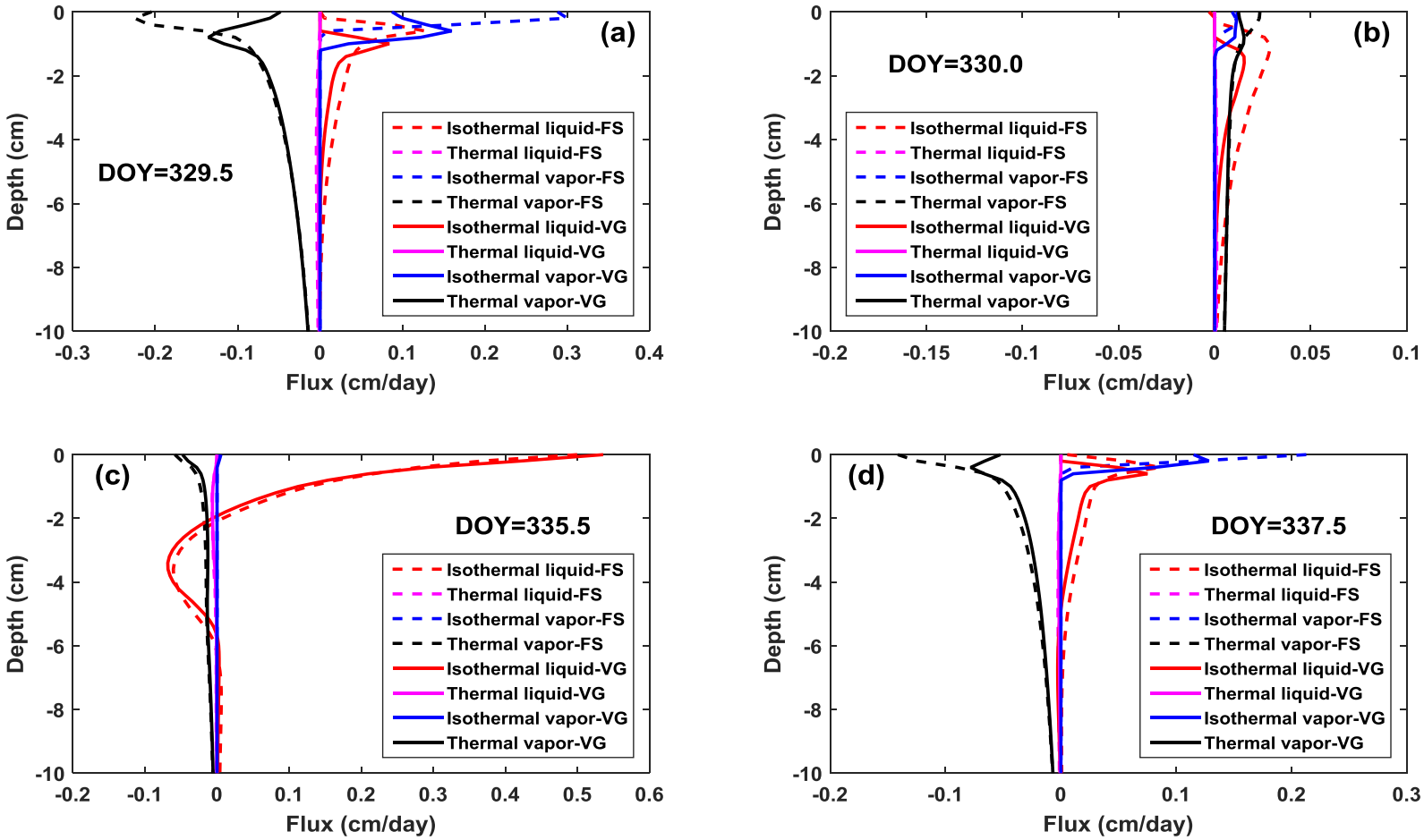

Figure 5.8 Vertical profiles of isothermal and thermal fluxes of liquid water and water vapor at DOY 329.5 (a), DOY 330.0 (b), DOY 335.5 (c), and DOY 337.5 (d) of synthetic loam between Fayer and Simmons (FS) and van Genuchten (VG) water retention curve models in coupled water, vapor and heat HYDRUS-1D modeling. Positive values indicate upward fluxes, while negative values indicate downward fluxes.

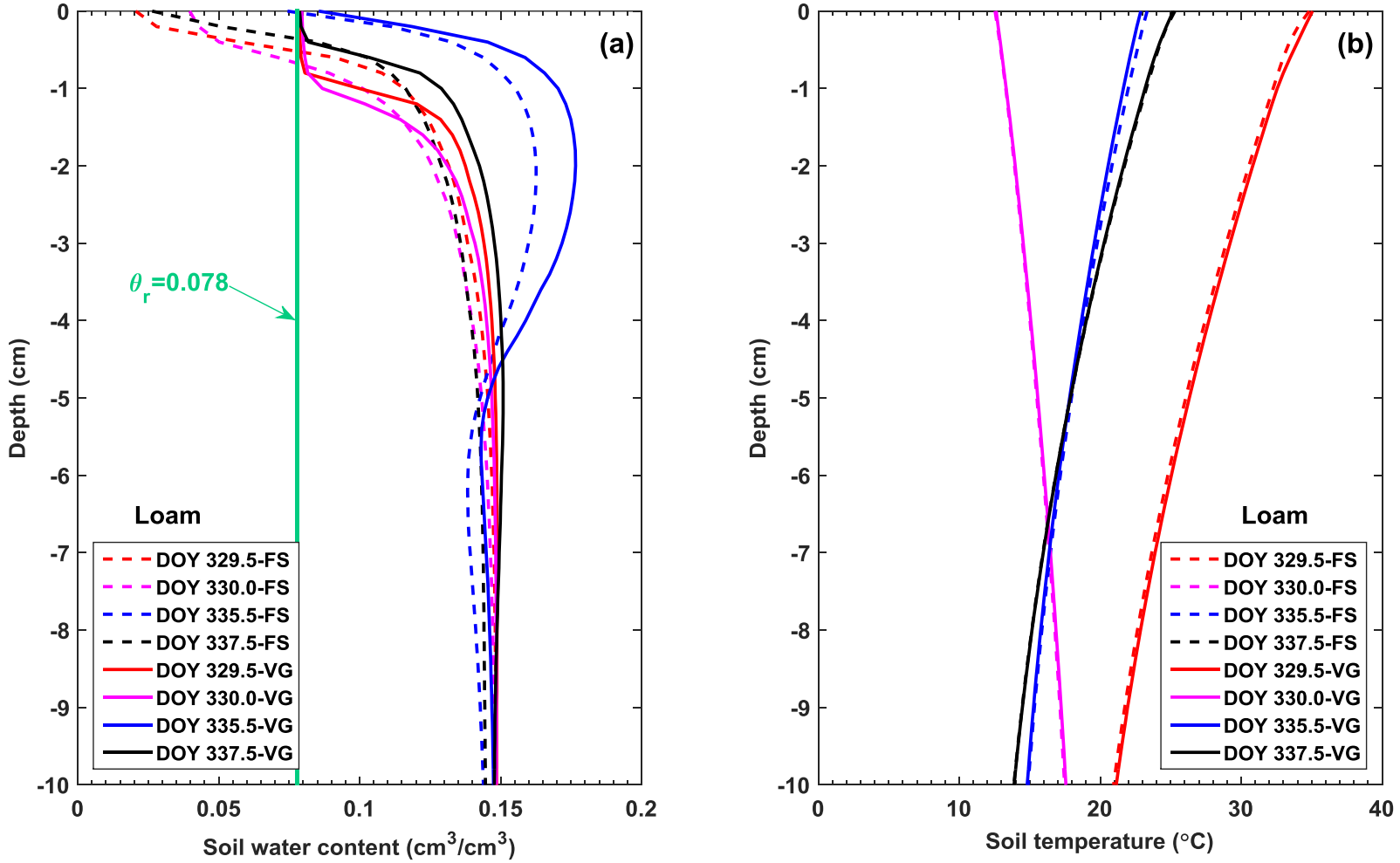

Figure 5.9 Vertical profiles of soil water content (a) and soil temperature (b) at DOY 329.5, DOY 330.0, DOY 335.5, and DOY 337.5 of synthetic loam between Fayer and Simmons (FS) and van Genuchten (VG) water retention curve models in coupled water, vapor and heat HYDRUS-1D modeling. Light irrigation was applied at DOY 334.95-335.00.

be liquid water delivered via the upward isothermal liquid water flux from the depths of around 8 cm and above (Figure 5.8a). The upward isothermal liquid water arriving at the top soil layer phase-changed to the isothermal water vapor, which further transferred toward the soil surface and supplied for the evaporation during daytime at DOY 329.5. This indicates that the phase change (i.e., vaporization) of liquid water did not take place at the exact soil surface, but inside the soil profiles adjacent to the soil surface (1 cm depth for the VG model and 0.4 cm depth for the FS model). The above discussion implies that the larger upward isothermal liquid water flux by FS model than that of VG model is the reason why the evaporation is significantly larger when accounting for the adsorptive water retention. Moreover, the larger upward isothermal liquid water flux by FS model than that of VG model is mainly attributed to the larger isothermal hydraulic conductivity of FS model in the dry range (Figure 5.10). This can be confirmed by the fact that the upward pressure head gradient of FS model is actually smaller than that of VG model in the top soil layer (as inferred in Figure 5.9a).

All the three component fluxes (i.e., isothermal liquid, isothermal and thermal vapor fluxes) were small and upward (Figure 5.8b) at DOY 330.0 (midnight) when the temperature gradient was upward during the nighttime (Figure 5.9b). Furthermore, both isothermal liquid water and thermal water vapor fluxes obtained by FS model are still larger than that of VG model, whereas the isothermal water vapor flux of FS model is very similar to that of VG model. Results of isothermal fluxes analysis indicated again that during the nighttime on DOY 330.0, isothermal liquid water transported from the deeper layers (around 10 cm depth and above) toward the drying front (i.e., the depth

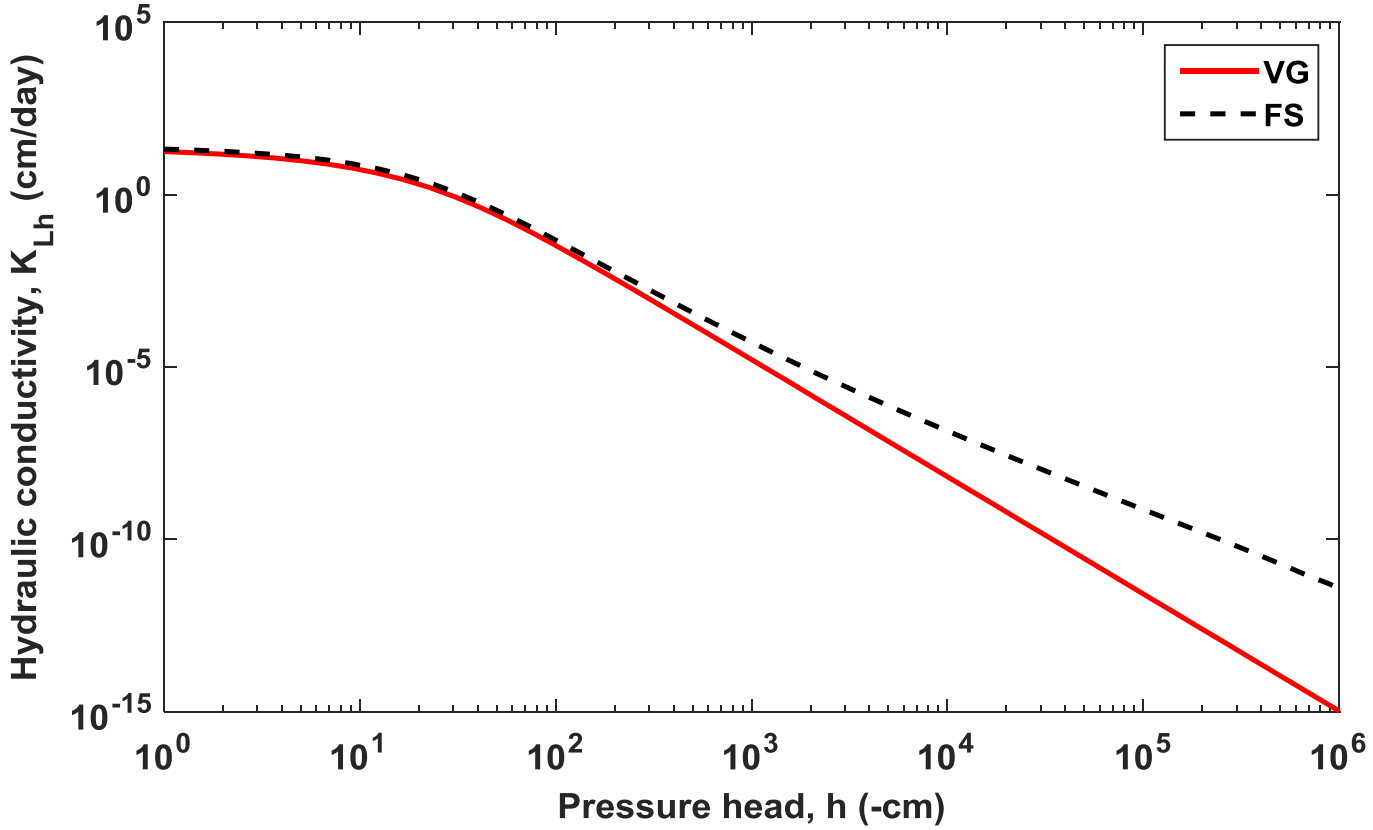

Figure 5.10 Isothermal hydraulic conductivity of synthetic loam calculated using Fayer and Simmons (FS) and van Genuchten (VG) water retention curve models.

where water vapor flux dominates the overall water flux), where it is phase-changed to water vapor. Owing to the absence of solar radiation during the nighttime (Figure 5.3a), the resulting latent heat flux during the night is relatively small. As a consequence, not much water vapor is transferred into the atmosphere by means of evaporation. On the contrary, liquid water transporting toward the soil surface accumulated at the vicinity of the drying front, leading to a slight increase in the soil water content. Such small increase in water content near the drying front during the nighttime is more significant for the FS model compared to that of VG model (Figure 5.9a). Soil water is found to eventually transfer back to the deeper layers via downward thermal water vapor flux during the daytime on following day.

The flux profiles are tremendously different after irrigation when the isothermal liquid water flux becomes dominant (Figure 5.8c) at DOY 335.5 (i.e., noon of DOY 335). Due to the irrigation, the moisture content in the shallow subsurface profiles increases, resulting in a noticeable downward isothermal liquid water flux between depths 2 and 6 cm. Whereas adjacent to the soil surface (around 2 cm depth and above), there exists a significantly large upward isothermal liquid water flux, which serves as a source of water for evaporation at daytime (Figure 5.7c). The upward isothermal water vapor flux is quite small at DOY 335.5 (Figure 5.8c), even for the depth very close to the soil surface. This indicates that the drying front is almost at the soil surface at DOY 335.5. There was a downward thermal water vapor flux induced by the downward temperature gradient at noon on DOY 335. The three component fluxes (isothermal liquid, isothermal and thermal vapor fluxes) of FS model are very close to that of VG

model. This is consistent with the fact that the evaporation rate at DOY 335.5 between FS and VG model is very similar with each other (Figure 5.7c).

With further and continuous drying after the irrigation that is applied at DOY 334.95-335.00, the flux profiles of FS and VG models at DOY 337.5 (Figure 5.8d) is again very similar to that of DOY 329.5, except the drying front is a little closer to the soil surface compared to that of DOY 329.5. However, with the continuously progressive drying, this drying front is found to gradually move downward, leading to a progressively thicker dry surface layer. For example, the drying front at DOY 337.5 is around at depth 0.2 cm (Figure 5.8d), whereas the drying front approximately recedes to 0.4 cm depth on DOY 339.5 (results not shown here).

The above analysis and discussions imply that the smaller isothermal hydraulic conductivity of VG model (consequently smaller upward isothermal liquid water flux of VG model) in the dry range is the main reason why the evaporation is significantly lower (underestimated) when neglecting the adsorptive water retention at the daytime of a typical dry day. As a matter of fact, it is inappropriate that the soil water content reduction stops at the residual water content as assumed by VG model (clearly seen in Figure 5.9a), particularly in the case of soil evaporation [*Silva and Grifoll*, 2007; *Sakai et al.*, 2011]. In reality, the continuous drying would eventually reduce the soil water content below its residual values. This process can only be captured by the full range water retention curve such as FS model but not VG model.

5.4.2 Riverside site, California results

5.4.2.1 Simulated and observed soil water content and temperature

Figure 5.11 displays the measured and simulated soil water contents (a-c) and soil temperatures (d-f) at three depths (2, 7, and 12 cm) using FS and VG water retention curve models in coupled water, vapor and heat HYDRUS-1D modeling from DOY 328 to 340 at the Riverside, California field experimental site (Arlington fine sandy loam). Simulated soil water contents are generally able to reproduce the measured values reasonably well at all three depths (Figure 5.11a-c) during the whole simulation period (DOY 328-340), even with the gradual decrease in soil water content at 2 cm depth before irrigation. Notice that the observed noise in measured water content values is inherent to the TDR measurements [*Cahill and Parlange*, 1998; *Saito et al.*, 2006]. Noticeable increase in the soil water content at 2 cm depth after two applied irrigation events (DOY 334.50-334.55 and 335.40-335.43) was simulated fairly well. The slight increase in soil water content at 7 cm depth after two irrigations was apparent in the model output. The predicted and observed soil water contents at 12 cm depth nearly did not change during the entire simulation period from DOY 328 to 340. In addition, the simulated soil water contents of FS model are very close to that obtained by the VG model at all three depths (Figure 5.11a-c), except the slight smaller simulated soil water content obtained by FS model than that of VG model at 2 cm depth after two irrigations (i.e., during DOY 336-340). This was further confirmed by the similar root mean square errors (RMSEs) among FS/VG models with the observed water contents, which were

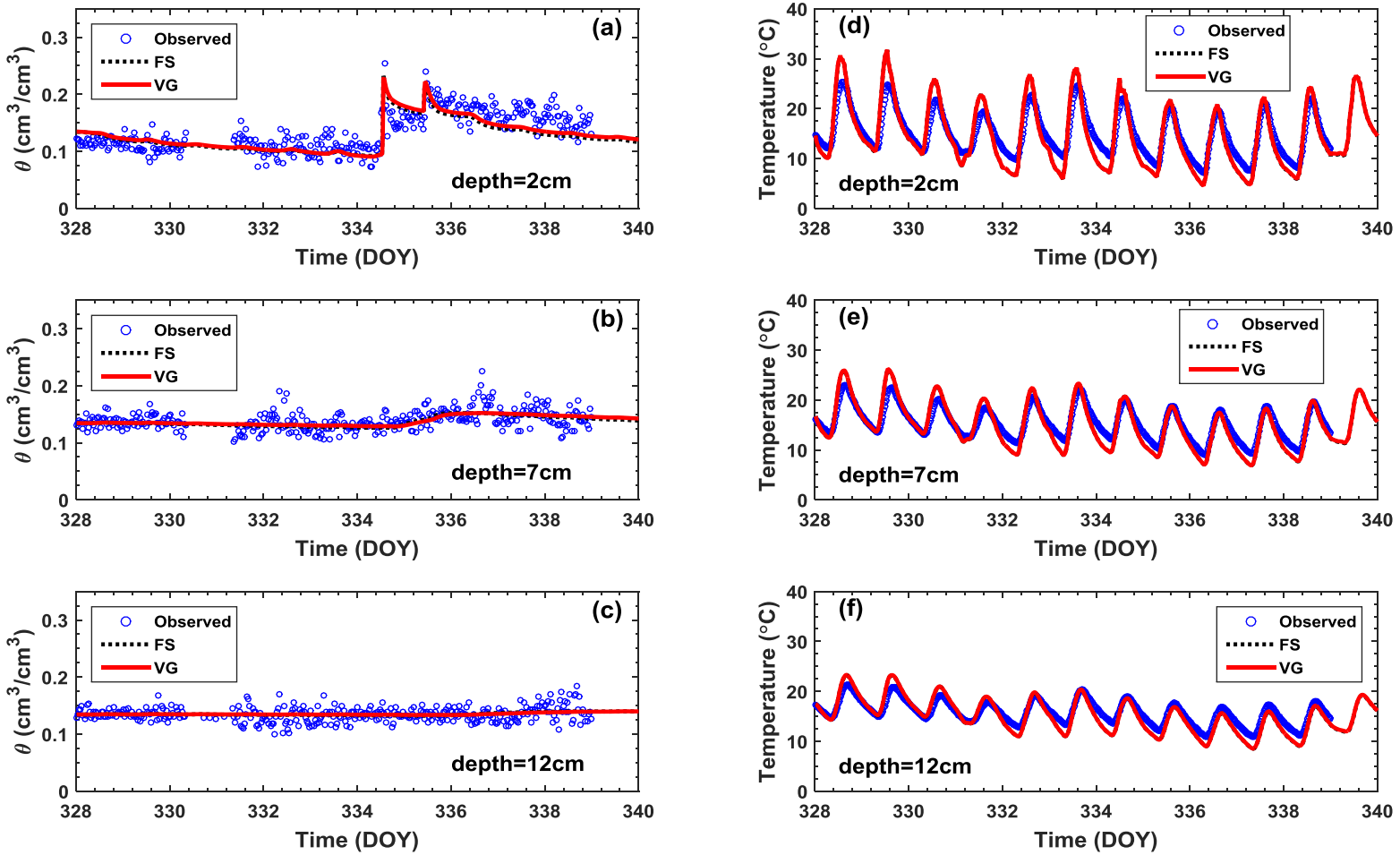

Figure 5.11 Soil water contents measured and simulated (a-c) and soil temperatures measured and simulated (d-f) at three depths (2, 7, and 12 cm) using Fayer and Simmons (FS) and van Genuchten (VG) water retention curve models in coupled water, vapor and heat HYDRUS-1D modeling from DOY 328 to DOY 340 at the Riverside, California field experimental site (Arlington fine sandy loam).

0.039/0.039, 0.042/0.043, and 0.040/0.040 (cm^3 cm^{-3}) at the depth of 2, 7, and 12 cm, respectively.

Both the modeled and observed soil temperatures display the typical sinusoidal diurnal pattern (Figure 5.11d-f). Owing to the attenuation of transferred heat energy, it is found that the amplitude of both the predicted and observed daily temperature changes reduced with depth from 2 cm to 12 cm. Except for the temperature amplitude, simulated temperatures generally agreed with the observed soil temperatures at three depths. The maximum differences between simulated and observed temperature values are being within a few degrees. Furthermore, the simulated soil temperatures of FS model are also very close to that obtained by VG model at all three depths (Figure 5.11d-f). The RMSEs between the simulated (FS model) and the measured soil temperatures are 2.619 ºC, 1.667 ºC, and 1.435 ºC at the depth 2, 7, and 12 cm, respectively, whereas for the VG model, the RMSEs are 2.626 ºC, 1.666 ºC, and 1.424 ºC at the three selected depths.

Figure 5.11 indicated that the effects of incorporating full range water retention curve (FS model) on simulated soil water contents and soil temperatures are not quite significant compared to that obtained by the VG model for the Riverside, California field site. This is mainly because the soil profiles are not very dry due to the two irrigation events occurring at DOY 334.50-334.55 and DOY 335.40-335.43, respectively. Furthermore, based on Figure 5.2a, the water retention curves between FS and VG models of this Arlington fine sandy loam are almost identical when the water content is above 0.03.

5.4.2.2 Simulated evaporation

No observed evaporation experimental data is available for the Riverside, California field site, therefore, only simulated evaporation is presented in this section. As shown in section 5.4.2.1, both simulated soil water contents and soil temperatures obtained by FS model are very similar to that of VG model, as such, the resulting evaporation between FS and VG models is also expected to be very close with each other. In fact, this is generally the case as shown in Figure 5.12. However, there is slight observed difference between FS and VG models for evaporation, particularly for the cumulative evaporation (Figure 5.12b). The cumulative evaporation with FS model (0.782 cm) is slightly (3.7%) greater than that with VG model (0.753 cm). This slight discrepancy in evaporation (cumulative evaporation in particular) is mainly caused by the very dry soil surface (reflected in Figure 5.13) even though the soil profile below the drying front (i.e., depth 2, 7, and 12 cm) is not dry at all. As seen in Figure 5.13, the soil surface absolute pressure head (suction head) at the daytime during DOY 328-334 (before irrigation) and DOY 338-340 (three days after irrigation) could be almost larger as 10^6 cm for both FS and VG models. Based on Figure 5.2a, when the surface absolute pressure head at around 10^6 cm for this Arlington fine sandy loam (θ_r =0.011 cm^3 cm^{-3}), the simulated soil surface water content and the resulting evaporation between FS and VG models should be slightly different. This indicated that despite the soil profile below the drying front is not dry at all, the soil surface can reach very dry status in the case of evaporation. As a result, the consideration of the adsorptive water retention to some

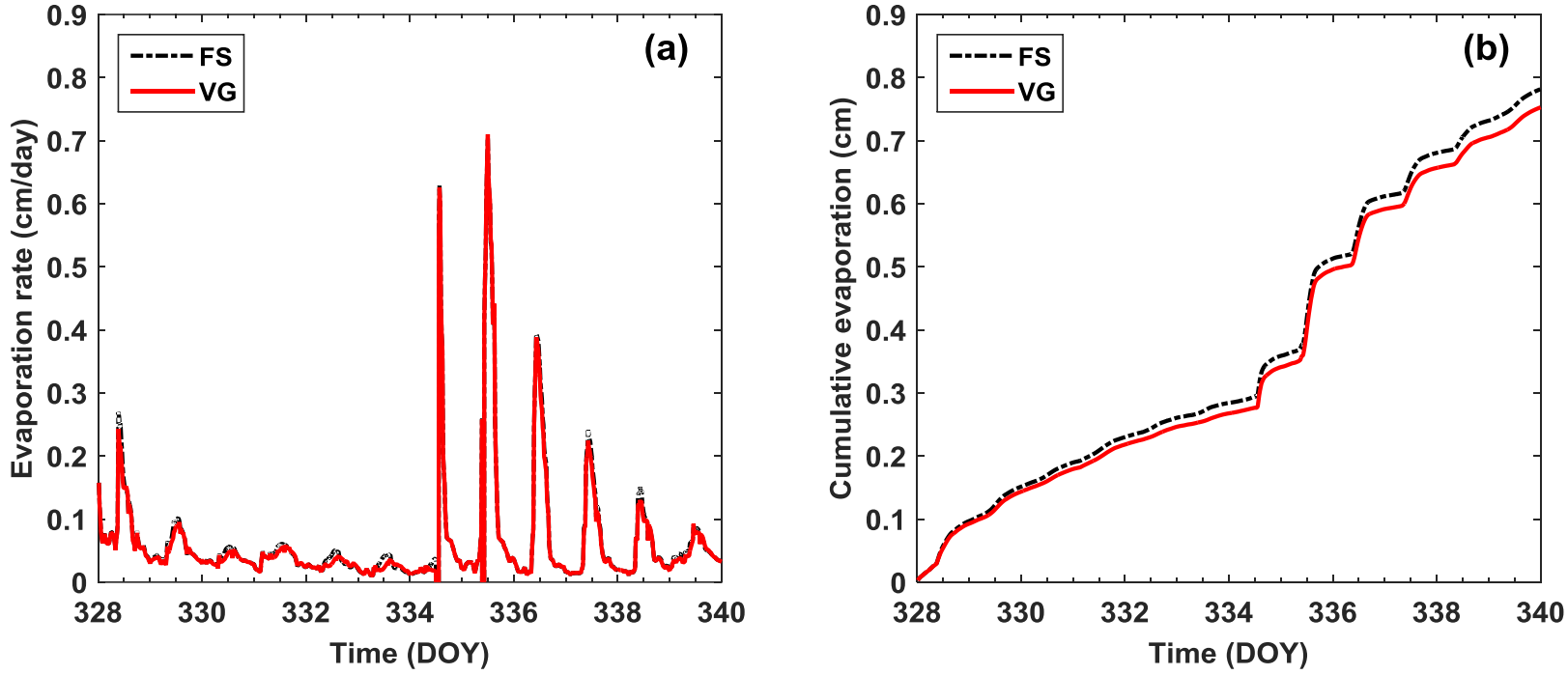

Figure 5.12 Simulated evaporation rate (a) and cumulative evaporation (b) between Fayer and Simmons (FS) and van Genuchten (VG) water retention curve models in coupled water, vapor and heat HYDRUS-1D modeling from DOY 328 to DOY 340 at the Riverside, California field experimental site (Arlington fine sandy loam).

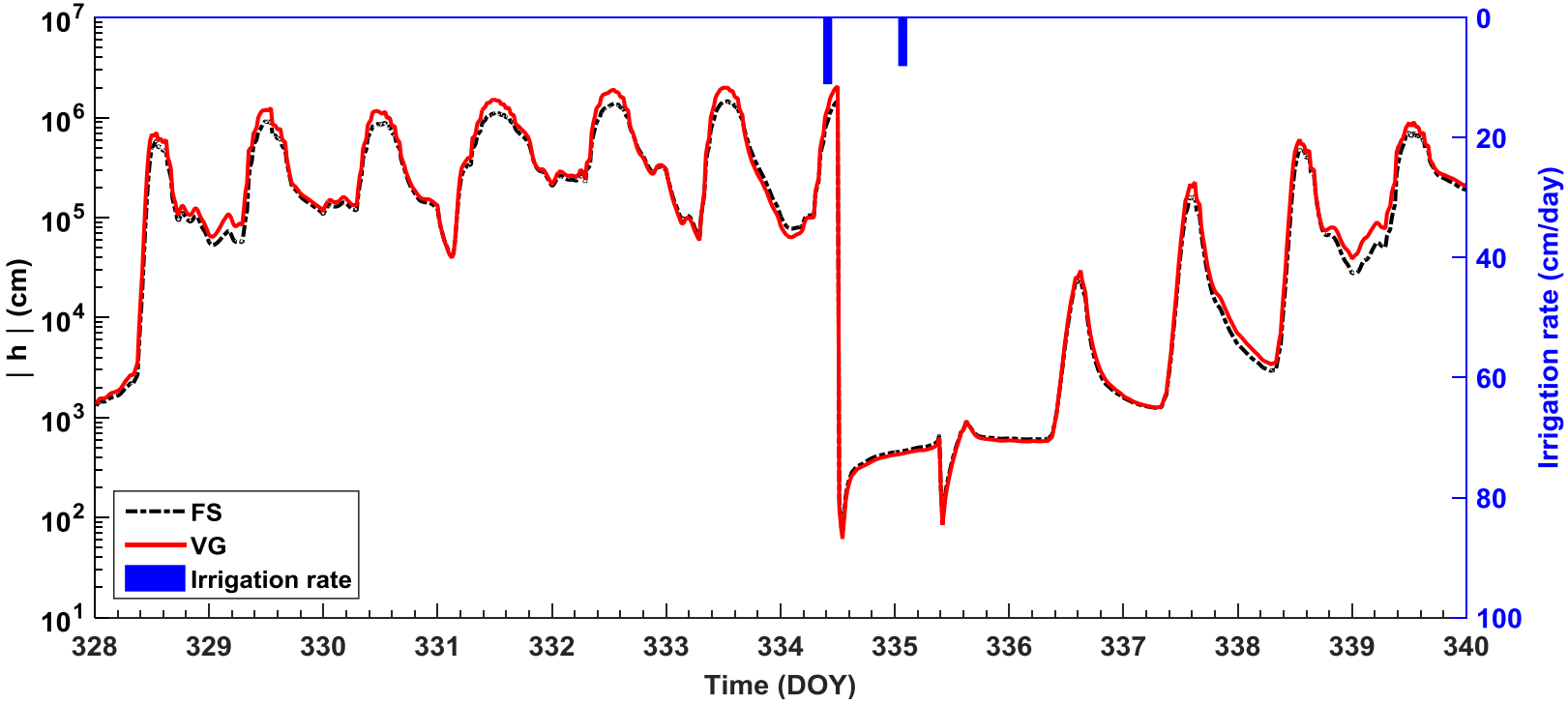

Figure 5.13 Temporal changes of the soil surface absolute pressure head simulated by Fayer and Simmons (FS) and van Genuchten (VG) water retention curve models (left y-axis) and two applied irrigation rates (right y-axis) from DOY 328 to DOY 340 at the Riverside, California field experimental site (Arlington fine sandy loam).

extent is still justified for better thermodynamic description of the soil surface, even for soils having a relatively small residual water content (θ_r =0.011 cm^3 cm^{-3} in this case).

5.4.3 Audubon site, Arizona results

5.4.3.1 Simulated and observed soil water content and temperature

Figure 5.14a-b shows the observed and simulated soil water contents at 10 and 20 cm depths, whereas Figure 5.14c-d plots the measured and simulated soil temperatures at 2 and 4 cm depths using the FS and VG water retention models in coupled water, vapor and heat modeling from DOY 278 to 290 at the Audubon, Arizona field experimental site (sandy loam). The simulated water contents of both FS and VG models at both 10 and 20 cm depths were almost constant during the simulation period. This indicated that the three small precipitation events (Figure 5.4e) occurred at DOY 280.48-280.50, 280.60-280.65, and 280.65-280.67, respectively, although increased the water content at the vicinity of the soil surface (results are not shown here owing to lack of observed moisture data in top 10 cm), were not able to efficiently infiltrate into the 10 cm depth. The simulated soil water contents obtained by the FS model agreed with the observed values much better than that of VG model. The RMSEs between the simulated (FS model) and the observed soil water content are 0.012 and 0.006 (cm^3 cm^{-3}) at the depth 10 and 20 cm, respectively, whereas for the VG model, the RMSEs are 0.027 and 0.014 (cm^3 cm^{-3}) at the two depths. The observed soil water contents are the daily averaged values, which are apparently smaller than the residual water content (θ_r =0.065 cm^3 cm^{-3}) of the sandy loam at the Audubon, Arizona field site. The simulated water contents obtained by the VG model were almost at residual water content, but cannot be

further smaller than 0.065 (cm^3 cm^{-3}) for both 10 cm and 20 cm depths (Figure 5.14a-b) during the whole simulation period (DOY 278-290). The simulated water contents of FS model, on the other hand, can be readily lower than 0.065 (cm^3 cm^{-3}) and generally matched the measured values reasonably well at both depths (Figure 5.14a-b). These results indicated that for very dry soil condition when observed water content are initially below the soil's residual values, accounting for adsorptive water retention is physically important and should not be neglected.

Similar to that of Riverside, California field site (Figure 5.11d-f), the simulated and observed soil temperatures at Audubon, Arizona site (Figure 5.14c-d) also illustrated the typical sinusoidal diurnal pattern at both 2 cm and 4 cm depths. Apart from the temperature amplitude, simulated temperatures fairly matched the observed soil temperatures at both depths. The maximum discrepancies between simulated and observed temperatures are within a few degrees. In addition, the simulated soil temperatures obtained by FS model are very close to that of VG model at both depths (Figure 5.14c-d). The RMSEs between the simulated (FS model) and the observed soil temperatures are 5.291 ºC and 5.204 ºC at the depth 2 and 4 cm, respectively, whereas for the VG model, the RMSEs are 5.005 ºC and 5.022 ºC at the two depths. The relatively noticeable differences between observed and modeled soil temperatures by both the FS and VG models were mainly attributed to the uncertainties in the thermal properties assigned to the coupled water, vapor and heat simulations in the modified HYDRUS-1D model.

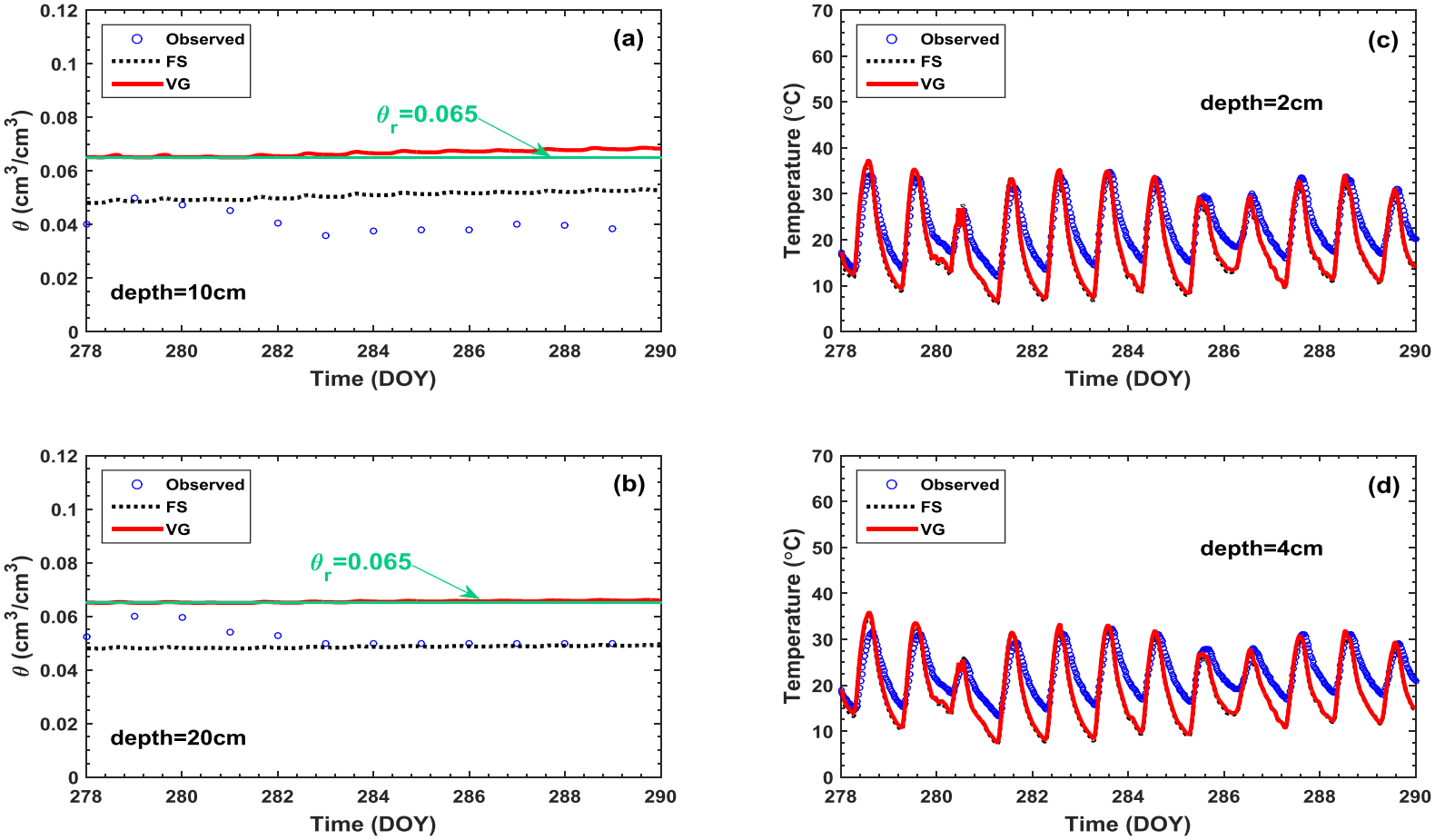

Figure 5.14 Soil water contents measured and simulated (a-b, 10 and 20 cm) and soil temperatures measured and simulated (c-d, 2 and 4 cm) at two depths using Fayer and Simmons (FS) and van Genuchten (VG) water retention curve models in coupled water, vapor and heat HYDRUS-1D modeling from DOY 278 to DOY 290 at the Audubon, Arizona field experimental site (sandy loam).

5.4.3.2 Simulated and observed evaporation

Based on the observed latent heat flux data (*LE*) and the latent heat of evaporation (*L*) (approximately 2.45×10^{6} J kg^{-1}), we obtained the observed evaporation rate for the Audubon, Arizona field site during DOY 278-290. Figure 5.15a plots the observed and calculated evaporation rate obtained by FS model, whereas the comparison between measured and simulated evaporation rate by VG model is shown in Figure 5.15b. As evident in Figure 5.15, the evaporation flux calculated by the FS model generally agreed with the measured evaporation rate much better than that of VG model. The RMSE between the simulated (FS model) and the observed evaporation rate is 0.046 (cm/day), however, for the VG model, the RMSE is 0.064 (cm/day) during the entire simulation period. Specifically, during the daytime of DOY 280-281 (during and right after precipitation), the calculated evaporation rate obtained by the VG model agreed with observed values slightly better than that of FS model. This is because the near surface soil moisture content obtained by VG model was larger than that of FS model (Figure 5.14a-b), therefore, the predicted evaporation rate by VG model is greater than that of FS model. As a result, the simulated evaporation rate obtained by VG model is slightly closer to the observed values than that of FS model on these relatively not very dry days. However, the VG model remarkably underestimated the observed evaporation rate at the daytime on DOY 278-279 (before precipitation) and DOY 282-290 (after precipitation), whereas such underestimation of evaporative flux was significantly reduced by the FS model at the daytime on these drying days (DOY 278-280 and DOY 283-290). Generally speaking, the overall improved and better agreement between

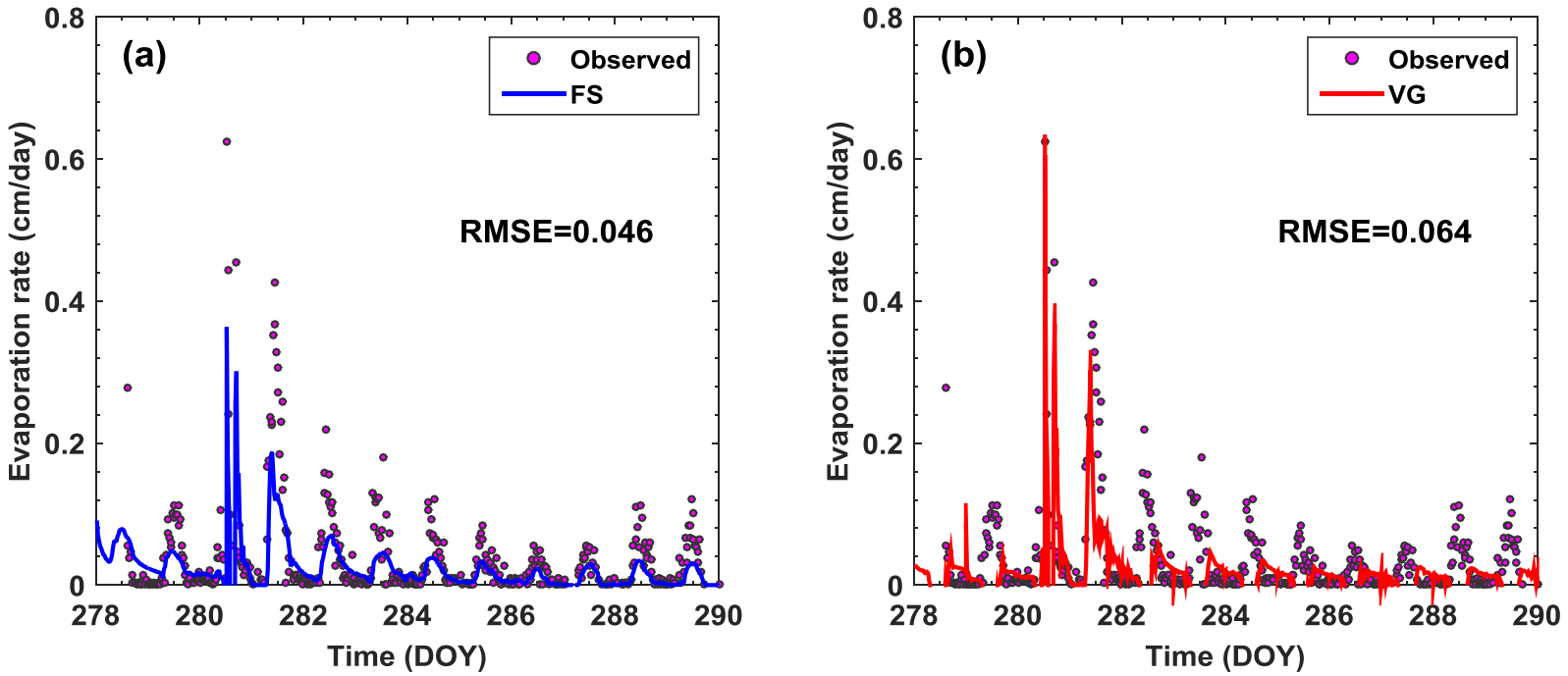

Figure 5.15 Comparison of observed and simulated evaporation rates using FS (a) and VG (b) water retention curve models in coupled water, vapor and heat HYDRUS-1D modeling from DOY 278 to DOY 290 at the Audubon, Arizona field experimental site (sandy loam).

observed and simulated evaporation rate by FS model than that of VG model corroborated the fact that water content is not allowed to be below the residual value as dictated by VG retention curve is physically unrealistic [*Silva and Grifoll*, 2007], particularly when investigating evaporation under dry soil conditions.

5.5 Summary and conclusion

Better understanding and modeling of coupled heat and water movement in vadose zone is significantly important for the improved descriptions of soil moisture content, temperature and evaporation characteristics in relatively dry soils under arid and semiarid (water-limited) conditions. The modified computer program HYDRUS-1D, used in this study to simulate the coupled water-vapor-heat transport, was mainly based on the *Philip and de Vries* [1957] theory and its extensions [*de Vries*, 1958; *Milly*, 1982]. The *Philip and de Vries* [1957] theory and its extensions [*de Vries*, 1958; *Milly*, 1982], even though physically incomplete [*Cahill and Parlange*, 1998; *Parlange et al.*, 1998; *Grifoll et al.*, 2005; *Smits et al.*, 2011], are still adopted successfully to describe coupled heat and water movement in low permeability ($<10^{-7}$ m^2) soils and across the soil-atmosphere interface under highly transient field conditions. However, it seems more appropriate but not common (quite limited) to adopt the full range water retention curves, which account for both capillary and adsorptive forces, in the coupled heat and water modeling. In this study, we attempt to investigate the effects of full range water retention curve on coupled heat and water transport simulation with a focus on soil moisture content, temperature and soil evaporative flux, based on two synthetic (sand and loam) and two field sites (Riverside, California and Audubon, Arizona) analysis.

The results of coupled heat and water numerical modeling of both synthetic sand and loam showed that when neglecting the adsorptive water retention (van Genuchten function), the resulting simulated soil water content would be larger, and the evaporative flux would be lower, respectively, compared to that obtained by the full range water retention model (Fayer and Simmons function). On the other hand, the simulated temperatures did not show noticeable differences between the FS and VG models. The detailed analysis of four component fluxes (isothermal and thermal fluxes of liquid water and water vapor) of synthetic loam implied that the underprediction of isothermal hydraulic conductivity of VG model in the dry range resulted in the evaporation underestimation when neglecting the adsorptive water retention. As such, it is largely inappropriate to assume that the soil water content reduction stops at the residual water content, particularly in the case of evaporation. The continuous drying (particularly in arid and semiarid regions where water is limited) is expected to eventually reduce the soil moisture content to below its residual values. These synthetic findings were further confirmed and corroborated by the Audubon, Arizona field experimental results.

The results from Riverside, California field experimental site showed that although the soil profile below the drying front is not dry at all, the soil surface still can reach very dry status, which would result in slightly observed differences in surface moisture content and evaporation between FS and VG models. As a result, the consideration of the adsorptive water retention is still needed for better thermodynamic description of the soil surface, a critical boundary for the coupling of land and atmosphere. To this end, as demonstrated in this study, it is highly recommended to use

full range water retention to simulate coupled heat and water movement in arid and semiarid regions, for the purpose of improved soil state variables (moisture content especially) and evaporation flux predictions.

6 NUMERICAL EVALUATION OF THE EFFECT OF FULL RANGE WATER RETENTION CURVE ON EVAPORATION AND WATER DISTRIBUTION FROM LAYERED POROUS MEDIA

6.1 Synopsis

Soil evaporation involves the coupled heat and mass transfer between the shallow subsurface and the atmosphere, and it is a critical hydrological component in arid and semiarid areas. The objective of this work is to investigate the effects of both full range water retention and layering characteristics on evaporation and water distribution in layered porous media by two synthetic simulations with three cases. The first case consisted of sand overlying sandy loam and sandy loam overlying sand, with homogeneous sand and sandy loam as checkup controls. In the second case, sand and loam were considered and in the third case sandy loam and loam were used. It was found that when ignoring the adsorptive water retention, the resulting simulated soil water content is greater, and the evaporative flux is smaller, respectively, compared to that of full range water retention model for both homogeneous and layered soil profiles in both synthetic simulations. Moreover, the layering thicknesses and sequences are significantly important for the water content distribution (creating discontinuity across layered interface) and overall evaporation dynamics. The fine over coarse configuration has the larger evaporation, whereas coarse over fine profile remarkably suppresses the evaporation. The results of this study are helpful for adopting appropriate mulching barriers aimed at reducing evaporative water losses.

6.2 Introduction

Evaporation from bare and sparse vegetated soils plays a pivotal role in the hydrologic cycle, particularly in the arid and semiarid areas and regions threatened by desertification [*Smits et al.*, 2012]. Soil evaporation profoundly affects mass and energy exchange between land surface and atmosphere, numerous chemical and microbiological activities in the vadose zone, and efficient agricultural water management [*Sakai et al.*, 2011; *Or et al.*, 2013]. It involves simultaneous heat and water transport including liquid flow, vapor diffusion, phase change, and liquid and vapor displacement, leading to a remarkably complicated physical process that is difficult to predict [*Lehmann et al.*, 2008; *Shokri et al.*, 2010; *Sakai et al.*, 2011; *Zeng et al.*, 2011; *Or et al.*, 2013; *Fetzer et al.*, 2017; *Vanderborght et al.*, 2017]. In the absence of a constant water supply from either top (through precipitation or irrigation) or bottom (through shallow water table) boundary, the soil water evaporation can be conceptualized as three stages: an initial constant-rate stage (stage 1), an intermediate falling-rate stage (stage 2), and a residual slow-rate stage (stage 3) [*Hillel*, 2004; *Zeng et al.*, 2011; *Nachshon et al.*, 2011]. The stage 1 evaporation is mainly controlled by atmospheric conditions (e.g., solar radiation, air temperature, humidity, and wind speed), whereas the stage 2 and stage 3 evaporation is mostly limited by the pore space and transport properties of porous media (e.g., porosity, hydraulic and thermal conductivities, and vapor diffusivity) [*Shokri et al.*, 2010; *Sakai et al.*, 2011; *Smits et al.*, 2012; *Assouline et al.*, 2014].

Stage 1 evaporation, characterized as an initially high and relatively constant evaporation rate, occurs and sustains as long as the progressively receding drying front

remains hydraulically connected to the evaporating porous surface via liquid capillary flow [*Lehmann et al.*, 2008; *Shokri et al.*, 2010; *Nachshon et al.*, 2011; *Or et al.*, 2013; *Assouline et al.*, 2014]. When hydraulic connection to the evaporating surface is lost, stage 2 evaporation starts. Drying rate during stage 2 reduces considerably because evaporation becomes vapor diffusion limited at the vicinity of the porous surface [*Hillel*, 2004; *Nachshon et al.*, 2011; *Assouline et al.*, 2014]. Stage 3 evaporation is formed when the evaporation front (vaporization plane) recedes deeply below the soil surface and drying is mainly controlled by diffusive water vapor transport [*Hillel*, 2004; *Nachshon et al.*, 2011]. This evaporation process conceptualization clearly indicated that Richards equation is typically only applicable to the stage 1 evaporation characterization [*Assouline et al.*, 2013, 2014]. However, for appropriate stage 2 and 3 evaporation descriptions, extension of Richards equation is necessary and warranted for both isothermal (coupled water-vapor) [*Ciocca et al.*, 2014; *Vanderborght et al.*, 2017] and nonisothermal (coupled water-vapor-heat) conditions [*Philip and de Vries*, 1957; *de Vries*, 1958; *Milly*, 1982; *Vanderborght et al.*, 2017].

Compared to the large number of studies of evaporation upon homogeneous soil profiles [e.g., *Bittelli et al.*, 2008; *Novak*, 2010, 2016; *Zeng et al.*, 2009, 2011; *Smits et al.*, 2011, 2012; *Assouline et al.*, 2013; *Grifoll*, 2013; *Ciocca et al.*, 2014; *Dijkema et al.*, 2017; *Yang et al.*, 2017a], evaporation dynamics in layered porous media received comparatively little attentions [*Shokri et al.*, 2010; *Or et al.*, 2013]. Additionally, most of the existing investigations focused on stage 1 evaporation from initially saturated layered soils based on laboratory columns experiments under the continuous drying top

boundary conditions [e.g., *Willis*, 1960; *Modaihsh et al.*, 1985; *Diaz et al.*, 2005; *Shokri et al.*, 2010; *Huang et al.*, 2013; *Assouline et al.*, 2014]. For instance, *Shokri et al.* [2010] investigated the evaporation behavior from initially saturated layered sand columns and found the significant impacts of layering thicknesses, sequences and positions as well as hydraulic characteristics of each layer on the water content distribution and overall evaporative water losses. More importantly, they proposed a composite characteristic length to determine drying front depth at end of stage 1 evaporation through layered soils. The derived composite characteristic length was experimentally tested via laboratory Hele-Shaw cells filled with layered coarse and fine sands with different structures (i.e., layering thicknesses, sequences and positions). It should be noticed that the concept of evaporative characteristic length was first developed by *Lehmann et al.* [2008] to predict end of stage 1 evaporation in homogeneous porous media through considering balance between capillary, gravity and viscous forces. The evaporative characteristic length was typically used as a measure of the maximum extent over which hydraulic continuity between the receding drying front and the evaporating surface was maintained [*Lehmann et al.*, 2008; *Shokri et al.*, 2010; *Or et al.*, 2013]. In addition, the characteristic length was dependent on the width of pore size distribution that can be deduced from the soil water retention curve. *Assouline et al.* [2014] recently explored and confirmed the effect of upper layer properties (e.g., layering thicknesses and sequences) on evaporation using modified definition of characteristic length and homogeneous and layered column experiments (packed with initially saturated sand (coarse), sandy loam (fine), fine overlying coarse, and coarse overlying fine with

different thicknesses). The work of *Assouline et al.* [2014] is mainly different with that of *Shokri et al.* [2010] in two aspects. The first is an explicit distinction between the capillary drying regime and the gravity-capillary drying regime in *Assouline et al.* [2014]. Secondly, the emphasis in the work of *Assouline et al.* [2014] is upon the use of characteristic length (modified definition) to predict the duration of stage 1 evaporation, instead of the prediction of drying front depth at end of stage 1 evaporation in *Shokri et al.* [2010]. Similarly, *Huang et al.* [2013] investigated the evaporation and water redistribution within layered soils (sand and silt) by means of a combination of laboratory column experiments and coupled water-vapor-heat numerical modeling. The column evaporation experiments in *Huang et al.* [2013] were conducted at continuous drying top boundary condition for the entire 62 days, but at constant head (via water reservoir) for the first 31 days, then zero flux bottom boundary condition for the next 31 days. *Huang et al.* [2013] found that the layered columns with silt (fine) at soil surface had larger evaporation than homogeneous sand and silt columns. Whereas the sand (coarse) overlying silt (fine) column resulted in the smallest evaporation. This observation is consistent with the results of *Shokri et al.* [2010] and *Assouline et al.* [2014]. The coupled water-vapor-heat numerical model with the calibrated hydraulic properties parameters [*Huang et al.*, 2013] still overestimated the water content in the sand layer and underestimated surface evaporation (especially for multilayered soil column), even though they intentionally specified a very low residual water content (0.005 cm^3 cm^{-3} for sand and 0.0095 cm^3 cm^{-3} for silt). The adoption of full range water

retention curve was suggested by *Huang et al.* [2013] to further improve the agreements between their simulated and observed values in future.

Most of the layered soils evaporation works cited above focused on continuous evaporative top boundary conditions, however, experiments (laboratory or field) and numerical modeling for layered soils that sought to undergo the diurnal temperature and humidity fluctuations experienced by natural soils are very scarce. In addition, natural evaporation in water limited areas (arid and semiarid regions) rarely starts from an initial period of artificial saturation or sustains by a shallow water table [*Scanlon and Milly*, 1994]. More importantly, as conjectured by *Huang et al.* [2013], it is necessary to use full range water retention curve to investigate evaporation process in arid and semiarid areas [*Scanlon et al.*, 1997; *Mohanty and Yang*, 2013; *Ciocca et al.*, 2014; *Yang et al.*, 2017a]. A recent synthetic experiments and field observed data analysis in homogeneous soil profile [*Yang et al.*, 2017a] clearly showed that the soil water content can be overestimated and the evaporative flux would be underestimated when ignoring the adsorptive water retention, but similar investigation in layered heterogeneous soils has not been conducted yet in *Yang et al.* [2017a]. On the other hand, the impact of full range water retention curve on state variables (water potential and temperature) in a layered Nevada desert soil was explored by *Andraski and Jacobson* [2000]. They found that the *Rossi and Nimmo* [1994] (RN) full range water retention curve can significantly improve the prediction of both water potentials in near-surface soils (especially under dry conditions) and temperatures throughout the layered soil profile. Unfortunately, *Andraski and Jacobson* [2000] has not investigated the effect of employing RN water

retention function on surface evaporative flux. Moreover, the comparison to homogeneous soil profile has not been studied neither by *Andraski and Jacobson* [2000]. So far it is basically unknown upon the effect of full range water retention curve on evaporation and water redistribution from layered porous media under diurnal temperature fluctuation conditions through either synthetic experiments or field observations. In this study, we attempt to address this unsolved issue by means of synthetic experiments analysis via extending the work of *Yang et al.* [2017a] to layered soil profiles.

Apart from the important meaning to hydrological and land-atmosphere interaction, insights gained from this research are significantly useful for designing appropriate mulching barriers to management of evaporative water losses. This is because the mulch layers frequently adopt the coarse material on soil surface aimed at reducing water losses from evaporation based on the fact that a coarse-over-fine configuration of layered soil profile decreases evaporation [*Modaihsh et al.*, 1985; *Yamanaka et al.*, 2004; *Diaz et al.*, 2005; *Shokri et al.*, 2010; *Assouline et al.*, 2014]. However, the moisture content of coarse textured soils (mulch layers) arrives at its residual value easily at relatively low suction head, and the retention model that neglects the adsorptive water retention would frequently lead to numerical simulation instabilities and underpredict the unsaturated hydraulic conductivity (hence evaporation) in the dry end [*Sakai et al.*, 2009, 2011; *Yang et al.*, 2017a]. In such cases, the use of full range water retention curve in the coupled water-vapor-heat modeling is warranted and important [*Sakai et al.*, 2009, 2011; *Yang et al.*, 2017a] however very few so far.

6.3 Materials and methods

6.3.1 Numerical model formulations

In this work, we focus on diurnal evaporation dynamics in water limited arid and semiarid regions where usually stage 2 and 3 evaporation occurs. Therefore, it is necessary to use the coupled water-vapor-heat transfer theory that was originally proposed by *Philip and de Vries* [1957] (hereafter PdV) and later extended by *de Vries* [1958] and *Milly* [1982] to describe stage 2 and 3 evaporation [*Vanderborght et al.*, 2017]. The modified computer program HYDRUS-1D [*Saito et al.*, 2006; *Šimůnek et al.*, 2008; *Sakai et al.*, 2009, 2011], employed in this research to model coupled water-vapor-heat transport, was primarily on the basis of the PdV theory and its extensions [*de Vries*, 1958; *Milly*, 1982]. The governing conservation equations of liquid water and water vapor flow and heat transfer in the unsaturated zone, as well as the related soil hydraulic and thermal properties adopted in modified HYDRUS-1D are described briefly in sections 6.3.1.1, 6.3.1.2 and 6.3.1.3, respectively. The initial and boundary conditions are presented briefly in section 6.3.1.4. More details can be readily found in *Saito et al.* [2006], *Šimůnek et al.* [2008], *Sakai et al.* [2009, 2011] and *Yang et al.* [2017a].

6.3.1.1 Mass and energy conservation equations

The governing mass balance equation for one-dimensional vertical flow of liquid water and water vapor in an unsaturated rigid bare soil is given as follows [*Saito et al.*, 2006]:

$$\frac{\partial \theta}{\partial t} = -\frac{\partial \left(q_{Lh} + q_{LT} \right)}{\partial z} - \frac{\partial \left(q_{vh} + q_{vT} \right)}{\partial z}$$

$$= \frac{\partial}{\partial z}\left[K_{Lh}\left(\frac{\partial h}{\partial z} + 1 \right) + K_{LT}\frac{\partial T}{\partial z} + K_{vh}\frac{\partial h}{\partial z} + K_{vT}\frac{\partial T}{\partial z} \right] \tag{6.1}$$

where θ is the total volumetric water content ($L^3\ L^{-3}$), defined as the sum of volumetric liquid water content θ_l ($L^3\ L^{-3}$) and volumetric water vapor content θ_v ($L^3\ L^{-3}$); t is time (T); q_{Lh} and q_{LT} are isothermal and thermal liquid water flux densities ($L\ T^{-1}$), respectively; q_{vh} and q_{vT} are isothermal and thermal water vapor flux densities ($L\ T^{-1}$), respectively; z is the spatial coordinate positive upward (L); h is the pressure head (i.e., negative suction head) (L); T is temperature (K); K_{Lh} ($L\ T^{-1}$) and K_{LT} ($L^2\ K^{-1}\ T^{-1}$) are the isothermal and thermal hydraulic conductivities for liquid phase fluxes owing to gradients in h and T, respectively; and K_{vh} ($L\ T^{-1}$) and K_{vT} ($L^2\ K^{-1}\ T^{-1}$) are isothermal and thermal vapor hydraulic conductivities for vapor phase fluxes, respectively.

The governing energy balance equation for one-dimensional vertical transport in an unsaturated rigid bare soil is represented as follows [*Saito et al.*, 2006]:

$$\frac{\partial C_p T}{\partial t} + L\frac{\partial \theta_v}{\partial t} = \frac{\partial}{\partial z}\left[\lambda(\theta)\frac{\partial T}{\partial z} \right] - C_l\frac{\partial q_L T}{\partial z} - C_v\frac{\partial q_v T}{\partial z} - L\frac{\partial q_v}{\partial z} \tag{6.2}$$

where $C_p = C_s\theta_s + C_l\theta_l + C_v\theta_v$ if assuming local thermal equilibrium (i.e., supposing temperatures in solid, liquid, and gas phases are the same); θ_s is volumetric fraction of solid phase ($L^3\ L^{-3}$); C_p, C_s, C_l, and C_v are volumetric heat capacities ($M\ L^{-1}\ T^{-2}\ K^{-1}$) of the moist soil, solid phase, liquid water, and water vapor, respectively; L is volumetric latent heat of vaporization of liquid water ($M\ L^{-1}\ T^{-2}$) and is expressed by $L = L_w\rho_w$, where L_w is latent heat of vaporization of liquid water ($L^2\ T^{-2}$) and ρ_w is

density of liquid water (M L^{-3}); $\lambda(\theta)$ is apparent thermal conductivity of moist soil (M L T^{-3} K^{-1}); and $q_L\,(=q_{Lh}+q_{LT})$ and $q_v\,(=q_{vh}+q_{vT})$ are the total flux densities of liquid water and water vapor (L T^{-1}), respectively.

6.3.1.2 Soil hydraulic properties

A variety of statistical models [e.g., *Yang and Mohanty*, 2015; *Yang et al.*, 2017b] have been developed to predict isothermal unsaturated hydraulic conductivity K_{Lh} from soil water retention function. Among the widely used, the statistical pore size distribution model derived by *Mualem* [1976] was used in this study and can be expressed as follows:

$$K_{Lh} = K_s S_e^{0.5}\left[\frac{\int_0^{S_e} dS_e/|h|}{\int_0^1 dS_e/|h|}\right]^2 \tag{6.3}$$

in which K_s is saturated hydraulic conductivity (L T^{-1}); and S_e is the effective saturation (dimensionless).

The water retention curve model proposed by *van Genuchten* [1980] is widely employed to describe water retention at wet and intermediate soil moisture content. The *van Genuchten* [1980] model, which accounts for capillary force only, is written as:

$$\theta_l(h) = \theta_r + (\theta_s - \theta_r)\left[1+|\alpha h|^n\right]^{-m} \tag{6.4}$$

in which θ_s and θ_r are saturated and residual water contents (L^3 L^{-3}), respectively; and α (L^{-1}), n (unitless), and $m\,(=1-1/n)$ are empirical shape parameters.

Inserting equation (6.4) into equation (6.3), one can acquire the K_{Lh} for van Genuchten model as:

$$K_{Lh} = K_s S_e^{0.5}\left[1-\left(1-S_e^{1/m}\right)^m\right]^2 \tag{6.5}$$

The van Genuchten (VG) model frequently failed to appropriately describe soil water retention in the dry range. The full range water retention curve model developed by *Fayer and Simmons* [1995], however, is able to characterize the soil water retention function well in both the wet and dry regions. The Fayer and Simmons (FS) model considers the adsorption of water on soil under dry conditions by means of revising the residual water content in VG model:

$$\theta_l(h) = \chi\theta_a + \left(\theta_s - \chi\theta_a\right)\left[1+\left|\alpha h\right|^n\right]^{-m} \tag{6.6}$$

where θ_a (L^3 L^{-3}) represents a fitting parameter representing volumetric water content when $|h|=1$; $\chi\theta_a$ is the adsorption of water on soil particle surface and χ is given as $\chi(h)=1-\ln(|h|)/\ln(|h_m|)$, in which h_m is the pressure head where water content equals to zero (L). According to *Fayer and Simmons* [1995], $|h_m|$ is usually taken to be 10^7 cm and might be larger for fine textured soils like clay.

The explicit analytical expression of isothermal hydraulic conductivity K_{Lh} for the FS model can be gained by substituting equation (6.6) into equation (6.3):

$$K_{Lh} = K_s S_e^{0.5}\left[\frac{\int_0^{S_e} dS_e/|h|}{\int_0^1 dS_e/|h|}\right]^2 = K_s S_e^{0.5}\left[\frac{\Gamma_s(h)}{\Gamma_{\max}}\right]^2 \tag{6.7}$$

The expressions of both $\Gamma_s(h)$ and $\Gamma_{\max}$ are comprehensively given in the appendix of *Fayer and Simmons* [1995].

Considering the temperature dependence of the pressure head, the thermal hydraulic conductivity K_{LT}, for thermal liquid water flux is defined as [*Noborio et al.*, 1996; *Saito et al.*, 2006]:

$$K_{LT} = K_{Lh}\left(hG_{wT}\frac{1}{\gamma_0}\frac{d\gamma}{dT} \right) \tag{6.8}$$

in which G_{wT} is the gain factor (unitless), which rectifies the temperature dependence of the surface tension [*Nimmo and Miller*, 1986]; γ is the surface tension of soil water (M T^{-2}); and γ_0 is the surface tension at 25°C, which is equal to 71.89 g s^{-2}.

The vapor hydraulic conductivities under isothermal condition K_{vh}, and under thermal condition K_{vT}, are, respectively, expressed as [*Noborio et al.*, 1996; *Fayer*, 2000]:

$$K_{vh} = \frac{D}{\rho_w}\rho_{sv}\frac{Mg}{RT}H_r \tag{6.9}$$

$$K_{vT} = \frac{D}{\rho_w}\eta H_r\frac{d\rho_{sv}}{dT} \tag{6.10}$$

where D is the vapor diffusivity in soil (L^2 T^{-1}); ρ_{sv} is saturated vapor density (M L^{-3}); M is molecular weight of water (M mol^{-1}) and equals to 0.018015 kg mol^{-1}; g is gravitational acceleration (L T^{-2}, =9.81 m s^{-2}); R is universal gas constant (M L^2 T^{-2} mol^{-1} K^{-1}, =8.314 J mol^{-1} K^{-1}); η is the enhancement factor (unitless) [*Cass et al.*, 1984];

and H_r represents the relative humidity (unitless) that can be calculated from the pressure head, h, using a thermodynamic relationship between liquid water and water vapor in porous media pores [*Philip and de Vries*, 1957] as $H_r = \exp(hMg / RT)$.

6.3.1.3 Soil thermal properties

The apparent thermal conductivity of soil, $\lambda(\theta)$, in equation (6.2) is defined as the sum of the thermal conductivity of soil in the absence of water flow ($\lambda_0(\theta)$) [*Chung and Horton*, 1987] and the macrodispersivity that is assumed to be a linear function of water velocity [*Hopmans et al.*, 2002]. The apparent thermal conductivity (M L T^{-3} K^{-1}), $\lambda(\theta)$, may thus be given as follows [*Saito et al.*, 2006]:

$$\lambda(\theta) = b_1 + b_2\theta + b_3\theta^{0.5} + \beta C_l |q_L| \tag{6.11}$$

where β is the thermal dispersivity (L) and b_1, b_2, and b_3 are the empirical regression parameters (M L T^{-3} K^{-1}) that are linked to soil textures (e.g., sand, loam, and clay) [*Chung and Horton*, 1987].

6.3.1.4 Initial and boundary conditions

Initial conditions for the water and heat balance equations are respectively denoted by:

$$h(z,0) = h_i(z) \tag{6.12}$$

$$T(z,0) = T_i(z) \tag{6.13}$$

in which $h_i(z)$ and $T_i(z)$ stand for the initial soil pressure head and soil temperature, respectively.

The top surface boundary conditions for field soils based on the surface mass and energy balance are, respectively, defined by:

$$q_w(0,t) = P - E \tag{6.14}$$

$$G(0,t) = R_n - H - LE \tag{6.15}$$

in which $q_w = q_L + q_v$ represents the total water flux density (L T^{-1}); P is the natural precipitation or human irrigation (L T^{-1}); E is the surface evaporation rate (L T^{-1}); G is the conductive soil heat flux density (M T^{-3}); R_n is the net radiation (M T^{-3}); H is the sensible heat flux density (M T^{-3}); LE is the latent heat flux density (M T^{-3}); and L is volumetric latent heat (M L^{-1} T^{-2}).

The net radiation, R_n, in the field can be denoted as:

$$R_n = R_{ns} + R_{nl} = (1-a)R_s + \varepsilon_s \sigma\left(\varepsilon_a T_a^4 - T_s^4\right) \tag{6.16}$$

where R_{ns} and R_{nl} are the net shortwave radiation and net longwave radiation, respectively (M T^{-3}); a is surface albedo (unitless); R_s represents incoming shortwave solar radiation (M T^{-3}); ε_s is the soil surface emissivity (unitless) describing the reflection of the longwave radiation at the soil surface; σ is the Stefan-Boltzmann constant (5.67×10^{-8} W m^{-2} K^{-4}); ε_a is atmospheric emissivity of clear sky (unitless); and T_a and T_s are the air temperature and soil surface temperature, respectively (K).

The sensible heat flux in equation (6.15) is represented as [*Saito et al.*, 2006]:

$$H = C_a \frac{T_s - T_a}{r_H} \tag{6.17}$$

in which C_a is the volumetric heat capacities (M L^{-1} T^{-2} K^{-1}) of air; and r_H is the aerodynamic resistance to heat transfer (T L^{-1}).

As described in the introduction section, generally soil surface evaporation is controlled sequentially by atmospheric conditions (stage 1 evaporation), surface moisture content, and water transport in the soil (stage 2 and 3 evaporation). A model considering all these factors can be written as [*Saito et al.*, 2006]:

$$E = \frac{\rho_{vs} - \rho_{va}}{\rho_w (r_a + r_s)} \tag{6.18}$$

where ρ_{vs} is the water vapor density at soil surface (M L^{-3}); ρ_{va} is the atmospheric vapor density (M L^{-3}); r_a is the aerodynamic resistance for water vapor transfer (T L^{-1}); and r_s is the soil surface resistance for water vapor transfer (T L^{-1}).

The aerodynamic resistance to heat transfer (r_H) is very close to the aerodynamic resistance to water vapor transfer (r_a), as such, it can be assumed that $r_H = r_a$. They can be computed as follows [*Saito et al.*, 2006; *Bittelli et al.*, 2008]:

$$r_H = r_a = \frac{1}{Uk^2}\left[\ln\left(\frac{z_m - d + z_{om}}{z_{om}}\right) + \phi_m\right] \cdot \left[\ln\left(\frac{z_h - d + z_{oh}}{z_{oh}}\right) + \phi_h\right] \tag{6.19}$$

in which z_m and z_h are the measurement heights of wind speed and temperature, respectively (L); d (L) is the zero plane displacement (=0 for bare soils); z_{om} and z_{oh} are the surface roughness lengths for momentum flux and heat flux, respectively (L); ϕ_m and ϕ_h are the atmospheric stability correction factors for momentum flux and heat flux, respectively (unitless); U is the measured wind speed (L T^{-1}) at height z_m ; and k is the

von Karman constant (=0.41). For bare soils, surface roughness values z_{om} and z_{oh} are both assumed to be equal to 0.001 m.

The soil surface resistance r_s for water vapor transfer suggested by *van de Griend and Owe* [1994] employed the following exponential function:

$$r_s = \begin{cases} r_{sl} \exp\left(A\left(\theta_{\min} - \theta_0\right)\right) & \theta_0 \le \theta_{\min} \\ r_{sl} & \theta_0 > \theta_{\min} \end{cases} \tag{6.20}$$

where r_{sl} (=10 s m^{-1}) is the resistance to molecular diffusion of water surfaces as a lower reference; A (=35.63) is the curve-fitted parameter (dimensionless); $\theta_{\min}$ (=0.15 L^3 L^{-3}) is the empirical minimum water content above which the soil is able to deliver vapor at a potential rate; and θ_0 (L^3 L^{-3}) is the soil moisture content in the top 1 cm. *Bittelli et al.* [2008] found that the *van de Griend and Owe* [1994] model used in this work resulted in the best estimates of soil evaporation after comparing three surface resistance expressions (i.e., *Sun* [1982], *Camillo and Gurney* [1986], and *van de Griend and Owe* [1994]).

Zero gradients of the pressure head and temperature are adopted as the boundary conditions at the bottom of the soil profile, $z = z_b$, and expressed by:

$$\frac{\partial h}{\partial z}\left(z_b, t\right) = 0 \tag{6.21}$$

$$\frac{\partial T}{\partial z}\left(z_b, t\right) = 0 \tag{6.22}$$

6.3.2 Synthetic analysis data

Two synthetic numerical simulations were conducted in this work with three cases using three soil types (sand, sandy loam, and loam). The VG model parameters for sand, sandy loam, and loam are all from *Carsel and Parrish* [1988], whereas the FS model parameters for sand are adopted on the basis of *Sakai et al.* [2011] and the FS model parameters for sandy loam and loam were from *Yang et al.* [2017a] according to the observation that water retention curve depicted by FS model is dissimilar with that of VG model only in low water content range [*Campbell and Shiozawa*, 1992; *Webb*, 2000; *Lebeau and Konrad*, 2010; *Zhang*, 2011; *Peters*, 2013].

Table 6.1 shows the hydraulic and thermal parameters for three soils. The thermal parameters b_1, b_2, and b_3 in equation (6.11) are based on *Chung and Horton* [1987]. Figure 6.1 plots the FS and VG soil water retention curves for the three soils. It can be seen from Figure 6.1 that the water retention curves from saturated to residual moisture content are basically the same between VG and FS models. The retention curves between VG and FS models display remarkably difference only in the dry range (residual and zero water content). The matric suction head (negative pressure head) in the dry range is a linear function of water content on a semilogarithmic plot [*Campbell and Shiozawa*, 1992] as FS water retention curve shows. On the other hand, the water content asymptotically approaches its residual value with the progressively increasing matric suction as VG water retention curve displays. In addition, the sand (Figure 6.1a) has smaller adsorptive water retention component than sandy loam (Figure 6.1b) and loam (Figure 6.1c) due to its comparatively a little lower residual water content.

Table 6.1 Hydraulic and thermal parameters used in the synthetic numerical simulations

Sample	Hydraulic Property						Thermal Conductivity		
	θ_s	θ_r	θ_a	α (cm^{-1})	n	K_s ($cm\ d^{-1}$)	b_1 ($W\ m^{-1}\ °C^{-1}$)	b_2 ($W\ m^{-1}\ °C^{-1}$)	b_3 ($W\ m^{-1}\ °C^{-1}$)
Sand (VG)[a]	0.430	0.045	/	0.145	2.68	712.8	0.228	-2.406	4.909
Sand (FS)[b]	0.430	/	0.0625	0.147	2.73	712.8	0.228	-2.406	4.909
Sandy Loam (VG)[a]	0.410	0.065	/	0.075	1.89	106.1	0.243	0.393	1.534
Sandy Loam (FS)[c]	0.410	/	0.108	0.080	1.95	106.1	0.243	0.393	1.534
Loam (VG)[a]	0.430	0.078	/	0.036	1.56	24.96	0.243	0.393	1.534
Loam (FS)[c]	0.430	/	0.160	0.038	1.65	24.96	0.243	0.393	1.534

[a]The van Genuchten (VG) model parameters for sand, sandy loam and loam are from *Carsel and Parrish* [1988].
[b]The Fayer and Simmons (FS) model parameters for sand are from *Sakai et al.* [2011].
[c]The Fayer and Simmons (FS) model parameters for sandy loam and loam are from *Yang et al.* [2017a].

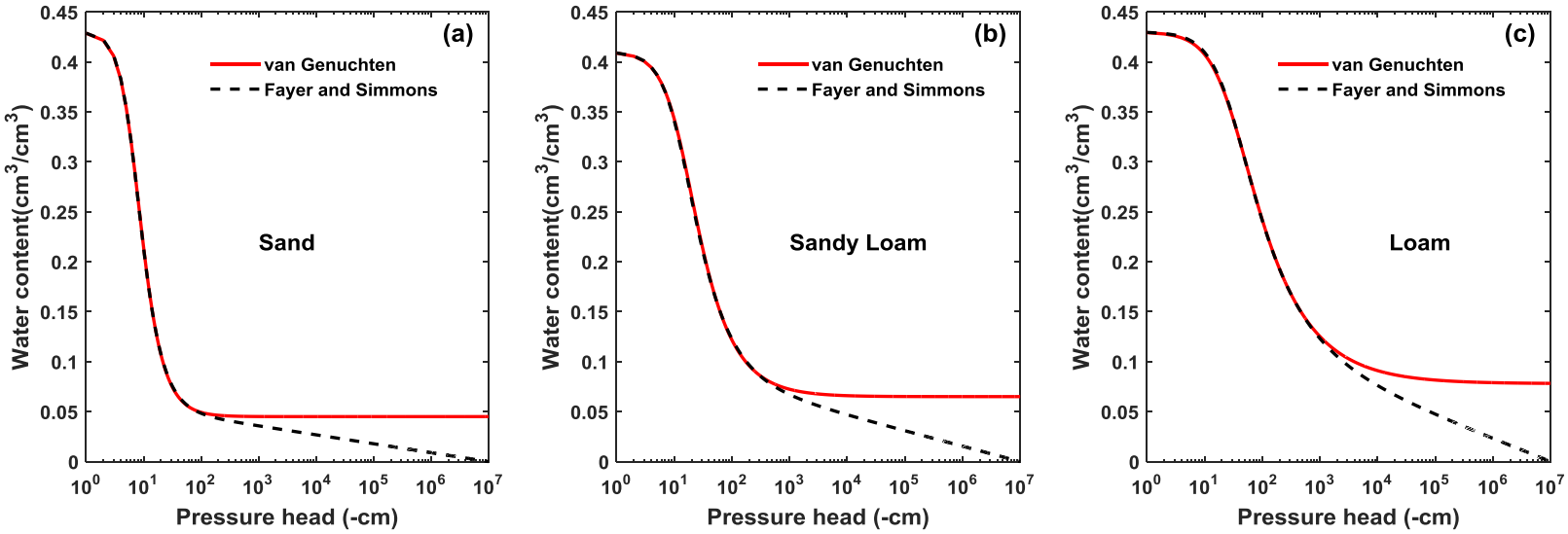

Figure 6.1 Unextended van Genuchten and extended full range Fayer and Simmons water retention curves of (a) sand, (b) sandy loam, and (c) loam used in the synthetic numerical simulations, based on the parameters shown in Table 6.1.

6.3.3 Numerical simulation procedure

The revised numerical HYDRUS-1D code [*Saito et al.*, 2006; *Šimůnek et al.*, 2008; *Sakai et al.*, 2009, 2011], which adopts the finite element method for spatial discretization and finite difference for temporal discretization, was employed to solve the coupled water-vapor-heat model described in section 6.3.1. The schematic diagram for soil sequences configuration (homogeneous and layered soil profiles) used in the two numerical simulations are illustrated in Figure 6.2 with top (case 1), middle (case 2) and bottom (case 3). The overlying layer was assumed to be 5 cm thick in layered soil profiles. The entire one-dimensional homogeneous and layered soil profiles were assumed to extend from $z = 0$ to $z = z_b = 50$ cm deep, with a spatial discretization of 0.2 cm (i.e., 251 nodes) for the two synthetic simulations. The discretization in time changed between a minimum and maximum time step that was determined by the time step criterions described in *Saito et al.* [2006] and *Sakai et al.* [2009, 2011].

The boundary conditions (for homogeneous and layered) and initial conditions for homogenous columns were shown in Table 6.2 and Table 6.3, respectively for the first and second synthetic numerical simulations. We adopted the same corresponding homogeneous columns initial conditions for respective textured soils in the layered soil columns. Figure 6.3 displays the diurnal meteorological data (hourly solar radiation, air temperature, wind speed, and relative humidity) for the Riverside, California field site (representing semiarid hydroclimate) used in the first synthetic simulation, which were downloaded from the California Irrigation Management Information System (CIMIS) website (http://www.cimis.water.ca.gov/WSNReportCriteria.aspx). No natural

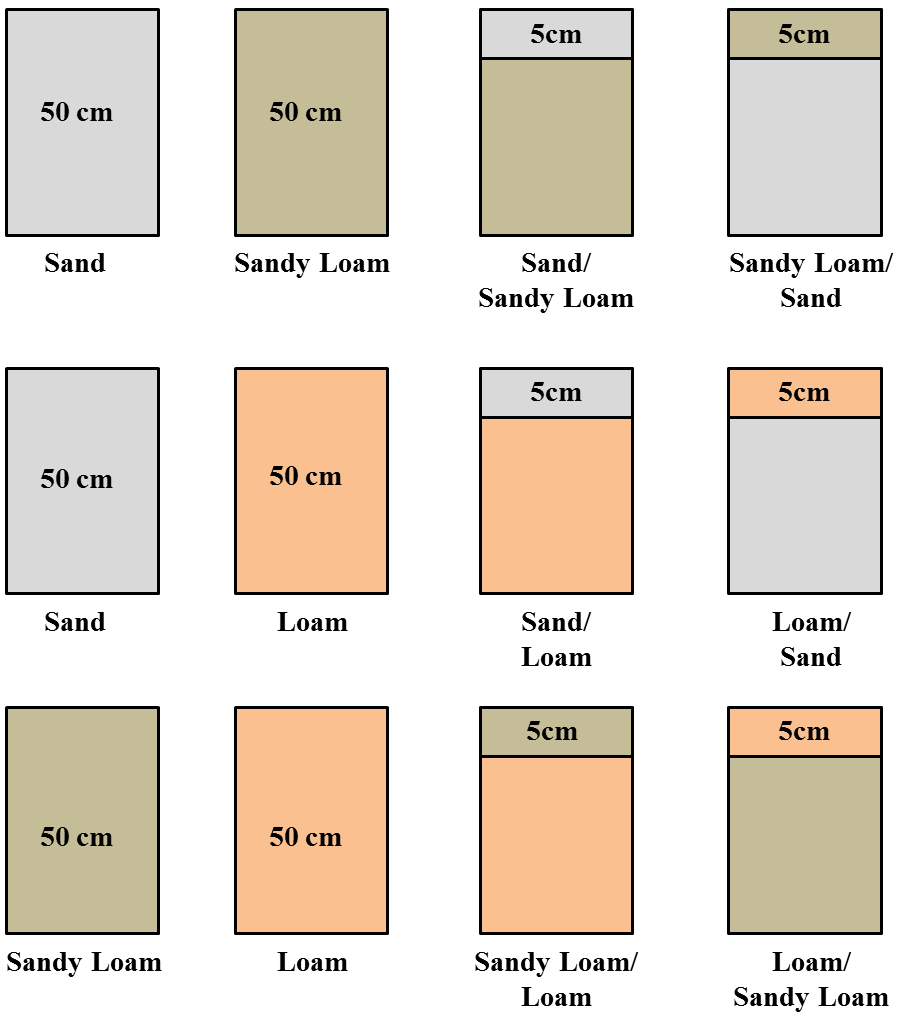

Figure 6.2 Schematic diagram of soil sequences configuration used in synthetic simulations, top (case 1), middle (case 2) and bottom (case 3).

Table 6.2 Initial and boundary conditions for the first synthetic numerical simulations

Scenarios	Processes	Initial Conditions[a]	Top Boundary Conditions	Bottom Boundary Conditions
Sand (VG)	Water balance	$h(z,0) = -45$	$q_w(0,t) = I_1 - E$	$\frac{\partial h}{\partial z}(50,t) = 0$
	Heat balance	$T(z,0) = 16 + \frac{22-16}{50} z$	$G(0,t) = R_n - H - LE$	$\frac{\partial T}{\partial z}(50,t) = 0$
Sand (FS)	Water balance	$h(z,0) = -46.4$	$q_w(0,t) = I_1 - E$	$\frac{\partial h}{\partial z}(50,t) = 0$
	Heat balance	$T(z,0) = 16 + \frac{22-16}{50} z$	$G(0,t) = R_n - H - LE$	$\frac{\partial T}{\partial z}(50,t) = 0$
Sandy Loam (VG)	Water balance	$h(z,0) = -1000$	$q_w(0,t) = I_1 - E$	$\frac{\partial h}{\partial z}(50,t) = 0$
	Heat balance	$T(z,0) = 16 + \frac{22-16}{50} z$	$G(0,t) = R_n - H - LE$	$\frac{\partial T}{\partial z}(50,t) = 0$
Sandy Loam (FS)	Water balance	$h(z,0) = -660$	$q_w(0,t) = I_1 - E$	$\frac{\partial h}{\partial z}(50,t) = 0$
	Heat balance	$T(z,0) = 16 + \frac{22-16}{50} z$	$G(0,t) = R_n - H - LE$	$\frac{\partial T}{\partial z}(50,t) = 0$
Loam (VG)	Water balance	$h(z,0) = -500$	$q_w(0,t) = I_1 - E$	$\frac{\partial h}{\partial z}(50,t) = 0$
	Heat balance	$T(z,0) = 16 + \frac{22-16}{50} z$	$G(0,t) = R_n - H - LE$	$\frac{\partial T}{\partial z}(50,t) = 0$
Loam (FS)	Water balance	$h(z,0) = -494.5$	$q_w(0,t) = I_1 - E$	$\frac{\partial h}{\partial z}(50,t) = 0$
	Heat balance	$T(z,0) = 16 + \frac{22-16}{50} z$	$G(0,t) = R_n - H - LE$	$\frac{\partial T}{\partial z}(50,t) = 0$

[a]These initial conditions (ICs) are for homogeneous soils, whereas for layered soils, adopting the same homogeneous ICs for respective textured soils. I_1 denotes the assumed irrigation rate (6.5 cm/day) at DOY 334.95-335.00.

Table 6.3 Initial and boundary conditions for the second synthetic numerical simulations

Scenarios	Processes	Initial Conditions[a]	Top Boundary Conditions	Bottom Boundary Conditions
Sand (VG)	Water balance	$h(z,0) = -45$	$q_w(0,t) = P - E$	$\frac{\partial h}{\partial z}(50,t) = 0$
	Heat balance	$T(z,0) = 19 + \frac{38-19}{50} z$	$G(0,t) = R_n - H - LE$	$\frac{\partial T}{\partial z}(50,t) = 0$
Sand (FS)	Water balance	$h(z,0) = -46.4$	$q_w(0,t) = P - E$	$\frac{\partial h}{\partial z}(50,t) = 0$
	Heat balance	$T(z,0) = 19 + \frac{38-19}{50} z$	$G(0,t) = R_n - H - LE$	$\frac{\partial T}{\partial z}(50,t) = 0$
Sandy Loam (VG)	Water balance	$h(z,0) = -1000$	$q_w(0,t) = P - E$	$\frac{\partial h}{\partial z}(50,t) = 0$
	Heat balance	$T(z,0) = 19 + \frac{38-19}{50} z$	$G(0,t) = R_n - H - LE$	$\frac{\partial T}{\partial z}(50,t) = 0$
Sandy Loam (FS)	Water balance	$h(z,0) = -660$	$q_w(0,t) = P - E$	$\frac{\partial h}{\partial z}(50,t) = 0$
	Heat balance	$T(z,0) = 19 + \frac{38-19}{50} z$	$G(0,t) = R_n - H - LE$	$\frac{\partial T}{\partial z}(50,t) = 0$
Loam (VG)	Water balance	$h(z,0) = -500$	$q_w(0,t) = P - E$	$\frac{\partial h}{\partial z}(50,t) = 0$
	Heat balance	$T(z,0) = 19 + \frac{38-19}{50} z$	$G(0,t) = R_n - H - LE$	$\frac{\partial T}{\partial z}(50,t) = 0$
Loam (FS)	Water balance	$h(z,0) = -494.5$	$q_w(0,t) = P - E$	$\frac{\partial h}{\partial z}(50,t) = 0$
	Heat balance	$T(z,0) = 19 + \frac{38-19}{50} z$	$G(0,t) = R_n - H - LE$	$\frac{\partial T}{\partial z}(50,t) = 0$

[a]These initial conditions (ICs) are for homogeneous soils, whereas for layered soils, adopting the same homogeneous ICs for respective textured soils.

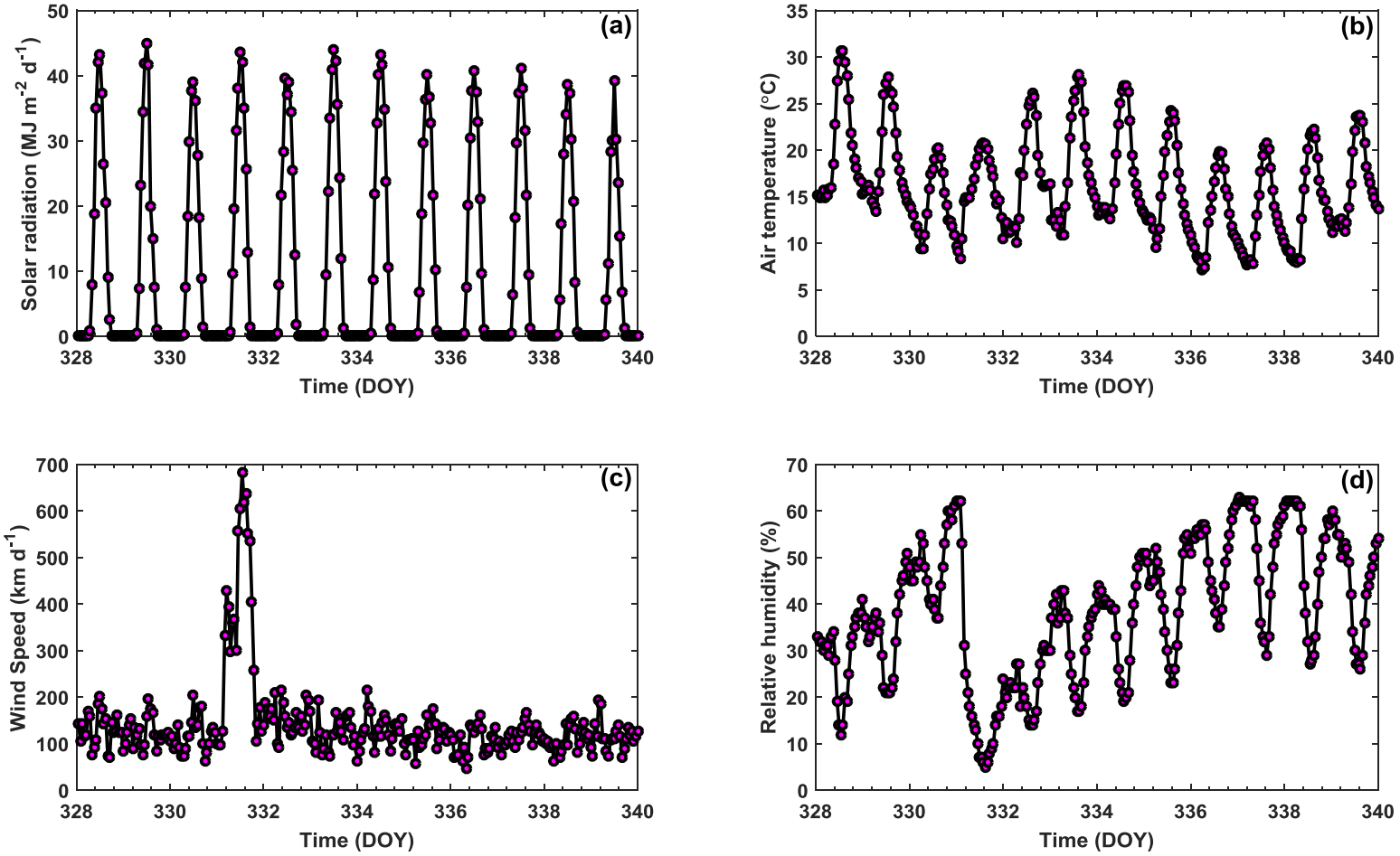

Figure 6.3 Diurnal changes of meteorological variables: (a) solar radiation, (b) air temperature, (c) wind speed, and (d) relative humidity during the simulation period from 24 November (Day of the Year (DOY) 328) to 6 December (DOY 340), 1995 at the nearby CIMIS U.C. Riverside weather station (hourly measured values) close to the University of California Agricultural Experimental Station-Riverside, California field site.

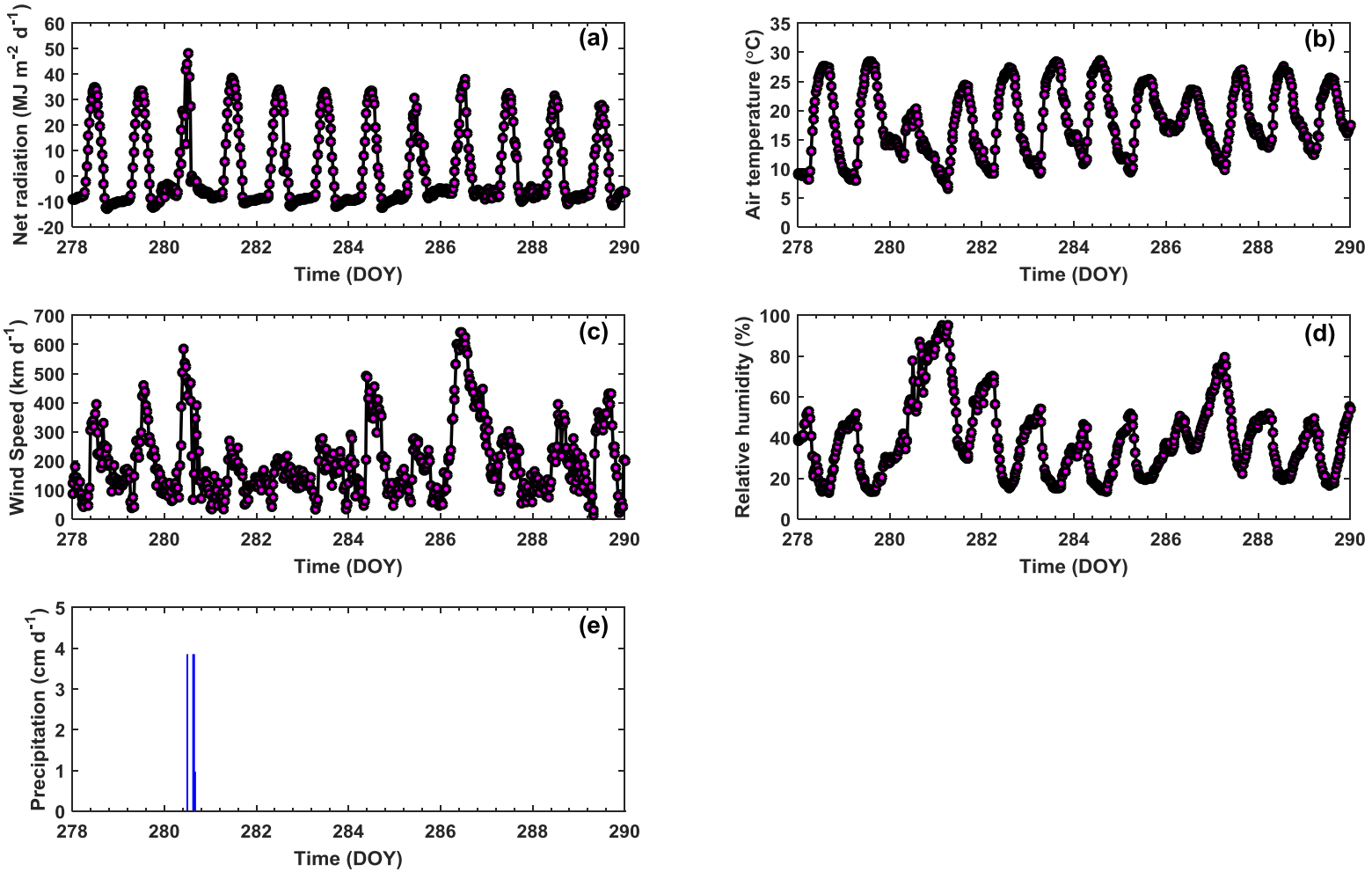

Figure 6.4 Diurnal changes of meteorological variables: (a) net radiation, (b) air temperature, (c) wind speed, (d) relative humidity, and (e) precipitation during the simulation period from 5 October (Day of the Year (DOY) 278) to 17 October (DOY 290), 2002 at the Audubon, Arizona field site.

precipitation was observed at the weather station during the simulation period DOY 328-340. Therefore, to mimic the natural precipitation, one irrigation rate (6.5 cm/day) occurring at DOY 334.95-335.00 was assumed (represented as I_1 in Table 6.2).

Figure 6.4 shows the meteorological data (half-hourly net radiation, air temperature, wind speed, relative humidity, and precipitation) for the Audubon, Arizona field site (representing arid hydroclimate) used in the second synthetic simulation, which were downloaded from AmeriFlux network (http://ameriflux.lbl.gov/sites/siteinfo/US-Aud). As seen in Figure 6.4e, there are three small precipitation events (3.84, 3.84 and 0.96 cm/day) occurring at DOY 280.48-280.50, DOY 280.60-280.65, and DOY 280.65-280.67, respectively, at the Audubon, Arizona field site. The diurnal meteorological data was needed to calculate the surface conductive soil heat flux and surface evaporation that was used as top boundary conditions for heat balance and water balance equations, respectively in both synthetic numerical simulations.

6.4 Results and discussions

The simulated soil water content, temperature, and evaporation of three cases for the first synthetic simulation were presented in section 6.4.1. The modelled soil state variables (water content and temperature) and surface evaporation flux results of three cases for the second synthetic simulation were given in section 6.4.2.

6.4.1 First synthetic simulation results

6.4.1.1 Case 1 homogeneous and layered sand and sandy loam results

6.4.1.1.1 Simulated soil water content and temperature in case 1

The simulated vertical profiles of soil water content and soil temperature at DOY 329.5, DOY 330.0, DOY 335.5, and DOY 337.5 between FS and VG water retention curve models for homogeneous sand, homogeneous sandy loam, sand overlying sandy loam and sandy loam overlying sand were shown in Figure 6.5a-6.5d and Figure 6.5e-6.5h, respectively. It was observed that the soil water content modelled by FS model is noticeably smaller than that of VG model, whereas the soil temperatures between FS and VG model are practically identical for both homogeneous and layered soil profiles. The presence of the textural contrast in soil profile produced the discontinuity in soil water content (Figures 6.5c and 6.5d), but the soil temperature was still continuous across the layered interface as Figures 6.5g and 6.5h showed. The temperature profile displayed a clear diurnal variation pattern, reflecting by the fact that soil surface has the highest temperature during daytime (e.g., DOY 329.5, 335.5 and 337.5) and smallest temperature during nighttime (e.g., DOY 330.0). Such diurnal temperature change (Figure 6.5e-6.5h) would create corresponding diurnal thermal vapor/liquid fluxes variation which was driven by the temperature gradient (Figure 5.8 in *Yang et al.* [2017a]). Furthermore, the vertical temperature profiles in layered columns were more determined by the overlying texture. For instance, the temperature profile of homogeneous sand (Figure 6.5e) was very similar to that of sand overlying sandy column (Figure 6.5g), whereas the homogeneous sandy loam's temperature profile

(Figure 6.5f) was similar to that of sandy loam overlying sand column (Figure 6.5h). This was probably due to that the heat from solar radiation transported from porous surface to the deeper soils during the daytime mainly through the soil heat conduction.

On the other hand, as can be seen from Figure 6.5c, in the sand overlying sandy loam column, the water content in the overlying sand layer increased slightly after the assumed irrigation. But the water content in the underlying sandy loam layer increased significantly between 5 cm and 9 cm depth induced by the infiltration after the assumed irrigation. This is because the sand has a relatively large isothermal hydraulic conductivity after irrigation (hence fast infiltration to the underlying sandy loam). In the reverse case (sandy loam overlying sand column), as Figure 6.5d shows, the irrigated water only infiltrated to the underlying sand between 5 cm and 6 cm owing to the relatively small isothermal hydraulic conductivity of above sandy loam even after irrigation. Most of the irrigated water was kept at the overlying sandy loam, causing the significant increase of soil water content of the overlying sandy loam layer. After irrigation, the water content of underlying sand only changed slightly (decreased from DOY 335.5 to DOY 337.5 at depth between 5 and 6 cm). This indicated that the above sandy loam (fine textured soil) created the slight capillary pumping to cause the water loss in the underlying sand (coarse textured soil) to contribute the soil surface evaporation. On the contrary, Figure 6.5c demonstrated that the overlying sand (coarse textured soil) was not able to result in the capillary pumping to extract water from underlying sandy loam (fine textured soil) to contribute the evaporation. This was confirmed by the continuous water content increase in the deeper underlying sandy loam

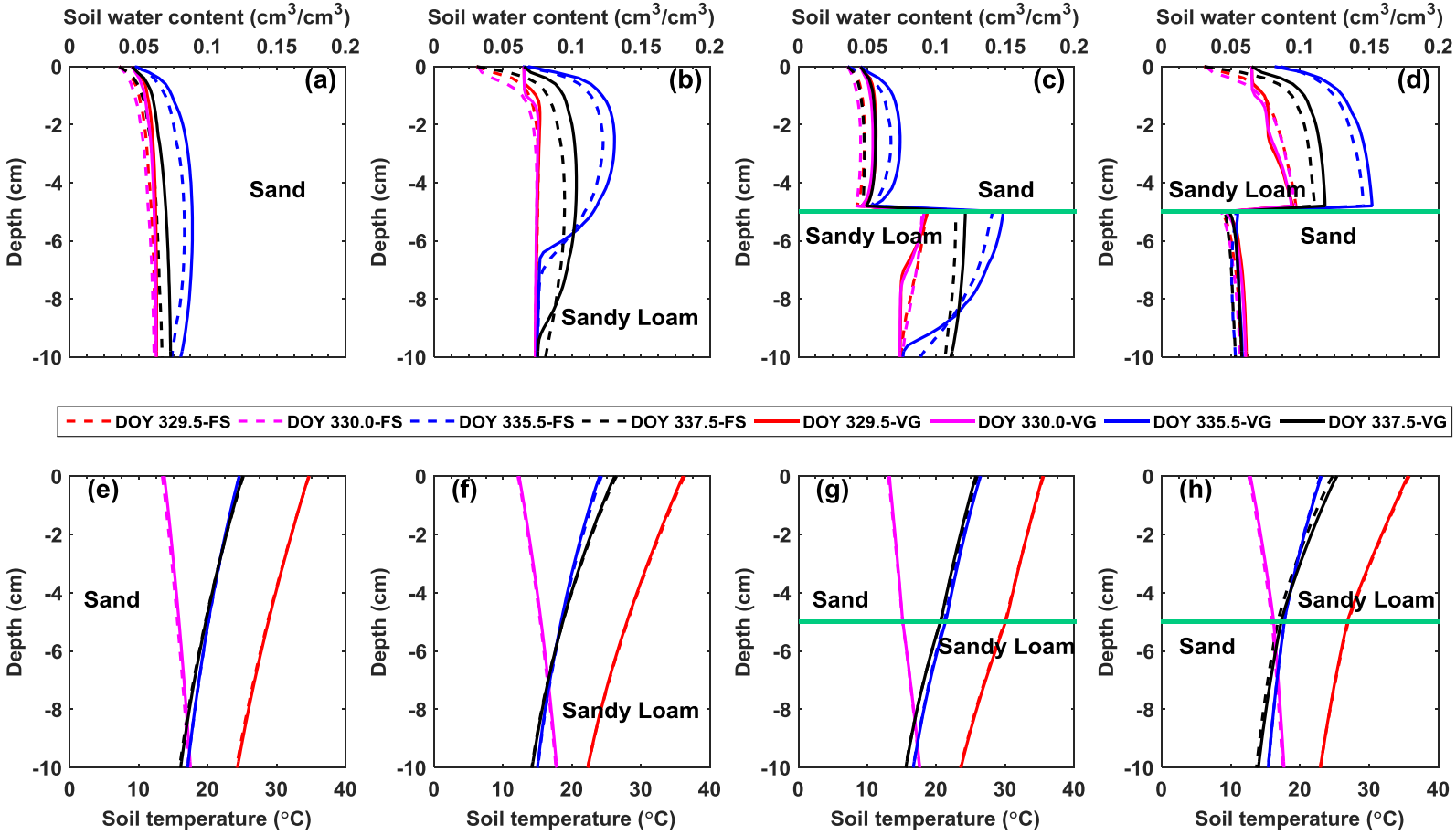

Figure 6.5 Vertical profiles of soil water content (a-d) and soil temperature (e-h) at DOY 329.5, DOY 330.0, DOY 335.5, and DOY 337.5 of case 1 (homogeneous and layered sand and sandy loam) between Fayer and Simmons (FS) and van Genuchten (VG) water retention curve models in the first synthetic simulation. Light irrigation was applied at DOY 334.95-335.00.

(9 cm to 10 cm depth from DOY 335.5 to DOY 337.5), indicating that the irrigated water continued to infiltrate to the deeper sandy loam but not contribute to the surface evaporation because of the hydraulic disconnectivity induced by the above sand (coarse textured soil). This phenomena was usually used as the basis for soil mulches (coarse soils in top layer) to suppress evaporation. The air-entry value of sand is approximately equal to 6.90 cm (reciprocal of sand α =0.145 cm^{-1}), comparatively, the air-entry value of sandy loam is about 13.33 cm (reciprocal of sandy loam α =0.075 cm^{-1}). From the air-entry value perspective, the sand also should be interpreted as coarse textured soil, whereas the loam should be regarded as the fine textured soil.

6.4.1.1.2 Simulated evaporation in case 1

Figure 6.6 and Figure 6.7 respectively display the diurnal evaporation rate and cumulative evaporation of homogeneous sand (a), homogeneous sandy loam (b), layered sand overlying sandy loam (c), and layered sandy loam overlying sand (d) between FS and VG water retention curve models. It was found that the evaporation with FS model is larger than that with VG model in both two homogeneous and two layered soil profiles. This can be seen more clearly from the cumulative evaporation results that are shown in Table 6.4 and Figure 6.7. In fact, the cumulative evaporation of FS model is 24.9%, 26.6%, 18.9%, 25.1% larger than that of VG model for homogeneous sand (Figure 6.7a), homogeneous sandy loam (Figure 6.7b), sand overlying sandy loam (Figure 6.7c), and sandy loam overlying sand (Figure 6.7d) columns, respectively. As four component fluxes (isothermal and thermal liquid and vapor flux) analyzed by *Yang et al.* [2017a], the soil evaporation is significantly underestimated when neglecting

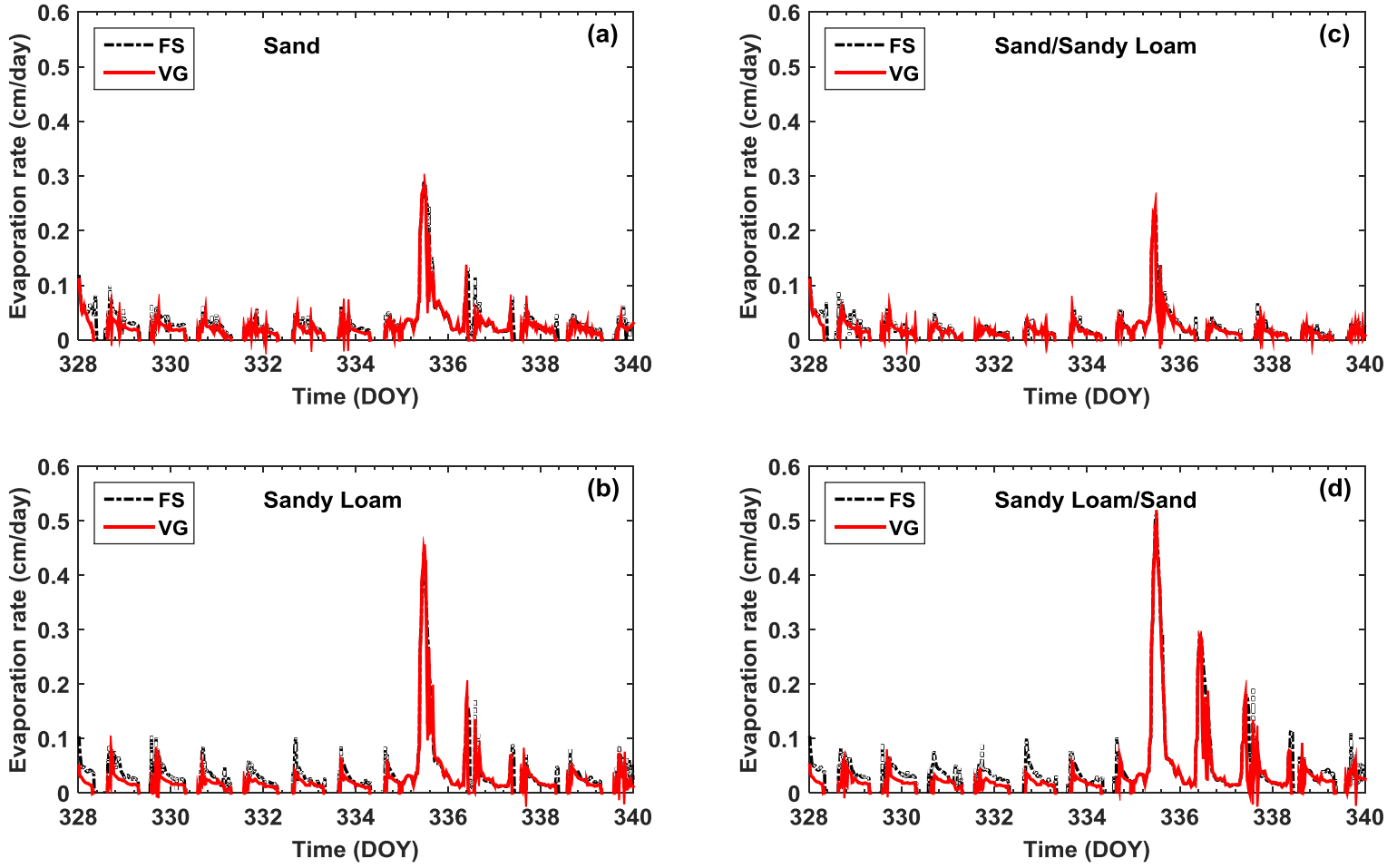

Figure 6.6 Evaporation rate of case 1 homogeneous sand (a), homogeneous sandy loam (b), layered sand overlying sandy loam (c), and layered sandy loam overlying sand (d) between Fayer and Simmons (FS) and van Genuchten (VG) water retention curve models in the first synthetic simulation.

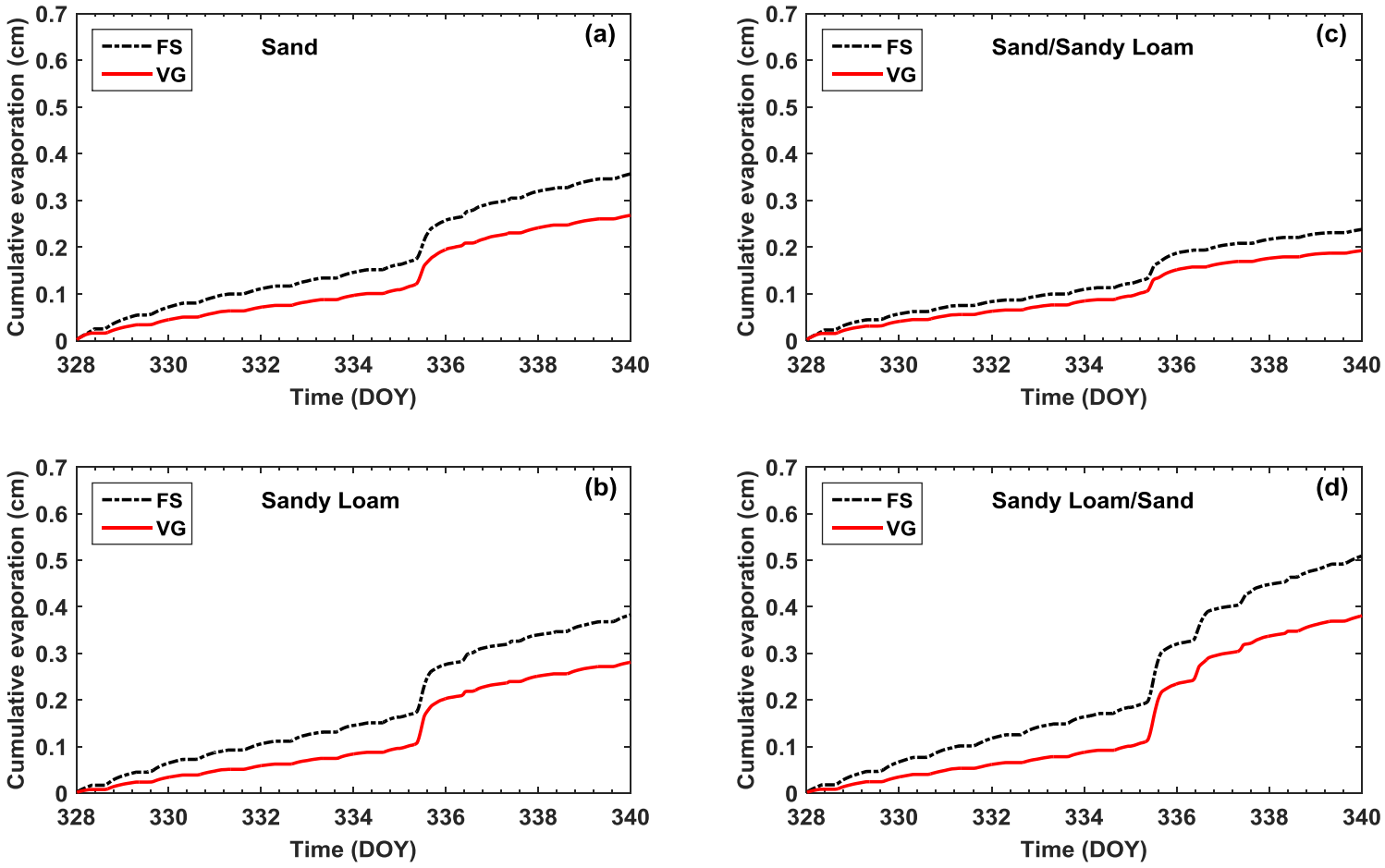

Figure 6.7 Cumulative evaporation of case 1 homogeneous sand (a), homogeneous sandy loam (b), layered sand overlying sandy loam (c), and layered sandy loam overlying sand (d) between Fayer and Simmons (FS) and van Genuchten (VG) water retention curve models in the first synthetic simulation.

Table 6.4 Cumulative evaporation of case 1 in the first synthetic numerical simulations

Cumulative Evaporation (cm)	Sand	Sandy Loam	Sand/Sandy Loam	Sandy Loam/Sand
FS	0.357	0.383	0.238	0.509
VG	0.268	0.281	0.193	0.381

Table 6.5 Cumulative evaporation of case 2 in the first synthetic numerical simulations

Cumulative Evaporation (cm)	Sand	Loam	Sand/Loam	Loam/Sand
FS	0.357	0.576	0.236	0.626
VG	0.268	0.448	0.194	0.472

Table 6.6 Cumulative evaporation of case 3 in the first synthetic numerical simulations

Cumulative Evaporation (cm)	Sandy Loam	Loam	Sandy Loam/Loam	Loam/Sandy Loam
FS	0.383	0.576	0.371	0.540
VG	0.281	0.448	0.271	0.432

adsorptive water retention because of much smaller isothermal hydraulic conductivity (hence isothermal liquid flux) of VG model in the dry range. This finding holds not only in homogeneous soil profiles shown in *Yang et al.* [2017a] but also in layered soil profile as shown in this work.

The diurnal evaporation pattern of homogeneous sand was similar to that of sand overlying sandy loam, whereas homogeneous sandy loam was similar to the sandy loam overlying sand. Here we focused on the two layered soil columns. For both sand overlying sandy loam (Figure 6.6c) and sandy loam overlying sand (Figure 6.6d) profiles, the evaporation rate of FS model is generally larger than that of VG model during DOY 328-334 when the soils are progressively drying before irrigation. The irrigation (6.5 cm/day) applied at DOY 334.95-335.00 effectively increased the water content at the vicinity of soil surface, which thence increased the evaporation rate at the daytime of DOY 335. Owing to the irrigation, the evaporation rate with FS model is very close to that with VG model during DOY 335-337 for both layered soils. Furthermore, the evaporation rate in sandy loam overlying sand gradually decreases after irrigation, whereas for sand overlying sandy loam, the evaporation rate decreases dramatically after one day of irrigation. With the continuous drying after irrigation, the evaporation flux with FS model is again greater than that with VG model from DOY 338-340 for both layered columns. The relatively different pattern of evaporation rate after irrigation in two different layered columns clearly demonstrated the effect of the layering thicknesses, sequences and positions on evaporation dynamics. In addition, the sandy loam overlying sand (fine over coarse) has the highest cumulative evaporation, whereas

sand overlying sandy loam (coarse over fine) has the smallest cumulative evaporation among the four soil columns investigated (Table 6.4). Compared to homogeneous sandy loam, the cumulative evaporation of sand overlying sandy loam (coarse over fine) is 37.9% and 31.3% smaller for FS and VG model, respectively. On the other side, compared to homogeneous sand, the cumulative evaporation of sandy loam overlying sand (fine over coarse) is 29.9% and 29.7% larger for FS and VG model, respectively.

6.4.1.2 Case 2 homogeneous and layered sand and loam results

6.4.1.2.1 Simulated soil water content and temperature in case 2

The simulated vertical profiles of soil water content and soil temperature at DOY 329.5, DOY 330.0, DOY 335.5, and DOY 337.5 between FS and VG water retention curve models for homogeneous sand, homogeneous loam, sand overlying loam and loam overlying sand were displayed in Figure 6.8a-6.8d and Figure 6.8e-6.8h, respectively. It was again found that the soil water content simulated by FS model is remarkably lower than that of VG model, whereas the soil temperatures between FS and VG model are almost the same for both homogeneous and layered profiles. The air-entry value of the sand is close to 6.90 cm (reciprocal of sand α =0.145 cm^{-1}), which corresponds to the coarse textured soil, and the air-entry value of loam is about equal to 27.78 cm (reciprocal of loam α =0.036 cm^{-1}), which corresponds to the fine textured soil. The textural contrast existing in the soil profile created the discontinuity in the soil water content (Figure 6.8c and 6.8d), the soil temperature, on the other hand, was continuous across the layered interface as Figures 6.8g and 6.8h displayed. Owing to the overlying sand's very large isothermal hydraulic conductivity after irrigation, the irrigated water

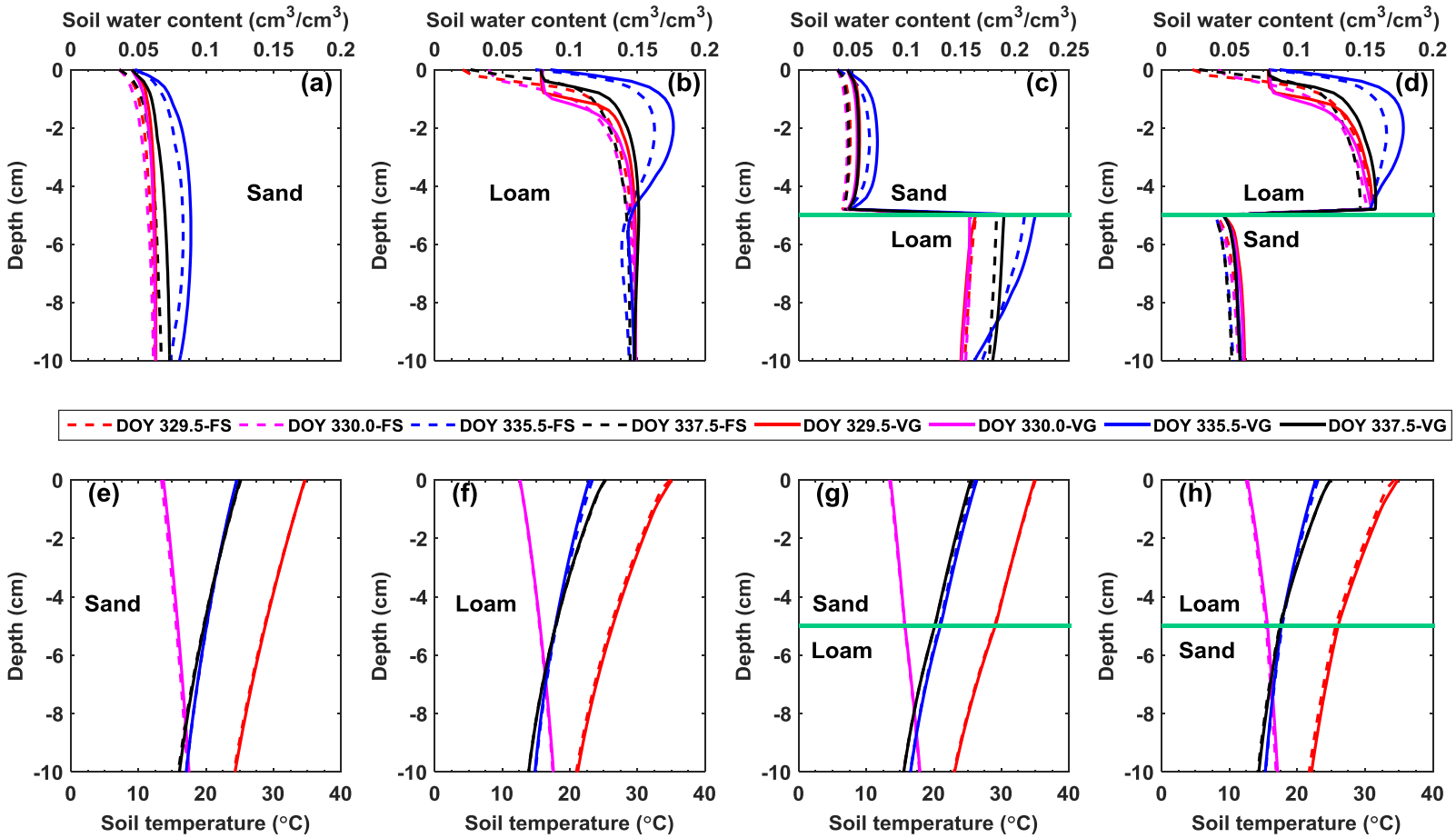

Figure 6.8 Vertical profiles of soil water content (a-d) and soil temperature (e-h) at DOY 329.5, DOY 330.0, DOY 335.5, and DOY 337.5 of case 2 (homogeneous and layered sand and loam) between Fayer and Simmons (FS) and van Genuchten (VG) water retention curve models in the first synthetic simulation. Light irrigation was applied at DOY 334.95-335.00.

would quickly infiltrate to the underlying loam soil and increase the loam's water content remarkably (see Figure 6.8c DOY 335.5). On the contrary, as Figure 6.8d showed, the overlying loam's isothermal hydraulic conductivity was comparatively small even after irrigation, hence, almost all the irrigated water would be retained in the above loam layer and no irrigated water infiltrated into the underlying sand layer. In fact, the continuously slightly decreasing soil water content in the underlying sand indicated that the above loam even extract part of water in the below sand layer to sustain the evaporation owing to the capillary pumping effect in fine over coarse layered profile. On the other hand, the above sand (coarse) cannot extract water from underlying loam (fine) to sustain evaporation as Figure 6.8c shows. The decreasing water content from DOY 335.5 to 337.5 in underlying loam layer is attributed to the redistribution and deep infiltration after irrigation but not evaporation water loss (as reflected by the increase of soil water content between 9 cm and 10 cm in the underlying loam layer). Therefore, as shown in Figure 6.8c, sand overlying loam (coarse over fine) will lead to the hydraulic disconnection to some extent in the evaporation case.

6.4.1.2.2 Simulated evaporation in case 2

The diurnal evaporation rate and cumulative evaporation of homogeneous sand (a), homogeneous loam (b), layered sand overlying loam (c), and layered loam overlying sand (d) between FS and VG water retention curve models are shown in Figure 6.9 and Figure 6.10, respectively. It was observed again that the evaporation with FS model is significantly greater than that with VG model in both two homogeneous and two layered soil profiles. As Table 6.5 and Figure 6.10 indicated, the cumulative evaporation of FS

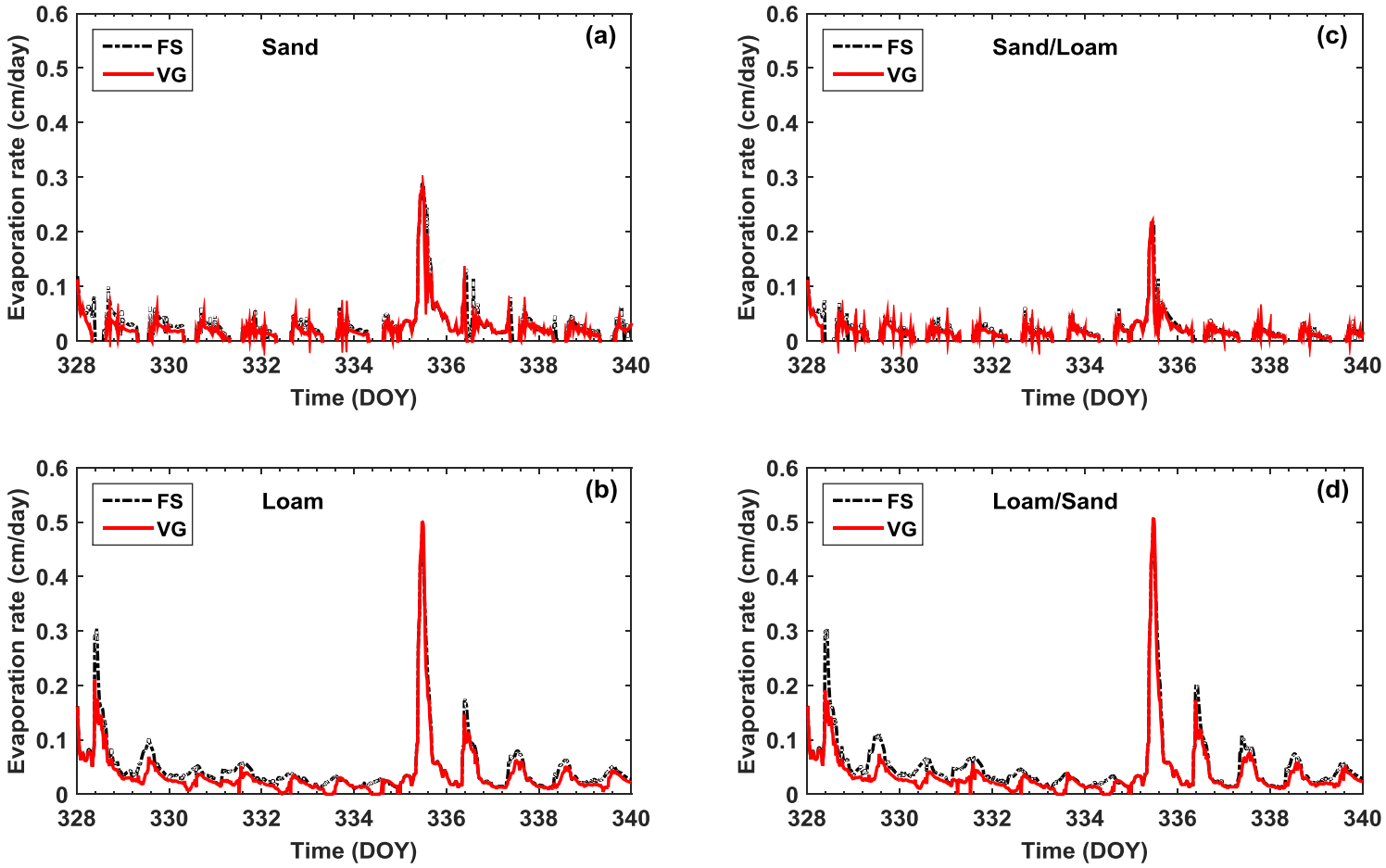

Figure 6.9 Evaporation rate of case 2 homogeneous sand (a), homogeneous loam (b), layered sand overlying loam (c), and layered loam overlying sand (d) between Fayer and Simmons (FS) and van Genuchten (VG) water retention curve models in the first synthetic simulation.

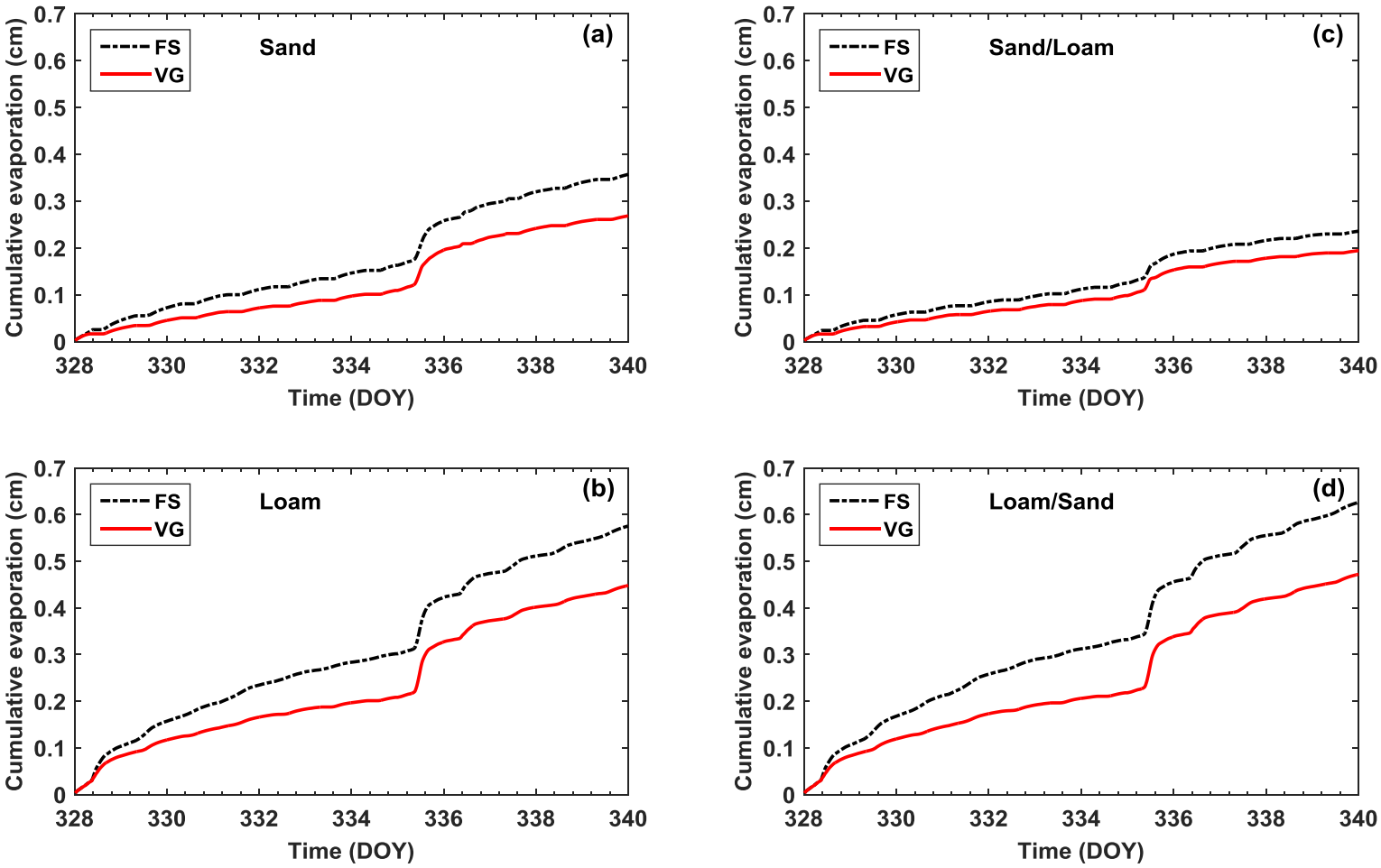

Figure 6.10 Cumulative evaporation of case 2 homogeneous sand (a), homogeneous loam (b), layered sand overlying loam (c), and layered loam overlying sand (d) between Fayer and Simmons (FS) and van Genuchten (VG) water retention curve models in the first synthetic simulation.

model was found to be 24.9%, 22.2%, 17.8%, 24.6% greater than that of VG model for homogeneous coarse sand (Figure 6.10a), homogeneous loam (Figure 6.10b), sand overlying loam (Figure 6.10c), and loam overlying sand (Figure 6.10d) soil profiles, respectively. These results again convincingly confirmed that not only in homogeneous [*Yang et al.*, 2017a] but also in layered soil profiles, the soil evaporation flux will be significantly underpredicted when ignoring adsorptive water retention.

From Figure 6.9a and Figure 6.9d, one can notice that the diurnal evaporation rate is significantly increased in loam overlying sand (Figure 6.9d) compared to that of homogeneous sand (Figure 6.9a) owing to the capillary pumping effect shown in soil water content vertical profiles. On the other hand, due to hydraulic disconnection, the diurnal evaporation rate is remarkably suppressed in sand overlying loam (Figure 6.9c) compared to that of homogeneous loam (Figure 6.9b). Furthermore, the loam overlying sand (fine over coarse) has the largest cumulative evaporation, and sand overlying loam (coarse over fine) has the smallest cumulative evaporation among the four investigated soil columns (Table 6.5). Compared to homogeneous sand, the cumulative evaporation of loam overlying sand (fine over coarse) is 43.0% and 43.2% larger for FS and VG model, respectively. Moreover, compared to homogeneous loam, the cumulative evaporation of sand overlying loam (coarse over fine) is 59.0% and 56.7% lower for FS and VG model, respectively.

6.4.1.3 Case 3 homogeneous and layered sandy loam and loam results

6.4.1.3.1 Simulated soil water content and temperature in case 3

The simulated vertical profiles of soil water content and soil temperature at DOY 329.5, DOY 330.0, DOY 335.5, and DOY 337.5 between FS and VG water retention curve models for homogeneous sandy loam, homogeneous loam, sandy loam overlying loam and loam overlying sandy loam were displayed in Figure 6.11a-6.11d and Figure 6.11e-6.11h, respectively. It was once again found that the soil water content modelled by FS model is significantly smaller than that of VG model, whereas the soil temperatures between FS and VG model are very similar for both homogeneous and layered profiles. The air-entry value of the sandy loam is around 13.33 cm (reciprocal of sandy loam α =0.075 cm^{-1}), which corresponds to the coarse textured soil, and the air-entry value of loam is approximately equal to 27.78 cm (reciprocal of loam α =0.036 cm^{-1}), which corresponds to the fine textured soil. The textural contrast existing in the soil profile created the discontinuity in the soil water content (Figure 6.11c and 6.11d), however, the soil temperature was continuous across the layered interface as Figures 6.11g and 6.11h showed. Due to the above sandy loam's comparatively greater isothermal hydraulic conductivity after irrigation, the irrigated water still can infiltrate to the underlying loam soil and increase the underlying loam's water content (Figure 6.11c DOY 335.5). On the contrary, as Figure 6.11d showed, the overlying loam's isothermal hydraulic conductivity was comparatively low even after irrigation, as a result, almost all the irrigated water was retained in the above loam layer and basically no irrigated water infiltrated into the underlying sandy loam layer. The progressively slightly decreasing

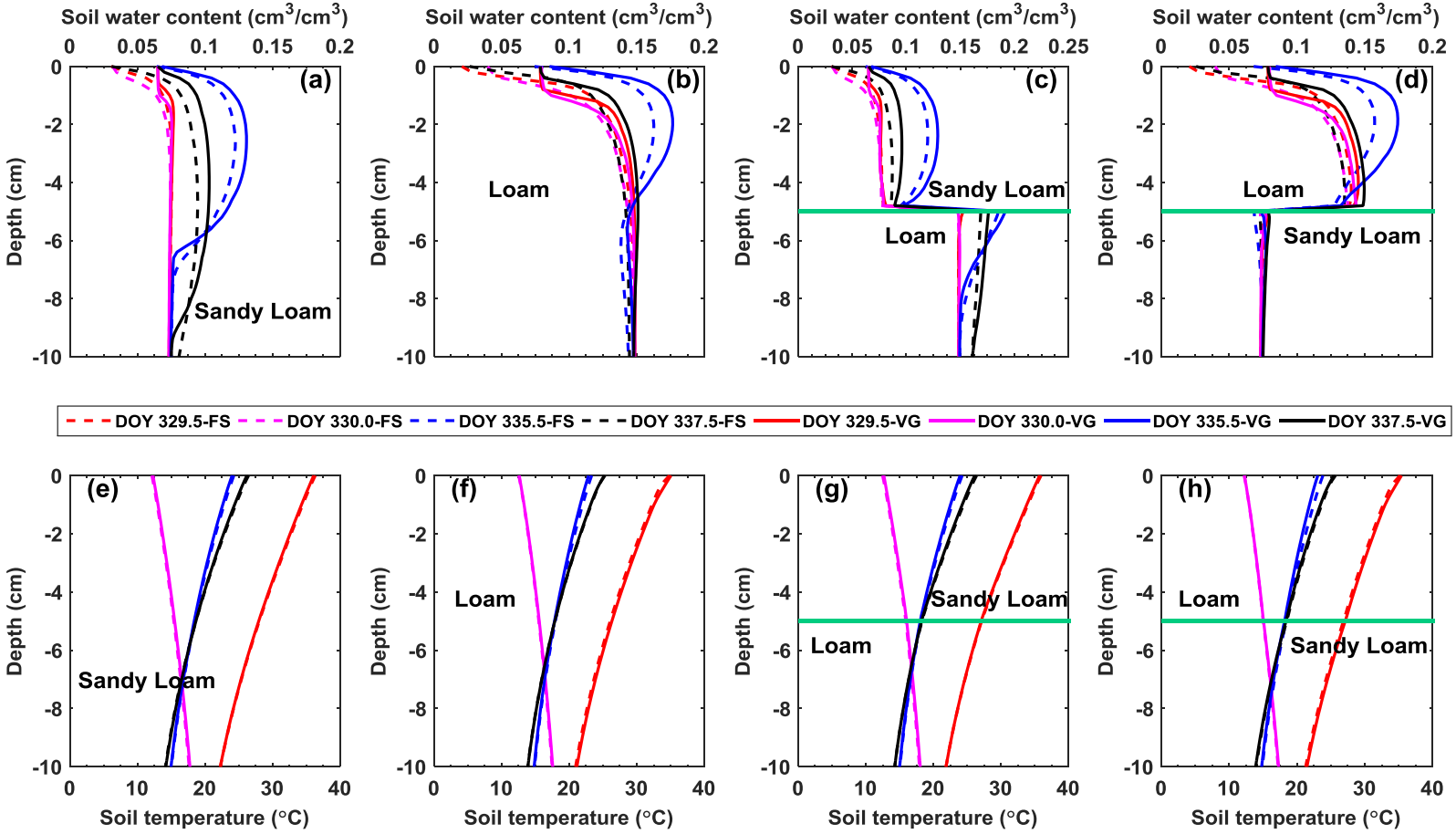

Figure 6.11 Vertical profiles of soil water content (a-d) and soil temperature (e-h) at DOY 329.5, DOY 330.0, DOY 335.5, and DOY 337.5 of case 3 (homogeneous and layered sandy loam and loam) between Fayer and Simmons (FS) and van Genuchten (VG) water retention curve models in the first synthetic simulation. Light irrigation was applied at DOY 334.95-335.00.

soil water content in the underlying sandy loam indicated that the above loam to some extent extracted part of water in the below sandy loam to contribute the evaporation because of the capillary pumping effect in the fine over coarse layered profile. On the other hand, the above sandy loam (coarse) was not able to extract water from underlying loam (fine) to sustain evaporation as Figure 6.11c displayed. The decreasing water content from DOY 335.5 to 337.5 in underlying loam layer was induced by the redistribution and deep infiltration after irrigation but not evaporation water loss (as reflected by the increase of soil water content between 6 cm and 10 cm depth in the underlying loam layer). Therefore, as shown in Figure 6.11c, sandy loam overlying loam (coarse over fine) led to the hydraulic disconnection in the evaporation case.

6.4.1.3.2 Simulated evaporation in case 3

The diurnal evaporation rate and cumulative evaporation of homogeneous sandy loam (a), homogeneous loam (b), layered sandy loam overlying loam (c), and layered loam overlying sandy loam (d) between FS and VG water retention curve models are presented in Figure 6.12 and Figure 6.13, respectively. It was noticed again that the evaporation with FS model is remarkably larger than that with VG model in both two homogeneous and two layered soil profiles. As Table 6.6 and Figure 6.13 indicated, the cumulative evaporation of FS model was found to be 26.6%, 22.2%, 27.0%, 20.0% larger than that of VG model for homogeneous sandy loam (Figure 6.13a), homogeneous loam (Figure 6.13b), sandy loam overlying loam (Figure 6.13c), and loam overlying sandy loam (Figure 6.13d) soil profiles, respectively.

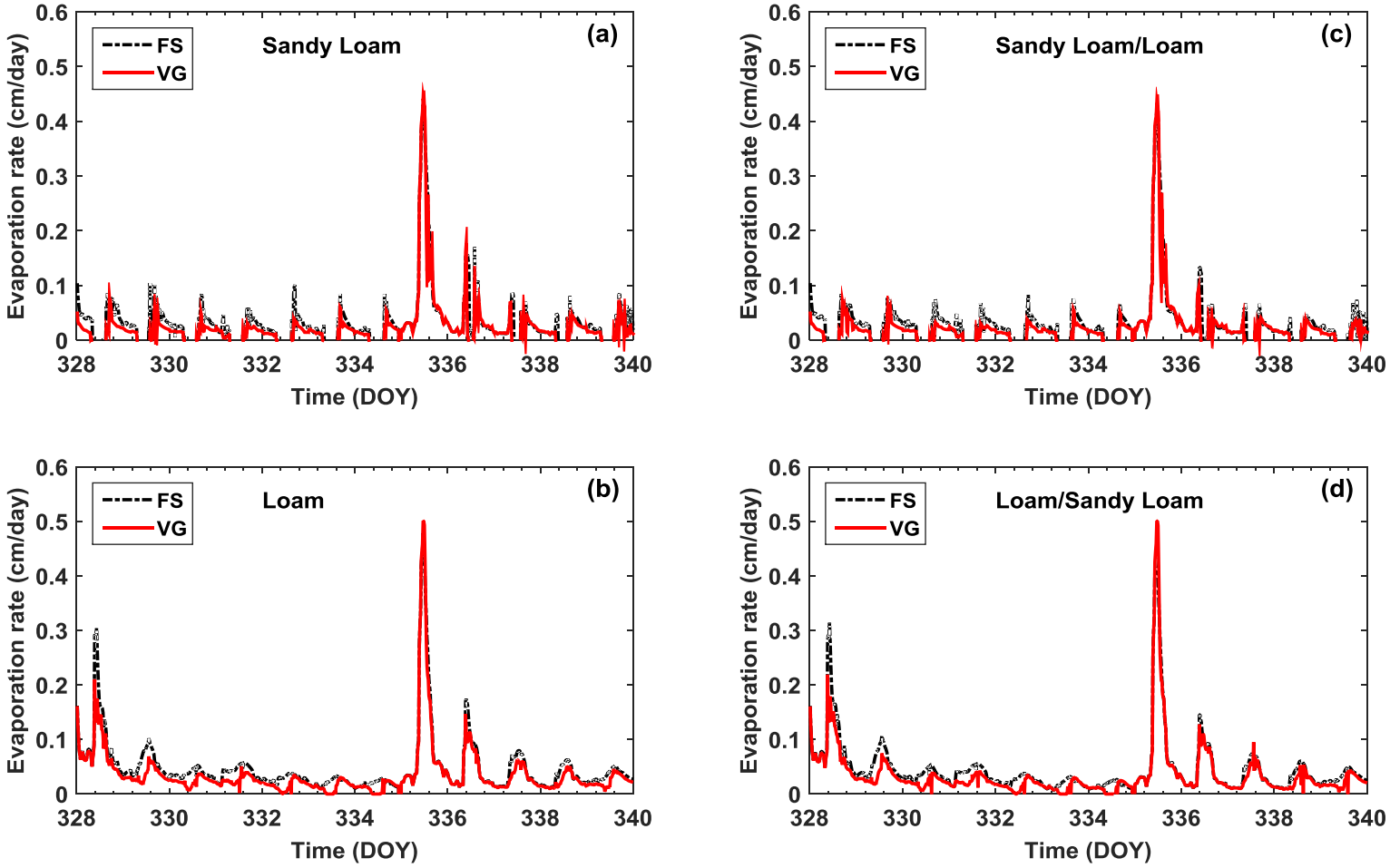

Figure 6.12 Evaporation rate of case 3 homogeneous sandy loam (a), homogeneous loam (b), layered sandy loam overlying loam (c), and layered loam overlying sandy loam (d) between Fayer and Simmons (FS) and van Genuchten (VG) water retention curve models in the first synthetic simulation.

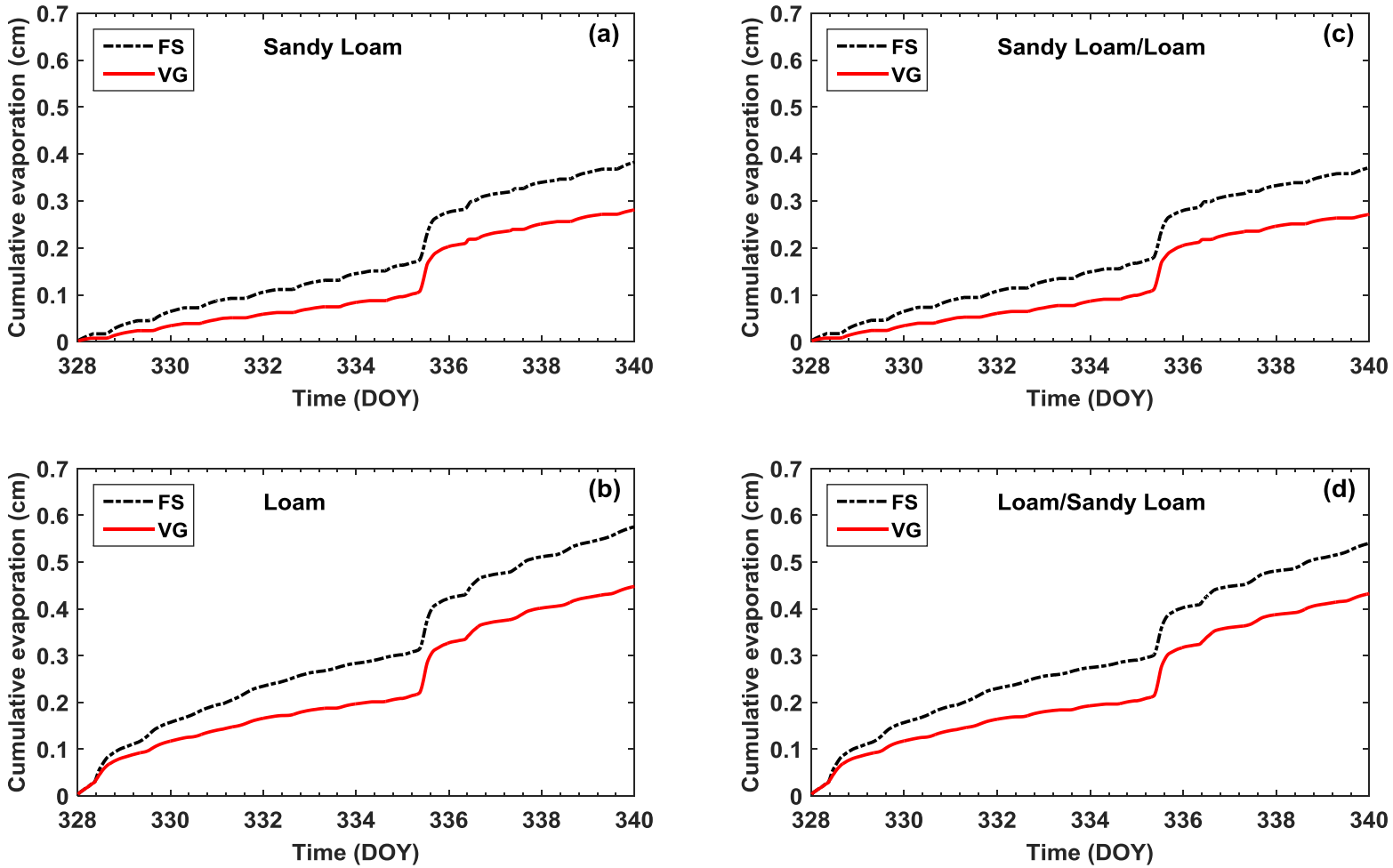

Figure 6.13 Cumulative evaporation of case 3 homogeneous sandy loam (a), homogeneous loam (b), layered sandy loam overlying loam (c), and layered loam overlying sandy loam (d) between Fayer and Simmons (FS) and van Genuchten (VG) water retention curve models in the first synthetic simulation.

From Figure 6.12a and Figure 6.12d, one can notice that the diurnal evaporation rate is increased in loam overlying sandy loam (Figure 6.12d) compared to that of homogeneous sandy loam (Figure 6.12a) due to the capillary pumping effect shown in soil water content vertical profiles. On the other hand, due to hydraulic disconnection, the diurnal evaporation rate is suppressed in sandy loam overlying loam (Figure 6.12c) compared to that of homogeneous loam (Figure 6.12b). In addition, as shown in Table 6.6, compared to homogeneous sandy loam, the cumulative evaporation of loam overlying sandy loam (fine over coarse) is 29.1% and 35.0% larger for FS and VG model, respectively. Furthermore, compared to homogeneous loam, the cumulative evaporation of sandy loam overlying loam (coarse over fine) is 35.6% and 39.5% lower for FS and VG model, respectively.

6.4.2 Second synthetic simulation results

6.4.2.1 Case 1 homogeneous and layered sand and sandy loam results

6.4.2.1.1 Simulated soil water content and temperature in case 1

The simulated vertical profiles of soil water content and soil temperature at DOY 279.5, DOY 280.0, DOY 282.5, and DOY 286.5 between FS and VG water retention curve models for homogeneous sand, homogeneous sandy loam, sand overlying sandy loam and sandy loam overlying sand were displayed in Figure 6.14a-6.14d and Figure 6.14e-6.14h, respectively. It was found that the soil water content modelled by FS model is smaller than that of VG model, whereas the soil temperatures between FS and VG model are almost similar for both homogeneous and layered soil profiles. The presence of the textural contrast in soil profile yielded the discontinuity in soil water content

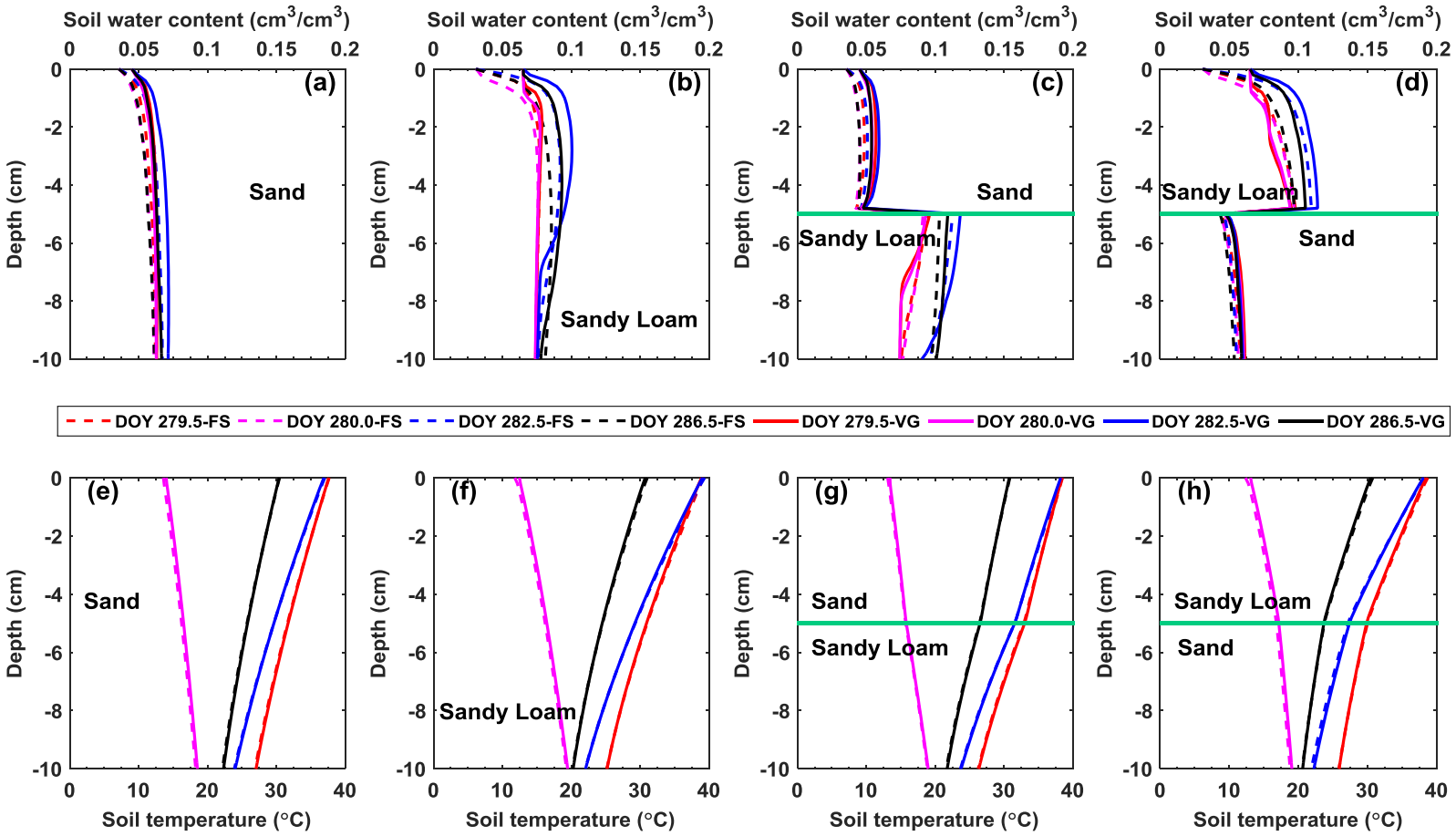

Figure 6.14 Vertical profiles of soil water content (a-d) and soil temperature (e-h) at DOY 279.5, DOY 280.0, DOY 282.5, and DOY 286.5 of case 1 (homogeneous and layered sand and sandy loam) between Fayer and Simmons (FS) and van Genuchten (VG) water retention curve models in the second synthetic simulation. Rainfall was occurred at DOY 280.48-280.50, DOY 280.60-280.65, and DOY 280.65-280.67, respectively.

(Figure 6.14c and 6.14d), but the soil temperature was continuous across the layered interface as Figures 6.14g and 6.14h showed. The temperature profile displayed a clear diurnal variation pattern, reflecting by that soil surface has the highest temperature during daytime (e.g., DOY 279.5, 282.5 and 286.5) and smallest temperature during nighttime (e.g., DOY 280.0). Such diurnal temperature change (Figure 6.14e-6.14h) resulted in corresponding diurnal thermal vapor/liquid fluxes variation which was driven by the temperature gradient. As can be seen from Figure 6.14c, in the sand overlying sandy loam column, the water content in the top sand layer increased only slightly after the precipitation that was concentrated on the daytime of DOY 280. But the water content in the underlying sandy loam layer increased significantly between 5 cm and 9 cm depth that was caused by the infiltration after the precipitation. This is mainly because the sand has a large isothermal hydraulic conductivity after precipitation (hence quick infiltration to the underlying sandy loam). In the reverse case (sandy loam overlying sand column), as Figure 6.14d showed, the rainfall water did not infiltrate to the underlying sand because of the relatively low isothermal hydraulic conductivity of above sandy loam and the overall small rainfall amount. All the rainfall water was retained at the overlying sandy loam, leading to the significant increase of soil water content of the top sandy loam layer. The water content of underlying sand slightly decreased during the whole simulation period. This indicated that the above sandy loam (fine textured soil) can lead to the slight capillary pumping to cause the water loss in the underlying sand (coarse textured soil) to contribute the surface evaporation. On the contrary, Figure 6.14c demonstrated that the overlying sand (coarse textured soil) cannot

cause the capillary pumping to extract water from underlying sandy loam (fine textured soil) to contribute the evaporation. This was further corroborated by the continuous water content increase in the deeper underlying sandy loam (9 cm to 10 cm depth from DOY 282.5 to DOY 286.5), indicating that the rainfall water continued to infiltrate to the deeper sandy loam due to the hydraulic disconnection caused by the above sand (coarse textured soil).

6.4.2.1.2 Simulated evaporation in case 1

Figure 6.15 and Figure 6.16 respectively illustrated the diurnal evaporation rate and cumulative evaporation of homogeneous sand (a), homogeneous sandy loam (b), sand overlying sandy loam (c), and sandy loam overlying sand (d) between FS and VG water retention curve models. It was observed that the evaporation with FS model is greater than that with VG model in all four soil profiles. This can be seen more clearly from the cumulative evaporation results that are shown in Table 6.7 and Figure 6.16. The cumulative evaporation of FS model is 20.9%, 25.6%, 13.7%, 28.8% greater than that of VG model for homogeneous sand (Figure 6.16a), homogeneous sandy loam (Figure 6.16b), sand overlying sandy loam (Figure 6.16c), and sandy loam overlying sand (Figure 6.16d) columns, respectively.

For both sand overlying sandy loam (Figure 6.15c) and sandy loam overlying sand (Figure 6.15d) profiles, the evaporation rate of FS model is generally greater than that of VG model during DOY 278-279 when the soils are continuously drying before precipitation. The rainfall (3.84, 3.84 and 0.96 cm/day) occurring at DOY 280.48-280.50, DOY 280.60-280.65, and DOY 280.65-280.67, respectively, increased the water

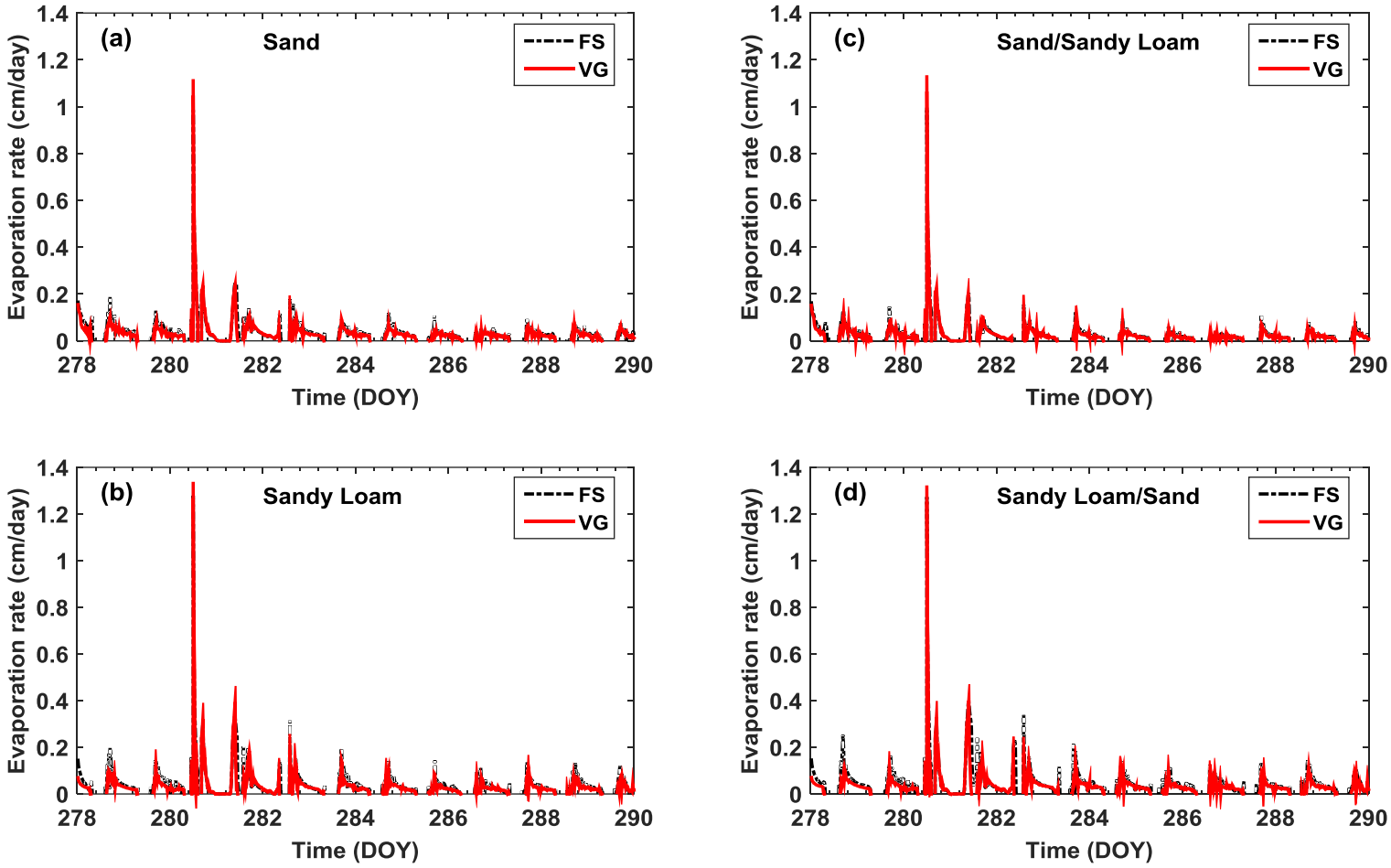

Figure 6.15 Evaporation rate of case 1 homogeneous sand (a), homogeneous sandy loam (b), layered sand overlying sandy loam (c), and layered sandy loam overlying sand (d) between Fayer and Simmons (FS) and van Genuchten (VG) water retention curve models in the second synthetic simulation.

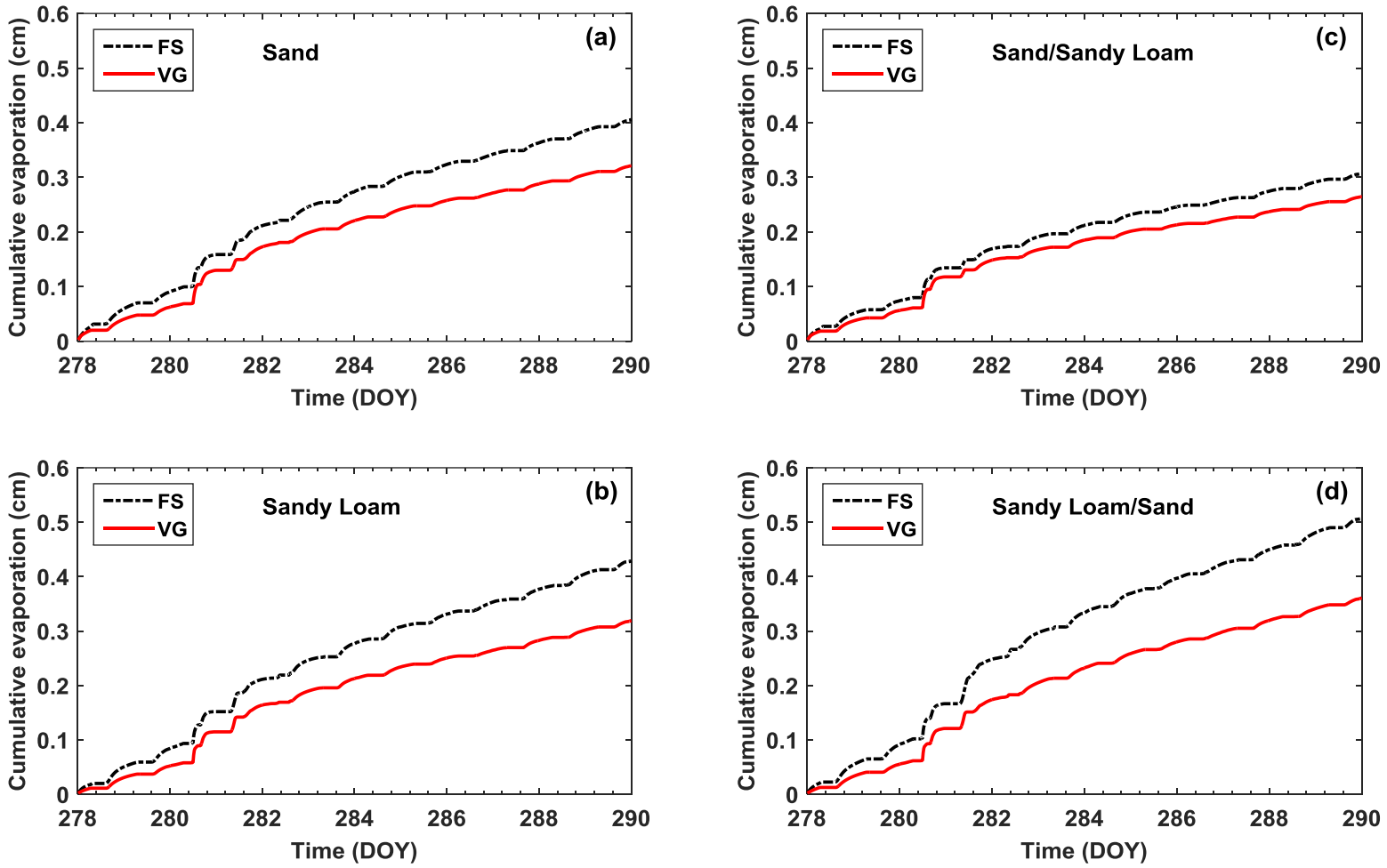

Figure 6.16 Cumulative evaporation of case 1 homogeneous sand (a), homogeneous sandy loam (b), layered sand overlying sandy loam (c), and layered sandy loam overlying sand (d) between Fayer and Simmons (FS) and van Genuchten (VG) water retention curve models in the second synthetic simulation.

Table 6.7 Cumulative evaporation of case 1 in the second synthetic numerical simulations

Cumulative Evaporation (cm)	Sand	Sandy Loam	Sand/Sandy Loam	Sandy Loam/Sand
FS	0.406	0.429	0.307	0.507
VG	0.321	0.319	0.265	0.361

Table 6.8 Cumulative evaporation of case 2 in the second synthetic numerical simulations

Cumulative Evaporation (cm)	Sand	Loam	Sand/Loam	Loam/Sand
FS	0.406	0.602	0.316	0.647
VG	0.321	0.470	0.275	0.486

Table 6.9 Cumulative evaporation of case 3 in the second synthetic numerical simulations

Cumulative Evaporation (cm)	Sandy Loam	Loam	Sandy Loam/Loam	Loam/Sandy Loam
FS	0.429	0.602	0.439	0.567
VG	0.319	0.470	0.327	0.452

content close to the soil surface, which thence significantly increased the evaporation rate at the daytime of DOY 280. Because of the precipitation, the evaporation rate with FS model is very similar to that with VG model during DOY 281-282 for both layered soils. With the continuous drying after rainfall, the evaporation flux with FS model is again greater than that with VG model from DOY 283-290 for both layered columns. In addition, the sandy loam overlying sand (fine over coarse) has the largest cumulative evaporation, whereas sand overlying sandy loam (coarse over fine) has the smallest cumulative evaporation among the four soil columns investigated (Table 6.7). Compared to homogeneous sandy loam, the cumulative evaporation of sand overlying sandy loam (coarse over fine) is 28.4% and 16.9% smaller for FS and VG model, respectively. On the contrary, compared to homogeneous sand, the cumulative evaporation of sandy loam overlying sand (fine over coarse) is 19.9% and 11.1% larger for FS and VG model, respectively.

6.4.2.2 Case 2 homogeneous and layered sand and loam results

6.4.2.2.1 Simulated soil water content and temperature in case 2

The simulated vertical profiles of soil water content and soil temperature at DOY 279.5, DOY 280.0, DOY 282.5, and DOY 286.5 between FS and VG water retention curve models for homogeneous sand, homogeneous loam, sand overlying loam and loam overlying sand were displayed in Figure 6.17a-6.17d and Figure 6.17e-6.17h, respectively. It was again found that the soil water content simulated by FS model is lower than that of VG model, whereas the soil temperatures between FS and VG model are almost the same for both homogeneous and layered profiles. The textural contrast

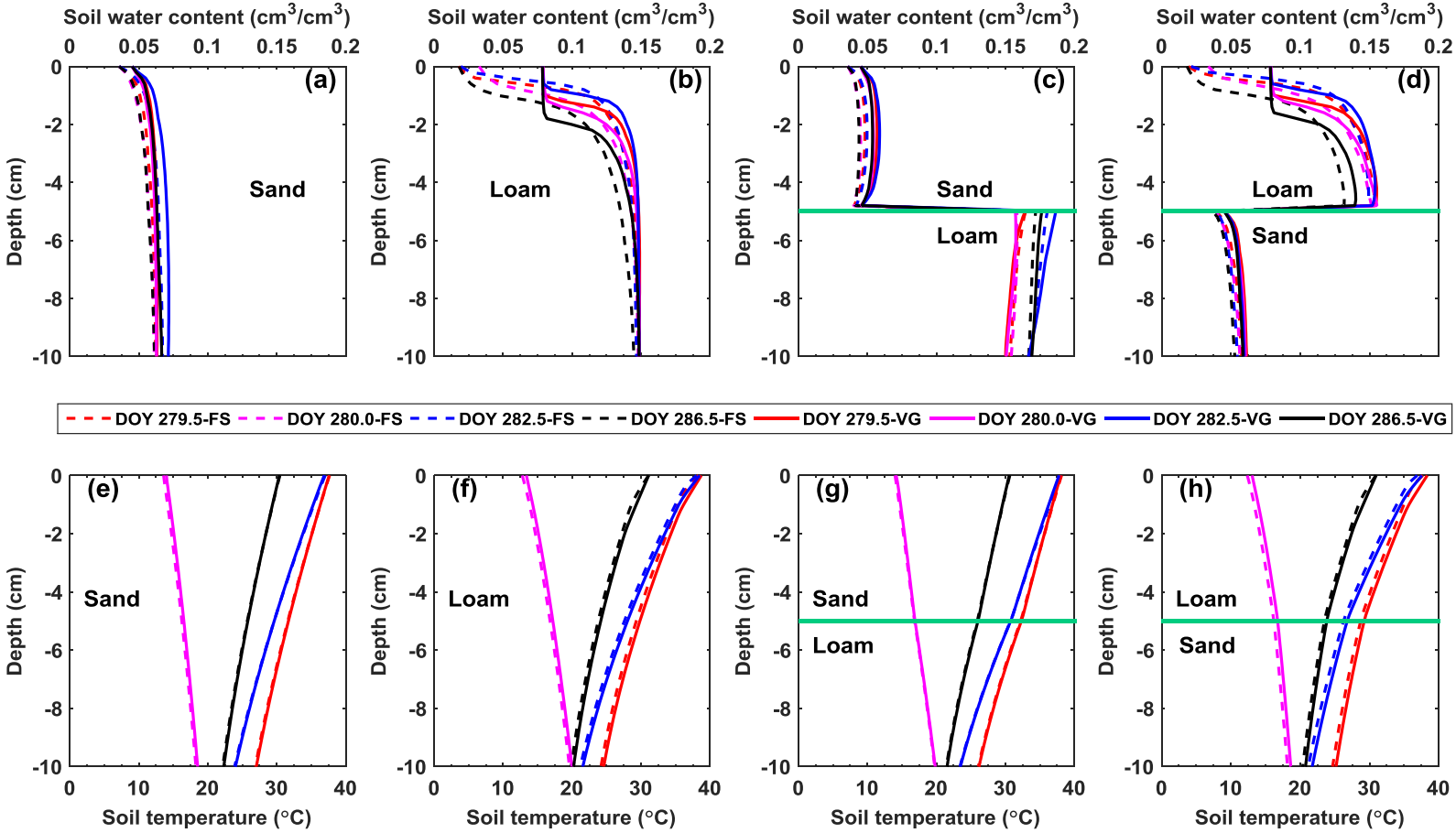

Figure 6.17 Vertical profiles of soil water content (a-d) and soil temperature (e-h) at DOY 279.5, DOY 280.0, DOY 282.5, and DOY 286.5 of case 2 (homogeneous and layered sand and loam) between Fayer and Simmons (FS) and van Genuchten (VG) water retention curve models in the second synthetic simulation. Rainfall was occurred at DOY 280.48-280.50, DOY 280.60-280.65, and DOY 280.65-280.67, respectively.

existing in the soil profile resulted in the discontinuity in the soil water content (Figure 6.17c and 6.17d), the soil temperature, on the other hand, was continuous across the layered interface as Figures 6.17g and 6.17h illustrated. Owing to the overlying sand's very large isothermal hydraulic conductivity after rainfall, the rainfall water would quickly infiltrate to the underlying loam soil and increase the loam's water content remarkably (see Figure 6.17c DOY 282.5). On the contrary, as Figure 6.17d showed, the overlying loam's isothermal hydraulic conductivity was comparatively small even after rainfall, hence, almost all the rainfall water would be kept in the above loam layer and no water infiltrated into the underlying sand layer. In fact, the continuously slightly decreasing soil water content in the underlying sand indicated that the above loam extracted part of water in the below sand layer to sustain the evaporation because of the capillary pumping effect in fine over coarse layered profile. On the other hand, the above sand (coarse) cannot extract water from underlying loam (fine) to sustain evaporation as Figure 6.17c showed. The decreasing water content from DOY 282.5 to 286.5 in underlying loam layer is attributed to the redistribution and deep infiltration after irrigation but not evaporation water loss (as reflected by the increase of soil water content between 9 cm and 10 cm in the underlying loam layer). Therefore, as shown in Figure 6.17c, sand overlying loam (coarse over fine) will lead to the hydraulic disconnection in the evaporation case.

6.4.2.2.2 Simulated evaporation in case 2

The diurnal evaporation rate and cumulative evaporation of homogeneous sand (a), homogeneous loam (b), sand overlying loam (c), and loam overlying sand (d)

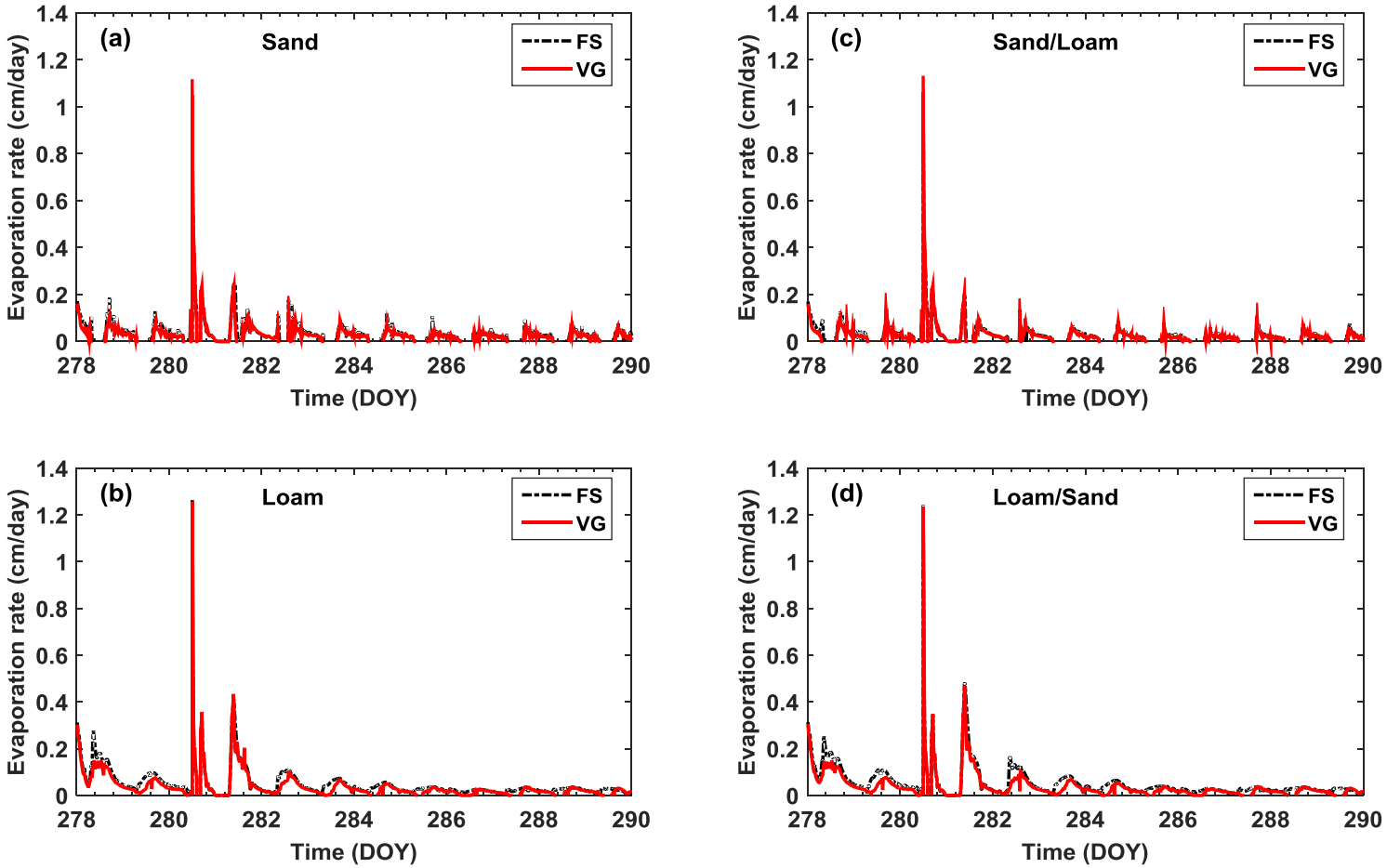

Figure 6.18 Evaporation rate of case 2 homogeneous sand (a), homogeneous loam (b), layered sand overlying loam (c), and layered loam overlying sand (d) between Fayer and Simmons (FS) and van Genuchten (VG) water retention curve models in the second synthetic simulation.

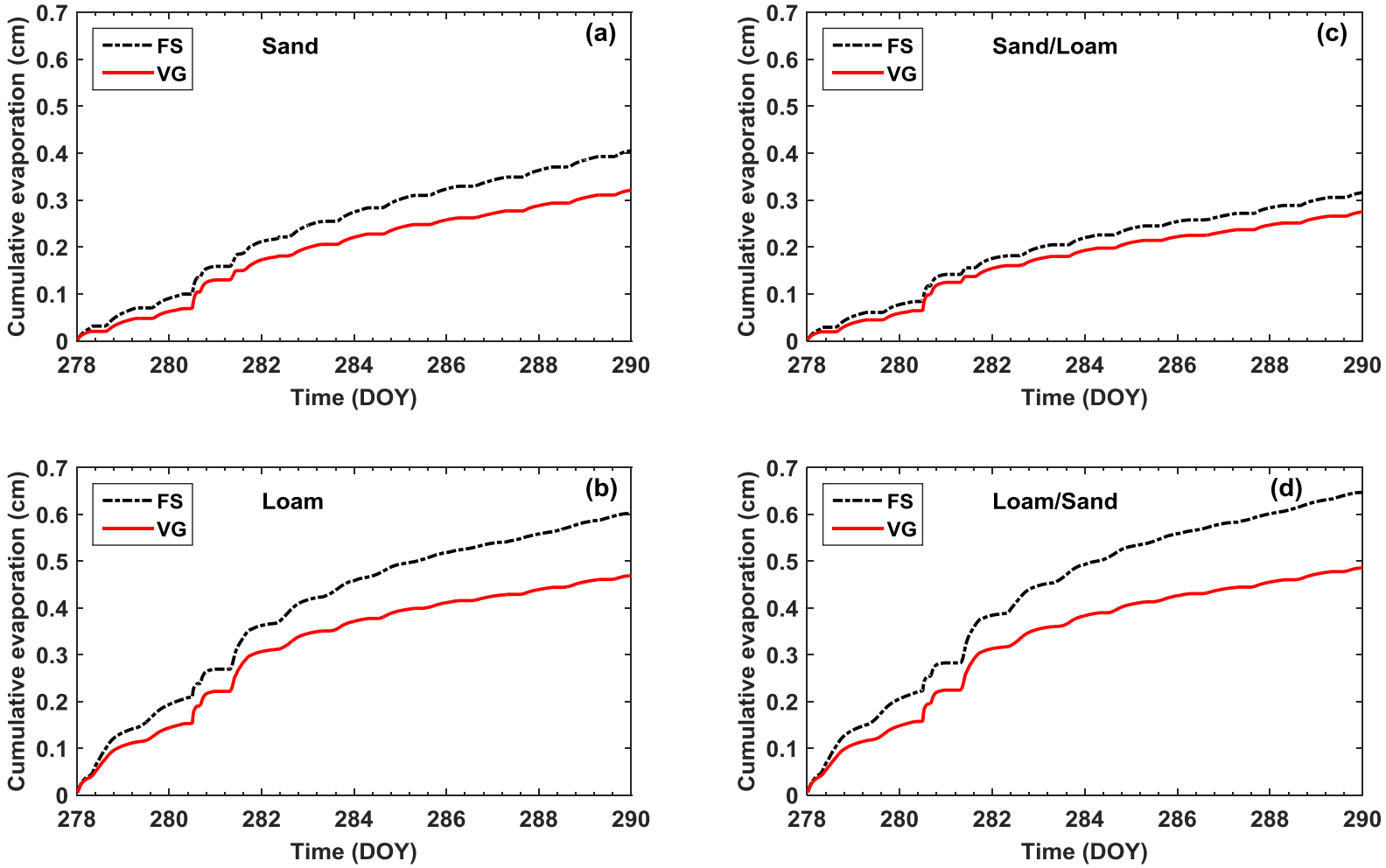

Figure 6.19 Cumulative evaporation of case 2 homogeneous sand (a), homogeneous loam (b), layered sand overlying loam (c), and layered loam overlying sand (d) between Fayer and Simmons (FS) and van Genuchten (VG) water retention curve models in the second synthetic simulation.

between FS and VG water retention curve models are shown in Figure 6.18 and Figure 6.19, respectively. It was observed again that the evaporation with FS model is significantly greater than that with VG model in both two homogeneous and two layered soil profiles. As Table 6.8 and Figure 6.19 showed, the cumulative evaporation of FS model was found to be 20.9%, 21.9%, 13.0%, 24.9% greater than that of VG model for homogeneous sand (Figure 6.19a), homogeneous loam (Figure 6.19b), sand overlying loam (Figure 6.19c), and loam overlying sand (Figure 6.19d) soil profiles, respectively.

From Figure 6.18a and Figure 6.18d, the diurnal evaporation rate is significantly increased in loam overlying sand (Figure 6.18d) compared to that of homogeneous sand (Figure 6.18a). On the other hand, the diurnal evaporation rate is suppressed in sand overlying loam (Figure 6.18c) compared to that of homogeneous loam (Figure 6.18b). Furthermore, the loam overlying sand (fine over coarse) has the largest cumulative evaporation, and sand overlying loam (coarse over fine) has the smallest cumulative evaporation among the four investigated soil columns (Table 6.8). Compared to homogeneous sand, the cumulative evaporation of loam overlying sand (fine over coarse) is 37.2% and 34.0% larger for FS and VG model, respectively. Moreover, compared to homogeneous loam, the cumulative evaporation of sand overlying loam (coarse over fine) is 47.5% and 41.5% lower for FS and VG model, respectively.

6.4.2.3 Case 3 homogeneous and layered sandy loam and loam results

6.4.2.3.1 Simulated soil water content and temperature in case 3

The simulated vertical profiles of soil water content and soil temperature at DOY 279.5, DOY 280.0, DOY 282.5, and DOY 286.5 between FS and VG water retention

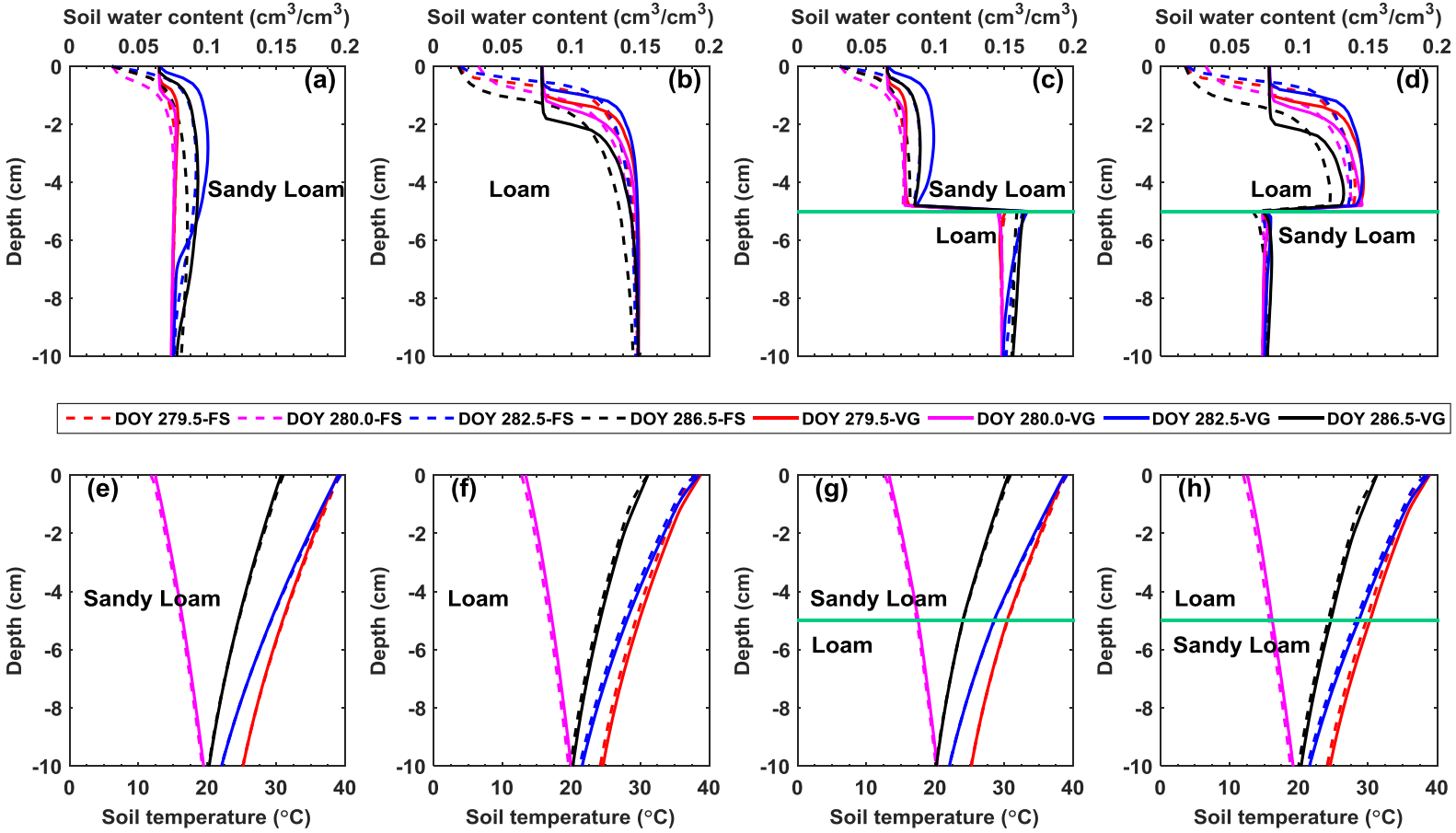

Figure 6.20 Vertical profiles of soil water content (a-d) and soil temperature (e-h) at DOY 279.5, DOY 280.0, DOY 282.5, and DOY 286.5 of case 3 (homogeneous and layered sandy loam and loam) between Fayer and Simmons (FS) and van Genuchten (VG) water retention curve models in the second synthetic simulation. Rainfall was occurred at DOY 280.48-280.50, DOY 280.60-280.65, and DOY 280.65-280.67, respectively.

curve models for homogeneous sandy loam, homogeneous loam, sandy loam overlying loam and loam overlying sandy loam were displayed in Figure 6.20a-6.20d and Figure 6.20e-6.20h, respectively. It was once again found that the soil water content modelled by FS model is significantly smaller than that of VG model, whereas the soil temperatures between FS and VG model are very similar for both homogeneous and layered profiles. The textural contrast existing in the soil profile created the discontinuity in the soil water content (Figure 6.20c and 6.20d), however, the soil temperature was continuous across the layered interface as Figures 6.20g and 6.20h showed. Due to the above sandy loam's comparatively greater isothermal hydraulic conductivity after rainfall, the rainfall water still can infiltrate to the underlying loam soil and increase the underlying loam's water content (Figure 6.20c DOY 282.5). On the contrary, as Figure 6.20d showed, the overlying loam's isothermal hydraulic conductivity was comparatively low even after rainfall, as a result, almost all the irrigated water was retained in the above loam layer and basically no water infiltrated into the underlying sandy loam layer. The progressively slightly decreasing soil water content in the underlying sandy loam indicated that the above loam to some extent extracted part of water in the below sandy loam to contribute the evaporation. On the other hand, the above sandy loam (coarse) was not able to extract water from underlying loam (fine) to sustain evaporation as Figure 6.20c displayed. The decreasing water content from DOY 282.5 to 286.5 in underlying loam layer was induced by the redistribution and deep infiltration after irrigation but not evaporation water loss (as reflected by the increase of soil water content between 6 cm and 10 cm in the underlying loam layer).

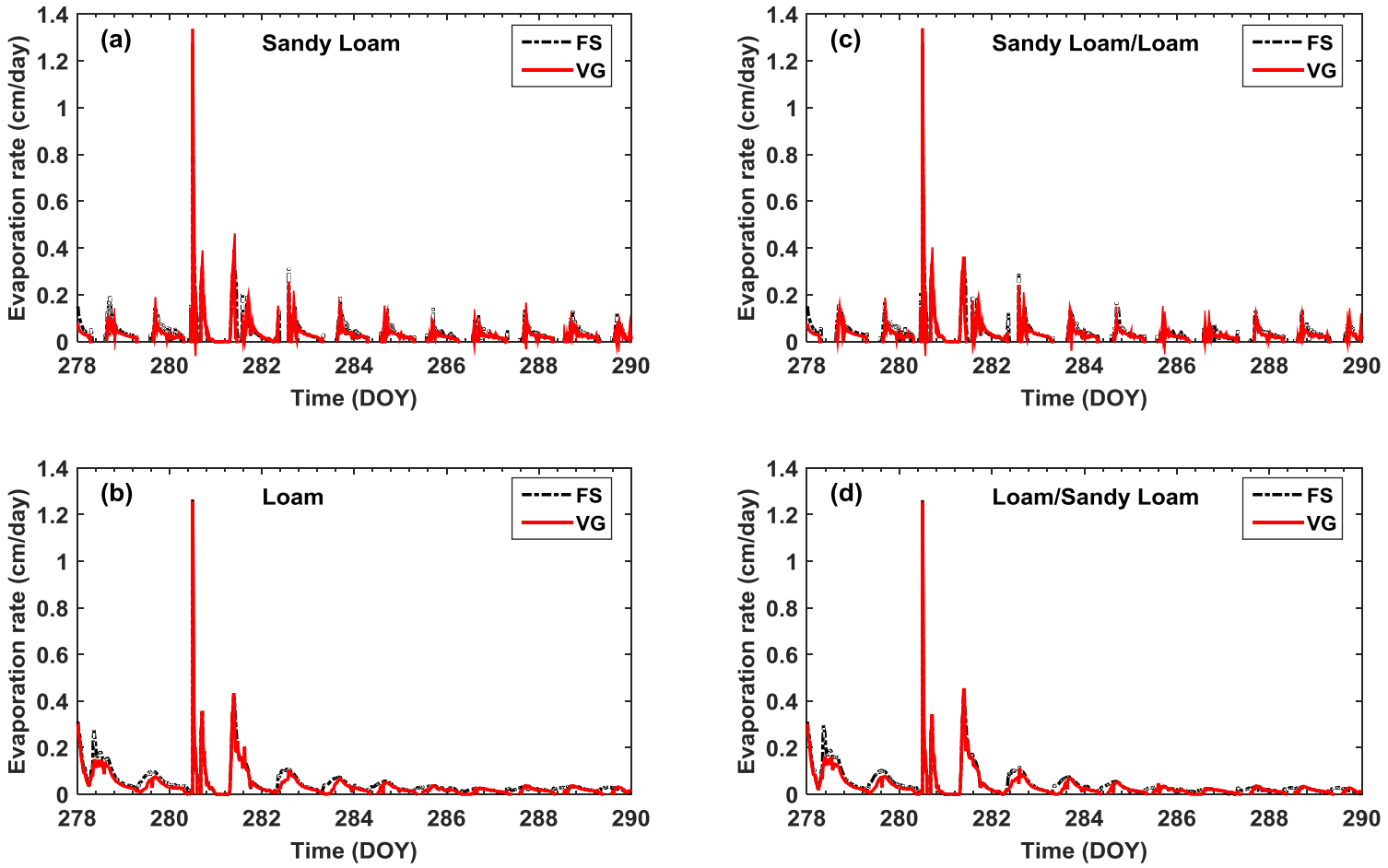

Figure 6.21 Evaporation rate of case 3 homogeneous sandy loam (a), homogeneous loam (b), layered sandy loam overlying loam (c), and layered loam overlying sandy loam (d) between Fayer and Simmons (FS) and van Genuchten (VG) water retention curve models in the second synthetic simulation.

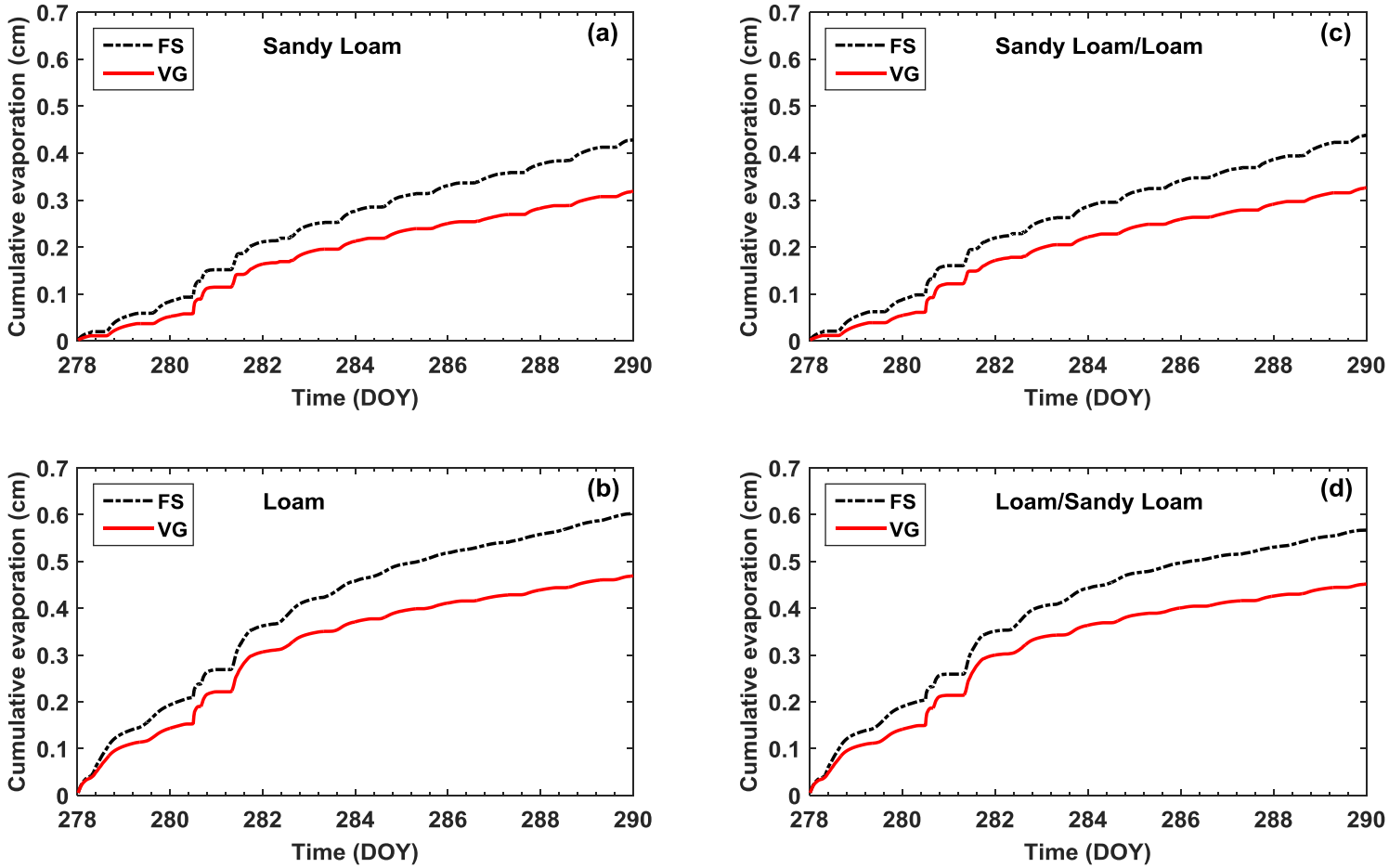

Figure 6.22 Cumulative evaporation of case 3 homogeneous sandy loam (a), homogeneous loam (b), layered sandy loam overlying loam (c), and layered loam overlying sandy loam (d) between Fayer and Simmons (FS) and van Genuchten (VG) water retention curve models in the second synthetic simulation.

6.4.2.3.2 Simulated evaporation in case 3

The diurnal evaporation rate and cumulative evaporation of homogeneous sandy loam (a), homogeneous loam (b), layered sandy loam overlying loam (c), and layered loam overlying sandy loam (d) between FS and VG water retention curve models are presented in Figure 6.21 and Figure 6.22, respectively. It was noticed again that the evaporation with FS model is remarkably larger than that with VG model in both two homogeneous and two layered soil profiles. As Table 6.9 and Figure 6.22 indicated, the cumulative evaporation of FS model was found to be 25.6%, 21.9%, 25.5%, 20.3% larger than that of VG model for homogeneous sandy loam (Figure 6.22a), homogeneous loam (Figure 6.22b), sandy loam overlying loam (Figure 6.22c), and loam overlying sandy loam (Figure 6.22d) soil profiles, respectively.

In addition, as shown in Table 6.9, compared to homogeneous sandy loam, the cumulative evaporation of loam overlying sandy loam (fine over coarse) is 24.3% and 29.4% larger for FS and VG model, respectively. Furthermore, compared to homogeneous loam, the cumulative evaporation of sandy loam overlying loam (coarse over fine) is 27.1% and 30.4% lower for FS and VG model, respectively.

To sum up, the above two synthetic simulation results evidently showed the influence of layering thicknesses, sequences and positions on the overall evaporation dynamics in layered porous media. These findings obtained under diurnal temperature and humidity top boundary condition in this work are consistent with the laboratory experimental results acquired by *Shokri et al.* [2010] and *Huang et al.* [2013] under

single continuous drying top boundary condition and the results of pore network simulation reported by *Pillai et al.* [2009].

6.5 Summary and conclusion

Soil evaporation involves the coupled heat and mass transfer between the shallow subsurface and the atmosphere, and it is a critical hydrological component in arid and semiarid areas. As a land-atmosphere interface process, the physical properties of the surface layer play a significant role in determining the evaporation dynamics. However, compared to large number of researches on evaporation from homogeneous soil profiles, evaporation dynamics in layered porous media remained understudied. Moreover, it is missing so far to investigate the impact of full range water retention curve on evaporation and water redistribution from layered porous media under diurnal temperature fluctuation conditions. To address this unknown issue, two synthetic experiments analysis (reflecting semiarid and arid top boundary conditions) were conducted in this study by means of extending the work of *Yang et al.* [2017a] to the layered soil profiles.

Both two synthetic simulation included the three cases. The first case consisted of sand overlying sandy loam and sandy loam overlying sand, with homogeneous sand and sandy loam as checkup controls. In case 2, sand and loam were considered whereas cases 3 used sandy loam and loam. It was found that when ignoring the adsorptive water retention (van Genuchten function), the resulting simulated soil water content would be greater, and the evaporative flux would be smaller, respectively, compared to that

acquired by full range water retention model (Fayer and Simmons function) for both homogeneous and layered soil profiles in both synthetic simulations.

Moreover, the textural contrast occurring in the soil profile produced the discontinuity in soil water content, but the soil temperature was continuous across the layered interface. The fine over coarse configuration resulted in higher evaporation, whereas coarse over fine profile led to the smaller evaporation among the three cases in both numerical simulations. These results demonstrated the significant effects of layering thicknesses, sequences and positions as well as hydraulic characteristics of each layer (e.g., adsorptive water retention, air-entry value) on the soil water content distribution and overall evaporation dynamics in layered porous media.

The insights obtained from this work are significantly helpful for designing appropriate mulching barriers aimed at reducing evaporative water losses. More importantly, the further consideration of full range water retention curve in the coupled water-vapor-heat modeling can improve the agreements between modelled and observed water content and evaporation for laboratory column experiment [*Huang et al.*, 2013] and field lysimeter experiment [*Dijkema et al.*, 2017].

7 GENERAL CONCLUSIONS

Simultaneous heat and mass transport in the vadose zone is in principle a multiphysics issue that involves hydro-thermal coupling. Addressing this issue appropriately has remarkable influences on a number of soil physical, chemical and biological processes. In particular, diurnal soil evaporation in arid and semiarid areas was closely related to this hydro-thermal multiphysics issue.

The literature review work presented in section 2 indicated that until now it is largely unclear on the transport parameterizations (e.g., relative air permeability) and their associated effects (e.g., extended full range water retention) on coupled heat and water transport modeling under highly transient field conditions. In order to address this limitation, this dissertation attempted to formulate and validate a predictive multiphysics modeling framework with its related improved transport parameterizations for coupled soil heat and water transport in both the homogeneous and heterogeneous shallow subsurface during section 3 to section 6.

In section 3, a generalized relative air permeability model with Kosugi water retention function was derived. The subsequent model and data comparison confirmed that the pore tortuosity and connectivity parameter for water and air relative permeability should be different. With the optimum tortuosity and connectivity for air phase, effective parameterizations of Burdine, Mualem and Alexander and Skaggs models for relative air permeability predictions were proposed.

Section 4 further investigated the predictive ability of ten relative air permeability models (seven of them were derived) by adopting the Assouline et al. water retention function. The model and data comparison showed that the effective parameterizations of Burdine, Mualem and Alexander and Skaggs relative air permeability models proposed in section 3 had the highest accuracy among ten investigated models.

Section 5 explored the influences of full range water retention curve on coupled heat and water transport in homogeneous low permeability soils via two synthetic experiments and two field observed data analysis. It was found that the evaporation rate is significantly underestimated when neglecting adsorptive water retention component in dry soils typically located in arid and semiarid regions. The underprediction of evaporation is mainly induced by isothermal hydraulic conductivity underestimation in the dry range when ignoring adsorptive water retention.

Section 6 studied the effects of full range water retention curve on evaporation and water redistribution from layered low permeability soils. It was concluded that both the layering thickness, sequences and positions and hydraulic characteristics of each textured layer (e.g., adsorptive water retention, air entry value, etc.) all have significant impacts on soil water content distribution and evaporation dynamics in layered porous media. This finding is potentially useful for designing appropriate mulch layer at the vicinity of soil surface aimed at reducing evaporative water losses in arid and semiarid areas.

To sum up, the improved relative air permeability parameterizations obtained with Kosugi and Assouline et al. water retention curve and the better physical understanding of evaporation dynamics using full range water retention for both homogeneous and layered low permeability soils will shed some new insights on coupled heat and water modeling in the vadose zone.

The future work should investigate this hydro-thermal coupling issue in high permeability porous media (structured soils and fractured rocks) because the forced and natural air/vapor convection should be very significant and relevant in such horizontally heterogeneous soil systems.

REFERENCES

Ahrenholz, B., J. Niessner, R. Helmig, and M. Krafczyk (2011), Pore-scale determination of parameters for macroscale modeling of evaporation processes in porous media, *Water Resour. Res.*, *47*, W07543, doi:10.1029/2010WR009519.

Alexander, L., and R. W. Skaggs (1986), Predicting unsaturated hydraulic conductivity from the soil water characteristic, *Trans. Am. Soc. Agric. Engineers*, *29*(1), 176-184.

Andraski, B. J., and E. A. Jacobson (2000), Testing a full-range soil-water retention function in modeling water potential and temperature, *Water Resour. Res.*, *36*(10), 3081-3089, doi:10.1029/2000WR900193.

Assouline, S. (2001), A model for soil relative hydraulic conductivity based on the water retention characteristic curve, *Water Resour. Res.*, *37*(2), 265-271, doi:10.1029/2000WR900254.

Assouline, S., A. Tuli, and J. W. Hopmans (2016), Evaluating the relative air permeability of porous media from their water retention curves, *Water Resour. Res.*, *52*, doi:10.1002/2015WR018286.

Assouline, S., and D. M. Tartakovsky (2001), Unsaturated hydraulic conductivity function based on a soil fragmentation process, *Water Resour. Res.*, *37*(5), 1309-1312, doi:10.1029/2000WR900332.

Assouline, S., and D. Or (2013), Conceptual and parametric representation of soil hydraulic properties: A review, *Vadose Zone J.*, *12*(4), 1-20, doi:10.2136/vzj2013.07.0121.

Assouline, S., D. Tessier, and A. Bruand (1998), A conceptual model of the soil water retention curve, *Water Resour. Res.*, *34*(2), 223-231, doi:10.1029/97WR03039.

Assouline, S., K. Narkis, R. Gherabli, P. Lefort, and M. Prat (2014), Analysis of the impact of surface layer properties on evaporation from porous systems using column experiments and modified definition of characteristic length, *Water Resour. Res.*, *50*, 3933-3955, doi:10.1002/2013WR014489.

Assouline, S., S. W. Tyler, J. S. Selker, I. Lunati, C. W. Higgins, and M. B. Parlange (2013), Evaporation from a shallow water table: Diurnal dynamics of water and heat at the surface of drying sand, *Water Resour. Res.*, *49*, 4022-4034, doi:10.1002/wrcr.20293.

Bachmann, J., R. Horton, T. Ren, and R. R. van der Ploeg (2001), Comparison of the thermal properties of four wettable and four water-repellent soils, *Soil Sci. Soc. Am. J.*, *65*(6), 1675-1679, doi:10.2136/sssaj2001.1675.

Banimahd, S. A., and Sh. Zand-Parsa (2013), Simulation of evaporation, coupled liquid water, water vapor and heat transport through the soil medium, *Agr. Water Manage.*, *130*, 168-177, doi:10.1016/j.agwat.2013.08.022.

Bear, J., J. Bensabat, and A. Nir (1991), Heat and mass transfer in unsaturated porous media at a hot boundary: I. One-dimensional analytical model, *Transp. Porous Media*, *6*(3), 281-298, doi:10.1007/BF00208954.

Bittelli, M., F. Ventura, G. S. Campbell, R. L. Snyder, F. Gallegati, and P. R. Pisa (2008), Coupling of heat, water vapor, and liquid water fluxes to compute evaporation in bare soils, *J. Hydrol.*, *362*(3-4), 191-205, doi:10.1016/j.jhydrol.2008.08.014.

Bixler, N. E. (1985), NORIA – A finite element computer program for analyzing water, vapor, air, and energy transport in porous media, *Report No. SAND84-2057, UC-70*, Sandia National Laboratories, Albuquerque, New Mexico.

Bouyoucos, G. J. (1915), Effect of temperature on movement of water vapor and capillary moisture in soils, *J. Agr. Res.*, *5*, 141-172.

Bowen, R. M. (1982), Compressible porous media models by use of the theory of mixtures, *Int. J. Eng. Sci.*, *20*(6), 697-735, doi:10.1016/0020-7225(82)90082-9.

Braud, I., A. C. Dantas-Antonino, M. Vauclin, J. L. Thony, and P. Ruelle (1995), A simple soil-plant-atmosphere transfer model (SiSPAT) development and field verification, *J. Hydrol.*, *166*(3-4), 213-250, doi:10.1016/0022-1694(94)05085-C.

Brooks, R. H., and A. T. Corey (1964), Hydraulic properties of porous media, *Hydrol. Pap. 3*, pp. 1-27, Colorado State Univ., Fort Collins, Colo.

Brooks, R. H., and A. T. Corey (1966), Properties of porous media affecting fluid flow, *J. Irrig. Drain. Div.*, *92*(IR2), 61-88.

Brubaker, K. L., and D. Entekhabi (1996), Analysis of feedback mechanisms in land-atmosphere interaction, *Water Resour. Res.*, *32*(5), 1343-1357, doi:10.1029/96WR00005.

Brutsaert, W. (1966), Probability laws for pore-size distributions, *Soil Sci.*, *101*(2), 85-92.

Brutsaert, W. (2005), *Hydrology: An Introduction*, Cambridge Univ. Press, Cambridge, U. K.

Burdine, N. T. (1953), Relative permeability calculations from pore size distribution data, *J. Pet. Technol.*, *5*(3), 71-78, doi:10.2118/225-G.

Cahill, A. T. and M. B. Parlange (1998), On water vapor transport in field soils, *Water Resour. Res.*, *34*(4), 731-739, doi:10.1029/97WR03756.

Cahill, A. T., and M. B. Parlange (2000), Reply [to 'Comment on "On water vapor transport in field soils" by Anthony T. Cahill and Marc B. Parlange'], *Water Resour Res*, *36*(10), 3107-3110, doi:10.1029/2000WR900123.

Camillo, P. J., and R. J. Gurney (1986), A resistance parameter for bare-soil evaporation models, *Soil Sci.*, *141*(2), 95-105, doi:10.1097/00010694-198602000-00001.

Campbell, G. S. (1985), *Soil Physics with BASIC*, Elsevier, New York.

Campbell, G. S., and S. Shiozawa (1992), Prediction of hydraulic properties of soils using particle-size distribution and bulk density data, in *Proceedings of the International Workshop on Indirect Methods for Estimating the Hydraulic Properties of Unsaturated Soils*, edited by M. T. van Genuchten, F. J. Leij, and L. J. Lund, pp. 317-328, Univ. of Calif., Riverside.

Campbell, G. S., C. Calissendorff, and J. H. Williams (1991), Probe for measuring soil specific heat using a heat-pulse method, *Soil Sci. Soc. Am. J.*, *55*(1), 291-293, doi:10.2136/sssaj1991.03615995005500010052x.

Carsel, R. F., and R. S. Parrish (1988), Developing joint probability distributions of soil water retention characteristics, *Water Resour. Res.*, *24*(5), 755-769, doi:10.1029/WR024i005p00755.

Cary, J. W. (1964), An evaporation experiment and its irreversible thermodynamics, *Int. J. Heat Mass Transfer*, *7*(5), 531-538, doi:10.1016/0017-9310(64)90050-X.

Cary, J. W. (1965), Water flux in moist soil: Thermal versus suction gradients, *Soil Sci.*, *100*(3), 168-175, doi:10.1097/00010694-196509000-00004.

Cary, J. W. (1966), Soil moisture transport due to thermal gradients: Practical aspects, *Soil Sci. Soc. Am. J.*, *30*(4), 428-433, doi:10.2136/sssaj1966.03615995003000040011x.

Cass, A., G. S. Campbell, and T. L. Jones (1984), Enhancement of thermal water vapor diffusion in soil, *Soil Sci. Soc. Am. J.*, *48*(1), 25-32, doi:10.2136/sssaj1984.03615995004800010005x.

Cassel, D. K., D. R. Nielsen, and J. W. Biggar (1969), Soil-water movement in response to imposed temperature gradients, *Soil Sci. Soc. Am. J.*, *33*(4), 493-500, doi: 10.2136/sssaj1969.03615995003300040007x.

Chen, J., J. W. Hopmans, and M. E. Grismer (1999), Parameter estimation of two-fluid capillary pressure-saturation and permeability functions, *Adv. Water Resour.*, *22*(5), 479-493, doi:10.1016/S0309-1708(98)00025-6.

Childs, S. W., and C. Malstaff. (1982), Heat and mass transfer in unsaturated porous media, *Final Report, PNL-4036*, Batelle Pacific Northwest Laboratories.

Chung, S.-O., and R. Horton (1987), Soil heat and water flow with a partial surface mulch, *Water Resour. Res.*, *23*(12), 2175-2186, doi:10.1029/WR023i012p02175.

Ciocca, F., I. Lunati, and M. B. Parlange (2014), Effects of the water retention curve on evaporation from arid soils, *Geophys. Res. Lett.*, *41*, 3110-3116, doi:10.1002/2014GL059827.

Cohen, Y., and P. A. Ryan (1989), Chemical transport in the top soil zone-the role of moisture and temperature gradients, *J. Hazard. Mater.*, *22*(3), 283-304, doi:10.1016/0304-3894(89)80002-0.

Collis-George, N. (1953), Relationship between air and water permeabilities in porous media, *Soil Sci.*, *76*(4), 239-250.

Corey, A. T. (1954), The interrelation between gas and oil relative permeabilities, *Prod. Mon.*, *19*(1), 38-41.

Davarzani, H., K. Smits, R. M. Tolene, and T. Illangasekare (2014), Study of the effect of wind speed on evaporation from soil through integrated modeling of the atmospheric boundary layer and shallow subsurface, *Water Resour. Res.*, *50*, 661-680, doi:10.1002/2013WR013952.

de Vries, D. A. (1958), Simultaneous transfer of heat and moisture in porous media, *Trans. Am. Geophys. Union*, *39*(5), 909-916, doi:10.1029/TR039i005p00909.

de Vries, D. A. (1963), Thermal properties of soils, in *Physics of Plant Environment*, edited by W. R. van Wijk, pp. 210-235, North-Holland Publ. Co., Amsterdam, Netherlands.

de Vries, D. A. (1987), The theory of heat and moisture transfer in porous media revisited, *Int. J. Heat Mass Transfer*, *30*(7), 1343-1350, doi:10.1016/0017-9310(87)90166-9.

Deb, S. K., M. K. Shukla, and J. G. Mexal (2011a), Numerical modeling of water fluxes in the root zone of a mature pecan orchard, *Soil Sci. Soc. Am. J.*, *75*(5), 1667-1680, doi:10.2136/sssaj2011.0086.

Deb, S. K., M. K. Shukla, P. Sharma, and J. G. Mexal (2011b), Coupled liquid water, water vapor, and heat transport simulations in an unsaturated zone of a sandy loam field, *Soil Sci.*, *176*(8), 387-398, doi:10.1097/SS.0b013e318221f132.

Demond, A. H., and P. V. Roberts (1993), Estimation of two-phase relative permeability relationships for organic liquid contaminants, *Water Resour. Res.*, *29*(4), 1081-1090, doi:10.1029/92WR02987.

Diaz, F., C. C. Jimenez, and M. Tejedor (2005), Influence of the thickness and grain size of tephra mulch on soil water evaporation, *Agric. Water Manage.*, *74*(1), 47-55, doi:10.1016/j.agwat.2004.10.011.

Dijkema, J., J. E. Koonce, R. M. Shillito, T. A. Ghezzehei, M. Berli, M. J. van der Ploeg, and M. Th. van Genuchten (2017), Water distribution in an arid zone soil: numerical analysis of data from a large weighing lysimeter, *Vadose Zone J.*, in press, doi:10.2136/vzj2017.01.0035.

Dury, O. (1997), Organic pollutants in unsaturated soils: Effect of butanol as a model contaminant on phase saturation and flow characteristics of a quartz sand packing, *Ph.D. thesis*, Swiss Fed. Inst. of Technol., Zürich, Switzerland.

Dury, O., U. Fischer, and R. Schulin (1999), A comparison of relative nonwetting-phase permeability models, *Water Resour. Res.*, *35*(5), 1481-1493, doi:10.1029/1999WR900019.

Falta, R. W., I. Javandel, K. Pruess, and P. A. Witherspoon (1989), Density-driven flow of gas in the unsaturated zone due to the evaporation of volatile organic compounds, *Water Resour. Res.*, *25*(10), 2159-2169, doi:10.1029/WR025i010p02159.

Fatt, I., and H. Dykstra (1951), Relative permeability studies, *J. Pet. Technol.*, *3*(9), 249-255, doi:10.2118/951249-G.

Fayer, M. J. (2000), UNSAT-H Version 3.0: Unsaturated soil water and heat flow model-theory, user manual, and examples, *Rep. No. PNNL-13249*, Pacific Northwest National Laboratory, Richland, WA.

Fayer, M. J., and C. S. Simmons (1995), Modified soil water retention functions for all matric suctions, *Water Resour. Res.*, *31*(5), 1233-1238, doi:10.1029/95WR00173.

Fayer, M. J., and T. L. Jones (1990), UNSAT-H Version 2.0: Unsaturated soil water and heat flow model, *Publ. PNL-6779*, Pac. Northwest Lab., Richland, Wash.

Feddes, R. A., P. Kabat, P. J. T. Vanbakel, J. J. B. Bronswijk, and J. Halbertsma (1988), Modelling soil water dynamics in the unsaturated zone-State of the art, *J. Hydrol.*, *100*(1-3), 69-111, doi:10.1016/0022-1694(88)90182-5.

Fetzer, T., J. Vanderborght, K. Mosthaf, K. M. Smits, and R. Helmig (2017), Heat and water transport in soils and across the soil-atmosphere interface: 2. Numerical analysis, *Water Resour. Res.*, *53*, 1080-1100, doi:10.1002/2016WR019983.

Fischer, U., O. Dury, H. Flühler, and M. T. van Genuchten (1997), Modeling nonwetting-phase relative permeability accounting for a discontinuous nonwetting phase, *Soil Sci. Soc. Am. J.*, *61*(5), 1348-1354, doi:10.2136/sssaj1997.03615995006100050009x.

Garcia Gonzalez, R., A. Verhoef, P. Luigi Vidale, and I. Braud (2012), Incorporation of water vapor transfer in the JULES land surface model: Implications for key soil variables and land surface fluxes, *Water Resour. Res.*, *48*, W05538, doi:10.1029/2011WR011811.

Garcia, C. A., B. J. Andraski, D. A. Stonestrom, C. A. Cooper, J. Šimůnek, and S. W. Wheatcraft (2011), Interacting vegetative and thermal contributions to water movement in desert soil, *Vadose Zone J.*, *10*(2), 552-564, doi:10.2136/vzj2010.0023.

Gaudu, R., and G. Bacon (1979), Numerical simulation of heat and mass transfer in unsaturated porous media, *Proc. 1st Int. Conf. Num. Meth. in Thermal Prob.*, Swansea, U.K., pp. 1122-1130.

Gerhard, J. I., and B. H. Kueper (2003), Relative permeability characteristics necessary for simulating DNAPL infiltration, redistribution, and immobilization in saturated porous media, *Water Resour. Res.*, *39*(8), 1213, doi:10.1029/2002WR001490.

Gerke, H. H. (2006), Preferential flow descriptions for structured soils, *J. Plant Nutr. Soil Sci.*, *169*(3), 382-400, doi:10.1002/jpln.200521955.

Ghanbarian-Alavijeh, B., and A. G. Hunt (2012), Comparison of the predictions of universal scaling of the saturation dependence of the air permeability with experiment, *Water Resour. Res.*, *48*, W08513, doi:10.1029/2011WR011758.

Goss, K.-U., and M. Madliger (2007), Estimation of water transport based on in situ measurements of relative humidity and temperature in a dry Tanzanian soil, *Water Resour. Res.*, *43*, W05433, doi:10.1029/2006WR005197.

Gran, M., J. Carrera, S. Olivella, and M. W. Saaltink (2011), Modeling evaporation processes in a saline soil from saturation to oven dry conditions, *Hydrol. Earth Syst. Sci.*, *15*, 2077-2089, doi:10.5194/hess-15-2077-2011.

Gray, W. G., and C. T. Miller (2005), Thermodynamically constrained averaging theory approach for modeling flow and transport phenomena in porous medium systems: 1. Motivation and overview, *Adv. Water Resour.*, *28*(2), 161-180, doi:10.1016/j.advwatres.2004.09.005.

Gray, W. G., C. T. Miller, and B. A. Schrefler (2013), Averaging theory for description of environmental problems: What have we learned?, *Adv. Water Resour.*, *51*, 123-138, doi:10.1016/j.advwatres.2011.12.005.

Grifoll, J. (2013), Contribution of mechanical dispersion of vapor to soil evaporation, *Water Resour. Res.*, *49*, doi:10.1002/wrcr.20105.

Grifoll, J., J. M. Gastó, and Y. Cohen (2005), Non-isothermal soil water transport and evaporation, *Adv. Water Resour.*, *28*(11), 1254-1266, doi:10.1016/j.advwatres.2005.04.008.

Groenevelt, P. H., and B. D. Kay (1974), On the interaction of water and heat transport in frozen and unfrozen soils: II. The liquid phase, *Soil Sci. Soc. Am. J.*, *38*(3), 400-404, doi:10.2136/sssaj1974.03615995003800030012x.

Gurr, C. G., T. J. Marshall, and J. T. Hutton (1952), Movement of water in soil due to a temperature gradient, *Soil Sci.*, *74*(5), 335-345.

Hassanizadeh, S. M., and W. G. Gray (1979a), General conservation equations for multi-phase systems: 1. Averaging procedure, *Adv. Water Resour.*, *2*, 131-144, doi:10.1016/0309-1708(79)90025-3.

Hassanizadeh, S. M., and W. G. Gray (1979b), General conservation equations for multi-phase system: 2. Mass, momenta, energy and entropy equations, *Adv. Water Resour.*, *2*, 191-203, doi:10.1016/0309-1708(79)90035-6.

Hassanizadeh, S. M., and W. G. Gray (1980), General conservation equations for multi-phase system: 3. Constitutive theory for porous media flow, *Adv. Water Resour.*, *3*(1), 25-40, doi:10.1016/0309-1708(80)90016-0.

Hassanizadeh, S. M., and W. G. Gray (1990), Mechanics and thermodynamics of multiphase flow in porous media including interphase boundaries, *Adv. Water Resour.*, *13*(4), 169-186, doi:10.1016/0309-1708(90)90040-B.

Hassanizadeh, S. M., and W. G. Gray (1993a), Toward an improved description of the physics of two-phase flow, *Adv. Water Resour.*, *16*(1), 53-67, doi:10.1016/0309-1708(93)90029-F.

Hassanizadeh, S. M., and W. G. Gray (1993b), Thermodynamic basis of capillary pressure in porous media, *Water Resour. Res.*, *29*(10), 3389-3405, doi:10.1029/93WR01495.

Heitman, J. L., and R. Horton (2011), Coupled heat and water transfer in soil, p. 155-162, In Gliński et al. (ed.), *Encyclopedia of Agrophysics*, Springer, Dordrecht, The Netherlands.

Heitman, J. L., R. Horton, T. J. Sauer, and T. M. DeSutter (2008a), Sensible heat observations reveal soil-water evaporation dynamics, *J. Hydrometeorol.*, *9*, 165-171, doi:10.1175/2007JHM963.1.

Heitman, J. L., R. Horton, T. Ren, I. N. Nassar, and D. D. Davis (2008b), A test of coupled soil heat and water transfer prediction under transient boundary temperatures, *Soil Sci. Soc. Am. J.*, *72*(5), 1197-1207, doi:10.2136/sssaj2007.0234.

Helmig, R. (1997), *Multiphase Flow and Transport Processes in the Subsurface: A Contribution to the Modeling of Hydrosystems*, Springer, New York.

Herkelrath, W. N. (1981), Comment on 'Analysis of water and heat flow in unsaturated-saturated porous media' by Marios Sophocleous, *Water Resour. Res.*, *17*(1), 255, doi:10.1029/WR017i001p00255.

Hilfer, R. (2006), Macroscopic capillarity and hysteresis for flow in porous media, *Phys. Rev. E*, *73*, 016307, doi:10.1103/PhysRevE.73.016307.

Hillel, D. (2004), *Introduction to Environmental Soil Physics*, Elsevier Academic Press, Amsterdam.

Hoffmann-Riem, H., M. T. van Genuchten, and H. Flühler (1999), General model for the hydraulic conductivity of unsaturated soils, in *Proc. Int. Workshop on Characterization and Measurement of the Hydraulic Properties of Unsaturated Porous Media*, edited by M. T. van Genuchten, F. J. Leij, and L. Wu, pp. 31-42, University of California, Riverside, Calif.

Honarpour, M. M., L. Koederitz, and A. H. Harvey (1986), *Relative Permeability of Petroleum Reservoirs*, CRC Press, Boca Raton, Fla.

Hopmans, J. W., J. Šimůnek, and K. L. Bristow (2002), Indirect estimation of soil thermal properties and water flux using heat pulse probe measurements: Geometry and dispersion effects, *Water Resour. Res.*, *38*(1), 1006, doi:10.1029/2000WR000071.

Hou, L., X.-S. Wang, B. X. Hu, J. Shang, and L. Wan (2016), Experimental and numerical investigations of soil water balance at the hinterland of the Badain Jaran Desert for groundwater recharge estimation, *J. Hydrol.*, *540*, 386-396, doi:10.1016/j.jhydrol.2016.06.036.

Huang, M., P. G. Bruch, and S. L. Barbour (2013), Evaporation and water redistribution in layered unsaturated soil profiles, *Vadose Zone J.*, *12*(1), 14 pp., doi:10.2136/vzj2012.0108.

Jackson, A. S., C. T. Miller, and W. G. Gray (2009), Thermodynamically constrained averaging theory approach for modeling flow and transport phenomena in porous medium systems: 6. Two-fluid-phase flow, *Adv. Water Resour.*, *32*(6), 779-795, doi:10.1016/j.advwatres.2008.11.010.

Jackson, R. D. (1973), Diurnal changes in soil water content during drying, in *Field Soil Water Regime*, Spec. Publ., 5, edited by R. R. Bruce et al., Soil Sci. Soc. Am. Proc., pp. 37-55.

Jackson, R. D., R. J. Reginato, B. A. Kimball, and F. S. Nakayama (1974), Diurnal soil-water evaporation: comparison of measured and calculated soil-water fluxes, *Soil Sci. Soc. Am. J.*, *38*(6), 861-866, doi:10.2136/sssaj1974.03615995003800060012x.

Ji, X.B., E.S. Kang, W.Z. Zhao, Z.H. Zhang, and B.W. Jin (2009), Simulation of heat and water transfer in a surface irrigated, cropped sandy soil, *Agric. Water Manage.*, *96*(6), 1010-1020, doi:10.1016/j.agwat.2009.02.008.

Judge, J., L. M. Abriola, and A. W. England (2003), Numerical validation of the land surface process component of an LSP/R model, *Adv. Water Resour.*, *26*(7), 733-746, doi:10.1016/S0309-1708(03)00048-4.

Jury, W. A., and J. Letey (1979), Water vapor movement in soil: Reconciliation of theory and experiment, *Soil Sci. Soc. Am. J.*, *43*(5), 823-827, doi:10.2136/sssaj1979.03615995004300050001x.

Kalaydjian, F. (1987), A macroscopic description of multiphase flow in porous media involving space time evolution of fluid/fluid interface, *Transp. Porous Media*, *2*(6), 537-552, doi:10.1007/BF00192154.

Katata, G., H. Nagai, H. Ueda, N. Agam, and P. R. Berliner (2007), Development of a land surface model including evaporation and adsorption processes in the soil for the land-air exchange in arid regions, *J. Hydrometeorol.*, *8*, 1307-1324, doi:10.1175/2007JHM829.1.

Kay, B. D., and P. H. Groenevelt (1974), On the interaction of water and heat transport in frozen and unfrozen soils: I. Basic theory; The vapor phase, *Soil Sci. Soc. Am. Proc.*, *38*(3), 395-400, doi:10.2136/sssaj1974.03615995003800030011x.

Khaleel, R. (2008), Interfacial area based variable tortuosity-connectivity for unsaturated media: A comparison using Miller-Miller scaling and Arya-Paris model, *Water Resour. Res.*, *44*, W09420, doi:10.1029/2007WR006572.

Khlosi, M., W. M. Cornelis, D. Gabriels, and G. Sin (2006), Simple modification to describe the soil water retention curve between saturation and oven dryness, *Water Resour. Res.*, *42*, W11501, doi:10.1029/2005WR004699.

Köhne, J. M., S. Köhne, and J. Šimůnek (2009), A review of model applications for structured soils: a) Water flow and tracer transport, *J. Contam. Hydrol.*, *104*(1-4), 4-35, doi:10.1016/j.jconhyd.2008.10.002.

Kosugi, K. (1994), Three-parameter lognormal distribution model for soil water retention, *Water Resour. Res.*, *30*(4), 891-901, doi:10.1029/93WR02931.

Kosugi, K. (1996), Lognormal distribution model for unsaturated soil hydraulic properties, *Water Resour. Res.*, *32*(9), 2697-2703, doi:10.1029/96WR01776.

Kosugi, K. (1999), General model for unsaturated hydraulic conductivity for soils with lognormal pore-size distribution, *Soil Sci. Soc. Am. J.*, *63*(2), 270-277, doi:10.2136/sssaj1999.03615995006300020003x.

Kuang, X., and J. J. Jiao (2011), A new model for predicting relative nonwetting phase permeability from soil water retention curves, *Water Resour. Res.*, *47*, W08520, doi:10.1029/2011WR010728.

Kueper, B. H., and E. O. Frind (1991), Two-phase flow in heterogeneous porous media: 1. Model development, *Water Resour. Res.*, *27*(6), 1049-1057, doi:10.1029/91WR00266.

Lebeau, M., and J.-M. Konrad (2010), A new capillary and thin film flow model for predicting the hydraulic conductivity of unsaturated porous media, *Water Resour. Res.*, *46*, W12554, doi:10.1029/2010WR009092.

Lehmann, P., S. Assouline, and D. Or (2008), Characteristic lengths affecting evaporative drying of porous media, *Phys. Rev. E*, *77*(5), 056309, doi:10.1103/PhysRevE.77.056309.

Leij, F. J., W. B. Russell, and S. M. Lesch (1997), Closed-form expressions for water retention and conductivity data, *Ground Water*, *35*(5), 848-858, doi:10.1111/j.1745-6584.1997.tb00153.x.

Levintal, E., M. I. Dragila, T. Kamai, and N. Weisbrod (2017), Free and forced gas convection in highly permeable, dry porous media, *Agric. For. Meteorol., 232*, 469-478, doi:10.1016/j.agrformet.2016.10.001.

Liu, Z., Y. Sun, and X. Yu (2012), Theoretical basis for modeling porous geomaterials under frost actions: a review, *Soil Sci. Soc. Am. J.*, *76*(2), 313-330, doi:10.2136/sssaj2010.0370.

Lu, S., T. Ren, Z. Yu, and R. Horton (2011), A method to estimate the water vapour enhancement factor in soil, *Eur. J. Soil Sci., 62*(4), 498-504, doi:10.1111/j.1365-2389.2011.01359.x.

Luckner, L., M. T. van Genuchten, and D. R. Nielsen (1989), A consistent set of parametric models for the two-phase flow of immiscible fluids in the subsurface, *Water Resour. Res., 25*(10), 2187-2193, doi:10.1029/WR025i010p02187.

Marle, C. M. (1981), From the pore scale to the macroscopic scale: Equations governing multiphase fluid flow through porous media, In *Proceedings of Euromech 143*, 57-61, Delft, Verruijt, A., and F. B. J. Barends (eds.).

Massman, W. J. (2012), Modeling soil heating and moisture transport under extreme conditions: Forest fires and slash pile burns, *Water Resour. Res., 48*, W10548, doi:10.1029/2011WR011710.

Miller, C. T., and W. G. Gray (2005), Thermodynamically constrained averaging theory approach for modeling flow and transport phenomena in porous medium systems: 2. Foundation, *Adv. Water Resour., 28*(2), 181-202, doi:10.1016/j.advwatres.2004.09.006.

Miller, C. T., C. N. Dawson, M. W. Farthing, T. Y. Hou, J. Huang, C. E. Kees, C. T. Kelley, and H. P. Langtangen (2013), Numerical simulation of water resources problems: Models, methods, and trends, *Adv. Water Resour.*, *51*, 405-437, doi:10.1016/j.advwatres.2012.05.008.

Miller, C. T., G. Christakos, P. T. Imhoff, J. F. McBride, J. A. Pedit, and J. A. Trangenstein (1998), Multiphase flow and transport modeling in heterogeneous porous media: challenges and approaches, *Adv. Water Resour.*, *21*(2), 77-120, doi:10.1016/S0309-1708(96)00036-X.

Milly, P. C. D. (1982), Moisture and heat transport in hysteretic, inhomogeneous porous media: A matric head-based formulation and a numerical model, *Water Resour. Res.*, *18*(3), 489-498, doi:10.1029/WR018i003p00489.

Milly, P. C. D. (1984), A linear analysis of thermal effects on evaporation from soil, *Water Resour. Res.*, *20*(8), 1075-1085, doi:10.1029/WR020i008p01075.

Milly, P. C. D. (1988), Advances in modeling of water in the unsaturated zone, *Transp. Porous Media*, *3*(5), 491-514, doi:10.1007/BF00138613.

Modaihsh, A. S., R. Horton, and D. Kirkham (1985), Soil water evaporation suppression by sand mulches, *Soil Sci.*, *139*(4), 357-361, doi:10.1097/00010694-198504000-00010.

Mohanty, B. P., and Z. Yang (2013), Comment on "A simulation analysis of the advective effect on evaporation using a two-phase heat and mass flow model" by Yijian Zeng, Zhongbo Su, Li Wan, and Jun Wen, *Water Resour. Res.*, *49*, 7831-7835, doi:10.1002/2013WR013489.

Mohanty, B. P., P. J. Shouse, and M. T. van Genuchten (1998), Spatio-temporal dynamics of water and heat in a field soil, *Soil Tillage Res.*, *47*(1-2), 133-143, doi:10.1016/S0167-1987(98)00084-1.

Morel-Seytoux, H. J., and J. A. Billica (1985a), A two-phase numerical model for prediction of infiltration: Applications to a semi-infinite soil column, *Water Resour. Res.*, *21*(4), 607-615, doi: 10.1029/WR021i004p00607.

Morel-Seytoux, H. J., and J. A. Billica (1985b), A two-phase numerical model for prediction of infiltration: Case of an impervious bottom, *Water Resour. Res.*, *21*(9), 1389-1396, doi: 10.1029/WR021i009p01389.

Morel-Seytoux, H. J., and J. R. Nimmo (1999), Soil water retention and maximum capillary drive from saturation to oven dryness, *Water Resour. Res.*, *35*(7), 2031-2041, doi:10.1029/1999WR900121.

Mortensen, A. P., J. W. Hopmans, Y. Mori, and J. Šimůnek (2006), Multi-functional heat pulse probe measurements of coupled vadose zone flow and transport, *Adv. Water Resour.*, *29*(2), 250-267, doi:10.1016/j.advwatres.2005.03.017.

Mosthaf, K., K. Baber, B. Flemisch, R. Helmig, A. Leijnse, I. Rybak, and B. Wohlmuth (2011), A coupling concept for two-phase compositional porous-medium and single-phase compositional free flow, *Water Resour. Res.*, *47*, W10522, doi:10.1029/2011WR010685.

Mosthaf, K., R. Helmig, and D. Or (2014), Modeling and analysis of evaporation processes from porous media on the REV scale, *Water Resour. Res.*, *50*, 1059-1079, doi:10.1002/2013WR014442.

Mualem, Y. (1976), A new model for predicting the hydraulic conductivity of unsaturated porous media, *Water Resour. Res.*, *12*(3), 513-522, doi:10.1029/WR012i003p00513.

Mualem, Y., and G. Dagan (1978), Hydraulic conductivity of soils: Unified approach to the statistical models, *Soil Sci. Soc. Am. J.*, *42*(3), 392-395, doi:10.2136/sssaj1978.03615995004200030003x.

Nachshon, U., N. Weisbrod, M. I. Dragila, and A. Grader (2011), Combined evaporation and salt precipitation in homogeneous and heterogeneous porous media, *Water Resour. Res.*, *47*, W03513, doi:10.1029/2010WR009677.

Nassar, I. N., and R. Horton (1989a), Water transport in unsaturated nonisothermal salty soil: I. Experimental results, *Soil Sci. Soc. Am. J.*, *53*(5), 1323-1329, doi:10.2136/sssaj1989.03615995005300050004x.

Nassar, I. N., and R. Horton (1989b), Water transport in unsaturated nonisothermal salty soil: II. Theoretical development, *Soil Sci. Soc. Am. J.*, *53*(5), 1330-1337, doi:10.2136/sssaj1989.03615995005300050005x.

Nassar, I. N., and R. Horton (1992), Simultaneous transfer of heat, water, and solute in porous media: I. Theoretical development, *Soil Sci. Soc. Am. J.*, *56*(5), 1350-1356, doi:10.2136/sssaj1992.03615995005600050004x.

Nassar, I. N., and R. Horton (1997), Heat, water, and solute transfer in unsaturated porous media: I. Theory development and transport coefficient evaluation, *Transp. Porous Media*, *27*(1), 17-38, doi:10.1023/A:1006583918576.

Nassar, I. N., and R. Horton (1999), Transport and fate of volatile organic chemicals in unsaturated, nonisothermal, salty porous media: 1. Theoretical development, *J. Hazard Mater.*, *69*(2), 151-167, doi:10.1016/S0304-3894(99)00099-0.

Nassar, I. N., H. M. Shafey, and R. Horton (1997), Heat, water, and solute transfer in unsaturated porous media: II. Compacted soil beneath plastic cover, *Transp. Porous Media*, *27*(1), 39-55, doi:10.1023/A:1006531901738.

Nassar, I. N., L. Ukrainczyk, and R. Horton (1999), Transport and fate of volatile organic chemicals in unsaturated, nonisothermal, salty porous media: 2. Experimental and numerical studies for benzene, *J. Hazard Mater.*, *69*(2), 169-185, doi:10.1016/S0304-3894(99)00100-4.

Nassar, I. N., R. Horton, and A. M. Globus (1992), Simultaneous transfer of heat, water, and solute in porous media: II. Experiment and analyses, *Soil Sci. Soc. Am. J.*, *56*(5), 1357-1365, doi:10.2136/sssaj1992.03615995005600050005x.

Nasta, P., N. Romano, S. Assouline, J. A. Vrugt, and J. W. Hopmans (2013a), Prediction of spatially variable unsaturated hydraulic conductivity using scaled particle-size distribution functions, *Water Resour. Res.*, *49*, 4219-4229, doi:10.1002/wrcr.20255.

Nasta, P., S. Assouline, J. B. Gates, J. W. Hopmans, and N. Romano (2013b), Prediction of unsaturated relative hydraulic conductivity from Kosugi's water retention function, *Procedia Environ. Sci.*, *19*, 609-617, doi:10.1016/j.proenv.2013.06.069.

Niessner, J. (2009), The role of interfacial area in two-phase flow in porous media-Bridging scales and coupling models-, *Habilitationsschrift*, Universität Stuttgart, Germany.

Niessner, J., and S. M. Hassanizadeh (2008), A model for two-phase flow in porous media including fluid-fluid interfacial area, *Water Resour. Res.*, *44*, W08439, doi:10.1029/2007WR006721.

Niessner, J., and S. M. Hassanizadeh (2009), Non-equilibrium interphase heat and mass transfer during two-phase flow in porous media-Theoretical considerations and modeling, *Adv. Water Resour.*, *32*(12), 1756-1766, doi:10.1016/j.advwatres.2009.09.007.

Nimmo, J. R., and E. E. Miller (1986), The temperature dependence of isothermal moisture vs. potential characteristics of soils, *Soil Sci. Soc. Am. J.*, *50*(5), 1105-1113, doi:10.2136/sssaj1986.03615995005000050004x.

Noborio, K., K. J. McInnes, and J. L. Heilman (1996), Measurements of soil water content, heat capacity, and thermal conductivity with a single TDR probe, *Soil Sci.*, *161*(1), 22-28.

Noborio, K., K. J. McInnes, and J. L. Heilman (1996), Two-dimensional model for water, heat, and solute transport in furrow-irrigated soil: II. Field evaluation, *Soil Sci. Soc. Am. J.*, *60*(4), 1010-1021, doi:10.2136/sssaj1996.03615995006000040008x.

Novak, M. D. (2010), Dynamics of the near-surface evaporation zone and corresponding effects on the surface energy balance of a drying bare soil, *Agric. For. Meteorol.*, *150*(10), 1358-1365, doi:10.1016/j.agrformet.2010.06.005.

Novak, M. D. (2012), Comment on "Evaporation from soils under thermal boundary conditions: Experimental and modeling investigation to compare equilibrium and nonequilibrium based approaches," by Kathleen M. Smits, Abdullah Cihan, Toshihiro Sakaki, and Tissa H. Illangasekare, *Water Resour. Res.*, *48*, W05549, doi:10.1029/2011WR011393.

Novak, M. D. (2016), Importance of soil heating, liquid water loss, and vapor flow enhancement for evaporation, *Water Resour. Res.*, *52*, 8023-8038, doi:10.1002/2016WR018874.

Or, D., and J. M. Wraith (2000), Comment on "On water vapor transport in field soils" by Anthony T. Cahill and Marc B. Parlange, *Water Resour. Res.*, *36*(10), 3103-3105, doi:10.1029/2000WR900124.

Or, D., P. Lehmann, E. Shahraeeni, and N. Shokri (2013), Advances in soil evaporation physics-A review, *Vadose Zone J.*, *12*(4), 16 pp., doi:10.2136/vzj2012.0163.

Parker, J. C., R. J. Lenhard, and T. Kuppusamy (1987), A parametric model for constitutive properties governing multiphase flow in porous media, *Water Resour. Res.*, *23*(4), 618-624, doi:10.1029/WR023i004p00618.

Parlange, M. B., A. T. Cahill, D. R. Nielsen, J. W. Hopmans, and O. Wendroth (1998), Review of heat and water movement in filed soils, *Soil Tillage Res.*, *47*(1-2), 5-10, doi:10.1016/S0167-1987(98)00066-X.

Passerat de Silans, A., L. Bruckler, J. L. Thony, and M. Vauclin (1989), Numerical modeling of coupled heat and water flows during drying in stratified bare soil-comparison with field observation, *J. Hydrol.*, *105*(1-2), 109-138, doi:10.1016/0022-1694(89)90099-1.

Peters, A. (2013), Simple consistent models for water retention and hydraulic conductivity in the complete moisture range, *Water Resour. Res.*, *49*, 6765-6780, doi:10.1002/wrcr.20548.

Peters, A., and W. Durner (2008), A simple model for describing hydraulic conductivity in unsaturated porous media accounting for film and capillary flow, *Water Resour. Res.*, *44*, W11417, doi:10.1029/2008WR007136.

Philip, J. R., and D. A. de Vries (1957), Moisture movement in porous materials under temperature gradients, *Trans. Am. Geophys. Union*, *38*(2), 222-232, doi:10.1029/TR038i002p00222.

Pillai, K. M., M. Prat, and M. Marcoux (2009), A study on slow evaporation of liquids in a dual-porosity porous medium using square network model, *Int. J. Heat Mass Transfer*, *52*(7-8), 1643-1656, doi:10.1016/j.ijheatmasstransfer.2008.10.007.

Pruess, K., and J. S. Y. Wang (2001), Numerical modeling of isothermal and nonisothermal flow in unsaturated fractured rock: A review, in *Flow and Transport Through Unsaturated Fractured Rock*, Geophys. Monogr. Ser., vol. 42, edited by D. D. Evans, T. J. Nicholson, and T. C. Rasmussen, pp. 19-32, AGU, Washington, D. C., doi:10.1029/GM042p0019.

Pruess, K., C. Oldenburg, and G. Moridis (1999), TOUGH2 user's guide, version 2.0, *Rep. LBNL-43134*, Lawrence Berkeley Natl. Lab., Berkeley, Calif.

Prunty, L. (1992), Thermally driven water and octane redistribution in unsaturated, closed soil cells, *Soil Sci. Soc. Am. J.*, *56*(3), 707-714, doi:10.2136/sssaj1992.03615995005600030006x.

Prunty, L. (2002), Soil water heat of transport, *J. Hydrol. Eng.*, *7*(6), 435-440, doi: 10.1061/(ASCE)1084-0699(2002)7:6(435).

Prunty, L. (2003), Soil water retention and conductivity when vapor flow is important, *J. Irrig. Drain. Eng.*, *129*(3), 201-207, doi:10.1061/(ASCE)0733-9437(2003)129:3(201).

Prunty, L. (2009), Soil water thermal liquid diffusivity, *Soil Sci. Soc. Am. J.*, *73*(3), 704-706, doi:10.2136/sssaj2008.0097.

Prunty, L., and R. Horton (1994), Steady-state temperature distribution in nonisothermal, unsaturated closed soil cells, *Soil Sci. Soc. Am. J.*, *58*(5), 1358-1363, doi:10.2136/sssaj1994.03615995005800050011x.

Purcell, W. R. (1949), Capillary pressures-Their measurement using mercury and the calculation of permeability therefrom, *Pet. Trans. AIME*, *186*, 39-48, doi:10.2118/949039-G.

Raats, P. A. C. (1975), Transformations of fluxes and forces describing the simultaneous transport of water and heat in unsaturated porous media, *Water Resour. Res.*, *11*(6), 938-942, doi:10.1029/WR011i006p00938.

Raats, P. A. C. (1992), A superclass of soils, in *Proc. Int. Workshop on Indirect Methods for Estimating the Hydraulic Properties of Unsaturated Soils*, edited by M. T. van Genuchten, F. J. Leij, and L. J. Lund, pp. 45-51, Riverside, CA, 11-13 Oct. 1989, University of California, Riverside, Calif.

Raats, P. A. C. (2001), Developments in soil-water physics since the mid 1960s, *Geoderma*, *100*(3-4), 355-387, doi:10.1016/S0016-7061(01)00028-3.

Reichman, R., S. R. Yates, T. H. Skaggs, and D. E. Rolston (2013a), Effects of soil moisture on the diurnal pattern of pesticide emission: Comparison of simulations with field measurements, *Atmos. Environ.*, *66*, 52-62, doi:10.1016/j.atmosenv.2012.04.047.

Reichman, R., S. R. Yates, T. H. Skaggs, and D. E. Rolston (2013b), Effects of soil moisture on the diurnal pattern of pesticide emission: Numerical simulation and sensitivity analysis, *Atmos. Environ.*, *66*, 41-51, doi:10.1016/j.atmosenv.2012.10.002.

Ren, T., K. Noborio, and R. Horton (1999), Measuring soil water content, electrical conductivity, and thermal properties with a thermo-time domain reflectometry probe, *Soil Sci. Soc. Am. J.*, *63*(3), 450-457, doi:10.2136/sssaj1999.03615995006300030005x.

Robinson, D. A., C. S. Campbell, J. W. Hopmans, B. K. Hornbuckle, S. B. Jones, R. Knight, F. Ogden, J. Selker, and O. Wendroth (2008), Soil moisture measurements for ecological and hydrological watershed-scale observatories: A review, *Vadose Zone J.*, *7*(1), 358-389, doi:10.2136/vzj2007.0143.

Rose, C. W. (1968a), Water transport in soil with a daily temperature wave. I. theory and experiment, *Aust. J. Soil Res.*, *6*(1), 31-44, doi:10.1071/SR9680031.

Rose, C. W. (1968b), Water transport in soil with a daily temperature wave. II. Analysis, *Aust. J. Soil Res.*, *6*(1), 45-57, doi:10.1071/SR9680045.

Ross, P. J., J. Willimas, and K. L. Bristow (1991), Equation for extending water-retention curves to dryness, *Soil Sci. Soc. Am. J.*, *55*(4), 923-927, doi:10.2136/sssaj1991.03615995005500040004x.

Rossi, C., and J. R. Nimmo (1994), Modeling of soil water retention from saturation to oven dryness, *Water Resour. Res.*, *30*(3), 701-708, doi:10.1029/93WR03238.

Rudiyanto, M. Sakai, M. Th. van Genuchten, A. A. Alazba, B. I. Setiawan, and B. Minasny (2015), A complete soil hydraulic model accounting for capillary and adsorptive water retention, capillary and film conductivity, and hysteresis, *Water Resour. Res.*, *51*, 8757-8772, doi:10.1002/2015WR017703.

Saito, H., and J. Šimůnek (2009), Effects of meteorological models on the solution of the surface energy balance and soil temperature variations in bare soils, *J. Hydrol.*, *373*(3-4), 545-561, doi:10.1016/j.jhydrol.2009.05.019.

Saito, H., J. Šimůnek, and B. P. Mohanty (2006), Numerical analysis of coupled water, vapor, and heat transport in the vadose zone, *Vadose Zone J.*, *5*(2), 784-800, doi:10.2136/vzj2006.0007.

Sakai, M., N. Toride, and J. Šimůnek. (2009), Water and vapor movement with condensation and evaporation in a sandy column, *Soil Sci. Soc. Am. J.*, *73*(3), 707-717, doi:10.2136/sssaj2008.0094.

Sakai, M., S. B. Jones, and M. Tuller (2011), Numerical evaluation of subsurface soil water evaporation derived from sensible heat balance, *Water Resour. Res.*, *47*, W02547, doi:10.1029/2010WR009866.

Scanlon, B. R. (1992), Evaluation of liquid and vapor water flow in desert soils based on chlorine 36 and tritium tracers and nonisothermal flow simulations, *Water Resour. Res.*, *28*(1), 285- 297, doi:10.1029/91WR02200.

Scanlon, B. R., and P. C. D. Milly (1994), Water and heat fluxes in desert soils: 2. Numerical simulations, *Water Resour. Res.*, *30*(3), 721-733, doi:10.1029/93WR03252.

Scanlon, B. R., J. P. Nicot, and J. W. Massmann (2002), Soil gas movement in unsaturated systems, in *Soil Physics Companion*, edited by A. W. Warrick, pp. 297-341, CRC Press, Boca Raton, Fla., doi:10.1201/9781420041651.ch8.

Scanlon, B. R., M. Christman, R. C. Reedy, I. Porro, J. Šimůnek, and G. N. Flerchinger (2002), Intercode comparisons for simulating water balance of surficial sediments in semiarid regions, *Water Resour. Res.*, *38*(12), 1323, doi:10.1029/2001WR001233.

Scanlon, B. R., S. W. Tyler, and P. J. Wierenga (1997), Hydrologic issues in arid, unsaturated systems and implications for contaminant transport, *Rev. Geophys.*, *35*(4), 461-490, doi:10.1029/97RG01172.

Schelde, K., A. Thomsen, T. Heidmann, P. Schjønning, and P.-E. Jansson (1998), Diurnal fluctuations of water and heat flows in a bare soil, *Water Resour. Res.*, *34*(11), 2919-2929, doi:10.1029/98WR02225.

Seki, K. (2007), SWRC fit - a nonlinear fitting program with a water retention curve for soils having unimodal and bimodal pore structure, *Hydrol. Earth Syst. Sci. Discuss.*, *4*, 407-437, doi:10.5194/hessd-4-407-2007.

Shahraeeni, E., and D. Or (2012), Pore scale mechanisms for enhanced vapor transport through partially saturated porous media, *Water Resour. Res.*, *48*, W05511, doi:10.1029/2011WR011036.

Shepherd, R., and R. J. Wiltshire (1995), An analytical approach to coupled heat and moisture transport in soil, *Transp. Porous Media*, *20*(3), 281-304, doi:10.1007/BF01073177.

Shokri, N., P. Lehmann, and D. Or (2009), Critical evaluation of enhancement factors for vapor transport through unsaturated porous media, *Water Resour. Res.*, *45*, W10433, doi:10.1029/2009WR007769.

Shokri, N., P. Lehmann, and D. Or (2010), Evaporation from layered porous media, *J. Geophys. Res.*, *115*, B06204, doi:10.1029/2009JB006743.

Sidiropoulos, E., and C. Tzimopoulos (1983), Sensitivity analysis of a coupled heat and mass transfer model in unsaturated porous media, *J. Hydrol.*, *64*(1-4), 281-298, doi:10.1016/0022-1694(83)90073-2.

Silva, O., and J. Grifoll (2007), A soil-water retention function that includes the hyper-dry region through the BET adsorption isotherm, *Water Resour. Res.*, *43*, W11420, doi:10.1029/2006WR005325.

Šimůnek, J., M. Šejna, H. Saito, M. Sakai, and M. T. van Genuchten (2008), The HYDRUS-1D software package for simulating the movement of water, heat, and

multiple solutes in variably saturated media, Version 4.0, *HYDRUS Software Series 3*, Dep. of Environ. Sci., Univ. of Calif. Riverside, Riverside, Calif, USA.

Šimůnek, J., N. J. Jarvis, M. T. van Genuchten, and A. Gärdenäs (2003), Review and comparison of models for describing non-equilibrium and preferential flow and transport in the vadose zone, *J. Hydrol.*, *272*(1-4), 14-35, doi:10.1016/S0022-1694(02)00252-4.

Smits, K. M., A. Cihan, T. Sakaki, and T. H. Illangasekare (2011), Evaporation from soils under thermal boundary conditions: Experimental and modeling investigation to compare equilibrium- and nonequilibrium-based approaches, *Water Resour. Res.*, *47*, W05540, doi:10.1029/2010WR009533.

Smits, K. M., A. Cihan, V. V. Ngo, and T. H. Illangasekare (2012), Reply to comment by Michael D. Novak on "Evaporation from soils under thermal boundary conditions: Experimental and modeling investigation to compare equilibrium and nonequilibrium based approaches", *Water Resour. Res.*, *48*, W05550, doi:10.1029/2011WR011609.

Smits, K. M., T. Sakaki, A. Limsuwat, and T. H. Illangasekare (2010), Thermal conductivity of sands under varying moisture and porosity in drainage-wetting cycles, *Vadose Zone J.*, *9*(1), 172-180, doi:10.2136/vzj2009.0095.

Smits, K. M., T. Sakaki, S. E. Howington, J. F. Peters, and T. H. Illangasekare (2013), Temperature dependence of thermal properties of sands across a wide range of temperatures (30-70ºC), *Vadose Zone J.*, *12*(1), doi:10.2136/vzj2012.0033.

Smits, K. M., V. V. Ngo, A. Cihan, T. Sakaki, and T. H. Illangasekare (2012), An evaluation of models of bare soil evaporation formulated with different land surface boundary conditions and assumptions, *Water Resour. Res.*, *48*, W12526, doi:10.1029/2012WR012113.

Sophocleous, M. (1979), Analysis of water and heat flow in unsaturated-saturated porous media, *Water Resour. Res.*, *15*(5), 1195-1206, doi:10.1029/WR015i005p01195.

Springer, D. S., H. A. Loaiciga, S. J. Cullen, and L. G. Everett (1998), Air permeability of porous materials under controlled laboratory conditions, *Ground Water*, *36*(4), 558-565, doi:10.1111/j.1745-6584.1998.tb02829.x.

Stonestrom, D. A. (1987), Co-determination and comparison of hysteresis-affected, parametric functions of unsaturated flow: Water-content dependence of matric pressure, air-trapping, and fluid permeabilities in a non-swelling soil, *PhD thesis*, Stanford Univ., Stanford, Calif.

Sun, S. F. (1982), Moisture and heat transport in a soil layer forced by atmospheric conditions, *MSc. Thesis*, 72 pp., Univ. of Conn., Storrs, Conn.

Sung, K., C. M. Yavuz, and M. C. Drew (2002), Heat and mass transfer in the vadose zone with plant roots, *J. Contam. Hydrol.*, *57*(1-2), 99-127, doi:10.1016/S0169-7722(01)00212-1.

Szymkiewicz, A., R. Helmig, and H. Kuhnke (2011), Two-phase flow in heterogeneous porous media with non-wetting phase trapping, *Transp. Porous Media*, *86*(1), 27-47, doi:10.1007/s11242-010-9604-x.

Taylor, S. A. and J. W. Cary (1964), Linear equations for the simultaneous flow of matter and energy in a continuous soil system, *Soil Sci. Soc. Am. Proc.*, *28*(2), 167-172, doi:10.2136/sssaj1964.03615995002800020013x.

Taylor, S. A., and L. Cavazza (1954), The movement of soil moisture in response to temperature gradients, *Soil Sci. Soc. Am. Proc.*, *18*(4), 351-358, doi:10.2136/sssaj1954.03615995001800040001x.

Ten Berge, H. F. M., and G. H. Bolt (1988), Coupling between liquid flow and heat flow in porous media: a connection between two classical approaches, *Transp. Porous Media*, *3*(1), 35-49, doi:10.1007/BF00222685.

Thomas, H. R., and M. R. Sansom (1995), Fully coupled analysis of heat, moisture, and air transfer in unsaturated soil, *J. Eng. Mech.*, *121*(3), 392-405, doi:10.1061/(ASCE)0733-9399(1995)121:3(392).

Thompson, S. E., C. J. Harman, A. G. Konings, M. Sivapalan, A. Neal, and P. A. Troch (2011), Comparative hydrology across AmeriFlux sites: The variable roles of climate, vegetation, and groundwater, *Water Resour. Res.*, *47*, W00J07, doi:10.1029/2010WR009797.

Touma, J., and M. Vauclin (1986), Experimental and numerical analysis of two-phase infiltration in a partially saturated soil, *Transp. Porous Media*, *1*(1), 27-55, doi:10.1007/BF01036524.

Trautz, A. C., K. M. Smits, and A. Cihan (2015), Continuum-scale investigation of evaporation from bare soil under different boundary and initial conditions: An

evaluation of nonequilibrium phase change, *Water Resour. Res.*, *51*, 7630-7648, doi:10.1002/2014WR016504.

Tsang, Y. W., J. T. Birkholzer, and S. Mukhopadhyay (2009), Modeling of thermally driven hydrological processes in partially saturated fractured rock, *Rev. Geophys.*, *47*, RG3004, doi:10.1029/2008RG000265.

Tuli, A., and J. W. Hopmans (2004), Effect of degree of fluid saturation on transport coefficient in disturbed soils, *Eur. J. Soil Sci.*, *55*(1), 147-164, doi:10.1046/j.1365-2389.2002.00493.x-i1.

Tuli, A., J. W. Hopmans, D. E. Rolston, and P. Moldrup (2005), Comparison of air and water permeability between disturbed and undisturbed soils, *Soil Sci. Soc. Am. J.*, *69*(5), 1361-1371, doi:10.2136/sssaj2004.0332.

Tuller, M., and D. Or (2001), Hydraulic conductivity of variably saturated porous media: Film and corner flow in angular pore space, *Water Resour. Res.*, *37*(5), 1257-1276, doi:10.1029/2000WR900328.

van de Griend, A. A., and M. Owe (1994), Bare soil surface resistance to evaporation by vapor diffusion under semiarid conditions, *Water Resour. Res.*, *30*(2), 181-188, doi:10.1029/93WR02747.

van Genuchten, M. T. (1980), A closed-form equation for predicting the hydraulic conductivity of unsaturated soils, *Soil Sci. Soc. Am. J.*, *44*(5), 892-898, doi:10.2136/sssaj1980.03615995004400050002x.

Vanderborght, J., A. Graf, C. Steenpass, B. Scharnagl, N. Prolingheuer, M. Herbst, H.-J. Hendricks Franssen and H. Vereecken (2010), Within-field variability of bare

soil evaporation derived from eddy covariance measurements, *Vadose Zone J.*, *9*(4), 943-954, doi:10.2136/vzj2009.0159.

Vanderborght, J., T. Fetzer, K. Mosthaf, K. M. Smits, and R. Helmig (2017), Heat and water transport in soils and across the soil-atmosphere interface: 1. Theory and different model concepts, *Water Resour. Res.*, *53*, 1057-1079, doi:10.1002/2016WR019982.

Wang, Y., J. Ma, Y. Zhang, M. Zhao, and W. M. Edmunds (2013), A new theoretical model accounting for film flow in unsaturated porous media, *Water Resour. Res.*, *49*, 5021-5028, doi:10.1002/wrcr.20390.

Wang, Z., J. Feyen, M. T. van Genuchten, and D. R. Nielsen (1998), Air entrapment effects on infiltration rate and flow instability, *Water Resour. Res.*, *34*(2), 213-222, doi: 10.1029/97WR02804.

Webb, S. W. (2000), A simple extension of two-phase characteristic curves to include the dry region, *Water Resour. Res.*, *36*(6), 1425-1430, doi:10.1029/2000WR900057.

Webb, S. W. (2006), Two-phase gas transport, In*: Ho, C.K., Webb, S.W. (Eds.)*, Gas Transport in Porous Media, Springer Verlag, pp. 55-70.

Webb, S. W., and C. K. Ho (1998), Review of enhanced vapor diffusion in porous media, *Rep. SAND98-1819C*, Sandia Natl. Lab., Albuquerque, N. M.

Weeks, L. V., S. J. Richards, and J. Letey (1968), Water and salt transfer in soil resulting from thermal gradients, *Soil Sci. Soc. Am. Proc.*, *32*(2), 193-197, doi:10.2136/sssaj1968.03615995003200020014x.

Weisbrod, N., and M. I. Dragila (2006), Potential impact of convective fracture venting on salt-crust buildup and ground-water salinization in arid environments, *J. Arid Environ.*, *65*(3), 386-399, doi:10.1016/j.jaridenv.2005.07.011.

Weisbrod, N., M. I. Dragila, U. Nachshon, and M. Pillersdorf (2009), Falling through the cracks: The role of fractures in Earth-atmosphere gas exchange, *Geophys. Res. Lett.*, *36*, L02401, doi:10.1029/2008GL036096.

Westcot, D. W., and P. J. Wierenga (1974), Transfer of heat by conduction and vapor movement in a closed soil system, *Soil Sci. Soc. Am. J.*, *38*(1), 9-14, doi:10.2136/sssaj1974.03615995003800010012x.

Wills, W. O. (1960), Evaporation from layered soils in the presence of a water table, *Soil Sci. Soc. Am. Proc.*, *24*(4), 239-242, doi:10.2136/sssaj1960.03615995002400040009x.

Yakirevich, A., P. Berliner, and S. Sorek (1997), A model for numerical simulating of evaporation from bare saline soil, *Water Resour. Res.*, *33*(5), 1021-1033, doi:10.1029/96WR03684.

Yamanaka, T., M. Inoue, and I. Kaihotsu (2004), Effects of gravel mulch on water vapor transfer above and below the soil surface, *Agric. Water Manage.*, *67*(2), 145-155, doi: 10.1016/j.agwat.2004.01.002.

Yang, Z., and B. P. Mohanty (2015), Effective parameterizations of three nonwetting phase relative permeability models, *Water Resour. Res.*, 51, 6520-6531, doi:10.1002/2014WR016190.

Yang, Z., B. P. Mohanty, Y. Efendiev, and R. F. Sviercoski (2017a), Effects of the full range water retention curve on coupled heat and water transport in the vadose zone, *Water Resour. Res.*, to be submitted.

Yang, Z., B. P. Mohanty, Y. Efendiev, and Z. Sheng (2017b), Prediction of relative air permeability from water retention function based on soil fragmentation process, *Water Resour. Res.*, to be submitted.

Zeng, Y., Z. Su, L. Wan, and J. Wen (2011a), A simulation analysis of the advective effect on evaporation using a two-phase heat and mass flow model, *Water Resour. Res., 47*, W10529, doi:10.1029/2011WR010701.

Zeng, Y., Z. Su, L. Wan, and J. Wen (2011b), Numerical analysis of air-water-heat flow in unsaturated soil: Is it necessary to consider airflow in land surface models?, *J. Geophys. Res., 116*, D20107, doi:10.1029/2011JD015835.

Zeng, Y., Z. Su, L. Wan, Z. Yang, T. Zhang, H. Tian, X. Shi, X. Wang, and W. Cao (2009), Diurnal pattern of the drying front in desert and its application for determining the effective infiltration, *Hydrol. Earth Syst. Sci.*, *13*(6), 703-714, doi:10.5194/hess-13-703-2009.

Zent, A. P., M. H. Hecht, D. R. Cobos, G. S. Campbell, C. S. Campbell, G. Cardell, M. C. Foote, S. E. Wood, and M. Mehta (2009), Thermal and Electrical Conductivity Probe (TECP) for Phoenix, *J. Geophys. Res., 114*, E00A27, doi:10.1029/2007JE003052.

Zent, A. P., M. H. Hecht, D. R. Cobos, S. E. Wood, T. L. Hudson, S. M. Milkovich, L. P. DeFlores, and M. T. Mellon (2010), Initial results from the thermal and

electrical conductivity probe (TECP) on Phoenix, *J. Geophys. Res.*, *115*, E00E14, doi:10.1029/2009JE003420.

Zhang, J., and A. K. Datta (2004), Some considerations in modeling of moisture transport in heating of hygroscopic materials, *Drying Tech.*, *22*(8), 1983-2008, doi:10.1081/DRT-200032740.

Zhang, Z. F. (2011), Soil water retention and relative permeability for conditions from oven-dry to full saturation, *Vadose Zone J.*, *10*(4), 1299-1308, doi:10.2136/vzj2011.0019.

Zhang, Z. F., M. Oostrom, and M. D. White (2016), Relative permeability for multiphase flow for oven-dry to full saturation conditions, *Int. J. Greenhouse Gas Control*, *49*, 259-266, doi:10.1016/j.ijggc.2016.02.029.

Zyvoloski, G. A., B. A. Robinson, Z. V. Dash, and L. L. Trease (1997), Summary of the models and methods for the FEHM application-A finite-element heat- and mass-transfer code, *Rep. LA-13307-MS*, Los Alamos Natl. Lab., Los Alamos, N. M.

APPENDIX A

COMMENT ON "A SIMULATION ANALYSIS OF THE ADVECTIVE EFFECT ON EVAPORATION USING A TWO-PHASE HEAT AND MASS FLOW MODEL" BY ZENG ET AL. [2011][*]

This appendix is a comment paper on the work of *Zeng et al.* [2011a]. It seems that in their work, (1) advective flux on increasing isothermal hydraulic conductivity is overestimated, (2) the effect of rainfall should be emphasized, and (3) soil hydraulic properties should be extended for the full range of saturation.

A1 Introduction

Zeng et al. [2011a] (hereafter referred to as Z11) recently proposed a Representative Elementary Volume (REV) scale two-phase heat and mass flow model and then used the developed model to investigate the usually ignored advective airflow effect on soil evaporation. The proposed model, consisting of balance equations of water (liquid and vapor), dry air, and heat, together with corresponding constitutive equations, is developed mainly on the basis of *Thomas and Sansom*'s [1995] model by additionally accounting for thermal liquid film flow [*Kay and Groenevelt*, 1974; *Milly*, 1982], water vapor dispersion [Z11], dry air diffusion and dispersion [Z11], and heat of wetting [*de Vries*, 1958; *Milly*, 1982]. Subsequently, the model was calibrated using the field measured soil temperature and soil moisture content collected from the Badain Jaran

[*]This appendix is reprinted with permission from "Comment on 'A simulation analysis of the advective effect on evaporation using a two-phase heat and mass flow model' by Yijian Zeng, Zhongbo Su, Li Wan, and Jun Wen" by Mohanty, B. P., and Z. Yang (2013), Water Resour. Res., 49, 7831-7835, doi:10.1002/2013WR013489, Copyright 2013 American Geophysical Union.

Desert, representing an extremely dry climate condition. The simulated soil temperature agreed reasonably well with the measured soil temperature at five depths (Z11, Figure 2), however, this is not the case for soil water content, particularly at depths of 20, 30, and 40cm (Z11, Figure 3). Z11 ascribed the mismatch between simulated and measured soil water content to two possible reasons: one is the likely incorrect assumption of homogeneous soil hydraulic parameters along the 5m simulation soil profile, the other is the possible low sensitivity of soil moisture sensor in measuring water content in extraordinarily dry environment. While we agree with the above two possible explanations, however, to our knowledge, other mechanisms such as adsorption component of the soil water retention which was ignored in Z11 could also be responsible for the mismatch between simulated and measured soil water content in desert soils (discussed later in section A4.1). Z11 then used the calibrated model to study advective airflow effect on evaporation in both low and high permeability soils and found that neglecting soil airflow could result in an underestimation of evaporation by 8.85% and 6.4% in low and high permeability soils, respectively, during the 6 day period. This underestimation error was more significant on the day right after a precipitation event (Z11, Figure 4) because the fine sand was moderately dry (not very dry) after this small rainfall event which occurred at the end of the first day. After systematically analyzing driving forces (soil air pressure gradient, soil matric potential gradient and soil temperature gradient) and conductivity fields (mainly thermal and isothermal hydraulic conductivity), Z11 concluded that the underestimation error of evaporation was mainly caused by underestimation of isothermal hydraulic conductivity

(which we agree with) by neglecting airflow (which we doubt). We commend Z11 for creatively investigating this often neglected advective airflow effect on soil evaporation and finding such insightful phenomena, however, it seems to us that the advective vapor flux on increasing isothermal hydraulic conductivity (hereafter denoted as K_{Lh}) is overestimated in Z11 analysis. In addition, the negligence of rainfall influence on discussing advective airflow effect and the neglect of extending the water retention function and K_{Lh} to oven-dry condition is unwarranted.

A2 Advective flux on increasing isothermal hydraulic conductivity is overestimated

A2.1 Conductivity normalized scale index should have "sign effect"

When defining normalized scale index (NSI) for conductivity (Z11, equation 21), Z11 claimed that "there is no positive or negative sign before the ratio of $\text{Cond}_{\text{no\_air}}$ to Cond_{air} because the conductivity is always positive." In this way, the NSI for conductivity was calculated by ignoring its "sign effect" corresponding to gradient. For instance, in Z11, Figure 7C at hours 0 (midnight) to 8 (early morning), the K_{Lh} with airflow in high permeability soils is very large compared to that without airflow (i.e., the NSI for K_{Lh} is large for this nighttime). However, during this nighttime period, the soil matric potential gradient is downward (Z11, Figure 7A), which means that the isothermal liquid flux (product of soil matric potential gradient and isothermal hydraulic conductivity) is also downward. This indicates that during and after rainfall in the evening, the moisture infiltration and redistribution processes occurred in the soil [*Zeng et al.*, 2009]. This is the reason why the soil moisture content at 10cm depth increased during the nighttime, which reflected the response of soil moisture to the precipitation

event at the end of day 1 [*Zeng et al.*, 2011b]. At hours 8 (early morning) to 18 (late afternoon), the difference of K_{Lh} between with airflow and no airflow is not very significant and the resulting NSI for K_{Lh} should be relatively small for this daytime. However, during this daytime period, the upward soil matric potential gradient results in upward isothermal liquid flux and based on Z11, a little smaller upward isothermal liquid flux with no airflow causes the corresponding underestimation error of evaporation induced by neglecting airflow during the daytime of the second day. Similar pattern could also be found in low permeability soils (Z11, Figure 9). This indicates that the NSI for K_{Lh} should also be averaged separately during the different time within one day (e.g., day/night) corresponding to the direction of hydraulic gradient. As such, it is physically unclear to obtain the conductivity NSI results in Z11 (i.e., NSI for K_{Lh} is 4.3 and 57.2 in the high and low permeability soils, respectively) via averaging for the whole second day. These calculations result in Z11 overestimated the advective airflow effect because the larger K_{Lh} with airflow (i.e., larger NSI for K_{Lh}) during the night used for soil water infiltration or redistribution during and after rainfall is also incorrectly used for soil evaporation during the daytime. In addition, similar to soil temperature gradient NSI calculation in Z11, the NSI for soil matric potential gradient calculation should also be averaged for daytime and nighttime explicitly in order to keep its physical meaning.

A2.2 Downward advective flux is the smallest on day 2

Z11 used the generalized form of Darcy's law in two phase flow theory to calculate advective vapor flux. Neglecting gravitational effect, the advective vapor flux is given by [after Z11]

$$q_v = \rho_v \frac{S_a k_g}{\mu_a} \nabla P_g = \rho_v \frac{\left(1-\frac{\theta}{n}\right) k_g}{\mu_a} \nabla P_g \qquad \text{(A.1)}$$

where q_v is advective vapor flux, ρ_v is density of vapor, $S_a (=1-\theta/n)$ is the degree of air saturation in the soil, θ is soil moisture content, n is porosity, k_g is intrinsic permeability of porous media, μ_a is dynamic viscosity of air, ∇ is gradient operator, and P_g is soil air pressure. Note that the relative air permeability is denoted as $S_a (=1-\theta/n)$ in equation (A.1) according to Z11 which is a linear relationship with soil moisture content for simplicity. Figure 5B in Z11 shows that for low permeability soils, the downward soil air pressure head gradient during day 3 to day 6 is larger than that on day 2, however, the soil moisture content (θ) during the same period (day 3 to day 6) should be smaller than that on day 2 (Z11, Figure 3) because of the soil evaporation. Then according to equation (A.1) shown above, the downward advective vapor flux on day 2 should be much smaller than that during day 3 to day 6. The same is true for high permeability soils. Meanwhile, Z11's logic for how the advective effect works is that the downward advective liquid and vapor fluxes induced by downward soil air pressure gradient during the daytime could moisten the near surface layer and consequently increase K_{Lh}. If airflow is ignored, the absence of such downward advective fluxes will

make the K_{Lh} nearly stable during the day (Z11, paragraph 51). Based on Z11's logic, the advective effect should be more evident during day 3 to day 6 but not day 2 since downward advective vapor fluxes are larger during day 3 to day 6 compared to that on day 2. This means that the underestimation error of evaporation induced by neglecting advective airflow should be larger during day 3 to day 6 and smaller on day 2. However, such reasoning contradicted the results presented in Figure 4 in Z11 which shows that among day 2 to day 6, the underestimation error is most significant on day 2 when the downward advective vapor flux is the smallest. Furthermore, Z11's logic could not explicitly explain the larger K_{Lh} (with airflow) during the nighttime than that during the daytime in both high and low permeability soils (Z11, Figures 7C, 9C). These arguments cast doubts on the advective airflow effect on enhancing isothermal hydraulic conductivity as assumed by Z11 and consequently invalidate Z11's conclusion that "when the soil was very dry (e.g., desert sand) the enhanced vapor transfer induced by the air pressure gradient can increase the hydraulic conductivity tremendously". In the above discussion, the advective liquid flux induced by soil air pressure gradient is ignored mainly because of its small order of magnitude compared to advective vapor flux during the daytime (Z11, Figure 10).

A3 The effect of rainfall should be emphasized

Without emphasizing the rainfall influence, it seems inappropriate to investigate the evaporation underestimation caused by ignoring airflow in Z11's analysis. To our understanding, the key to explain the second day's underestimation error of evaporation induced by ignoring airflow is to interpret why the soil moisture content in the upper soil

layers with airflow is higher than that without airflow during and after the precipitation event occurring at the end of first day (Figure 9 in *Zeng et al.* [2011b]). One of the possible reasons is that the air viscous resistance effect [*Morel-Seytoux and Billica*, 1985a], which is considered in the Z11's proposed two-phase heat and mass flow model through the air balance equation, to some extent retarded the infiltrated water originated from the rainfall to move into the deeper soil layers and thus kept the near-surface soil layers wetter, particularly during the nighttime of the second day. To this end, the larger soil moisture content in the upper soil layers with airflow (corresponding to larger K_{Lh} with airflow) would cause higher soil evaporation during the daytime on day 2. Air compression effects [*Morel-Seytoux and Billica*, 1985b] or air entrapment effects [*Wang et al.*, 1998], which could also result in the retardation of infiltrated water, are less likely in Z11 case due to the relatively open soil column system (no ponding or surface runoff in the soil surface and bottom boundary is also open) where mobile air cannot be confined. As such, the rainfall influence on discussing advective airflow effect should not be ignored in Z11 case. In other words, without this rainfall event, we could expect that during the entire 6 days, the evaporation rate between with-airflow and without-airflow should be the same just as the first day shows. Furthermore, Z11 did not explicitly explain why the evaporation rate is the largest at the end of the first day but not during the daytime of the second day (when soil water content is highest among the 6 days) after the rainfall event. We suggest it is probably related to the upper boundary condition adopted in Z11 work.

A4 Soil hydraulic properties should be extended for the full range saturation

A4.1 Extending soil water retention to account for adsorption forces

Z11 used the classical parametric models of *van Genuchten* [1980]-*Mualem* [1976] (VGM) to calculate isothermal unsaturated hydraulic conductivity K_{Lh}. However, the VGM model is typically applicable in the wet to moderately wet range where water is mainly held by capillary forces and is known to underestimate K_{Lh} under moderately dry and dry conditions where isothermal liquid film flow induced by adsorption forces dominates [*Rossi and Nimmo*, 1994; *Tuller and Or*, 2001]. Therefore, a large number of efforts were made to extend the classical capillary force based water retention curve models [*Brooks and Corey*, 1964; *van Genuchten*, 1980] to include the adsorption forces [*Ross et al.*, 1991; *Campbell and Shiozawa*, 1992; *Rossi and Nimmo*, 1994; *Fayer and Simmons*, 1995; *Morel-Seytoux and Nimmo*, 1999; *Webb*, 2000; *Khlosi et al.*, 2006; *Lebeau and Konrad*, 2010; *Zhang*, 2011] in order that these extended models could be used to appropriately simulate soil water movement particularly under dry conditions. For instance, *Andraski and Jacobson* [2000] incorporated the *Rossi and Nimmo* [1994] full-range water retention function in the UNSAT-H numerical model [*Fayer and Jones*, 1990] to simulate coupled water, heat and vapor transport in a layered Nevada desert soil. They found that Rossi and Nimmo (RN) function could improve prediction of not only water potential in near surface soil layers (particularly under dry conditions) but also temperature throughout the soil profile. Recently, *Sakai et al.* [2009, 2011] also adopted the *Fayer and Simmons* [1995] full-range water retention function in their coupled water and heat modeling.

Table A1 Soil hydraulic property parameters used in the synthetic numerical simulations

Sample	θ_s	$\theta_r(\theta_a)$	α (cm^{-1})	n	K_s (cm d^{-1})
Sand (Z11)[a]	0.382	0.017	0.00236	3.6098	172.8
Sand (This study)[a]	0.382	0.037	0.00236	3.8000	172.8

[a]Z11 corresponded to the van Genuchten-Mualem (VGM) model
[a]This study corresponded to the Fayer and Simmons-Mualem (FSM) model

Similar to the work of *Andraski and Jacobson* [2000] and *Sakai et al.* [2009, 2011], a synthetic coupled water-vapor-heat simulation analysis was conducted to investigate the necessity of adopting full-range water retention function under dry conditions. The soil hydraulic parameters employed for the sand are shown in Table A1, in which Z11 and this study corresponded to VGM model and *Fayer and Simmons* [1995]-*Mualem* [1976] (FSM) model parameterization, respectively. HYDRUS-1D code [*Šimůnek et al.*, 2008] was adopted to implement the synthetic simulation, which is similar to the scenario of *Saito et al.* [2006]. Figure A1(a) shows that the simulated soil water content at 20cm depth with FSM model is smaller than that with VGM model (the same trend for 30 and 40 cm depths, results not shown). This indicated that if such full-range water retention function was also used in Z11 simulation, the overestimation of simulated soil water content (compared to the measured ones) at 20, 30 and 40 cm depths would probably be reduced. Figure A1(b) displays that the evaporation rate with FSM model is typically larger than that with VGM model during the daytime of Day of the Year (DOY) 328-DOY 334 when the soil is continuously dry. The assumed rainfall occurred at the beginning of DOY 335 effectively increased the soil water content and

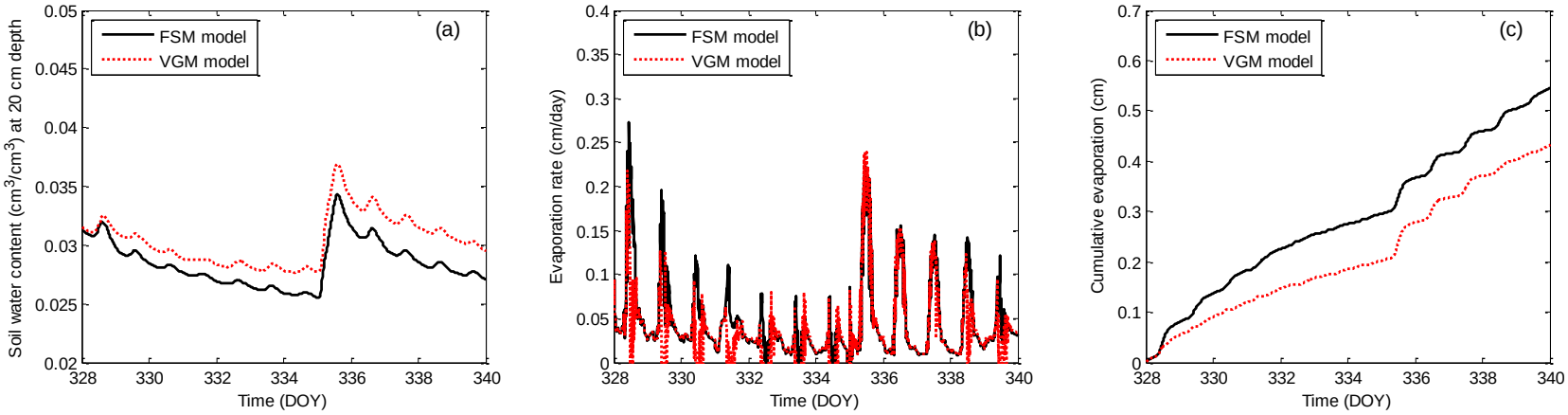

Figure A1 (a) Soil water content at 20cm depth (b) evaporation rate (c) cumulative evaporation between Fayer and Simmons-Mualem (FSM) and van Genuchten-Mualem (VGM) model during the simulation time period (Day of the Year [DOY] 328-DOY 340).

consequently enhanced the evaporation rate at the daytime of DOY 335. However, due to this rainfall event, the evaporation rate with FSM model is very similar to that with VGM model during DOY 335-DOY 337 when the soil is not very dry. With the further drying of the soil, the evaporation rate with FSM model is again larger than that with VGM model during DOY 338-DOY 340. Figure A1(c) shows that during the whole simulation period (DOY 328-DOY 340), the cumulative evaporation with FSM model (0.544 cm) is larger than that with VGM model (0.432 cm). Figures A1(b) and A1(c) indicated that without accounting for adsorption component in the soil water retention curve, the evaporation would be underestimated under dry soil conditions. This synthetic simulation results suggest that in Z11 case, although on day 2 (right after the rainfall) when the soil is not very dry, accounting for adsorption component in the soil water retention curve is probably not highly significant, however, employing full range water retention function is still important for a relatively complete investigation of evaporation underestimation mechanisms in Z11, particularly for day 1 and day 3 to day 6 when the soil is dry.

A4.2 Extending soil hydraulic conductivity to account for film flow

Meanwhile, extending the capillary flow based relative hydraulic conductivity model [e.g., *Mualem*, 1976] to include isothermal film flow could be found in the work of *Peters and Durner* [2008], *Lebeau and Konrad* [2010], and *Zhang* [2011]. *Peters and Durner* [2008] simulated an isothermal evaporation scenario and found that the evaporation rate could be underestimated by more than an order of magnitude by neglecting film flow in the hydraulic conductivity model. Similar results also could be

found in *Vanderborght et al.*'s [2010] work. Furthermore, the field experimental results in a dry Tanzanian soil by *Goss and Madliger* [2007] also indicated that the evaporation rate would be underestimated due to the underestimation of hydraulic conductivity coefficients caused by neglecting adsorbed water films. Although including isothermal film flow would not induce significant improvement in soil hydraulic conductivity calculation as long as the soil water retention is already extended to oven-dry condition (Figure 16 and Table 4 in *Lebeau and Konrad* [2010]), however, for a comparatively complete investigation of the full-range soil hydraulic conductivity parameterization effect on the soil evaporation, it seems still necessary to extend the soil hydraulic conductivity model to include the isothermal film flow processes in Z11 case, particularly for those days when the soil is so dry that the K_{Lh} calculated by VGM model almost approaches zero (Z11, paragraph 49).

Given the importance of employing full range saturation soil hydraulic properties when simulating coupled water and heat transfer under low soil water content environments such as desert [*Scanlon et al.*, 1997] or after forest fires [*Massman*, 2012], it is suggested that accounting for adsorption force in water retention curve and isothermal film flow in soil hydraulic conductivity probably should not be neglected in Z11 case. *Smits et al.* [2012] were perhaps the first to take into account full range saturation parameterization of both water retention function and unsaturated hydraulic conductivity in the coupled water-air-heat numerical simulation.

A5 Conclusion

In summary, the work presented by Z11 is undoubtedly challenging and intriguing. Whether the enhanced vapor transfer induced by soil air pressure gradient is important or not is still not conclusive. For example, *Rose* [1968] found that the advective vapor flow caused by air pressure gradient only accounted for 0.1% of the total vapor flux under his experimental condition. In Z11's analysis, the authors concluded that the enhanced vapor transfer caused by the downward air pressure gradient could increase isothermal hydraulic conductivity remarkably and thus indirectly leads to the high upward isothermal liquid flux, which will contribute to soil evaporation during the daytime. However, the above discussions indicated that Z11 probably overestimates the advective vapor flux capability on increasing isothermal hydraulic conductivity. Under Z11's unique field experimental condition, the rainfall influence on the advective airflow effect should not be ignored. The infiltrated water originated from the precipitation could probably be retarded by the air viscous resistance effects and this resulted in the higher soil water content in the upper soil layers with airflow during the whole second day, which consequently caused the larger soil evaporation rate with the airflow model. Furthermore, negligence of accounting for adsorptive component of soil water retention and isothermal film flow of unsaturated hydraulic conductivity renders the Z11's analysis incomplete given the overall dry soil condition in Z11.

APPENDIX B

DERIVATION OF THE GENERALIZED NPRP FORMULATION WITH KOSUGI WRF

Due to $\int_{S_e}^{1} \frac{dS_e}{h^\beta} = \int_0^1 \frac{dS_e}{h^\beta} - \int_0^{S_e} \frac{dS_e}{h^\beta}$ (B.1)

Substituting equation (3.3) into $\int_0^{S_e} \frac{dS_e}{h^\beta}$ leads to the integrals

$$\int_0^{S_e} \frac{dS_e}{h^\beta} = \frac{1}{\sqrt{2\pi}\sigma} \int_{h(S_e)}^{+\infty} \frac{1}{h^{\beta+1}} e^{-\frac{(\ln h - \ln h_m)^2}{2\sigma^2}} dh \quad \text{(B.2)}$$

The change of variables $t = \ln h - \ln h_m = \ln(h/h_m)$ yields

$$\int_0^{S_e} \frac{dS_e}{h^\beta} = \frac{e^{\frac{1}{2}\beta^2\sigma^2}}{(h_m)^\beta} \frac{1}{\sqrt{2\pi}} \int_{\frac{\ln(h/h_m)}{\sigma}+\beta\sigma}^{+\infty} e^{-\frac{1}{2}\left(\frac{t}{\sigma}+\beta\sigma\right)^2} d\left(\frac{t}{\sigma}+\beta\sigma\right) \quad \text{(B.3)}$$

Substituting $y = (t/\sigma + \beta\sigma)$ into equation (B.3) leads to

$$\int_0^{S_e} \frac{dS_e}{h^\beta} = \frac{e^{\frac{1}{2}\beta^2\sigma^2}}{(h_m)^\beta} \frac{1}{\sqrt{2\pi}} \int_y^{+\infty} e^{-\frac{1}{2}y^2} dy \quad \text{(B.4)}$$

According to the definition of complementary error function, equation (B.4) becomes

$$\int_0^{S_e} \frac{dS_e}{h^\beta} = \frac{1}{(h_m)^\beta} e^{\frac{1}{2}\beta^2\sigma^2} \left\{ \frac{1}{2} erfc\left[\frac{\ln(h/h_m)}{\sqrt{2}\sigma} + \frac{\beta\sigma}{\sqrt{2}} \right] \right\} \quad \text{(B.5)}$$

Similarly, substituting equation (3.3) into $\int_0^1 \frac{dS_e}{h^\beta}$ leads to the integrals

$$\int_0^1 \frac{dS_e}{h^\beta} = \frac{1}{\sqrt{2\pi}\sigma} \int_0^{+\infty} \frac{1}{h^{\beta+1}} e^{-\frac{(\ln h - \ln h_m)^2}{2\sigma^2}} dh \quad \text{(B.6)}$$

which becomes

$$\int_0^1 \frac{dS_e}{h^\beta} = \frac{1}{(h_m)^\beta} e^{\frac{1}{2}\beta^2\sigma^2} \tag{B.7}$$

Based on equation (3.3), one obtains

$$\frac{\ln(h/h_m)}{\sqrt{2}\sigma} = erfc^{-1}(2S_e) \tag{B.8}$$

Finally, substituting equation (B.1), (B.5), (B.7) and (B.8) into equation (3.4) gives

$$k_{rn} = (1-S_e)^\alpha \left\{ 1 - \frac{1}{2} erfc\left[erfc^{-1}(2S_e) + \frac{\beta\sigma}{\sqrt{2}} \right] \right\}^\eta \tag{B.9}$$

which is equal to equation (3.5).

APPENDIX C

RESULTS ON THE LOGARITHMIC SCALE

This appendix material includes the graphs which are obtained using the objective function C.1 shown below.

$$RMSE = \sqrt{\frac{1}{N-m}\sum_{i=1}^{N}\left[\log 10\left(k_{rn,i}\right) - \log 10\left(\hat{k}_{rn,i}\left(S_{ei}\right)\right)\right]^2} \tag{C.1}$$

where $k_{rn,i}$ and $\hat{k}_{rn,i}\left(S_{ei}\right)$ are the observed and calculated relative gas permeability, respectively. N is the number of measurements for each experimental sample and m is the number of fitted parameters.

It can be noticed that the fitting results on the logarithmic scale obtained here are similar to that acquired on the linear scale which is presented in the section 3. That is, the Burdine, Mualem and Alexander and Skaggs models, if used in their original form, but applied to the nonwetting phase, will lead to the worst predictions of measured relative gas permeability. However, allowing one parameter (either one) among the three semi-empirical parameters (α, β and η) of the generalized nonwetting phase relative permeability model to vary can improve the fit significantly, and further increasing the degrees of freedom to two and three yields an even better fit, though with less improvement as compared to the one fitted parameter case.

Figure C1 (logarithmic scale) corresponds to Figure 3.2 (linear scale).

Figure C2 (logarithmic scale) corresponds to Figure 3.3 (linear scale).

Figure C3 (logarithmic scale) corresponds to Figure 3.4 (linear scale).

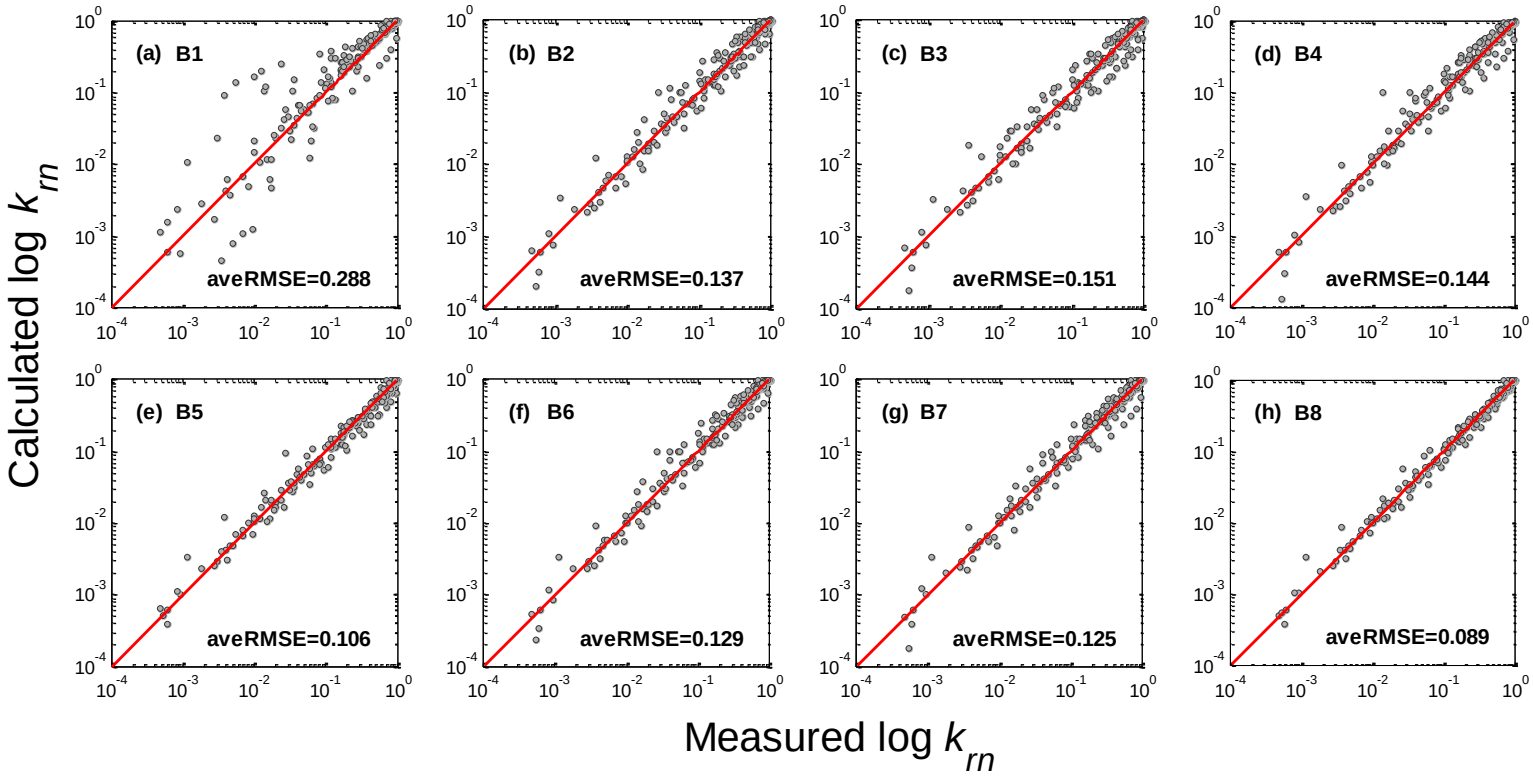

Figure C1 Scatter charts of measured versus calculated relative gas permeability for the cases (a) B1, (b) B2, (c) B3, (d) B4, (e) B5, (f) B6, (g) B7, and (h) B8 for the 17 data sets obtained with the objective function C.1.

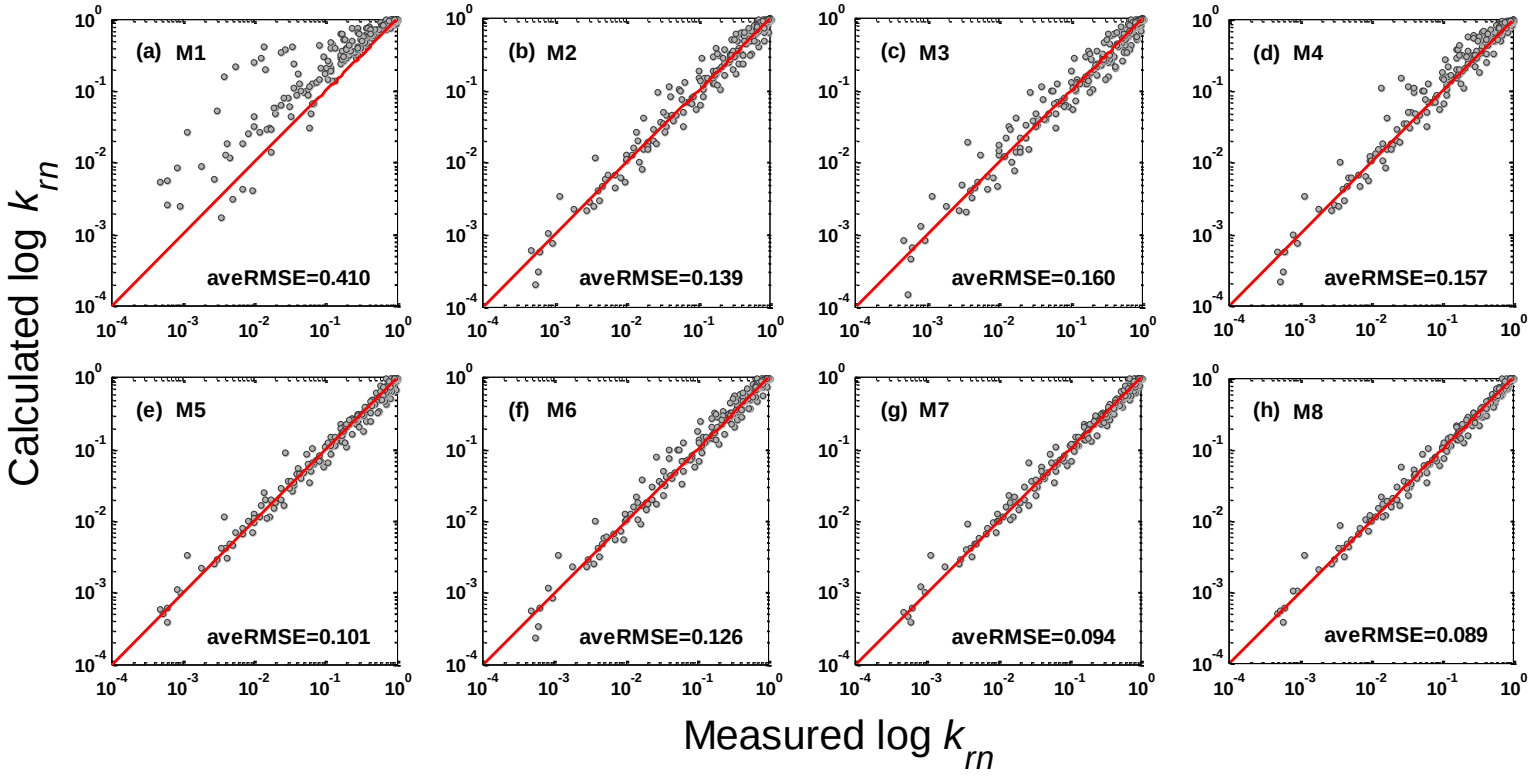

Figure C2 Scatter charts of measured versus calculated relative gas permeability for the methods (a) M1, (b) M2, (c) M3, (d) M4, (e) M5, (f) M6, (g) M7, and (h) M8 for the 17 data sets obtained with the objective function C.1.

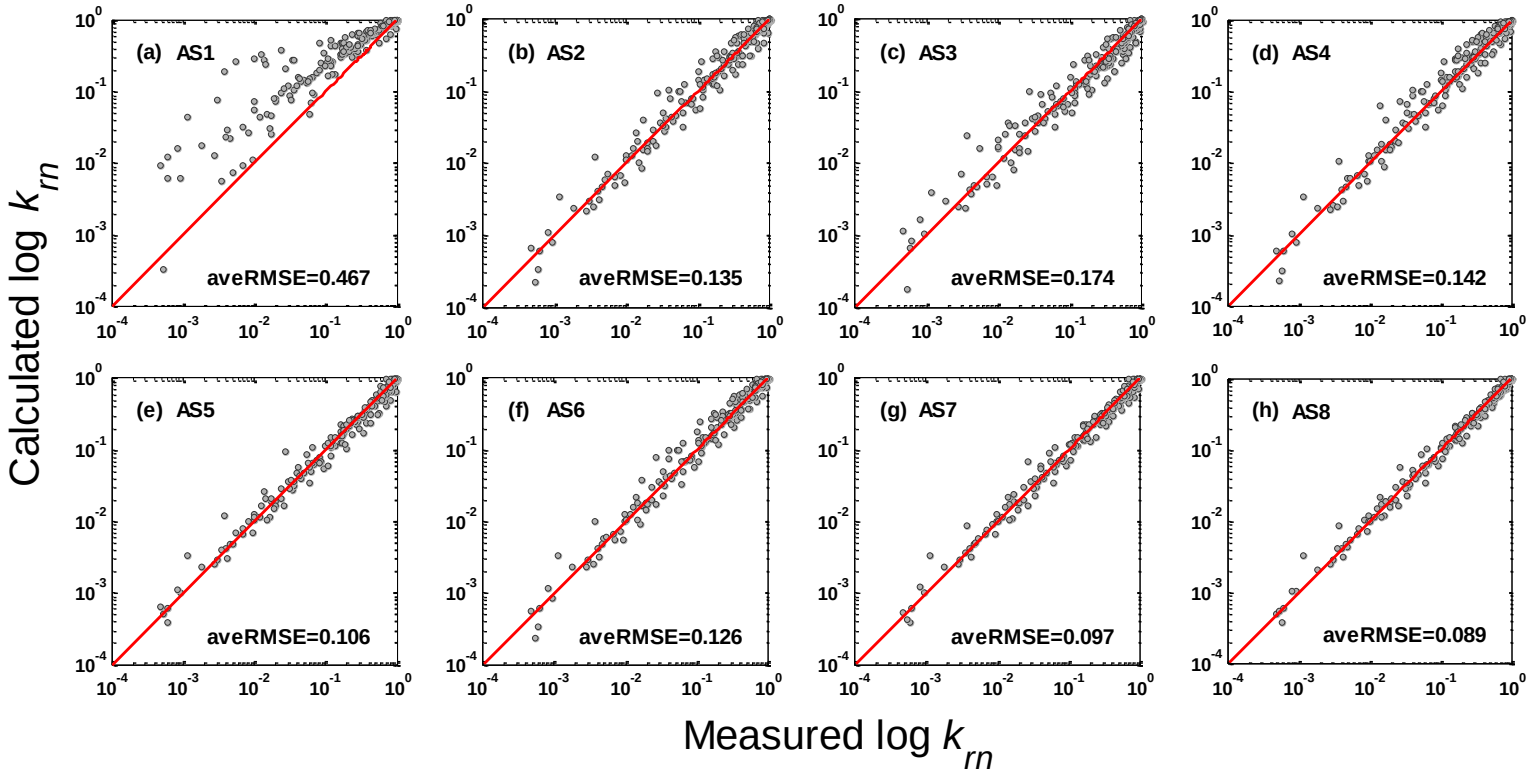

Figure C3 Scatter charts of measured versus calculated relative gas permeability for the methods (a) AS1, (b) AS2, (c) AS3, (d) AS4, (e) AS5, (f) AS6, (g) AS7, and (h) AS8 for the 17 data sets obtained with the objective function C.1.

APPENDIX D

DERIVATION OF THE ASSOULINE ET AL.–BURDINE (AB) MODEL FOR RELATIVE AIR PERMEABILITY GIVEN IN TABLE 4.2 AS EQUATION (4.8)

Based on the equation (4.5) and Table 4.1, the Burdine relative permeability model is given as

$$k_{ra} = (1-S_e)^2\left[\frac{\int_{S_e}^{1}\frac{dS_e}{h^2}}{\int_0^1\frac{dS_e}{h^2}}\right] = (1-S_e)^2\left[\frac{\int_0^1\frac{dS_e}{h^2}-\int_0^{S_e}\frac{dS_e}{h^2}}{\int_0^1\frac{dS_e}{h^2}}\right] = (1-S_e)^2\left[1-\frac{\int_0^{S_e}\frac{dS_e}{h^2}}{\int_0^1\frac{dS_e}{h^2}}\right] \tag{D.1}$$

Substituting equation (4.1) into $\int_0^{S_e}\frac{dS_e}{h^2}$ leads to the integrals

$$\int_0^{S_e}\frac{dS_e(h)}{h^2(S_e)} = -\xi\mu\int_{h_L}^{h(S_e)}\frac{1}{h^4}\left(\frac{1}{h}-\frac{1}{h_L}\right)^{\mu-1}\exp\left[-\xi\left(\frac{1}{h}-\frac{1}{h_L}\right)^{\mu}\right]dh \tag{D.2}$$

The change of variables $t = \left(h^{-1}-h_L^{-1}\right)^{\mu}$ yields

$$\int_0^{S_e}\frac{dS_e(h)}{h^2(S_e)} = \xi\int_0^t\frac{1}{h^2}e^{-\xi t}dt = \xi\int_0^t\left(t^{2/\mu}+\frac{2}{h_L}t^{1/\mu}+\frac{1}{h_L^2}\right)e^{-\xi t}dt \tag{D.3}$$

According to the definition of incomplete gamma function $\gamma(s,x)=\int_0^x t^{s-1}e^{-t}dt$ and due to $\int_0^x t^{s-1}e^{-\varepsilon t}dt = \varepsilon^{-s}\gamma(s,\varepsilon x)$ as well as $x = \left(h(S_e)^{-1}-h_L^{-1}\right)^{\mu}$, equation (D.3) becomes

$$\int_0^{S_e}\frac{dS_e(h)}{h^2(S_e)} = \xi^{-2/\mu}\gamma\left(1+\frac{2}{\mu},\xi x\right)+\frac{2}{h_L}\xi^{-1/\mu}\gamma\left(1+\frac{1}{\mu},\xi x\right)-\frac{1}{h_L^2}\left(e^{-\xi x}-1\right) \tag{D.4}$$

Since $\gamma\left(1+\frac{1}{\mu},\xi x\right) = \frac{1}{\mu}\gamma\left(\frac{1}{\mu},\xi x\right)-(\xi x)^{\frac{1}{\mu}}e^{-\xi x}$, and

$\gamma\left(1+\frac{2}{\mu},\xi x\right) = \frac{2}{\mu}\gamma\left(\frac{2}{\mu},\xi x\right)-(\xi x)^{\frac{2}{\mu}}e^{-\xi x}$, equation (D.4) eventually becomes

$$\int_0^{S_e} \frac{dS_e}{h^2} = \xi^{-2/\mu}\frac{2}{\mu}\gamma\left(\frac{2}{\mu},\xi x\right) + \frac{2}{h_L}\xi^{-1/\mu}\frac{1}{\mu}\gamma\left(\frac{1}{\mu},\xi x\right) - \frac{1}{h^2}e^{-\xi x} + \frac{1}{h_L^2} \tag{D.5}$$

Similarly, substituting equation (4.1) into $\int_0^1 \frac{dS_e}{h^2}$ yields the integrals

$$\int_0^1 \frac{dS_e(h)}{h^2(S_e)} = -\xi\mu\int_{h_L}^0 \frac{1}{h^4}\left(\frac{1}{h}-\frac{1}{h_L}\right)^{\mu-1}\exp\left[-\xi\left(\frac{1}{h}-\frac{1}{h_L}\right)^{\mu}\right]dh \tag{D.6}$$

Since at $S_e = 1$, $h = 0$, therefore, $x = \left(h^{-1} - h_L^{-1}\right)^{\mu} \to \infty$, in addition, because of

$$\gamma\left(\frac{1}{\mu},\infty\right) = \Gamma\left(\frac{1}{\mu}\right), \quad \gamma\left(\frac{2}{\mu},\infty\right) = \Gamma\left(\frac{2}{\mu}\right), \quad \text{and} \quad \lim_{h\to 0}\frac{1}{h^2}\exp\left[-\xi\left(\frac{1}{h}-\frac{1}{h_L}\right)^{\mu}\right] = 0, \tag{D.6}$$

finally becomes

$$\int_0^1 \frac{dS_e}{h^2} = \xi^{-2/\mu}\frac{2}{\mu}\Gamma\left(\frac{2}{\mu}\right) + \frac{2}{h_L}\xi^{-1/\mu}\frac{1}{\mu}\Gamma\left(\frac{1}{\mu}\right) + \frac{1}{h_L^2} \tag{D.7}$$

Finally, substituting equations (D.5) and (D.7) into equation (D.1) gives

$$k_{ra} = \left(1-S_e\right)^2\left[1 - \frac{\xi^{-2/\mu}\frac{2}{\mu}\gamma\left(\frac{2}{\mu},\xi x\right) + \frac{2}{h_L}\xi^{-1/\mu}\frac{1}{\mu}\gamma\left(\frac{1}{\mu},\xi x\right) - \frac{1}{h^2}e^{-\xi x} + \frac{1}{h_L^2}}{\xi^{-2/\mu}\frac{2}{\mu}\Gamma\left(\frac{2}{\mu}\right) + \frac{2}{h_L}\xi^{-1/\mu}\frac{1}{\mu}\Gamma\left(\frac{1}{\mu}\right) + \frac{1}{h_L^2}}\right] \tag{D.8}$$

which is equal to equation (4.8) shown in table 4.2.